View metadata, citation and similar papers at core.ac.uk
brought to you by CORE
provided by Repositori d'Objectes Digitals per a l'Ensenyament la Recerca i la Cultura

Facultat de Física
Departament de Física Teòrica

ELECTROMAGNETIC INTERACTIONS OF LIGHT HADRONS IN COVARIANT CHIRAL PERTURBATION THEORY

Ph.D. THESIS
November 13, 2016

Programa de Doctorat en Física

Submitted by:
Astrid Nathalie Hiller Blin

Supervised by:
Manuel Vicente Vacas
Cosupervised by:
Eulogio Oset Baguena

Kam, kam.
Kam ein Wort, kam.
kam durch die Nacht,
Wollt leuchten, wollt leuchten.

Asche.
Asche, Asche.
Nacht.

ENGFÜHRUNG, Paul Celan

D. Manuel Vicente Vacas, Profesor Titular de Física Teórica de la Universidad de Valencia, y D. Eulogio Oset Baguena, Catedrático de la Universidad de Valencia,

> CERTIFICAN: Que la presente Memoria *Electromagnetic interactions of light hadrons in covariant chiral perturbation theory* ha sido realizada bajo nuestra dirección en el Departament de Física Teòrica de la Universidad de Valencia por Astrid Nathalie Hiller Blin como Tesis para obtener el grado de Doctor en Física

Y para que así conste se presenta la referida Memoria, firmando el presente certificado.

Fdo: Manuel Vicente Vacas

Fdo: Eulogio Oset Baguena

CONTENTS

1 Introduction 1

2 Theoretical Tools 5

2.1 Chiral Lagrangians . . . 5

2.1.1 Transformations under chiral symmetry . . . 6

2.1.2 Formalism for $SU(2)$ . . . 7

2.1.3 Formalism for $SU(3)$ . . . 10

2.2 Power counting . . . 13

3 Neutral pion photoproduction 15

3.1 Introduction . . . 15

3.2 Formalism for pion photoproduction . . . 20

3.3 Calculation in chiral perturbation theory . . . 24

3.3.1 Renormalization . . . 27

3.3.2 Wave-function renormalization . . . 27

3.3.3 Higher-order corrections to low-energy constants . . . 29

3.4 Results . . . 32

3.4.1 Contributions up to $\mathcal{O}(p^3)$ . . . 32

3.4.2 Contributions up to $\mathcal{O}(p^{7/2})$ . . . 35

3.4.3 Photon asymmetries and differential cross sections . . . 38

3.4.4 Multipoles . . . 42

3.5 Summary and outlook . . . 44

4 Hyperon forward spin polarizabilities 47

4.1 Introduction . . . 47

4.2 Formalism for Compton scattering . . . 50

4.3 Theoretical model . . . 51

4.4 Results and discussion . . . 55
4.4.1 $SU(2)$ results revisited . . . 55
4.4.2 Extension to the $SU(3)$ sector . . . 56
4.5 Summary and outlook . . . 60

5 Octet-baryon electromagnetic form factors 63
5.1 Introduction . . . 63
5.2 Formalism . . . 67
5.2.1 Baryon form factors . . . 67
5.2.2 Calculation within chiral perturbation theory . . . 67
5.2.3 Vector-meson contributions . . . 71
5.2.4 Transverse electromagnetic densities . . . 74
5.3 Results and discussion . . . 77
5.3.1 Predictive contributions to the electric form factor . . . 77
5.3.2 Spectral functions . . . 81
5.3.3 Charge and magnetic transverse densities . . . 89
5.4 Summary and outlook . . . 93

6 CP-violating η and η' decays: relation with the neutron electric dipole moment 97
6.1 Introduction . . . 97
6.2 The CP violating $\eta^{(\prime)} \to \pi\pi$ decay . . . 99
6.3 The CP-violating coupling of the η and the η' to the nucleon . . . 100
6.4 The CP-conserving coupling of the η and the η' to the nucleon . . . 104
6.5 Couplings with vector mesons . . . 105
6.6 Calculation of the nucleon EDM . . . 106
6.7 Summary and outlook . . . 111

7 Summary and conclusions 113

8 Resumen en español 121
8.1 Objetivos . . . 121
8.2 Metodología . . . 125
8.3 Resultados . . . 127

Appendix A Multipole decomposition of amplitudes 135

Appendix B List of diagrams and amplitudes 139
B.1 Amplitudes of pion photoproduction . . . 139
B.2 Compton-scattering amplitudes . . . 148

Appendix C Algebra for loop calculations 155

Appendix D Computational tools 159
D.1 FORM 159
D.2 Mathematica 160
D.2.1 FeynCalc and LoopTools 160
D.2.2 Determining the PCBT 161
D.3 Numerics 161

List of figures 163

List of tables 167

Glossary 171

Acknowledgements 173

Bibliography 175

CHAPTER **1**

INTRODUCTION

The interactions between light hadrons and photon fields are an important probe of the structure of matter and the underlying strong interaction. Their fundamental properties are described by quantum chromodynamics (QCD). At high energies, this theory is well understood and tested in a perturbative approach with quark and gluon fields as degrees of freedom. At low energies, however, QCD is non-perturbative, and many details remain unclear. These are the energies necessary to describe interactions between the hadrons at distances larger than their size.

Processes that involve electromagnetic interactions with hadrons have been thoroughly studied throughout the decades, both in experimental facilities, as well as from the theoretical point of view. Here I will focus on the low-energy limit of a few of them, namely the photoproduction of neutral pions, as well as Compton and elastic electron scattering off baryon targets. In particular, this thesis contains the following main studies at energies where QCD is non-perturbative: the extraction of the cross sections of pion photoproduction, the study of baryon polarizabilities and electromagnetic form factors, and a calculation of CP-violating decays in nature. They shed light onto the baryons' inner structure, giving information about their densities and, as a consequence, indirectly also their parton distributions. Furthermore, they lead to a better understanding of the interaction between and within hadrons. By studying cross sections one also gets information about resonant states that arise due to the excitation of the light hadrons. They appear as poles in the amplitudes of the electromagnetic interactions studied, considerably affecting the behaviour of the observables.

In order to motivate the choice of the global theoretical framework for this thesis, Chiral Perturbation Theory (ChPT), it is important to first understand QCD, its underlying theory. As mentioned, this gauge theory successfully

describes strong interactions at high energies, taking quarks and gluons as degrees of freedom for matter and exchange-particle fields, respectively. At energies of a few GeV and higher, the quarks confined in hadrons can be treated as asymptotically free, and methods of perturbative QCD can be used in an expansion in orders of the strong coupling constant $\alpha_s \ll 1$. The corresponding symmetry group, (colour) $SU(3)$, is non-Abelian. This leads to gluon-field self-interactions, affecting the running of the strong coupling: at low energies, or equivalently at large distances, the value of α_s grows. At a scale of $\Lambda \approx 1$ GeV, the strong coupling constant α_s becomes too high, and perturbative QCD breaks down. This scale corresponds to lengths greater than the size of the nucleon, and therefore may also be understood as a confinement scale for the quarks within it.

The processes in this thesis take place at center-of-mass energies well below Λ. Due to the breakdown of the perturbative series of QCD in this energy region, an alternative approach is needed. Many models fulfilling some low-energy theorems (LETs) deduced from QCD, gauge invariance and other symmetries were abundantly employed to study this kind of processes. However, no systematic method existed that would allow to calculate higher orders in momenta or masses of the particles, in order to go beyond the low-energy limits. Thus, it is of advantage to find an effective field theory (EFT) that maintains the symmetries of QCD, and on top of that is applicable to the study of all these low-energy processes, in a systematic and comprehensive fashion.

Throughout the following chapters, I focus on the light hadrons, i.e., those composed only by the u, d and s quarks, which obey an approximate (flavour) $SU(3)$ symmetry. In the relativistic limit of vanishing light-quark masses, the left- and right-handed quark fields q_L and q_R are decoupled from each other, which leads to a theory invariant under chiral transformations, discussed in Chapter 2. Two observations suggest that a spontaneous breaking of this symmetry of the chiral limit of QCD happens. On the one hand, in nature the pseudoscalar meson-octet members have a mass which is small in relation to the scale Λ. These mesons are therefore good candidates for the Goldstone bosons of a spontaneous symmetry breaking. On the other hand, the baryon-octet members appear only with positive parity, while an exact symmetry would call for the existence of the corresponding negative-parity states with the same masses. Indeed, in the fermion sector it is the spontaneous breaking of chiral symmetry that generates the masses of the $SU(3)$ baryon flavour octet, which in the chiral limit are degenerate. Additionally, the masses of the pseudo-Goldstone bosons are interpreted as a consequence of an explicit symmetry breaking due to the non-vanishing quark masses.

In fact, in the frame of ChPT, these spontaneously and explicitly broken symmetries are used as a basis to construct the interaction Lagrangians, lead-

ing to an EFT of QCD at low energies. Instead of taking α_s as the perturbation parameter, now a combined chiral expansion in powers of external momenta and of the Goldstone-meson masses is made, both of which are small when compared to the confinement scale. The degrees of freedom of QCD, the quarks and the gluons, are integrated out, and the interactions described are directly between the compound states, the baryons and the mesons. This EFT is valid for energy regions significantly lower than $\Lambda \approx 1$ GeV, which correspond to distances larger than the baryon size.

The current-quark masses of the u and the d are much smaller than any hadronic scale, therefore guaranteeing a fast convergence of the chiral series when treating pion interactions only, i.e., when considering an $SU(2)$ flavour symmetry. The extension of ChPT to $SU(3)$ to accommodate the s quark, and thus the full pseudoscalar meson octet, requires great care, since this quark's current mass is closer to the order of magnitude of the scale Λ. The inclusion of baryons in ChPT introduces an additional scale, the baryon mass in the chiral limit.

How fast the ChPT calculations converge strongly depends on the degrees of freedom included. In this work, I did not only take into account the interactions with the spin-1/2 baryon octet — the nucleons and hyperons —, but also with the spin-3/2 resonances. These form an isospin quadruplet in $SU(2)$ and a decuplet in $SU(3)$. They couple strongly to the baryon octet, and therefore appear very easily as excited states, or resonances, of the spin-1/2 states. Knowing this, it is clear that they are expected to give important contributions to processes that range in energies close to their masses. This is indeed the case of the reactions studied in the following chapters. Needless to say, they have masses larger than Λ. In fact, when introducing these states into the framework of ChPT, one obtains an additional small parameter apart from the small meson masses and external momenta: the difference between the decuplet and the octet-baryon masses.

Divergences in ChPT are renormalized order by order, by absorbing them into the coefficients of the most general Lagrangian. This procedure leads to the appearance of low-energy constants (LECs), which have to be determined by data fits. This reduces the predictive quality of the theory. Nevertheless, many of these constants have already been determined over the past few decades, and one can use their literature values in order to make new predictions.

When including baryons in ChPT, the chiral power counting in terms of momenta and masses is spoiled. This is due to their mass being of the order of Λ. As a result, a priori there is no clear way to associate a specific chiral order with a definite number of loops. This was first resolved by treating the baryons in the non-relativistic limit of heavy-baryon ChPT (HBChPT) [1].

This framework was applied, e.g., for the extraction of baryon electromagnetic form factors in Ref. [2]. A relativistic alternative approach to evaluate the loop corrections has been proposed in the late 1990's [3–5]. This so-called infrared regularization (IR) separates the loop integration into an infrared-singular and an infrared-regular part. The singular part satisfies power counting, whereas the regular one can be absorbed into local counter terms of the Lagrangian. This technique solves the power-counting problem of relativistic baryon ChPT.

In the scope of this thesis, calculations have been made with another relativistic renormalization procedure, the Extended On Mass Shell (EOMS) scheme [6, 7]. It fully satisfies analyticity, and usually converges faster than non-relativistic approaches and the IR scheme. Divergences and power-counting breaking terms (PCBT) that spoil the chiral series have fully analytical expressions. Therefore, they can be identified with terms of the Lagrangian, and absorbed into the corresponding LECs. This scheme has shown to be successful in many works [8–20], and can be implemented in a straightforward way.

The present thesis contains four main studies. Each is described in a dedicated chapter with separate introductions and conclusions. Nevertheless, a global description of the ChPT formalism, which applies to all of them, is given in Chapter 2. In Chapter 3, I show my work on studying the neutral pion photoproduction off proton targets, which relies on an $SU(2)$ framework. This framework is extended to $SU(3)$ in Chapter 4, in order to embed the s quark. There, the forward spin polarizabilities of nucleons and hyperons are studied with the help of Compton scattering. Also within $SU(3)$, Chapter 5 focuses on elastic electron scattering for the extraction of baryon electromagnetic form factors. These are then related to charge and magnetic densities via a dispersive analysis. Chapter 6 shows a study of the connection between flavour-conserving processes that show strong CP violation and the nucleon electric dipole moment (EDM). Finally, I present the conclusions of the work in Chapter 7, as well as an outlook to possible extensions of the processes studied.

CHAPTER **2**

THEORETICAL TOOLS

2.1 Chiral Lagrangians

In this chapter, I introduce the main language used throughout this thesis, Chiral Perturbation Theory. Chiral effective-Lagrangian techniques were introduced by Weinberg and Dashen [21, 22] in the late 1960's to simplify current-algebra calculations. Originally developed for the lightest pseudo-Goldstone bosons by Gasser and Leutwyler, ChPT emerged as an effective field theory for pion dynamics [23, 24]. It is constructed by taking into consideration the most general interactions allowed by the symmetries of QCD. The lowest chiral order is a tree-level description, while higher orders also include loop corrections. In this expansion, the interaction among the pions is weak, and can be treated perturbatively. In the chiral limit of vanishing light-quark masses and at leading order, all scattering processes among the pions are determined by only one parameter, the weak decay constant of the pion F_π. It sets the relevant scale of chiral symmetry to $\Lambda \simeq 4\pi F_\pi \simeq 1$ GeV [25]. This is also the scale of spontaneous chiral-symmetry breaking and of the breakdown of perturbative QCD.

In Sec. 2.1.1, I give a brief introduction on the transformations under which the chiral Lagrangians remain invariant. The construction of the Lagrangian and a general good overview on ChPT and its applications to nucleons and nuclei is given in Refs. [26, 27], and a more pedagogical review in the work of Scherer [28]. The inclusion of the spin-3/2 states is very well discussed in Ref. [29].

Throughout the thesis, I use two formulations of ChPT. In Sec. 2.1.2, I begin with the formalism based on an $SU(2)$ chiral symmetry. It describes processes with photons, pions, nucleons and the $\Delta(1232)$, and is used in Chapter 3. In Sec. 2.1.3, this framework is extended to an $SU(3)$ symmetry, adding kaons,

the η, hyperons and the remaining baryon-decuplet members to the particle spectrum. This formalism is used in Chapters 4 to 6. Furthermore, I stress the connection between the two formalisms, in particular concerning the relations between the low-energy constants.

2.1.1 Transformations under chiral symmetry

ChPT relies on the global $SU_L(n_F) \times SU_R(n_F)$ symmetry of the massless QCD Lagrangian. Here, the left-handed (L) and right-handed (R) fields are transformed separately, and n_F is the number of light quarks taken into account. In the present work, this means either $SU(2)$, if only the u and d quarks are considered, or $SU(3)$, for the inclusion of the s quark.

In $SU(2)$, the matter fields and external fields considered are mesons U, photons v_μ, nucleons Ψ and the spin-3/2 resonance Δ_μ. Under the $SU(2)$ chiral symmetry, they transform as [28, 29]:

$$\begin{aligned} U &\to RUL^\dagger, \\ v_\mu &\to K v_\mu K^\dagger + \mathrm{i}(\partial_\mu K)K^\dagger, \\ \Psi &\to K\Psi, \\ \Delta_\mu &\to K_4 \Delta_\mu, \end{aligned} \tag{2.1}$$

where R and L are elements of $SU(2)_R$ and $SU(2)_L$, respectively. This means that they can be written as

$$\exp\left[-\mathrm{i}\sum_{a=1}^{3} c_a \frac{\sigma_a}{2}\right], \tag{2.2}$$

where the c_a are real numbers and the σ_a are the generating matrices of the considered groups, namely the $SU(2)$ Pauli matrices (for $SU(3)$, the generating matrices are the eight Gell-Mann matrices). The covariant derivatives of the fields are defined such that they transform like the fields themselves. Furthermore,

$$\begin{aligned} K &= \sqrt{RUL^\dagger}^{-1} R \sqrt{U}, \\ K_4 &= T^{a\dagger} K T^b K^{ab}, \quad K^{ab} = \frac{\mathrm{Tr}(\sigma^a K \sigma^b K^\dagger)}{2}, \end{aligned} \tag{2.3}$$

and the transition matrices T between isospin-1/2 and isospin-3/2 states are defined below.

Note that in $SU(3)$ the transformations are analogous, with the difference that the octet baryons B transform as

$$B \to KBK^\dagger, \tag{2.4}$$

and the decuplet baryons T_μ defined in Eq. (2.39) as

$$T_\mu^{abc} \to K_T^{ad} K_T^{be} K_T^{cf} T_\mu^{def}, \tag{2.5}$$

where K_T^{ab} is the matrix element in row a and column b of the matrix K.

2.1.2 Formalism for $SU(2)$

In order to construct the Lagrangians, one has to decide on how to express them in terms of a power-counting scheme. ChPT has originally been developed to describe meson interactions and their couplings to the electromagnetic field [23, 24, 30]. There, a simultaneous expansion with respect to the small pion mass and small external momenta, each of chiral order $\mathcal{O}(p)$, is made. The leading-order Lagrangian that fulfills the symmetries introduced in Sec. 2.1.1 is then of chiral $\mathcal{O}(p^2)$, and given by

$$\mathcal{L}_\pi^{(2)} = \frac{F_0^2}{4} \mathrm{Tr}\big[\mathrm{D}_\mu U (\mathrm{D}^\mu U)^\dagger + \chi U^\dagger + U \chi^\dagger\big]. \tag{2.6}$$

The covariant derivative on the meson fields

$$U = \exp\left(\frac{\mathrm{i}\Pi}{F_0}\right), \quad \Pi = \begin{pmatrix} \pi^0 & \sqrt{2}\pi^+ \\ \sqrt{2}\pi^- & -\pi^0 \end{pmatrix} \tag{2.7}$$

acts as

$$\mathrm{D}_\mu U = \partial_\mu U - \mathrm{i} r_\mu U + \mathrm{i} U l_\mu, \tag{2.8}$$

with the external right and left-handed fields r_μ and l_μ, and where F_0 is related to the pion-decay constant F_π via $F_0 = F_\pi + \mathcal{O}(p^2)$. The explicit breaking of the chiral symmetry is given by the term χ [31]. In the isospin limit of equal pion masses m_π, it is given by $\chi = m_\pi^2$. The photon field $\mathcal{A}_\mu$ couples through

$$r_\mu = l_\mu = v_\mu = \frac{e}{2} \mathcal{A}_\mu (\mathbb{I}_2 + \sigma_3), \tag{2.9}$$

where σ_3 is the diagonal Pauli matrix, v_μ the photon vector field and e the (negative) electron charge.

The processes described in this thesis also include interactions with nucleons, so one additionally needs the Lagrangians describing these degrees of freedom.

The naming conventions for the LECs used here follow those introduced in Ref. [32]. The first-order Lagrangian is given by

$$\mathcal{L}_N^{(1)} = \bar{\Psi}\left(\mathrm{i}\not{D} - m + \frac{g_0}{2}\not{u}\gamma_5\right)\Psi, \tag{2.10}$$

where Ψ is the nucleon doublet $(p,n)^T$ with mass m, and the covariant derivative is given by

$$\mathrm{D}_\mu = (\partial_\mu + \Gamma_\mu)\,, \quad \Gamma_\mu = \frac{1}{2}\left[u^\dagger(\partial_\mu - \mathrm{i}r_\mu)u + u(\partial_\mu - \mathrm{i}l_\mu)u^\dagger\right]. \tag{2.11}$$

The meson fields appear through $u^2 = U$ and

$$u_\mu = \mathrm{i}\left[u^\dagger(\partial_\mu - \mathrm{i}r_\mu)u - u(\partial_\mu - \mathrm{i}l_\mu)u^\dagger\right]. \tag{2.12}$$

The LEC g_0 is the leading contribution to the physical axial-vector coupling constant $g_A = g_0 + \mathcal{O}(p^2)$.

At second order, the only relevant terms for this thesis are

$$\mathcal{L}_N^{(2)} = \frac{1}{8m}\bar{\Psi}\left(c_6 f_{\mu\nu}^+ + c_7 \mathrm{Tr}\left[f_{\mu\nu}^+\right]\right)\sigma^{\mu\nu}\Psi + \ldots, \tag{2.13}$$

where

$$f_{\mu\nu}^+ = u f_{\mu\nu}^L u^\dagger + u^\dagger f_{\mu\nu}^R u, \quad f_{\mu\nu}^R = f_{\mu\nu}^L = \partial_\mu v_\nu - \partial_\nu v_\mu - \mathrm{i}\left[v_\mu, v_\nu\right] \tag{2.14}$$

for the processes considered here, and where

$$\sigma^{\mu\nu} = \mathrm{i}\gamma^{\mu\nu} = \frac{\mathrm{i}}{2}\left[\gamma^\mu, \gamma^\nu\right]. \tag{2.15}$$

For the proton-photon coupling, the LECs c_6 and c_7 appear as the combination $\tilde{c}_{67} = c_6 + c_7$. More terms appear in the second-order Lagrangian, but they describe only vertices that do not appear in the processes considered in the present thesis.

Finally, at third order, the relevant terms of the Lagrangian are

$$\begin{aligned}\mathcal{L}_N^{(3)} =& d_8 \frac{\mathrm{i}}{2m}\left\{\bar{\Psi}\varepsilon^{\mu\nu\alpha\beta}\mathrm{Tr}\left[\tilde{f}_{\mu\nu}^+ u_\alpha\right]\mathrm{D}_\beta\Psi\right\} + \text{h.c.} \\ &+ d_9 \frac{\mathrm{i}}{2m}\left\{\bar{\Psi}\varepsilon^{\mu\nu\alpha\beta}\mathrm{Tr}\left[f_{\mu\nu}^+\right]u_\alpha \mathrm{D}_\beta\Psi\right\} + \text{h.c.} \\ &+ d_{16}\frac{1}{2}\left\{\bar{\Psi}\gamma^\mu\gamma_5\mathrm{Tr}[\chi_+]u_\mu\Psi\right\}\end{aligned}$$

$$+d_{18}\frac{\mathrm{i}}{2}\left\{\bar{\Psi}\gamma^{\mu}\gamma_5[\mathrm{D}_{\mu},\chi_-]\Psi\right\}+\ldots, \tag{2.16}$$

where

$$\tilde{f}^{+}_{\mu\nu}=f^{+}_{\mu\nu}-\frac{1}{2}\mathrm{Tr}[f^{+}_{\mu\nu}],\quad \chi_{\pm}=u^{\dagger}\chi u^{\dagger}\pm u\chi^{\dagger}u. \tag{2.17}$$

Here, I use the convention $\varepsilon^{0123}=-\varepsilon_{0123}=-1$. For the process studied in Chapter 3, the LECs appear in the combinations $\tilde{d}_{89}=d_8+d_9$ and $\tilde{d}_{168}=2d_{16}-d_{18}$.

One possible description of the couplings with the $\Delta(1232)$ uses consistent Lagrangians which ensure the decoupling of the spurious spin-1/2 components of the Rarita–Schwinger (RS) field $\Delta_\nu=(\Delta^{++}_\nu,\Delta^{+}_\nu,\Delta^{0}_\nu,\Delta^{-}_\nu)^T$ of mass M_Δ [29, 33–35]. The relevant pieces are

$$\begin{aligned}
\mathcal{L}^{(1)}_{\Delta\pi N}=&\frac{\mathrm{i}h_A}{2F_0M_\Delta}\bar{\Psi}T^a\gamma^{\mu\nu\lambda}(\partial_\mu\Delta_\nu)(\mathrm{D}^{ab}_\lambda\pi^b)+\mathrm{h.c.},\\
\mathcal{L}^{(2)}_{\Delta\pi N}=&\frac{h_1}{2F_0M_\Delta^2}\bar{\Psi}T^a\gamma^{\mu\nu\lambda}(\partial_\lambda\not{\partial}\pi^a)(\partial_\mu\Delta_\nu)+\mathrm{h.c.},\\
\mathcal{L}^{(2)}_{\Delta\gamma N}=&\frac{3\mathrm{i}eg_M}{2m(m+M_\Delta)}\bar{\Psi}T^3(\partial_\mu\Delta_\nu)\tilde{F}^{\mu\nu}+\mathrm{h.c.},\\
\mathcal{L}^{(3)}_{\Delta\gamma N}=&-\frac{3eg_E}{2m(m+M_\Delta)}\bar{\Psi}T^3\gamma_5(\partial_\mu\Delta_\nu)F^{\mu\nu}+\mathrm{h.c.},
\end{aligned} \tag{2.18}$$

where

$$\gamma^{\mu\nu\lambda}=\frac{1}{2}\left\{\gamma^{\mu\nu},\gamma^{\lambda}\right\},\quad \mathrm{D}^{ab}_\lambda\pi^b=\delta^{ab}\partial_\lambda\pi^b-\mathrm{i}eQ^{ab}_\pi\mathcal{A}_\lambda\pi^b,\quad Q^{ab}_\pi=-\mathrm{i}\epsilon^{ab3}, \tag{2.19}$$

and π^a are the isospin-triplet pion-field components

$$\begin{aligned}
\pi^1&=\frac{\pi^++\pi^-}{\sqrt{2}}\\
\pi^2&=\mathrm{i}\frac{\pi^+-\pi^-}{\sqrt{2}},\\
\pi^3&=\pi^0.
\end{aligned} \tag{2.20}$$

The electromagnetic field and its dual are given by

$$F^{\mu\nu}=\partial^\mu\mathcal{A}^\nu-\partial^\nu\mathcal{A}^\mu,$$

$$\tilde{F}^{\mu\nu} = \frac{1}{2}\epsilon^{\mu\nu\alpha\beta}F_{\alpha\beta}, \tag{2.21}$$

respectively. There are two couplings (h_A, h_1) for the pion transition and two (g_M, g_E) for the electromagnetic transition between the spin-3/2 states and the nucleons. The latter starts only at second chiral order. Therefore, diagrams in the present thesis which involve photons and include the $\Delta(1232)$ are necessarily higher-order corrections. At third order, the Lagrangian contains an additional $\gamma N\Delta$ Coulomb coupling which vanishes for real photons. The values for h_A and h_1 are related to the Δ width [36]. The couplings g_M and g_E can be obtained in fits to pion electromagnetic production at energies around the resonance peak [37]. The conventions and definitions for the isospin operators T^i follow Ref. [29]:

$$\begin{aligned}
T^1 =& \frac{1}{\sqrt{6}}\begin{pmatrix} -\sqrt{3} & 0 & 1 & 0 \\ 0 & -1 & 0 & \sqrt{3} \end{pmatrix}, \\
T^2 =& \frac{-\mathrm{i}}{\sqrt{6}}\begin{pmatrix} \sqrt{3} & 0 & 1 & 0 \\ 0 & 1 & 0 & \sqrt{3} \end{pmatrix}, \\
T^3 =& \sqrt{\frac{2}{3}}\begin{pmatrix} 0 & 1 & 0 & 0 \\ 0 & 0 & 1 & 0 \end{pmatrix}.
\end{aligned} \tag{2.22}$$

2.1.3 Formalism for $SU(3)$

In $SU(3)$, the Lagrangians involve the pseudoscalar octet mesons ϕ, the octet baryons B, the decuplet baryons T_μ and the photons $v_\mu = e\mathcal{A}_\mu Q$. The corresponding matrices are defined in Eqs. (2.30) to (2.32) and (2.39). The lowest-order chiral Lagrangian involving only photons and the two hadron octets reads

$$\mathcal{L} = \mathcal{L}^{(2)}_{\phi\phi} + \mathcal{L}^{(1)}_{\phi B}, \tag{2.23}$$

where

$$\mathcal{L}^{(2)}_{\phi\phi} = \frac{F_0^2}{4}\mathrm{Tr}\left(u_\mu u^\mu + \chi_+\right) \tag{2.24}$$

is the $\mathcal{O}(p^2)$ meson Lagrangian, and

$$\mathcal{L}^{(1)}_{\phi B} = \mathrm{Tr}\left(\bar{B}(\mathrm{i}\not{D} - m)B\right) + \frac{D}{2}\mathrm{Tr}\left(\bar{B}\gamma^\mu\gamma_5\left\{u_\mu, B\right\}\right) + \frac{F}{2}\mathrm{Tr}\left(\bar{B}\gamma^\mu\gamma_5\left[u_\mu, B\right]\right) \tag{2.25}$$

is the $\mathcal{O}(p^1)$ Lagrangian that includes octet baryons. The commutator and anticommutator refer to flavour space. Here, m and F_0 denote the baryon octet

mass and the meson-decay constant, respectively, both in the chiral limit. The vielbein u_μ and the covariant derivative D_μ read

$$u_\mu = \mathrm{i}\left\{u^\dagger, \nabla_\mu u\right\}, \tag{2.26}$$

$$\mathrm{D}_\mu B = \partial_\mu B + [\Gamma_\mu, B], \tag{2.27}$$

where

$$\nabla_\mu u = \partial_\mu u - \mathrm{i}(v_\mu + a_\mu)u + \mathrm{i}u(v_\mu - a_\mu), \tag{2.28}$$

$$\Gamma_\mu = \frac{1}{2}[u^\dagger, \partial_\mu u] - \frac{\mathrm{i}}{2}u^\dagger(v_\mu + a_\mu)u - \frac{\mathrm{i}}{2}u(v_\mu - a_\mu)u^\dagger. \tag{2.29}$$

When working exclusively with external photon fields, the axial field a_μ can be set to 0. The LECs D and F are determined from nucleon and hyperon β decays, where the combination $F + D$ corresponds to the LEC g_0 in the $SU(2)$ limit. The explicit forms of the 3×3 charge matrix Q, and of the 3×3 matrices for mesons ϕ and baryons B are given in terms of the Gell-Mann matrices λ_i:

$$Q = \frac{1}{2}\left(\lambda_3 + \frac{\lambda_8}{\sqrt{3}}\right) = \begin{pmatrix} \frac{2}{3} & 0 & 0 \\ 0 & -\frac{1}{3} & 0 \\ 0 & 0 & -\frac{1}{3} \end{pmatrix}, \tag{2.30}$$

$$\phi = \frac{1}{\sqrt{2}}\sum_{a=1}^{8}\lambda_a\phi^a = \begin{pmatrix} \frac{1}{\sqrt{2}}\pi^0 + \frac{1}{\sqrt{6}}\eta & \pi^+ & K^+ \\ \pi^- & -\frac{1}{\sqrt{2}}\pi^0 + \frac{1}{\sqrt{6}}\eta & K^0 \\ K^- & \bar{K}^0 & -\frac{2}{\sqrt{6}}\eta \end{pmatrix} \tag{2.31}$$

and

$$B = \frac{1}{\sqrt{2}}\sum_{a=1}^{8}\lambda_a B^a = \begin{pmatrix} \frac{1}{\sqrt{2}}\Sigma^0 + \frac{1}{\sqrt{6}}\Lambda & \Sigma^+ & p \\ \Sigma^- & -\frac{1}{\sqrt{2}}\Sigma^0 + \frac{1}{\sqrt{6}}\Lambda & n \\ \Xi^- & \Xi^0 & -\frac{2}{\sqrt{6}}\Lambda \end{pmatrix}. \tag{2.32}$$

Note that the usual convention for the meson field ϕ in Eq. (2.31) differs from the $SU(2)$ case of Π in Eq. (2.7), when reduced to it, by an overall factor $\sqrt{2}$. Therefore,

$$u^2 = U = \exp\left(\frac{\mathrm{i}\sqrt{2}\phi}{F_0}\right). \tag{2.33}$$

Otherwise, definitions and conventions are as introduced in Sec. 2.1.2.

In the present work, the baryon decuplet is also included. The relevant terms of the Lagrangian that couples these decuplet fields T_μ to the octets of baryons and mesons are given in Refs. [19, 38, 39], where the lowest-order terms read

$$\begin{aligned}\mathcal{L}^{(1)}_{T\phi} =& \bar{T}^{abc}_\mu(\mathrm{i}\gamma^{\mu\nu\alpha}\mathrm{D}_\alpha - M_\Delta\gamma^{\mu\nu})T^{abc}_\nu \\ &+ \frac{\mathrm{i}\mathcal{H}}{M_\Delta F_0}\bar{T}^{abc}_\mu\gamma^{\mu\nu\rho\sigma}\gamma_5(\partial_\rho T^{abd}_\nu)\partial_\sigma\phi^{cd},\end{aligned} \tag{2.34}$$

$$\mathcal{L}^{(1)}_{TB\phi} = \frac{\mathrm{i}\mathcal{C}}{M_\Delta}\epsilon^{ilm}\left[(\partial_\mu\bar{T}^{ijk}_\nu)\gamma^{\mu\nu\rho}u^{jl}_\rho B^{km} + \mathrm{h.c.}\right]. \tag{2.35}$$

Here,

$$\gamma^{\mu\nu\rho\sigma} = \frac{1}{2}\left[\gamma^{\mu\nu\rho},\gamma^\sigma\right]. \tag{2.36}$$

The covariant derivative acts on the decuplet as

$$\mathrm{D}_\alpha T^{abc}_\nu = \partial_\alpha T^{abc}_\nu + (\Gamma_\alpha, T_\nu)^{abc}, \tag{2.37}$$

$$(X,Y)^{abc} = X^{ad}Y^{dbc} + X^{bd}Y^{adc} + X^{cd}Y^{abd}. \tag{2.38}$$

The vielbein u_ρ is defined in Eq. (2.26). The decuplet states T^{ijk}_μ of mass M_Δ are given by

$$\begin{aligned}T^{111}_\mu =& \Delta^{++}_\mu\,,\ T^{112}_\mu = \frac{1}{\sqrt{3}}\Delta^{+}_\mu\,,\ T^{122}_\mu = \frac{1}{\sqrt{3}}\Delta^{0}_\mu\,,\ T^{222}_\mu = \Delta^{-}_\mu\,,\\ T^{113}_\mu =& \frac{1}{\sqrt{3}}\Sigma^{*+}_\mu\,,\ T^{123}_\mu = \frac{1}{\sqrt{6}}\Sigma^{*0}_\mu\,,\ T^{223}_\mu = \frac{1}{\sqrt{3}}\Sigma^{*-}_\mu\,,\\ T^{133}_\mu =& \frac{1}{\sqrt{3}}\Xi^{*0}_\mu\,,\ T^{233}_\mu = \frac{1}{\sqrt{3}}\Xi^{*-}_\mu\,,\ T^{333}_\mu = \Omega^{-}_\mu.\end{aligned} \tag{2.39}$$

When performing the calculations with the $SU(3)$ Lagrangian, and then setting the kaon and η loops to zero, one reproduces the $SU(2)$ result with the LEC correspondence $\mathcal{C} = -\frac{h_A}{2\sqrt{2}}$ and $\mathcal{H} = -\frac{\sqrt{2}H_A}{2}$. Nevertheless, when including the additional $SU(3)$ loops, a new fit to decay-width data has to be performed [19], and those new values should be used for $\mathcal{C}$ and $\mathcal{H}$ in the calculations.

One next-to-leading order term is also needed in the present thesis, in particular for Chapter 4. It describes the electromagnetic transition between the decuplet and the octet baryons. It is added by extending Eq. (2.18) to $SU(3)$:

$$\mathcal{L}^{(2)}_{TB} = \frac{3\mathrm{i}eg_M}{\sqrt{2}m(m+M_\Delta)}\bar{B}^{ab}\varepsilon^{cda}Q^{ce}(\partial_\mu T_\nu)^{dbe}\tilde{F}^{\mu\nu} + \mathrm{h.c.}\,. \tag{2.40}$$

2.2 Power counting

While the baryon ChPT power-counting problem [40] is solved in the EOMS scheme as explained in Appendix C, special care is needed when taking the spin-3/2 states into account. Besides the pion mass and the external momenta, another small parameter appears, $\delta = M_\Delta - m \approx 300$ MeV, which is heavier than $m_\pi \approx 140$ MeV, but small when compared to the spontaneous symmetry-breaking scale $\Lambda \sim m$.

The propagator for a spin-3/2 state with four-momentum p^μ takes the RS form

$$S_\Delta^{\alpha\beta}(p) = \frac{\not{p} + M_\Delta}{p^2 - M_\Delta^2 + \mathrm{i}\varepsilon}\left[-g^{\alpha\beta} + \frac{1}{d-1}\gamma^\alpha\gamma^\beta \right.$$
$$\left. + \frac{1}{(d-1)M_\Delta}(\gamma^\alpha p^\beta - \gamma^\beta p^\alpha) + \frac{d-2}{(d-1)M_\Delta^2}p^\alpha p^\beta\right]. \tag{2.41}$$

Here, d is the number of dimensions of the Minkowski space, which after dimensional regularization is set to $d = 4$. For details see Appendix C. As the Δ propagator appears in the context of a virtual state excited from a nucleon with momentum p_{nucl} by a small external momentum p_{ext}, one can write the real part of the denominator as

$$p^2 - M_\Delta^2 = (p_{\text{nucl}} + p_{\text{ext}})^2 - M_\Delta^2 = (m - M_\Delta)(m + M_\Delta) + \mathcal{O}(p_{\text{ext}})$$
$$= -(m + M_\Delta)\delta + \mathcal{O}(p_{\text{ext}}). \tag{2.42}$$

As a result, one sees that the propagator in Eq. (2.41) is of the order of $\delta^{-1} = (M_\Delta - m)^{-1}$.

There are two ways of treating this additional scale, both of which are considered in the present thesis. The appropriate choice depends on the energy region of the process in question.

Following Ref. [41], in the low-energy range, where the beam energies are close to the pion mass, I count δ^2 as being of $\mathcal{O}(p)$, since $(\delta/\Lambda)^2 \approx (m_\pi/\Lambda)$. In that work, it is explained that this avoids the Δ contributions to be overestimated relatively to those of the nucleons, in the low-energy region. This is especially true when taking the chiral limit of vanishing pion masses, but non-zero δ. Taking this into account, the δ power counting then defines the order D of a diagram with L loops, V^k vertices from a Lagrangian $\mathcal{L}^{(k)}$ of order k, N_π pionic propagators, N_N nucleonic propagators and N_Δ propagators for the $\Delta(1232)$ as

$$D = 4L + \sum_{k=1}^{\infty} kV^k - 2N_\pi - N_N - \frac{1}{2}N_\Delta. \tag{2.43}$$

This rule is used in Chapters 3 and 4.

For Chapter 5, the range of energies studied reaches values of similar size to δ. In this case, it is more reasonable to treat δ as being of the same order as those external energies, $\mathcal{O}(p)$, as otherwise one would underestimate the Δ effects. The power of a diagram is therefore counted as

$$D = 4L + \sum_{k=1}^{\infty} kV^k - 2N_\pi - N_N - N_\Delta. \tag{2.44}$$

This approach is called small-scale expansion (SSE) [42, 43].

For studies over broad energy ranges, one needs to use a globally valid counting. In Ref. [41], it was suggested that the price is of having higher-order corrections than needed in the low-energy region. In the present thesis, there is no case where the transition region is studied, and therefore I either choose Eq. (2.43) or Eq. (2.44), depending on the considered energies.

Naturally, the above considerations are also valid for the $SU(3)$ case, and can be directly adopted for it.

CHAPTER **3**

NEUTRAL PION PHOTOPRODUCTION

3.1 Introduction

Pion photoproduction on nucleons takes place via the four channels

$$\begin{aligned}
\gamma + p &\to \pi^0 + p \\
\gamma + p &\to \pi^+ + n \\
\gamma + n &\to \pi^0 + n \\
\gamma + n &\to \pi^- + p,
\end{aligned} \tag{3.1}$$

of which the latter two can only be measured via deuteron targets or the study of the inverse process $\pi^- + p \to \gamma + n$.

Near threshold, the amplitude of these reactions is dominated by dipole transitions of electric s-wave and d-wave nature, and by magnetic p-waves. A small contribution arises from the electric quadrupole as well. In fact, the electric dipole moment of the $\gamma + p \to \pi^0 + p$ reaction vanishes in the chiral limit ($m_\pi = 0$), and it is very small at the physical point where the pion mass is much smaller than the nucleon mass. Therefore, at low and intermediate energies, the neutral pion production cross section seems to be driven by the magnetic dipole transition to the $\Delta(1232)$, and the quadrupole transition could gain more relative importance as well. In contrast, for the charged channels, the electric dipole clearly dominates close to threshold, while the magnetic contribution starts to be dominant at energies close to the Δ resonance peak. The cross sections of these channels close to threshold are large, which can be seen in theoretical models and in the experiment.

The process of pion photoproduction has been intensely studied for more than 60 years, both from the empirical and from the theoretical point of view.

With the ever-growing experimental possibilities of high-precision measurements, the theoretical models have constantly been put to a test, leading to a continuous development of the theory in this field.

Kroll and Rudermann [44] performed the pioneering work for pion photoproduction at threshold, where the lowest order in the pion-nucleon mass-ratio expansion was computed. This was done in a model-independent way, imposing only gauge and Lorentz invariance, and treating the nucleon as being static and pointlike, to which the photon couples minimally. In this Kroll-Ruderman theorem, the amplitude of π^0 photoproduction vanishes. The work was improved in Refs. [45, 46] with current algebra and the partial conservation of the axial current.

As mentioned before, charged pion photoproduction has a relatively large cross section close to threshold. It can be well described by just tree-level diagrams, which lead to a substantial EDM. However, the neutral pion channels present a much smaller cross section, which in the chiral limit of massless pions has a vanishing s-wave contribution. With the possibility of measuring the pion photoproduction processes [47–50], it became clear that, while the low-energy theorems describe the data well for charged pions, this is not the case for the $\gamma + p \to p + \pi^0$ process. Modern approaches using effective field theorys based on QCD, such as ChPT, lead, at the lowest order, to the same LETs. Thus, they also fail to reproduce the neutral pion-photoproduction data.

These suppressed lower-order contributions present an opportunity to study the relevance of the higher-order effects. Such advances were first made by Bernard et al. [51, 52]. Using ChPT, they showed the need to reach higher orders in the chiral expansion, which amounts to including loop contributions, in order to successfully describe the near-threshold strong energy dependence of the cross sections. However, introducing baryons as degrees of freedom in ChPT leads to a breaking of the power-counting scheme in the evaluation of the loops [40]. This problem was solved in later works, where the calculations were repeated in HBChPT, which systematically restores the power counting [1, 53]. This considerably reduced the discrepancies, resulting in a very good agreement between the data existing at the time and an analysis in fourth chiral order [54].

Recently, new high-precision near-threshold data have been made available by the Mainz Microtron (MAMI), including differential cross sections and photon asymmetries with a narrow binning in both photon energies and scattering angles [55]. Fernández-Ramírez et al. showed that, in the light of these high-quality results, the $\mathcal{O}(p^4)$ HBChPT approaches failed to describe the neutral pion photoproduction process at energies higher than 20 MeV above threshold [56]. In their work, they also analysed the effect of imposing unitarity, which did not improve the situation. In fact, in particular the p-wave energy

slope is not reproduceable. This is reflected in their results for the multipole M_1^+. Furthermore, the differential cross sections at higher energies are underestimated. Their conclusion was that relativistic effects and the explicit inclusion of the $\Delta(1232)$ resonance might be needed. Due to the magnetic-dipole excitation nature of the latter, it has an important effect on M_1^+, already at tree level.

The mentioned slow convergence was not solved either by the introduction of alternative renormalization schemes for the power-counting problem of baryons, as is the case of EOMS [6, 7]. This is a fully covariant approach that, unlike the nonrelativistic HBChPT, satisfies analyticity, and usually converges faster. While this model successfully describes (among others) pion scattering, baryon masses, magnetic moments, and axial form factors [8–20], the description of the neutral pion photoproduction on protons in a fully covariant calculation up to fourth chiral order does not show improvements with respect to the HBChPT approach. This was discussed in Ref. [57], where the authors also obtained an underestimation of the M_1^+ multipole. On top of that, they fail to pin down one of the LECs related to d-waves. In the analysis of the experiment, the important influence of d-waves was shown, but the corresponding multipoles could not be separated. As a consequence, the multipole E_2^- can not be well estimated, and this directly affects the extraction of E_0^+. For a good convergence at even higher energies, one would need to take into account higher-order corrections, at the price of many unknown LECs. The importance of the $\Delta(1232)$ inclusion was stressed in the follow-up work [58].

In the present chapter, I explore the explicit inclusion of the $\Delta(1232)$ resonance as an additional degree of freedom, as already suggested in Refs. [42, 55, 56, 58]. The goal is to improve the chiral convergence of the neutral pion photoproduction with the data still close to threshold, but at energies higher than 20 MeV above it. As mentioned before, when compared to the charged channels, low-energy neutral pion photoproduction is particularly sensitive to chiral dynamics, due to the very small contribution of the electric dipole. This is reflected in the smallness of the lower-order terms. As can be seen in Fig. 3.1, the total cross section in this energy region is globally dominated by the magnetic dipole excitation of the $\Delta(1232)$. Its contribution is mainly a p-wave, which makes it the more relevant the further one is from threshold. While at threshold it vanishes, its contribution grows rapidly with the energy. Therefore, it is a good candidate for the origin of the strong energy dependence of the cross section.

Naturally, one could alternatively take the effect of the $\Delta(1232)$ into account by absorbing it into the LECs, and by including higher-order corrections. Nevertheless, there are several reasons justifying the preference for an explicit inclusion. On the one hand, the energy region considered is close to

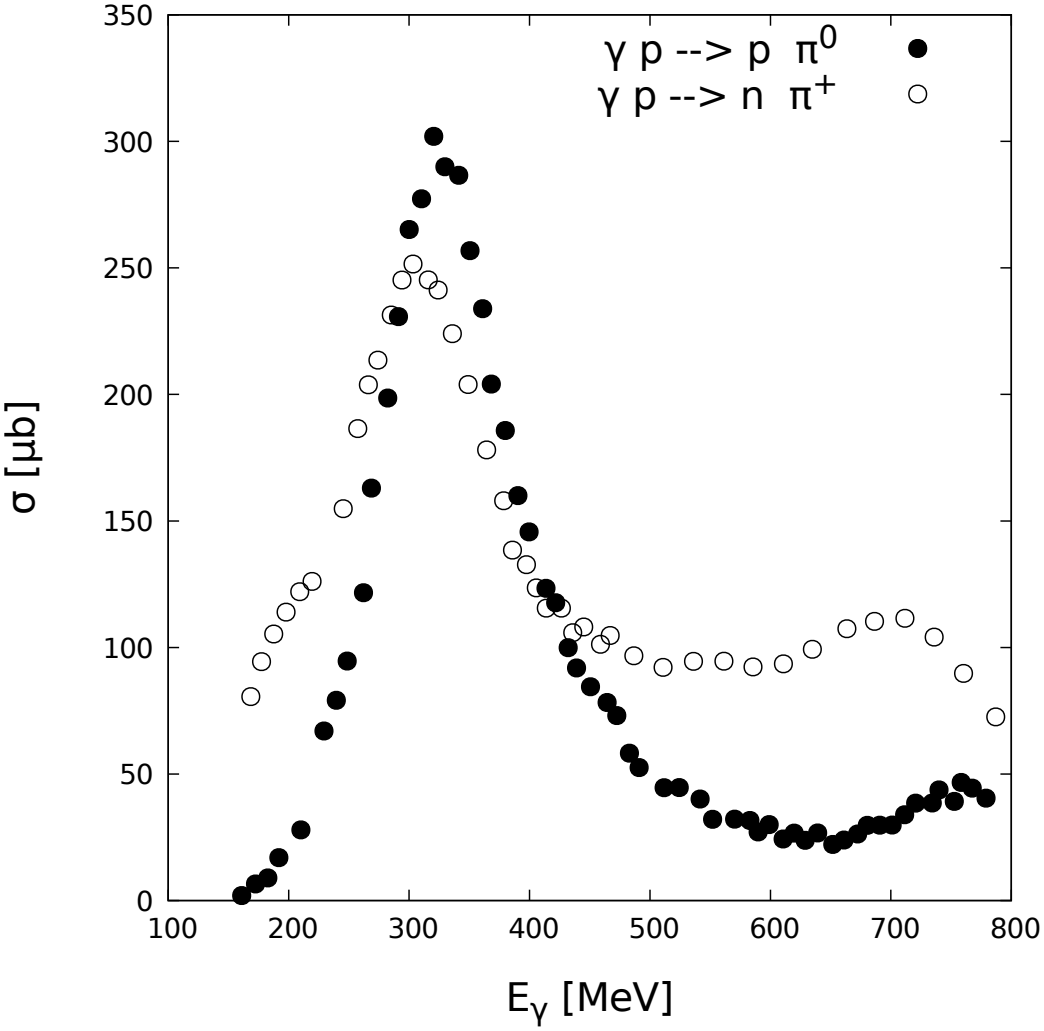

Figure 3.1.: Total cross sections for the two channels of pion photoproduction off proton targets. Data from Refs. [59, 60].

the resonance's mass, which leads to a strong energy dependence. This cannot be described by a static LEC. On the other hand, with the Δ one expects a much better convergence even at lower chiral orders, thus removing the dependence on too many unknown parameters. Lastly, by avoiding the implicit inclusion of the Δ as a modification of the LECs' values, and instead considering it explicitly, one preserves the natural size of these constants. For the energy region described in this chapter, well below the $\Delta(1232)$ peak, higher nucleon-excitation contributions do not need to be taken into account.

The effect of the $\Delta(1232)$ resonance in low-energy processes has already been studied for Compton scattering [41, 61], πN scattering [62], and pion electro- and photoproduction [37, 63, 64]. The influence on neutral pion photoproduction close to threshold has first been studied in HBChPT [42, 54], finding only moderate effects. This could be due to the fact that the baryon propagators in these HBChPT works are calculated in the static limit. A consideration of the Δ propagator's full energy dependence could allow for a more accurate description of the rapid cross-section growth with the energy.

In Refs. [65, 66], we applied the full consideration of the $\Delta(1232)$ propagator in the process of neutral pion photoproduction for the first time, in an approach with the EOMS relativistic renormalization scheme. Later, conference proceedings with a similar approach in HBChPT at $\mathcal{O}(p^4)$ were published [67]. Both our and their work show a clear improvement when the Δ resonance is included, and this is the focus of the chapter at hand. When explicitly adding the contributions of the $\Delta(1232)$ resonance, an additional small quantity automatically appears in the ChPT calculations, the difference between the $\Delta(1232)$ and the nucleon masses. As was explained in Chapter 2, it is appropriate to use the δ chiral power counting [41], since energies sufficiently far away from the $\Delta(1232)$ resonance peak are being treated.

Although it is beyond the scope of this thesis, I would like to briefly comment on the approaches needed to reach higher energies. At the $\Delta(1232)$ resonance peak, the amplitude needs to be regularized. This can be done by taking into account the Δ width. Alternatively, a unitarized coupled-channel approach of ChPT can be taken as a tool which dynamically generates resonances and creates the correct behaviour of the amplitudes in the resonance region. The nucleon-resonance region of pion photoproduction has been well described in this way in Refs. [68–72]. A study for the non-resonant high-energy regime in a Regge model has been performed by Mathieu et al. [73], with the ultimate goal of connecting it to the resonance region, e.g., via finite-energy sum rules.

Here, at energies closer to threshold, I will at first focus on introducing the $\Delta(1232)$ resonance at tree level in the δ counting scheme. This corresponds to an $\mathcal{O}(p^3)$ calculation, and introduces only two LECs, g_M and h_A, with well established literature values. The results show an immediate improvement of

the agreement with the data for both differential cross sections and photon asymmetries, even at photon energies above 200 MeV in the laboratory frame.

In order to test the convergence of the theory, and aiming for an even further improvement of the model, I also discuss the extension to the next order, $\mathcal{O}(p^{7/2})$, which implies the inclusion of the set of one-loop diagrams with one single $\Delta(1232)$ propagator. These do not require any additional couplings, but a new tree diagram appears which generates the poorly known LEC g_E. It turns out that the model describes the process very well, even when the tight constraints on the LECs from other observables are taken into account.

After this introductory section, the remaining chapter is organized as follows: in Sec. 3.2, the general model-independent formalism for the description of the $\gamma p \to p\pi^0$ reaction amplitudes is presented. In Sec. 3.3, the necessary considerations for the calculations in ChPT are introduced, which include the treatment of PCBT, the wave-function renormalization (WFR), and the corrections of LECs due to higher-order contributions. Some comments on how the LECs are constrained are also given. In Sec. 3.4, I show and discuss the results for cross sections, photon asymmetries and multipoles. A summary and outlook for the chapter are given in Sec. 3.5.

3.2 Formalism for pion photoproduction

In Fig. 3.2 the $\gamma p \to p\pi^0$ process is shown. The four-momenta $k = (k_0, \vec{k}\,)$, $q = (q_0, \vec{q}\,)$, $p = (E_i, \vec{p}\,)$ and $p' = (E_f, \vec{p}\,')$ belong to the incoming photon, the produced π^0, the incoming and the outgoing protons, respectively. The scattering amplitude $\mathcal{M}$ can be parameterized as

$$\epsilon_\mu \mathcal{M}^\mu = \bar{u}(p')\left(V_N q\cdot\epsilon\gamma_5 + V_K q\cdot\epsilon \not{k}\gamma_5 + V_E \not{\epsilon}\gamma_5 + V_{EK}\not{\epsilon}\not{k}\gamma_5\right) u(p), \tag{3.2}$$

where V_N, V_K, V_E and V_{EK} are complex structure functions of the photon energy k_γ in the laboratory frame and the angle θ between incoming photon and outgoing pion. When studying electroproduction, that is photoproduction with virtual photons, two additional linearly independent amplitudes appear, which do not have to be considered here, in the case of real photons. The Dirac spinors $u(p)$ and $\bar{u}(p') = u^\dagger(p')\gamma_0$ are those of the nucleon in the initial and final states, respectively, and ϵ is the photon polarization.

Although the representation above cannot be further reduced, there is an equivalent one that is commonly used, because it has the advantage of being explicitly current conserving by definition. It has the form [74]

$$\epsilon_\mu \mathcal{M}^\mu = \epsilon_\mu \bar{u}(p')\left(\sum_{i=1}^{4} A_i M_i^\mu\right) u(p), \tag{3.3}$$

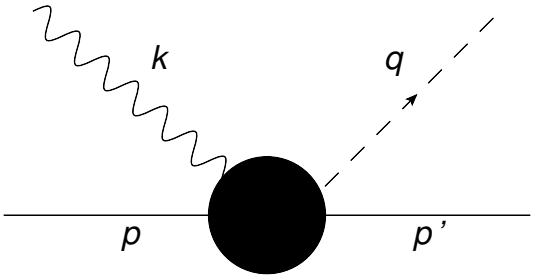

Figure 3.2.: Generic representation of the pion photoproduction process. The incoming photon and proton momenta are given by k and p, while those of the outgoing neutral pion and proton are denoted by q and p', respectively.

where

$$\begin{aligned}
\epsilon \cdot M_1 =& \mathrm{i}\not{k}\not{\epsilon}\gamma_5, \\
\epsilon \cdot M_2 =& \mathrm{i}(p' \cdot \epsilon \; k \cdot q - q \cdot \epsilon \; k \cdot (p + p'))\gamma_5, \\
\epsilon \cdot M_3 =& \mathrm{i}(\not{\epsilon} k \cdot q - \not{k} q \cdot \epsilon)\gamma_5, \\
\epsilon \cdot M_4 =& \mathrm{i}(\not{\epsilon} k \cdot (p + p') - \not{k} p' \cdot \epsilon - 2m\not{k}\not{\epsilon})\gamma_5.
\end{aligned} \tag{3.4}$$

Here, m is the nucleon mass. The conversion between parameterizations is straightforward ($p \cdot \epsilon = 0$ in the center-of-mass system):

$$\begin{aligned}
A_1 =& \mathrm{i}\left(V_{EK} - \frac{m}{k \cdot p}\left(V_E + k \cdot q V_K\right)\right), \\
A_2 =& \mathrm{i}\frac{V_N}{2k \cdot p}, \\
A_3 =& \mathrm{i}\left(V_K\left(1 - \frac{k \cdot q}{2k \cdot p}\right) - \frac{V_E}{2k \cdot p}\right), \\
A_4 =& -\frac{\mathrm{i}}{2k \cdot p}\left(V_E + k \cdot q V_K\right).
\end{aligned} \tag{3.5}$$

For the calculation of the multipoles, a third representation in terms of the Chew–Goldberger–Low–Nambu (CGLM) amplitudes [75] is convenient,

$$\epsilon_\mu \mathcal{M}^\mu = \frac{4\pi W}{m} \chi_f^\dagger \mathcal{F} \chi_i, \tag{3.6}$$

where χ_i and χ_f are the initial and final-state Pauli spinors, respectively, and $W = \sqrt{s}$ is the center-of-mass energy. For real photons and in the Coulomb gauge, the amplitude $\mathcal{F}$ may be written as

$$\mathcal{F} = \mathrm{i}\vec{\sigma}\cdot\vec{\epsilon}\,\mathcal{F}_1 + \vec{\sigma}\cdot\hat{q}\;\vec{\sigma}\cdot\hat{k}\times\vec{\epsilon}\,\mathcal{F}_2 + \mathrm{i}\vec{\sigma}\cdot\hat{k}\;\hat{q}\cdot\epsilon\mathcal{F}_3 + \mathrm{i}\vec{\sigma}\cdot\hat{q}\;\hat{q}\cdot\epsilon\;\mathcal{F}_4, \tag{3.7}$$

with $\vec{\sigma}$ the vector of Pauli matrices. For the conversion between parameterizations, in agreement with literature [52, 58, 75], I obtain

$$\epsilon_\mu \bar{u}(p')\left(\sum_{i=1}^{4} A_i M_i^\mu\right) u(p) = \frac{4\pi W}{m}\chi_f^\dagger \mathcal{F}\chi_i, \tag{3.8}$$

with

$$\begin{aligned}
\mathcal{F}_1 =& \frac{\sqrt{(E_i+m)(E_f+m)}}{8\pi W}\Bigg[-\left(k_0+\frac{k_0^2}{E_i+m}\right)A_1 - k\cdot q A_3 \\
&+\left(-k_0^2+2k_0m+\frac{2k_0^2m}{E_i+m}-k_0(E_i+E_f)-k_0|\vec{q}|\cos\theta\right)A_4\Bigg], \\
\mathcal{F}_2 =& \frac{\sqrt{(E_i+m)(E_f+m)}}{8\pi W}|\vec{q}|\Bigg[\left(\frac{k_0}{E_f+m}+\frac{k_0^2}{(E_i+m)(E_f+m)}\right)A_1 \\
&-\frac{k_0 k\cdot q}{(E_i+m)(E_f+m)}A_3 \\
&-\left(k_0\frac{k_0^2+2k_0m+k_0(E_i+E_f)+k_0|\vec{q}|\cos\theta}{(E_i+m)(E_f+m)}+\frac{2k_0m}{E_f+m}\right)A_4\Bigg], \\
\mathcal{F}_3 =& \frac{\sqrt{(E_i+m)(E_f+m)}}{8\pi W}|\vec{q}|\Bigg[-k_0^2\frac{E_i+E_f+k_0+q_0}{E_i+m}A_2 \\
&+\left(k_0+\frac{k_0^2}{E_i+m}\right)(A_4-A_3)\Bigg], \\
\mathcal{F}_4 =& \frac{\sqrt{(E_i+m)(E_f+m)}}{8\pi W}|\vec{q}|^2\Bigg[\left(k_0\frac{k_0+E_i+E_f+q_0}{E_f+m}\right)A_2 \\
&+\left(\frac{k_0}{E_f+m}+\frac{k_0^2}{(E_i+m)(E_f+m)}\right)(A_4-A_3)\Bigg].
\end{aligned} \tag{3.9}$$

The data of Refs. [55, 57] that this chapter's model is compared with is for unpolarized angular cross sections

$$\frac{\mathrm{d}\sigma}{\mathrm{d}\Omega} = \frac{|\vec{q}|m^2}{2\pi W(s-m^2)} \sum_{\epsilon} \frac{\mathrm{Tr}\left[\mathcal{M}^* \cdot (\not{p}' + m) \cdot \mathcal{M} \cdot (\not{p} + m)\right]}{2} \tag{3.10}$$

and linearly polarized photon asymmetries

$$\Sigma = \frac{\mathrm{d}\sigma_\perp - \mathrm{d}\sigma_\parallel}{\mathrm{d}\sigma_\perp + \mathrm{d}\sigma_\parallel}, \tag{3.11}$$

with $d\sigma_\perp$ and $d\sigma_\parallel$ the angular cross sections for photon polarizations perpendicular and parallel to the reaction plane, respectively. In the CGLM representation, the differential cross section and photon asymmetry are usually written with the help of the response functions

$$\begin{aligned} R_T =& |\mathcal{F}_1|^2 + |\mathcal{F}_2|^2 + \frac{1}{2}\sin^2\theta\left(|\mathcal{F}_3|^2 + |\mathcal{F}_4|^2\right) \\ &- \mathrm{Re}\left[2\cos\theta\mathcal{F}_1^*\mathcal{F}2 - \sin^2\theta\left(\mathcal{F}_1^*\mathcal{F}_4 + \mathcal{F}_2^*\mathcal{F}_3 + \cos\theta\mathcal{F}_3^*\mathcal{F}_4\right)\right] \end{aligned} \tag{3.12}$$

and

$$\begin{aligned} R_{TT} =& \frac{1}{2}\sin^2\theta\left(|\mathcal{F}_3|^2 + |\mathcal{F}_4|^2\right) \\ &+ \mathrm{Re}\left[\sin^2\theta\left(\mathcal{F}_1^*\mathcal{F}_4 + \mathcal{F}_2^*\mathcal{F}_3 + \cos\theta\mathcal{F}_3^*\mathcal{F}_4\right)\right], \end{aligned} \tag{3.13}$$

with which one obtains

$$\frac{\mathrm{d}\sigma}{\mathrm{d}\Omega_\pi} = \frac{|\vec{q}|}{k_\gamma} R_T \quad \text{and} \quad \Sigma = -\frac{R_{TT}}{R_T}. \tag{3.14}$$

As for the lowest multipoles E_{0+}, M_{1+}, M_{1-} and E_{1+}, they read [52]:

$$\mathcal{E} = \int_{-1}^{1} \mathrm{d}x\ \mathcal{P}\ \mathcal{F}, \tag{3.15}$$

where

$$\mathcal{E} = \begin{pmatrix} E_{0+} \\ M_{1+} \\ M_{1-} \\ E_{1+} \end{pmatrix}, \qquad \mathcal{F} = \begin{pmatrix} \mathcal{F}_1(x) \\ \mathcal{F}_2(x) \\ \mathcal{F}_3(x) \\ \mathcal{F}_4(x) \end{pmatrix},$$

$$\mathcal{P} = \begin{pmatrix} \frac{1}{2}P_0(x) & -\frac{1}{2}P_1(x) & 0 & \frac{1}{6}\left[P_0(x) - P_2(x)\right] \\ \frac{1}{4}P_1(x) & -\frac{1}{4}P_2(x) & \frac{1}{12}\left[P_2(x) - P_0(x)\right] & 0 \\ -\frac{1}{2}P_1(x) & \frac{1}{2}P_0(x) & \frac{1}{6}\left[P_0(x) - P_2(x)\right] & 0 \\ \frac{1}{4}P_1(x) & -\frac{1}{4}P_2(x) & \frac{1}{12}\left[P_0(x) - P_2(x)\right] & \frac{1}{10}\left[P_1(x) - P_3(x)\right] \end{pmatrix}. \tag{3.16}$$

Here, $x = \cos(\theta)$, and P_l are the Legendre polynomials for an angular momentum l. Furthermore, it is convenient to use the reduced multipoles

$$\bar{M}_{1\pm} = \frac{M_{1\pm}}{|\vec{q}|} \quad \text{and} \quad \bar{E}_{1+} = \frac{E_{1+}}{|\vec{q}|}, \tag{3.17}$$

because for energies close to threshold the multipoles for $l = 1$ are linearly related to the absolute value of the pion momentum. More general expressions (for $l > 1$) can be found in Appendix A, as well as other relations of interest between observables and multipoles.

3.3 Calculation in chiral perturbation theory

In this chapter, the MAMI pion-photoproduction data [55, 57] is analysed using a fully covariant ChPT framework, and including the $\Delta(1232)$ resonance as an explicit degree of freedom. In the counting scheme of Eq. (2.43), diagrams involving the Δ start at $\mathcal{O}(p^{5/2})$. All the tree-level and loop diagrams contributing to the channel considered up to $\mathcal{O}(p^{7/2})$ can be found depicted in Figs. 3.3 to 3.6. The analytical expressions of the amplitudes can be found in Appendix B. Throughout this chapter, the isospin limit of equal nucleon masses and also of equal pion masses was taken.

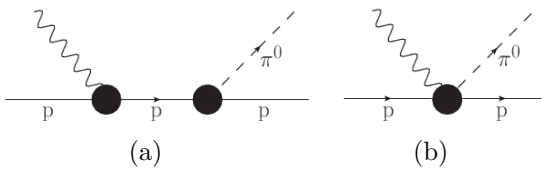

Figure 3.3.: Tree diagrams for the π^0 photoproduction off protons. The crossed terms are also included in the calculation. The black dots represent vertices of chiral order p^1 to p^3. Diagram b) starts at $\mathcal{O}(p^3)$.

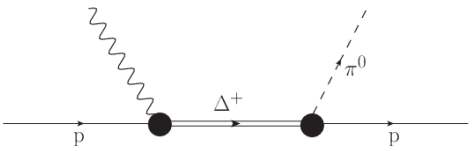

Figure 3.4.: Δ tree diagram for the π^0 photoproduction off protons. The crossed term is also included in the calculation.

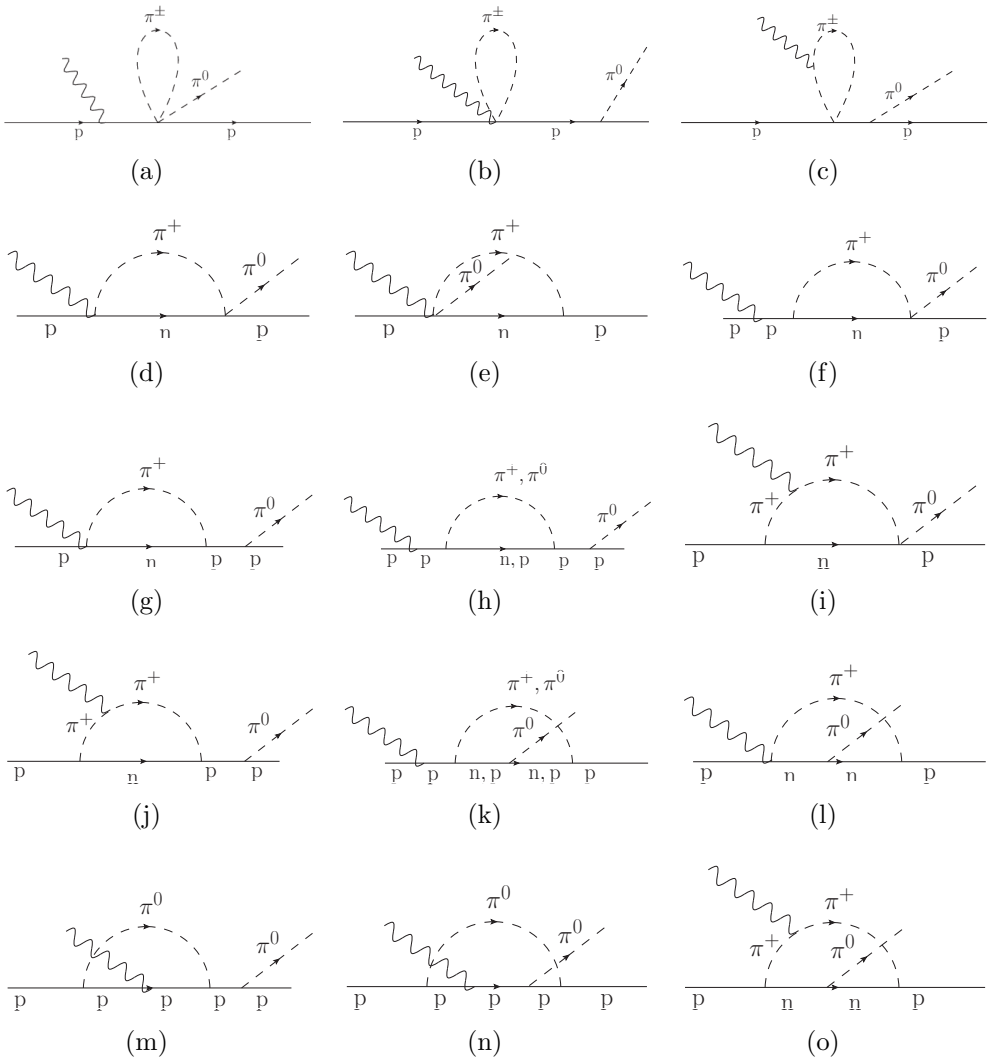

Figure 3.5.: Loop diagrams for the π^0 photoproduction off protons including only the nucleonic intermediate states. The crossed terms are also calculated.

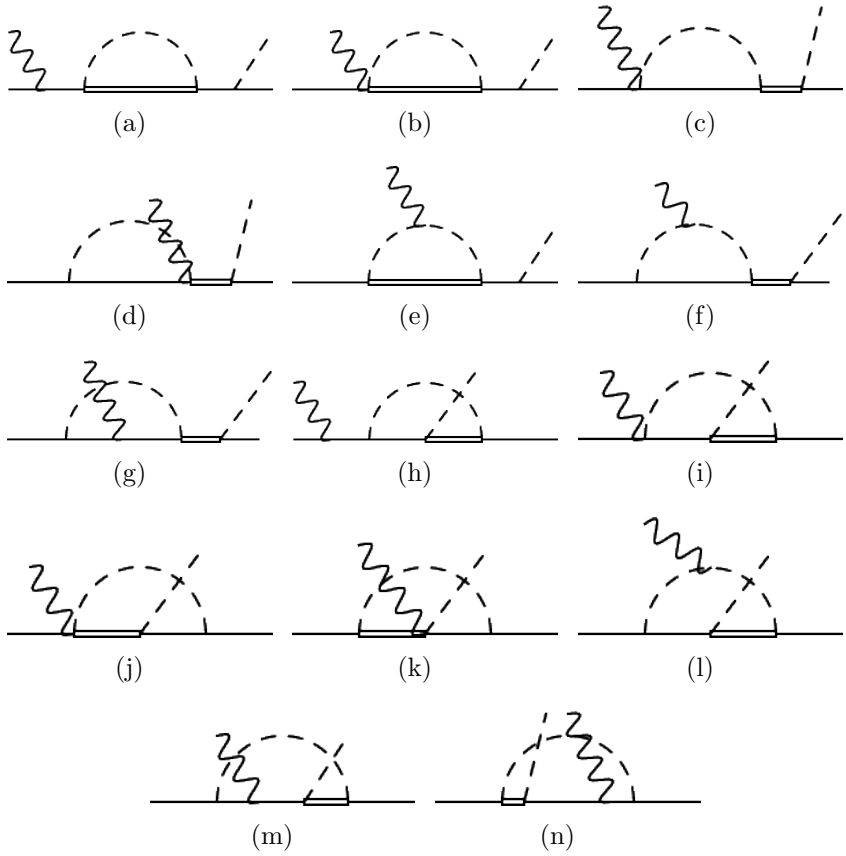

Figure 3.6.: Loop diagrams for the π^0 photoproduction off protons for the Δ intermediate states. The crossed terms are also calculated.

3.3.1 Renormalization

The diagrams have been evaluated applying the EOMS renormalization scheme, with the help of FORM [76, 77] and FeynCalc [78, 79]. First, the infinities were removed using $\widetilde{MS}$, the modified minimal subtraction (MS) scheme [80], see Appendix C. Then, also the PCBT were absorbed into LECs. In order to do so, the amplitudes were expanded around the small chiral parameters, and only those terms were kept that were at least of the diagrams' nominal order, see also Appendix D. As in Ref. [62], the three small parameters chosen for the expansion were the mass m_π, the Mandelstam variable t of $\mathcal{O}(p^2)$, and $\nu = (s-u)/(4m)$, with s and u the Mandelstam variables of $\mathcal{O}(p)$. When introducing the $\Delta(1232)$ resonance, an additional small parameter δ appears, which is the difference between the Δ mass and the nucleon mass, $\delta = M_\Delta - m$.

The tree-level diagrams and those diagrams from Fig. 3.5 which exclusively contain mesons in the loops do not break the power counting. The analytical expression I obtain for the PCBT in the nucleonic sector, i.e., for the remaining loops in Fig. 3.5, reads

$$\frac{\mathrm{i}eg_A^3 m}{32F_\pi^3\pi^2}\left[\left(4\nu - 3\frac{m_\pi^2}{\nu}\right)\not{\epsilon}\gamma_5 + \left(3 - 3\frac{m_\pi^2}{\nu^2}\right)\not{\epsilon}\not{k}\gamma_5 + \frac{1}{\nu}q\cdot\epsilon\not{k}\gamma_5 - \frac{2m}{\nu}q\cdot\epsilon\gamma_5\right]. \tag{3.18}$$

The additional PCBT coming from the introduction of the Δ loops are obtained analogously, but have large expressions which are therefore not shown here. Instead, the methods to reproduce them are explained in Appendix D, along with the computational tools needed.

3.3.2 Wave-function renormalization

In order to systematically take into account all the higher-order contributions up to the order studied, $\mathcal{O}(p^{7/2})$, the WFR was taken into account for the external proton and pion legs of the tree diagrams of $\mathcal{O}(p^1)$. This correction amounts to multiplying this tree-level amplitude by $Z_p\sqrt{Z_\pi}$, which adds corrections of $\mathcal{O}(p^2)$. The $\mathcal{O}(p^1)$ amplitude therefore contains correction terms of $\mathcal{O}(p^3)$. All the corrections to higher-order amplitudes or to the external photon leg would be at least of $\mathcal{O}(p^4)$.

The EOMS-renormalized analytical expression for the correction factor of the proton legs, depicted in Fig. 3.7, reads [62]

$$Z_p = \frac{1}{1-\Sigma_p'}\bigg|_{\not{p}=m}$$

$$=1-\frac{3g_A^2m_\pi^2}{32\pi^2F_\pi^2m^2(4m^2-m_\pi^2)}\left[2m_\pi(m_\pi^2-3m^2)\sqrt{4m^2-m_\pi^2}\arccos\left(\frac{m_\pi}{2m}\right)\right.$$

$$\left.+(m_\pi^2-4m^2)\left((2m_\pi^2-3m^2)\log\left(\frac{m_\pi}{m}\right)-2m^2\right)\right]+Z_p^\Delta+\mathcal{O}(p^4), \tag{3.19}$$

where Σ_p is the self-energy of the proton. When considering the $\Delta(1232)$ as an intermediate state, one has to take into account the self-energy loop of Fig. 3.7(b) that enters the WFR. Up to $\mathcal{O}(p^2)$, I obtain the analytical expression

$$Z_p^\Delta=\frac{h_A^2}{768\pi^2F_\pi^2m^4M_\Delta^2}\left\{48m_\pi^2m^5\left(m+M_\Delta\right)\log\left(\frac{m}{M_\Delta}\right)\right.$$

$$-\left(m-M_\Delta\right)^2\left(m+M_\Delta\right)^4\left(5m^2-2mM_\Delta+3M_\Delta^2\right)\log\left(\frac{\left(m^2-M_\Delta^2\right)^2}{M_\Delta^4}\right)$$

$$+2\Big(5m^8+8m^7M_\Delta-6m^6\left(2m_\pi^2+M_\Delta^2\right)-12m^5M_\Delta\left(m_\pi^2+M_\Delta^2\right)-6m_\pi^4m^4$$

$$-2m^2\left(-3m_\pi^4M_\Delta^2+2m_\pi^6+M_\Delta^6\right)+4mM_\Delta\left(M_\Delta^2-m_\pi^2\right)^3+3\left(m_\pi^2-M_\Delta^2\right)^4\Big)\log\left(\frac{m_\pi}{M_\Delta}\right)$$

$$-m_\pi^2m^2\Big(2m^4+8m^3M_\Delta+m^2\left(4M_\Delta^2-5m_\pi^2\right)-8mM_\Delta\left(m_\pi^2-2M_\Delta^2\right)$$

$$+6\left(-3m_\pi^2M_\Delta^2+m_\pi^4+3M_\Delta^4\right)\Big)$$

$$+2\sqrt{\left(m-m_\pi-M_\Delta\right)\left(m+m_\pi-M_\Delta\right)}\left(\left(m-m_\pi+M_\Delta\right)\left(m+m_\pi+M_\Delta\right)\right)^{3/2}$$

$$\times\left(5m^4-2m^3M_\Delta-2m^2\left(m_\pi^2+M_\Delta^2\right)+2mM_\Delta\left(M_\Delta^2-m_\pi^2\right)-3\left(m_\pi^2-M_\Delta^2\right)^2\right)$$

$$\times\left[\operatorname{arctanh}\left(\frac{m^2+m_\pi^2-M_\Delta^2}{\sqrt{\left(m-m_\pi-M_\Delta\right)\left(m+m_\pi-M_\Delta\right)\left(m-m_\pi+M_\Delta\right)\left(m+m_\pi+M_\Delta\right)}}\right)\right.$$

$$\left.\left.+\operatorname{arctanh}\left(\frac{m^2-m_\pi^2+M_\Delta^2}{\sqrt{\left(m-m_\pi-M_\Delta\right)\left(m+m_\pi-M_\Delta\right)\left(m-m_\pi+M_\Delta\right)\left(m+m_\pi+M_\Delta\right)}}\right)\right]\right\}. \tag{3.20}$$

Figure 3.7.: Diagrams contributing to the proton self-energy with nucleon (a) and Δ (b) loop contributions.

As for the pion-leg WFR and renormalization of the pion-decay constant, I use the well-known expressions from Ref. [23]:

$$F_\pi = F + \frac{m_\pi^2}{F}\left[L_4 - \frac{1}{16\pi^2}\log\left(\frac{m_\pi^2}{m^2}\right)\right] + \mathcal{O}(p^3),$$

$$Z_\pi = 1 - \frac{m_\pi^2}{F_\pi^2}\left[2L_4 + \frac{1}{16\pi^2}\log\left(\frac{m_\pi^2}{m^2}\right)\right] + \mathcal{O}(p^3), \tag{3.21}$$

where L_4 is a LEC appearing in the next-to-leading order pion Lagrangian. For the $\mathcal{O}(p)$ diagrams, the factor $\sqrt{Z_\pi}/F$ can be expanded around the pion mass,

$$\frac{\sqrt{Z_\pi}}{F} = \frac{1}{F_\pi} - \frac{3m_\pi^2 \log\left(\frac{m_\pi^2}{m^2}\right)}{32\pi^2 F_\pi^3} + \mathcal{O}(p^3), \tag{3.22}$$

therefore leading to an expression which up to the order considered does not depend on L_4.

3.3.3 Higher-order corrections to low-energy constants

The LECs appearing in the leading-order Lagrangian have to be corrected up to the order considered, $\mathcal{O}(p^{7/2})$. For the nucleon mass m appearing in the nucleon propagator of the leading-order tree-level diagrams this means that it has to be calculated with corrections coming from higher-order self-energy loops. The EOMS-renormalized contributions to the physical nucleon mass coming from the loops in Fig. 3.7 are given by [62]

$$m_N = m - 4c_1 m_\pi^2 - \frac{3g_A^2 m_\pi^3}{64\pi^2 F_\pi^2}\left[\frac{m_\pi}{m}\log\left(\frac{m_\pi^2}{m^2}\right) - 4\sqrt{1-\frac{m_\pi^2}{4m^2}}\arccos\left(\frac{m_\pi}{2m}\right)\right]$$

$$+ m_N^\Delta + \mathcal{O}(p^4), \tag{3.23}$$

where c_1 is a LEC appearing in the nucleon Lagrangian of $\mathcal{O}(p^2)$. For the correction m_N^Δ arising from the loop with a Δ propagator, I obtain

$$m_N^\Delta = \frac{h_A^2}{768 m^3 \pi^2 F_\pi^2 M_\Delta^2} \Bigg\{ m_\pi^2 \Big(2m_\pi^4 - \left(7m^2 + 4M_\Delta m + 6M_\Delta^2\right) m_\pi^2$$

$$+ 2\left(m - M_\Delta\right)\left(m + M_\Delta\right)^3 \Big) m^2$$

$$+ 2\left[m^3 + 2M_\Delta m^2 - 2\left(2m_\pi^2 + M_\Delta^2\right) m - 6M_\Delta\left(m_\pi^2 + M_\Delta^2\right)\right] m^5 \log\left(\frac{m_\pi^2}{m^2}\right)$$

$$+ 2\left(\left(m - M_\Delta\right)^2 - m_\pi^2\right)\left(m - m_\pi + M_\Delta\right)^2$$

$$\times \sqrt{\left(m - m_\pi - M_\Delta\right)\left(m + m_\pi - M_\Delta\right)\left(m - m_\pi + M_\Delta\right)}\left(m + m_\pi + M_\Delta\right)^{5/2}$$

$$\times \log\left(\frac{M_\Delta}{m}\right)$$

$$+ 2\frac{\left(\left(m - M_\Delta\right)^2 - m_\pi^2\right)^2\left(m - m_\pi + M_\Delta\right)^3\left(m + m_\pi + M_\Delta\right)^{5/2}}{\sqrt{\left(m - m_\pi - M_\Delta\right)\left(m + m_\pi - M_\Delta\right)\left(m - m_\pi + M_\Delta\right)}}$$

$$\times \log\left(\frac{m_\pi}{m}\right)$$

$$- \frac{\left(\left(m - M_\Delta\right)^2 - m_\pi^2\right)^2\left(m - m_\pi + M_\Delta\right)^3\left(m + m_\pi + M_\Delta\right)^{5/2}}{\sqrt{\left(m - m_\pi - M_\Delta\right)\left(m + m_\pi - M_\Delta\right)\left(m - m_\pi + M_\Delta\right)}}$$

$$\times \log\left(\frac{\left(-m^2 + m_\pi^2 + M_\Delta^2 + \sqrt{m^4 - 2\left(m_\pi^2 + M_\Delta^2\right)m^2 + \left(M_\Delta^2 - m_\pi^2\right)^2}\right)^2}{4m^4}\right)$$

$$- \left(m - M_\Delta\right)\left(m + M_\Delta\right)^3\left[2\left(-2m^2 + M_\Delta m - 2M_\Delta^2\right) m_\pi^2 + \left(m^2 - M_\Delta^2\right)^2\right]$$

$$\times \log\left(\frac{\left(m^2 - M_\Delta^2\right)^2}{m^4}\right)$$

$$- 2\Bigg[m^8 + 2M_\Delta m^7 - 2\left(2m_\pi^2 + M_\Delta^2\right) m^6 - 6M_\Delta\left(m_\pi^2 + M_\Delta^2\right) m^5$$

$$+ 6m_\pi^4 m^4 + 6M_\Delta \left(m_\pi^4 - M_\Delta^4\right) m^3 - 2\left(2m_\pi^6 - 3M_\Delta^2 m_\pi^4 + M_\Delta^6\right) m^2$$

$$+ 2M_\Delta \left(M_\Delta^2 - m_\pi^2\right)^3 m + \left(M_\Delta^2 - m_\pi^2\right)^4 \Bigg] \log\left(\frac{m_\pi}{m}\right)$$

$$+ 2\log\left(\frac{M_\Delta}{m}\right) \Bigg[m_\pi^8 - 2\left(2m^2 + M_\Delta m + 2M_\Delta^2\right) m_\pi^6$$

$$+ 6\left(m^4 + M_\Delta m^3 + M_\Delta^2 m^2 + M_\Delta^3 m + M_\Delta^4\right) m_\pi^4 + (m - M_\Delta)^3 (m + M_\Delta)^5$$

$$+ 2\left(-2m^6 - 3M_\Delta m^5 + 3M_\Delta^5 m + 2M_\Delta^6\right) m_\pi^2 \Bigg] \Bigg\}. \tag{3.24}$$

The $\mathcal{O}(p^2)$ correction to m_N is consequently approximately given by

$$\begin{aligned} m_2 =& m - 4c_1 m_\pi^2 \\ =& m_N + \frac{3g_A^2 m_\pi^3}{64\pi^2 F_\pi^2} \left[\frac{m_\pi}{m_N} \log\left(\frac{m_\pi^2}{m_N^2}\right) - 4\sqrt{1 - \frac{m_\pi^2}{4m_N^2}} \arccos\left(\frac{m_\pi}{2m_N}\right) \right] \\ & - m_N^\Delta + \mathcal{O}(p^4), \end{aligned} \tag{3.25}$$

where, for m_N^Δ, the mass m in Eq. (3.24) can also be set to the physical mass m_N.

The EOMS-renormalized expression for g_A, when including nucleonic intermediate states only, is given by [10, 62]

$$\begin{aligned} g_A = g_0 + 4m_\pi^2 d_{16} - \frac{g_A m_\pi^2}{16\pi^2 F_\pi^2 m^2} \Bigg[& \frac{(3g_A^2 + 2)m_\pi^3 - 8(g_A^2 + 1)m^2 m_\pi}{\sqrt{4m^2 - m_\pi^2}} \arccos\left(\frac{m_\pi}{2m}\right) \\ & + (3g_A^2 + 2)m^2 + ((4g_A^2 + 2)m^2 - (3g_A^2 + 2)m_\pi^2) \log\left(\frac{m_\pi}{m}\right) \Bigg] + \mathcal{O}(p^{7/2}). \end{aligned} \tag{3.26}$$

The inclusion of the $\Delta(1232)$-loop diagrams leads to further corrections to g_A. They have been analyzed in an EOMS $SU(3)$ calculation [19], leading to small contributions (of the order of 5 to 10 %). In the scope of the present thesis, these corrections have not been considered, as they would merely mean a shift of the parameter d_{18} without otherwise affecting the quality of the fit: in the present calculations, Eq. (3.26) is used to determine d_{16} from g_A and the fit

parameter g_0, because the constant d_{16} only enters in the evaluation of two tree diagrams of $\mathcal{O}(p^3)$, always in combination with d_{18}.

In this work, I opted to consistently introduce the corrections to the constants in the Lagrangians, by applying them only to the first-order tree-level diagrams: there, g_0 is taken for the axial-vector coupling, m_2 for the propagator mass, F for the pion-decay constant, and the WFR is multiplied to this amplitude. For all the higher-order tree and loop diagrams, the physical constants g_A, m_N and F_π are taken, as otherwise corrections of order higher than $\mathcal{O}(p^{7/2})$ would be introduced. Furthermore, this scheme allows for a better comparison with the results obtained in the EOMS $\mathcal{O}(p^3)$ calculation of pion-nucleon scattering by Alarcon et al. [62].

3.4 Results

The aim of the study in this chapter is to test the convergence of the model by comparing observables to the experimental data from Ref. [55]. The linearly polarized photon asymmetry and the differential cross section have been measured in a photon-energy range from pion-production threshold up to over 200 MeV in the laboratory frame, with an unprecedented precision and for a wide range of scattering angles.

In Sec. 3.4.1, at first the $\mathcal{O}(p^3)$ calculation is shown, establishing the relevance of including the $\Delta(1232)$ as an explicit degree of freedom. The importance of obtaining LECs consistent with calculations done by other groups for other processes is stressed, especially for those works that also use the EOMS scheme up to the same chiral order. Next, in Sec. 3.4.2, the results for the $\mathcal{O}(p^{7/2})$ calculation are introduced, in order to test the convergence of the chiral series and to estimate the importance of including the $\Delta(1232)$ loop diagrams at higher energies. Finally, the resulting observables are shown in Secs. 3.4.3 and 3.4.4.

3.4.1 Contributions up to $\mathcal{O}(p^3)$

At $\mathcal{O}(p^3)$, the contributions stem from the tree diagrams in Figs. 3.3 and 3.4, as well as from the loop diagrams of Fig. 3.5. The loop diagrams which include Δ propagators, shown in Fig. 3.6, start at $\mathcal{O}(p^{7/2})$, and are therefore not considered in this initial study. They are introduced in Sec. 3.4.2.

In order to discuss the results, at first I want to comment on how the constants are treated. As previously mentioned, g_A, m_N and F_π are fixed to their physical values, and they are used instead of the LECs g_0, m and F, respectively, everywhere but in the lowest-order diagrams. The difference in the

results between taking the physical values and choosing the chiral limit of the LECs is, of course, of higher order.

At the order considered here, the mass corrections and WFR in Eqs. (3.19) and (3.25) can be truncated at order p^3. This is equivalent to saying that it is not necessary to consider the corrections to these constants arising from loops which include Δ propagators, as depicted in Fig. 3.7(b). Similarly, the constant g_0 is fixed to the value obtained at the same chiral order in Ref. [19], $g_0 = 1.16$. In the leading-order amplitude, the LEC F and the WFR for the pion leg are simultaneously corrected, as is shown in Eq. (3.22).

The $\pi N\Delta$ coupling h_A, related to the $\Delta(1232)$ width, is fixed to 2.85 [37]. The best-fit value for h_1 has been found to be 0.6 in Ref. [29]. There, the authors ascertain that the quality of the fits does almost not change when setting h_1 to zero. As was done in that work, this piece is neglected in the following. The $\gamma N\Delta$ coupling g_E is set to zero for this $\mathcal{O}(p^3)$ calculation, as the diagram where it appears is of $\mathcal{O}(p^{7/2})$.

The remaining LEC combinations $\tilde{c}_{67}$, $\tilde{d}_{89}$, $\tilde{d}_{168}$ and g_M are left as fitting parameters. I would like to stress here that $d_{168} = 2d_{16} - d_{18}$ is related to g_A and g_0 via Eq. (3.26). Therefore, one can in principle disentangle d_{16} and d_{18}, fixing one of them and fitting only the other. The results are equivalent to fitting their combination.

In Table 3.1, the results of the fit at this order are shown. Just as we found in Ref. [65], the agreement with the data is excellent, which can be read from the low reduced χ^2 value, χ^2_{red}.

g_0	$\tilde{c}_{67}$	$\tilde{d}_{89} \cdot m_N^2$	$\tilde{d}_{168} \cdot m_N^2$	g_M	χ^2_{red}
1.16	2.32	1.28	-10.1	3.08	0.79

Table 3.1.: LEC values for the $\mathcal{O}(p^3)$ calculation. The fixed value is in boldface.

A fit without the inclusion of the $\Delta(1232)$ diagrams confirmed what has already been shown in Ref. [57]: it is impossible to reproduce the drastic variation of the differential cross-section data with the photon energy at this chiral order. Only when including the Δ degrees of freedom there is a strong improvement in the agreement with the data, more importantly even at photon energies higher than 200 MeV in the laboratory frame.

In the following, I discuss the results for the LECs. The constant $\tilde{c}_{67}$ can be fixed from the proton magnetic moment. Using the model of Ref. [16], where only the isovector combination was presented, leads to the value $\tilde{c}_{67} = 2.3$ at $\mathcal{O}(p^3)$ and $\tilde{c}_{67} = 2.5$ when Δ loops are included. Although the parameter $\tilde{c}_{67}$ is let free, it should converge towards this value. As one can see in Table 3.1,

this is indeed the case, although no restrictions to this LEC were made when fitting.

The LEC $\tilde{d}_{89}$ has not yet been restricted by any alternative estimates in the particular renormalization scheme used throughout this thesis. Therefore it was let free in the fits and does obtain a natural size, i.e., a value that is between -10 and 10, as is to be expected in order to maintain a reasonable chiral counting for the Lagrangians.

The LECs d_{16} and d_{18} require more focused attention. They appear in the combination $\tilde{d}_{168} = 2d_{16} - d_{18}$ in the amplitude at tree level. Actually, they are also strongly correlated with g_0, which can be clearly seen when studying the error correlation matrix in fits that include the g_0 as a free variable. To illustrate this, when fixing $g_0 = 1.05$, which is also a value given in Ref. [19], $m_N^2\,\tilde{d}_{168}$ is modified from -10.1 to -6.9, while maintaining the other LECs and producing the same χ^2.

At $\mathcal{O}(p^2)$ the constant g_A appears in the tree diagram, and also at $\mathcal{O}(p^3)$ in the loop diagrams. Since g_A is given by a combination of g_0 and d_{16}, but not d_{18}, see Eq. (3.26), this leads to a disentaglement of d_{16} and d_{18}. In fact, by setting g_A to its physical value, one can estimate d_{16} from the fit of g_0, and consequently calculate d_{18} from the fit of $\tilde{d}_{168}$.

However, this leads to positive values for d_{18} in disagreement with other calculations [62]. But this result is very sensitive to higher-order choices, amongst which the use of g_A vs. g_0 for loops or the application of the WFR for the higher-order diagrams. In order to give an estimate on how the higher orders are related to the LEC $\tilde{d}_{168}$, contributions of $\mathcal{O}(p^4)$ were included explicitly via the contact terms of that order in the amplitude. The expressions can be obtained from Appendix C of Ref. [58]. The present study led to the conclusion that $\tilde{d}_{168}$ is very sensitive to the LECs $\tilde{e}_{48}$, $\tilde{e}_{50}$ and $\tilde{e}_{112}$. Just as an example, when taking $\tilde{e}_{48} = -4.5\ \mathrm{GeV}^{-3}$, then $m_N^2 \cdot \tilde{d}_{168}$ is modified from -10.1 to -0.4. This leads to negative values for d_{18}, consistent with other works [62], while letting the other constants and the χ^2 nearly untouched.

The couplings arising from the inclusion of the Δ at $\mathcal{O}(p^3)$ are g_M and h_A — the LEC g_E only appears at next order. While h_A is fixed to the value 2.85 as mentioned above, for g_M the fit yields a value consistent with 2.9, given in Ref. [37] in a study of pion electroproduction in the Δ region, as well as with the value of $g_M = 3.16 \pm 0.16$ obtained from the Δ electromagnetic decay in Ref. [61]. This leads to the nontrivial conclusion that the neutral pion photoproduction data are indeed strongly sensitive to the size of the Δ contribution, even close to threshold. Although it is a higher-order contribution, I would like to stress that the additional inclusion of the tree diagram that contains the g_E coupling leads to a change of the fit result for g_M to 2.9 and $g_E = -1$. This is in full agreement with Ref. [37], where this additional coupling is present.

3.4.2 Contributions up to $\mathcal{O}(p^{7/2})$

To build upon the work of Sec. 3.4.1, the next step in the calculation is the inclusion of the diagrams of $\mathcal{O}(p^{7/2})$ in the δ-counting. These include the Δ tree diagram with the g_E coupling and the loop diagrams with Δ propagators shown in Fig. 3.6. The only additional coupling constant, and therefore the only additional fitting parameter, is g_E. The loop diagrams depend only on the well known LECs g_A and h_A.

As in the previous section, I use the results of Ref. [19] for the value of the constant g_0. In their model, when including the $\Delta(1232)$ loops, g_0 varies between 1.05 and 1.08. Indeed, the parameter can be very well determined from the β-decay data. Therefore, for the fit I constrain the parameter within these limits. The remaining LECs $\tilde{c}_{67}$, $\tilde{d}_{89}$, $\tilde{d}_{168}$, g_M and g_E are left as fitting parameters. Now the full expressions for the mass and WFR corrections in Eqs. (3.19) and (3.25) have to be used.

g_0	$\tilde{c}_{67}$	$\tilde{d}_{89} \cdot m_N^2$	$\tilde{d}_{168} \cdot m_N^2$	g_M	g_E	χ^2_{red}
1.05	2.45	1.67	-9.7	2.28	3.30	0.80
1.05	2.29	1.17	-10.4	**2.90**	3.53	0.96

Table 3.2.: LEC values in the different versions of the $\mathcal{O}(p^{7/2})$ model. Fixed values appear in boldface. Note that in the fit g_0 is constrained to values between 1.05 and 1.08.

The results of the fit are shown in Table 3.2. Furthermore, the behaviour of the χ^2 as a function of the photon energy is shown in Fig. 3.8(a), comparing three different scenarios. First, a very basic model with tree-level diagrams only and no Δ is used. One sees that, immediately starting from threshold, the model is not able to reproduce the data, showing very high χ^2_{red} values. When the nucleonic loop diagrams are included as well, the convergence gets slightly better, but only up to around 20 MeV above threshold, confirming the findings of previous works [56, 57], as shown in Fig. 3.8(b). There, for consistency reasons, I only show the results in Ref. [57], as they compare the relativistic and HBChPT calculations in the same framework, while the implementation in Ref. [56] was slightly different. The qualitative behaviour is the same, though. Finally, when including the full model, the convergence is very good, even at photon energies higher than 200 MeV in the laboratory frame.

One can see that the χ^2_{red} is of similar quality to the one obtained in the $\mathcal{O}(p^3)$ calculation. This points to a convergence of the chiral series. This happens

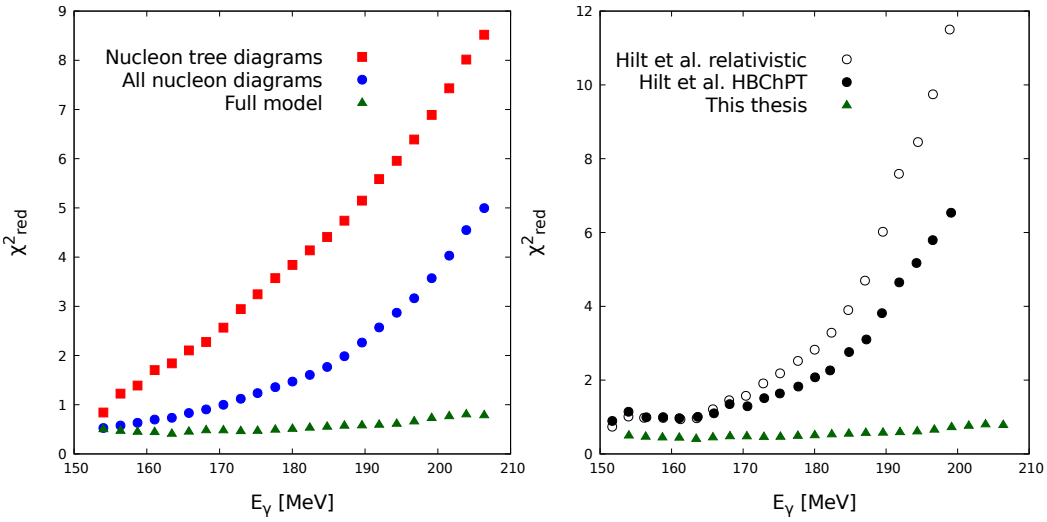

Figure 3.8.: Convergence of the chiral models at different photon energies in the laboratory frame. In the left panel, I show my calculation for three models: including only nucleon tree-level diagrams (red squares), adding the nucleonic loop contributions (blue circles), and finally the full model with the $\Delta(1232)$ resonance (green triangles). In the right panel, I compare the full model of this thesis (green triangles) with the relativistic IR (open circles) and HBChPT (filled circles) models from Ref. [57].

even though there is an additional LEC, which would a priori mean more freedom for the fit. The Δ loop terms do not appear to further improve the agreement with the data with respect to the Δ tree diagrams. This tendency is noticeable in the g_M and h_A parameters of the Δ Lagrangian, which in the fits prefer going towards lower values. In fact, the χ^2 would sensibly decrease if one allowed for a 10% reduction of the $\pi N\Delta$ coupling constant h_A. It is more sensible, though, to keep the well established result obtained from the Δ width.

In the literature, there are several works that study the value of g_M, using the same Lagrangian as in the present work. It varies from 2.6 ± 0.2 [81] in a HBChPT calculation of Compton scattering to $g_M = 2.8 \pm 0.2$ [63] (pion photoproduction), $g_M = 2.9$ [37, 82] (pion electroproduction) and $g_M = 3.16 \pm 0.16$ [61] (Δ electromagnetic decay). The latter two, which correspond to covariant chiral calculations just as this work, prefer the larger values. Although the fitting result obtained for g_M is quite low, we do however find that fixing it to $g_M = 2.9$ does not considerably worsen the fit. Even in that case the χ^2_{red} is still lower than 1. Moreover, this behaviour is not surprising and consistent with power counting: the work in which we obtained g_M from the $\Delta(1232)$ electromagnetic decay rate [61], shown in Chapter 4, amounts to a leading-order approximation. This is sufficient for the $\mathcal{O}(p^3)$ calculation of the previous section. But here next-to-leading order effects in the determination of g_M should also enter the $\mathcal{O}(p^{7/2})$ calculation of the pion photoproduction, and a reasonable deviation from $g_M = 3.16 \pm 0.16$ is to be expected.

In the lower-order calculation performed in Sec. 3.4.1, the term containing the parameter g_E is negligible, and the fit results are only slightly modified by changing its value. Here, in a higher-order calculation, this is not the case. The fit is worsened in its absence and shows to be quite sensitive to its value. The literature values for g_E vary from -7 to 2 [37, 63, 81], although the later works prefer $g_E = -1$. However, in the fits shown here, g_E prefers positive values. Moreover, this term is indispensably relevant for the E_1^+ multipole close to threshold, as are the loop diagrams appearing together with g_E.

Less drastic changes are found for the parameters $\tilde{d}_{89}$ and $\tilde{c}_{67}$, which only mildly vary due to the inclusion of this higher order. In particular, it is interesting that $\tilde{c}_{67}$ is slightly larger, again consistent with the tendency seen in Ref. [16] when the Δ loops were included. These particular LECs do not correlate strongly with the other fit parameters.

Contrariwise, the $\tilde{d}_{168}$ parameter is again strongly correlated to g_0. Changes of the order of 10% in g_0 lead to changes of 30% in $\tilde{d}_{168}$, while maintaining the same values for the other fitting parameters and for the χ^2. As discussed before, $\tilde{d}_{168}$ is very sensitive to higher-order contributions. Again estimating their effects by introducing some $\mathcal{O}(p^4)$ contact terms in the fit, one sees that

choosing $\tilde{e}_{48} = -6.0$ GeV^{-3} leads to $m_N^2 \cdot \tilde{d}_{168} = 3.1$, which corresponds to a negative d_{18}, $m_N^2 \cdot \tilde{d}_{89} = 1.1$, $g_M = 2.9$, $g_E = 2.1$ and $\chi^2_{\text{red}} = 0.67$. Interestingly, most LECs are quite stable except for the strongly modified $\tilde{d}_{168}$ and also g_E, which changes by 40 %. Similar results are obtained when including the other contact terms. Therefore, large changes are expected for these two parameters in a higher-order calculation.

3.4.3 Photon asymmetries and differential cross sections

The $\mathcal{O}(p^{7/2})$ fit results are compared with the data in Figs. 3.9 and 3.10. In spite of the small error bars of the differential cross sections, and despite the fact that they vary more than one order of magnitude in size over the range of energies studied, the agreement is excellent.

As seen experimentally, the distributions are backward peaked. At higher energies, there is a slight but systematic underestimation (overestimation) at forward (backward) angles, respectively. The experimental uncertainties for the linear photon asymmetries are larger, but nonetheless provide a very stringent test on the model, especially as the signal grows as a function of the photon energy. Although there exist much less data and the error bars are larger than for the differential cross sections, the contribution of the photon-asymmetry fit to the full χ^2 is of similar magnitude. This is interesting, and leads to the conclusion that more attention has to be paid to the convergence between model and experiment for this observable.

I show the results at two extreme energies in Fig. 3.11, close to threshold and at the highest energy measured in the data set considered. I plot the results of the full model without Δ, and I also show the size of the Δ diagrams alone, when using the parameter set of the best fit. Just as expected, the fit of $\mathcal{O}(p^3)$ including only nucleonic mechanisms, which is also shown, is not very good. The asymmetry and the shape of the angular distribution are acceptably reproduced, but the energy dependence is much too weak. This leads to an overestimation of the low-energy data and underestimation at high energies. Without the Δ contributions it seems to be necessary to include even higher orders than those calculated so far in previous works. When incorporating the Δ, the agreement is radically improved. As is shown in the figure, this is even more so at high energies, where the relative size of the Δ contributions is larger, helping to reproduce the energy dependence of the cross section. Therefore, it is the interplay between nucleonic and Δ mechanisms that simultaneously accomplishes the description of both the angular shape and the energy slope of this observable.

It is important to stress that there are only five fitting parameters, two of which are actually constrained by literature values, for around 800 data points.

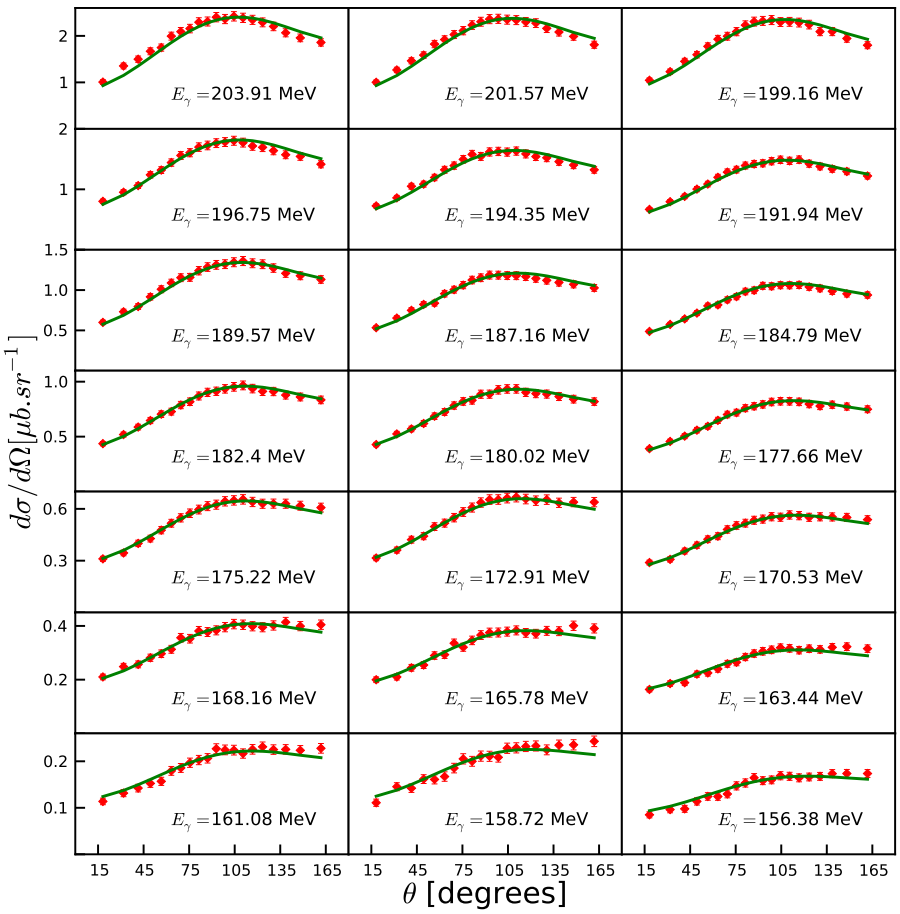

Figure 3.9.: Differential cross section as a function of the pion angle at different energies. The solid line corresponds to the best-fit theoretical model at $\mathcal{O}(p^{7/2})$. The experimental points are from Refs. [55, 83].

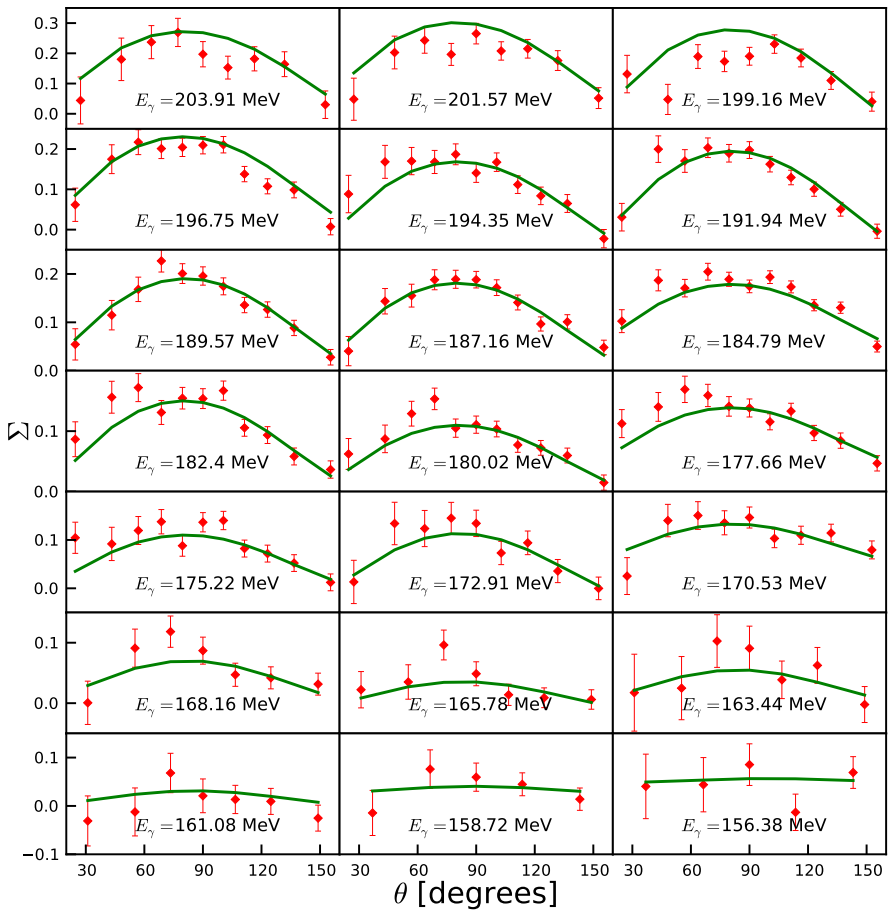

Figure 3.10.: Photon asymmetry as a function of the pion angle at different energies. The solid line corresponds to the best-fit theoretical model at $\mathcal{O}(p^{7/2})$. The experimental points are from Refs. [55, 83].

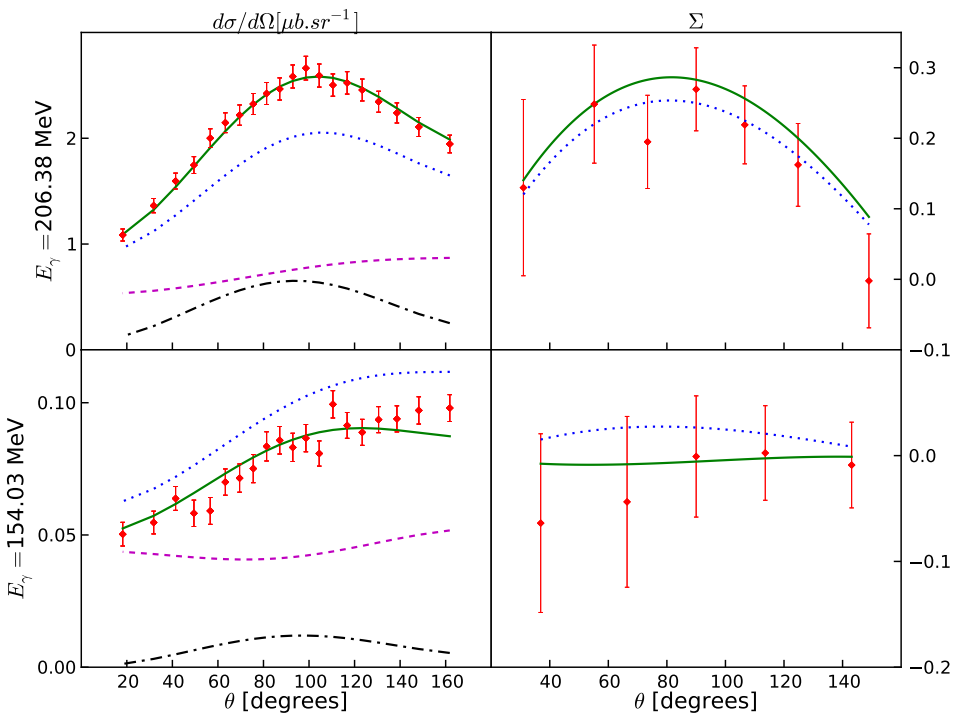

Figure 3.11.: Photon asymmetry and differential cross section as a function of the pion angle at two different photon energies: close to the threshold and at above 200 MeV in the laboratory frame. The solid, dashed, dash-dotted and dotted lines correspond to the full model, the full model without the Δ, the full model without the nucleon contributions and the best nucleonic fit without the Δ, respectively. The experimental points are from Refs. [55, 83].

It is an impressive outcome that the χ^2_{red} is lower than 1 over this wide range of energies and scattering angles.

3.4.4 Multipoles

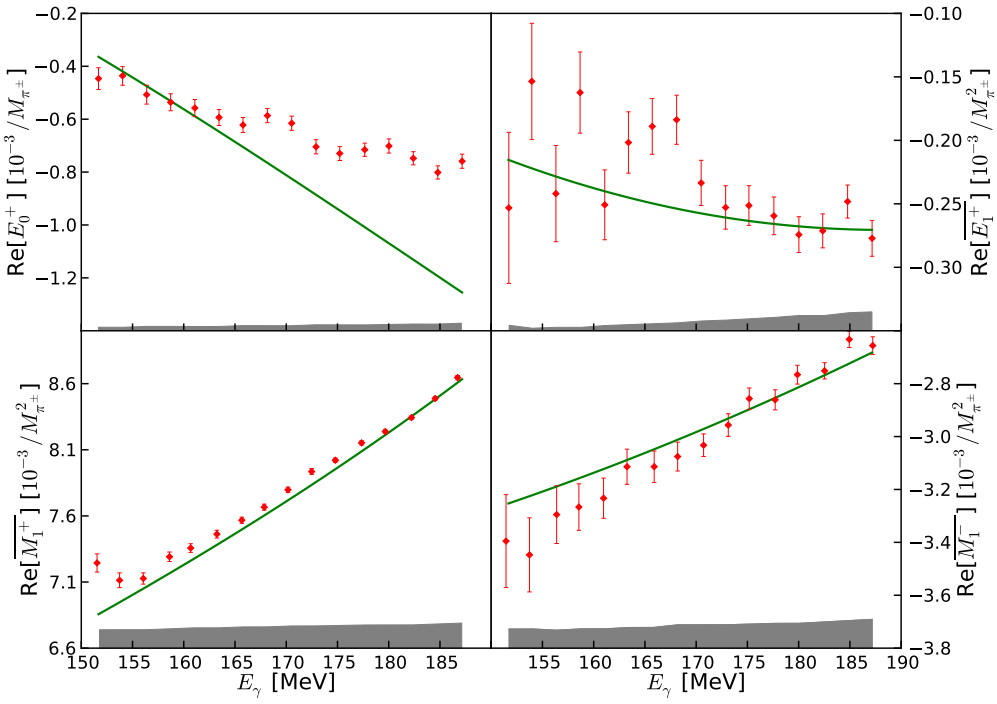

Figure 3.12.: Real part of s-wave and p-wave multipoles from Ref. [55] — see also Ref. [56] — vs. our full-model calculation, as a function of the photon energy. The error bars are only statistical errors. The gray band above the energy axis shows the systematic error of the data [55].

Additionally to the photon asymmetries and differential cross sections, in Ref. [55] also the multipoles of $l = 0, 1$ were extracted. They are shown, compared to the present chapter's model, in Fig. 3.12. Unlike the other observables, I do not use these data for the fit, but only compare them with the fit to the other observables. The reason for this is that the multipoles are themselves experimentally obtained from the differential cross-section data. The imaginary part of the multipole E_0^+ has also been extracted for the first time in Ref. [84], and is shown in Fig. 3.13. From the experimental point of view, it is related to the cross section of transverse polarized targets.

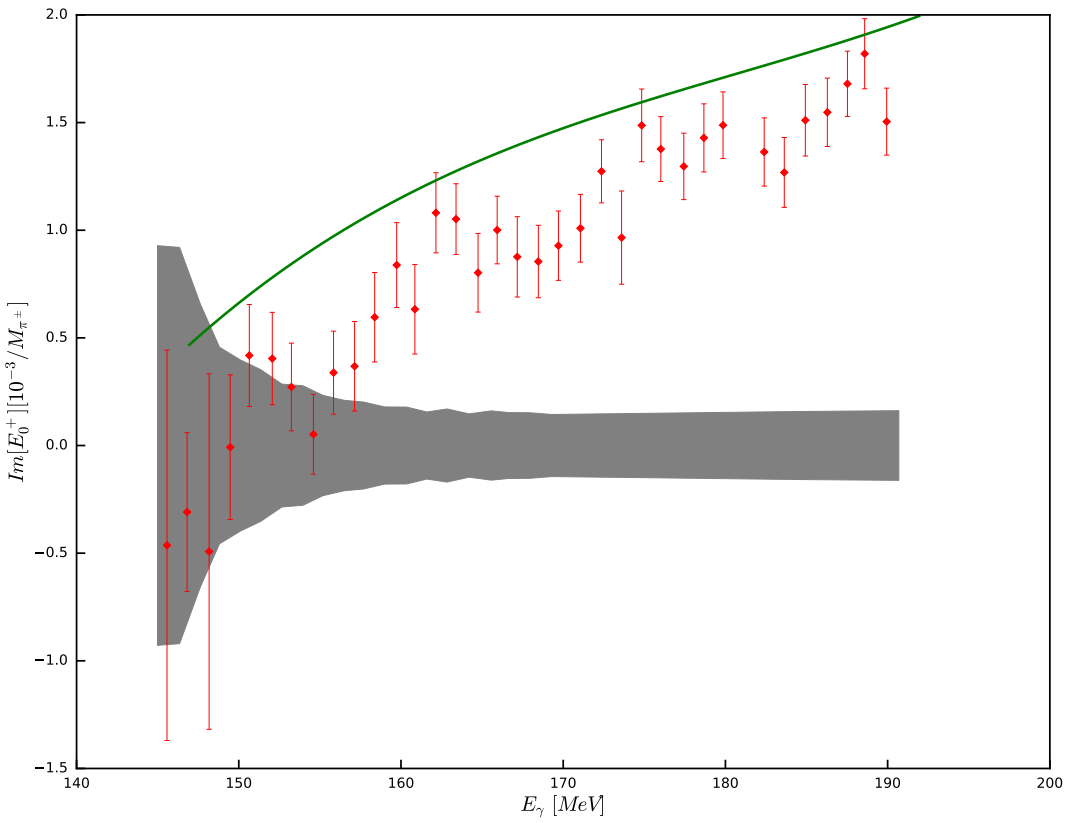

Figure 3.13.: Imaginary part of the multipole E_0^+ from Ref. [84] vs. our full-model calculation, as a function of the photon energy. The error bars are only statistical errors. The gray band above the energy axis shows the systematic error of the data.

The agreement between the data and the model for multipoles with $l = 1$ is very good. In fact, the quality for M_1^- and E_1^+ is similar to that of the $\mathcal{O}(p^4)$ covariant ChPT calculation from Ref. [57]. Moreover, also the large M_1^+ multipole is well reproduced, and it gets a substantially lower slope than in Ref. [57], despite the fact that that work was a higher-order calculation. This leads to the conclusion that the Δ plays a major role in this particular multipole.

The case of the E_0^+ is slightly different. The model reproduces it well close to threshold, but estimates too high absolute values at larger energies. This kind of behaviour was also seen in Ref. [57]. Furthermore, the imaginary part is globally overestimated. An explanation for this are the assumptions that had to be made on the partial-wave decomposition when extracting the experimental values. The angular momentum was taken to be $l \leq 2$, and only the real parts of the p and d-waves were taken into account. Of course, as can be seen in Appendix A, the amplitude decomposition in principle is an infinite sum over partial waves. One can naturally neglect partial waves of higher angular momentum, but it is important to carefully choose where to cut the series.

An important source of uncertainty is the influence of d-waves that can be sizable and grow fast with energy. In Ref. [84], e.g., the d-waves were included as fixed Born terms. In Refs. [85, 86] it was found that these d-waves drastically contribute to the result extracted for E_0^+. In the calculation in the chapter at hand, the d-wave contribution comes mainly from the crossed tree diagrams, and is therefore small. There could be large d-wave contributions coming from the $\mathcal{O}(p^4)$ Lagrangian terms, which could strongly modify the $l = 2$ multipole E_2^- that mixes with E_0^+. Therefore, the discrepancies could be explained by these changes.

3.5 Summary and outlook

In the present chapter, the study of the neutral pion photoproduction off the proton at low energies has been introduced, using covariant ChPT with the explicit inclusion of the $\Delta(1232)$ resonance. The renormalization scheme used was EOMS and a full calculation up to order $p^{7/2}$ in the δ counting was made. Comparing the $\mathcal{O}(p^{7/2})$ and $\mathcal{O}(p^3)$ calculations, a good chiral convergence has been found, the changes being quite small when going from the lower to the higher order. However, as pointed out in previous works, even at the low energies discussed here, some $\mathcal{O}(p^4)$ contributions could be relevant. For instance, in the present model there is a quite small d-wave. The consideration of higher-order terms could modify that and, indirectly, affect the extraction of the E_0^+ multipole.

The model agrees well with the experimental differential cross sections and photon asymmetries of Ref. [55], from threshold up to photon energies above 200 MeV in the laboratory frame. This extends the range of convergence from previous works of a higher chiral order, $\mathcal{O}(p^4)$, in both HBChPT and covariant ChPT. In the present work, I confirm the results from Ref. [57], where models without the Δ only reproduce the data very close to threshold, and I show that there is a huge improvement when taking into consideration the $\Delta(1232)$ mechanisms.

This is a nontrivial outcome of the work, because the LECs are mostly constrained by other observables. In particular, g_0, $\tilde{c}_{67}$, h_A and g_M are bound by the nucleon axial-vector coupling, the proton magnetic moment, the strong and the elecromagnetic decays of the $\Delta(1232)$, respectively. The fits shown here are compatible with these constraints. The LECs $\tilde{d}_{168}$ and g_E appearing in higher-order Lagrangians are partially constrained as well, by the Goldberger-Treiman relation and the ratio between the nucleon-to-Δ electric quadrupole and magnetic dipole transitions, $R_{EM} = E_2/M_1$ [37], respectively. However, the outcome is that they are sensitive to higher-order corrections, which are not within the scope of the present work.

This study is not only an important contribution to the understanding of the behaviour of the observables in the photoproduction of neutral pions, but also a very satisfactory test of the convergence and validity of covariant ChPT.

A natural extension is to consider isospin-breaking effects. Although they are higher-order corrections, it remains true that the study of the cusp effect is not possible in the isospin limit, as it appears at the opening of the charged pion channels. Therefore, in order to fully reproduce the data even directly at threshold, this mass splitting due to the breaking of isospin has to be considered.

CHAPTER **4**

HYPERON FORWARD SPIN POLARIZABILITIES

4.1 Introduction

Compton-scattering processes on compound targets are of great interest in order to extract information about their inner structure, such as their charges, magnetic momenta and polarizabilities. In particular, polarizabilities are related to the deformation of the charge distribution when subjected to an external electromagnetic field.

In this chapter, I focus on a particular case, the forward spin polarizability γ_0. In order to see its significance, it is important to first understand the meaning of baryon polarizabilities in terms of the orders of a low-energy expansion: when the Compton-scattering amplitude is expanded in the photon energy ω, the constant and linear terms contain information about global properties as the charge and the anomalous magnetic moment of the probed system. At order ω^2, the spin-independent (SI) polarizabilities α_E and β_M appear, which are related to the electric and magnetic dipole moments, respectively. For protons and neutrons, they have been extensively studied both theoretically [87] and in experimental facilities such as MAMI, described, e.g., in Ref. [88]. Nucleons are the only baryons for which this experimental information exists at the moment, since other baryons, such as nucleon excitations or hyperons, suffer from very short lifetimes.

Here I concentrate on the coefficients that appear at $\mathcal{O}(\omega^3)$. These are the four spin-dependent (SD) polarizabilities γ_i [89, 90]. They reflect the response of the system's spin to deformations relative to the spin axis, induced by external electromagnetic fields. They are related to the excitation of the spin-1/2 targets via an electric ($E1$) or magnetic ($M1$) dipole transition, fol-

lowed by a deexcitation to a spin-1/2 final state through a dipole ($E1$, $M1$) or quadrupole ($E2$, $M2$) transition: γ_{E1} as $E1 \to E1$, γ_{E2} as $M1 \to E2$, γ_{M1} as $M1 \to M1$, and γ_{M2} as $E1 \to M2$ [91]. The particular combination $\gamma_\pi = -\gamma_{M2} - \gamma_{E1} + \gamma_{E2} + \gamma_{M1}$ is known as backward spin polarizability, while the forward spin polarizability is given by $\gamma_0 = -\gamma_{M2} - \gamma_{E1} - \gamma_{E2} - \gamma_{M1}$. These are the only SD quantities measured so far, representing scattering in the extreme backward and forward direction, respectively. A good theoretical overview can be found in Ref. [92], and different approaches to the calculation of these quantities are reviewed in Refs. [93–95].

While the theoretical calculation is pretty straightforward, the spin polarizabilities are difficult to access experimentally. At low energies, they are strongly suppressed since they appear only at $\mathcal{O}(\omega^3)$. At high energies, the slow convergence of the model-independent low-energy expansions leads to a less accurate extraction from data. Regardless of these difficulties, experiments to reliably assess the nucleon spin polarizabilities have been proposed and conducted at MAMI.

Conveniently, the polarizabilities can be related to the experimental photoabsorption cross sections via sum rules. An example is the Baldin sum rule [96], which relates α_E and β_M to the total photoabsorption cross section of the nucleon. The SD piece of the amplitude is connected to scattering cross sections via the Gerasimov–Drell–Hearn (GDH) sum rule [97, 98] and the Gell-Mann, Goldberger and Thirring (GGT) sum rule [99]. The first one establishes a relation for the nucleon anomalous magnetic moment: it is connected to the difference between the two SD doubly-polarized total absorption cross sections for real photon scattering. They are the cross sections for photon helicities parallel and antiparallel to the nucleon helicity. The second sum rule represents a different moment of the same physical observable, giving a relation for the polarizability γ_0. Thus, it allows the use of the same experimental analysis data sets in both cases. This provides sensitive tests of convergence that ultimately allow the experimental access to γ_0 [100].

These relations prompted the extension to the study of structure functions in virtual Compton scattering (VCS) [101]. In forward VCS on the nucleon, the quantities related to the nucleon structure are related to the electroproduction cross sections. At large virtuality, they yield the Bjorken [102, 103] and the Burkhardt–Cottingham (BC) [104] sum rules of deep inelastic scattering. The Bjorken sum rule describes the difference between the proton's and the neutron's first moments of one of the helicity structure functions. A relation for the first moment of the other SD structure function is given by the BC sum rule. These sum rules allow to interpolate between large virtuality (short-distance probe) and low-energy photons (long-distance probe) and shed light on the transition from the parton regime of perturbative QCD to the

non-perturbative resonance regime. They have been experimentally tested in Refs. [105–107].

Experimental results for the proton γ_0 were obtained in Refs. [108, 109] and, more recently, in Ref. [110]. Furthermore, dispersion-relation studies have been performed in Ref. [111] for both nucleon spin polarizabilities. For more recent results, a good overview is given in Ref. [112], which includes also the results of Refs. [113, 114].

Concerning the theoretical approach, the nucleon structure has been thoroughly studied with the help of EFTs on Compton-scattering data [41, 115, 116]. A study comparing different EFT models has been performed in Ref. [117]. Early calculations in models of ChPT that include only nucleonic intermediate states have been made both in a HBChPT approach as well as in fully covariant calculations [118]. In Refs. [101, 119, 120], the theory was extended such as to include spin-3/2 intermediate states, namely the $\Delta(1232)$ resonance. It was found that the inclusion of the latter greatly improved the convergence between theory and empirical evidence, which can be explained by the proximity of the photon energies to the $\Delta(1232)$ excitation energy.

It is interesting to consider the theoretical studies not only for nucleons, but also for hyperons, which cannot yet be empirically assessed. This allows one to give predictions important for the further understanding of these nucleon-like states with strangeness content. Furthermore, this means considering ChPT in $SU(3)$ models so as to include the s quark additionally to the u and d quarks, therefore being a further probe of these models. First results in this direction were obtained with the help of HBChPT [121], and later improved in our work [122].

In the present chapter, I follow the assumption that, just as in the case of the nucleons in $SU(2)$, also the $SU(3)$ flavour predictions are expected to be more reliable when using a fully covariant model that introduces the decuplet of spin-3/2 baryon resonances. Along these lines, I present the calculation of the SD amplitude of Compton scattering including corrections induced by using a fully covariant version of ChPT. This was shown in our work in Ref. [61].

As I explain in Sec. 4.3, the third chiral order is the leading order for the calculation of the quantity γ_0. At this order, γ_0 only depends on known LECs, and does not contain divergences or PCBT. Therefore, the results are a pure prediction of $SU(3)$ baryon ChPT, and the values obtained provide a good test for this theory. This is one of the reasons why the study of the polarizabilities is so valuable.

The outline of this chapter is as follows. In Sec. 4.2, I give a model-independent introduction to the tools needed to extract and understand the quantity γ_0 from Compton scattering, including also kinematical considerations. In Sec. 4.3, I show the theoretical tools used, in the light of the ChPT

framework. The results are discussed in Sec. 4.4. Finally, I briefly summarize the status of the results in Sec. 4.5.

4.2 Formalism for Compton scattering

The parameterization of the scattering amplitude off baryons for photons with energy ω, and with incoming and outgoing 4-polarizations ϵ^μ and ϵ'^μ, respectively, is fairly simplified when restricting it to the forward scattering of real photons, and taking the center-of-mass frame as the reference system. It can then be decomposed into a spin-dependent and into a spin-independent part, $\mathcal{M}^{\mathrm{SD}}_{\mu\nu}$ and $\mathcal{M}^{\mathrm{SI}}_{\mu\nu}$, with structure functions f_{SD} and f_{SI}, respectively: [27]

$$\begin{aligned}\epsilon^\mu \mathcal{M}_{\mu\nu}\epsilon'^{*\nu} &= \epsilon^\mu \mathcal{M}^{\mathrm{SI}}_{\mu\nu}\epsilon'^{*\nu} + \epsilon^\mu \mathcal{M}^{\mathrm{SD}}_{\mu\nu}\epsilon'^{*\nu} \\ &= 4\pi\left[f_{\mathrm{SI}}(\omega)\vec{\epsilon}^{\,*}\cdot\vec{\epsilon} + f_{\mathrm{SD}}(\omega)\mathrm{i}\vec{\sigma}\cdot(\vec{\epsilon}^{\,*}\times\vec{\epsilon})\right].\end{aligned} \tag{4.1}$$

Here, $\vec{\sigma}$ is the vector of Pauli matrices. Using gauge invariance, Lorentz invariance and crossing symmetry, the low-energy expansion in ω leads to

$$f_{\mathrm{SI}}(\omega) = -\frac{\alpha Z}{m} + (\alpha_E + \beta_M)\omega^2 + \mathcal{O}(\omega^4) \tag{4.2}$$

and

$$f_{\mathrm{SD}}(\omega) = -\frac{\alpha}{2m^2}\kappa_N^2\omega + \gamma_0\omega^3 + \mathcal{O}(\omega^5), \tag{4.3}$$

with α the fine structure constant, Z the baryon charge, m its mass, and κ_N the anomalous magnetic moment. The leading term of the SI amplitude is the Thomson term and the term proportional to ω^2 is the Rayleigh scattering term, which contains information about the electric and the magnetic polarizabilities, α_E and β_M. Concerning the SD piece of the amplitude, the term proportional to ω^3 assumes particular interest, as it is proportional to the forward spin polarizability γ_0. Combining Eqs. (4.1) and (4.3), the latter is therefore extracted via the master formula

$$\gamma_0\left[\vec{\sigma}\cdot(\vec{\epsilon}^{\,*}\times\vec{\epsilon}\,)\right] = -\frac{\mathrm{i}}{4\pi}\frac{\partial}{\partial\omega^2}\frac{\epsilon^\mu\mathcal{M}^{\mathrm{SD}}_{\mu\nu}\epsilon'^{*\nu}}{\omega}\bigg|_{\omega=0}. \tag{4.4}$$

Thus, to obtain γ_0 it is necessary to calculate $\epsilon^\mu\mathcal{M}^{\mathrm{SD}}_{\mu\nu}\epsilon'^{*\nu}$ from the effective chiral Lagrangians described in Sec. 2.1.3, and to perform a low-energy expansion up to ω^3.

If one does not restrict oneself to forward scattering, then the SD piece of the amplitude for real Compton scattering is more generally given by [123]

$$\epsilon^\mu\mathcal{M}^{\mathrm{SD}}_{\mu\nu}\epsilon'^{*\nu} = -\frac{4\pi W}{m}\omega^3\mathrm{i}\vec{\sigma}\cdot(\vec{\epsilon}^{\,*}\times\vec{\epsilon})$$

$$\times \left(\gamma_{E1}(\omega) + \cos(\theta)\gamma_{M1}(\omega) + \gamma_{M2}(\omega) + \cos(\theta)\gamma_{E2}(\omega)\right), \quad (4.5)$$

where θ is the scattering angle, W the total center-of-mass energy and γ_i the four SD polarizabilities. It is important to note that the Weyl gauge $\epsilon_0 = \epsilon_0' = 0$ is used. From Eq. (4.5), one can see that the spin polarizabilities γ_0 and γ_π are the amplitude's leading coefficients for $\theta = 0$ and $\theta = \pi$, respectively, at the limit of vanishing ω:

$$\gamma_\pi = -\gamma_{E1} + \gamma_{M1} - \gamma_{M2} + \gamma_{E2}$$

and

$$\gamma_0 = -\gamma_{E1} - \gamma_{M1} - \gamma_{M2} - \gamma_{E2}. \quad (4.6)$$

It is also important to mention the GGT sum rule which, from the empirical side, connects γ_0 to the nucleon photo-absorption cross sections $\sigma_{3/2}$ and $\sigma_{1/2}$, with total helicities 3/2 (for parallel photon and target helicities) and 1/2 (for antiparallel photon and target helicities) [100]

$$\gamma_0 = -\frac{1}{4\pi^2}\int_{\omega_0}^{\infty} \mathrm{d}\omega \frac{\sigma_{3/2}(\omega) - \sigma_{1/2}(\omega)}{\omega^3}, \quad (4.7)$$

originally found in Ref. [99]. The energy ω_0 denotes the threshold for an associated neutral pion in the intermediate state.

4.3 Theoretical model

In this chapter, a covariant ChPT calculation is performed, up to the chiral order $\mathcal{O}(p^{7/2})$. I use the δ-counting scheme [81] explained in Sec. 2.2, while a similar study in Ref. [119] used the SSE power counting [42, 43]. As in Chapter 3, the spin-3/2 couplings are introduced in a consistent dynamics, and their full propagator is used [29, 33–35]. Most of the theoretical tools needed for the calculations were already introduced in Chapter 2. Here, I therefore focus on some additional points particular for the present chapter.

As a low-energy expansion of the calculated expressions is to be made, and only the terms proportional to ω^3 are to be kept, one can easily see that the chiral amplitudes up to $\mathcal{O}(p^2)$ do not enter the quantity γ_0. Only at $\mathcal{O}(p^3)$ does one get the first contributions, which furthermore arise exclusively from loop diagrams. As a consequence, there are no unknown LECs. The only tree diagram that has to be taken into account in this work appears at order $\mathcal{O}(p^{7/2})$ in the δ-counting scheme.

The extension to $\mathcal{O}(p^{7/2})$ by including the spin-3/2 sector, i.e., by considering the decuplet of spin-3/2 resonances, has several advantages when compared

to performing a $\mathcal{O}(p^4)$ calculation. On the one hand, one is obviously taking into account terms of a lower order in the chiral expansion, which means that their contributions should be more significant if the series is to converge. On the other hand, at a full $\mathcal{O}(p^4)$ calculation, more LECs would enter the result, leading to higher uncertainties depending on how well-established these constants are. Also, at $\mathcal{O}(p^{7/2})$ the results are independent of any renormalization schemes, because the divergent pieces of the amplitude are irrelevant for γ_0. For the above reasons, the calculations are of a predictive nature for the studied quantity. Finally, another important reason to mention is independent of the methods of ChPT, being based on more general considerations: at the considered energies of real Compton scattering (RCS), one is close to the decuplet resonance mass, and therefore its effect is already felt. Thus, it is to be expected that the contributions from the spin-3/2 baryons are of more impact than the higher-order corrections to the effects from the spin-1/2 baryons.

As mentioned in Sec. 2.1.3, at the considered order the coupling g_M has to be taken into account. It describes the electromagnetic decays of the decuplet into the octet baryons. The numerical value for the coupling constant g_M, well studied for $SU(2)$, has not yet been determined when extending the model to $SU(3)$. Therefore, the quality of the predictions very much depends on the assumptions made for the value of this constant. Following the method of Ref. [119], one can estimate it by calculating the width of the electromagnetic decay of the $\Delta(1232)$ with mass M_Δ into the nucleon with mass m:

$$\Gamma_\Delta^{\mathrm{EM}} = -2\mathrm{Im}(\Sigma_\Delta^{\mathrm{EM}}) = \frac{e^2 g_M^2 (M_\Delta - m)^3 (M_\Delta + m)^3}{4 M_\Delta^3 m^2 \pi}, \tag{4.8}$$

where $\Sigma_\Delta^{\mathrm{EM}}$ is the electromagnetic Δ self-energy amplitude. Therefore, using the relation

$$\Gamma_\Delta^{\mathrm{EM}} / (\Gamma_\Delta^{\mathrm{EM}} + \Gamma_\Delta^{\mathrm{Strong}}) = 0.55\% ... 0.65\% \tag{4.9}$$

and the strong decay width $\Gamma_\Delta^{\mathrm{Strong}} = (118 \pm 2)\mathrm{MeV}$ [124], one gets the value $g_M = 3.16 \pm 0.16$. Since data on the electromagnetic decays of the full decuplet are sparse and contain large errors, a determination of g_M in the $SU(3)$ version is not viable. Therefore, in this chapter, g_M in $SU(3)$ is also fixed to the $\Delta \longrightarrow \gamma N$ decay, that is the value of $g_M = 3.16 \pm 0.16$ is used. Naturally, the central value of g_M is expected to suffer some change when going from $SU(2)$ to $SU(3)$.

The diagrams contributing to the forward spin polarizability γ_0 are shown in Figs. 4.1 and 4.2. The calculation of the amplitudes corresponding to each of these diagrams is performed in the rest frame of the baryon, and the expressions are shown in Appendix B. In the present section, I mainly focus on the methodology to extract the polarizability. Due to the forward scattering, the initial and final photon 4-momenta and 4-polarizations are the

same: $q^\mu = q'^\mu = (\omega, \vec{q})$ and $\epsilon^\mu = \epsilon'^\mu = (0, \vec{\epsilon})$. Here, the Weyl gauge is used. Furthermore, in the following the baryon rest frame is taken, where for forward Compton scattering the initial and the final proton 4-momenta read $p^\mu = p'^\mu = (m, 0, 0, 0)$. This leads to the condition $p \cdot \epsilon = 0$.

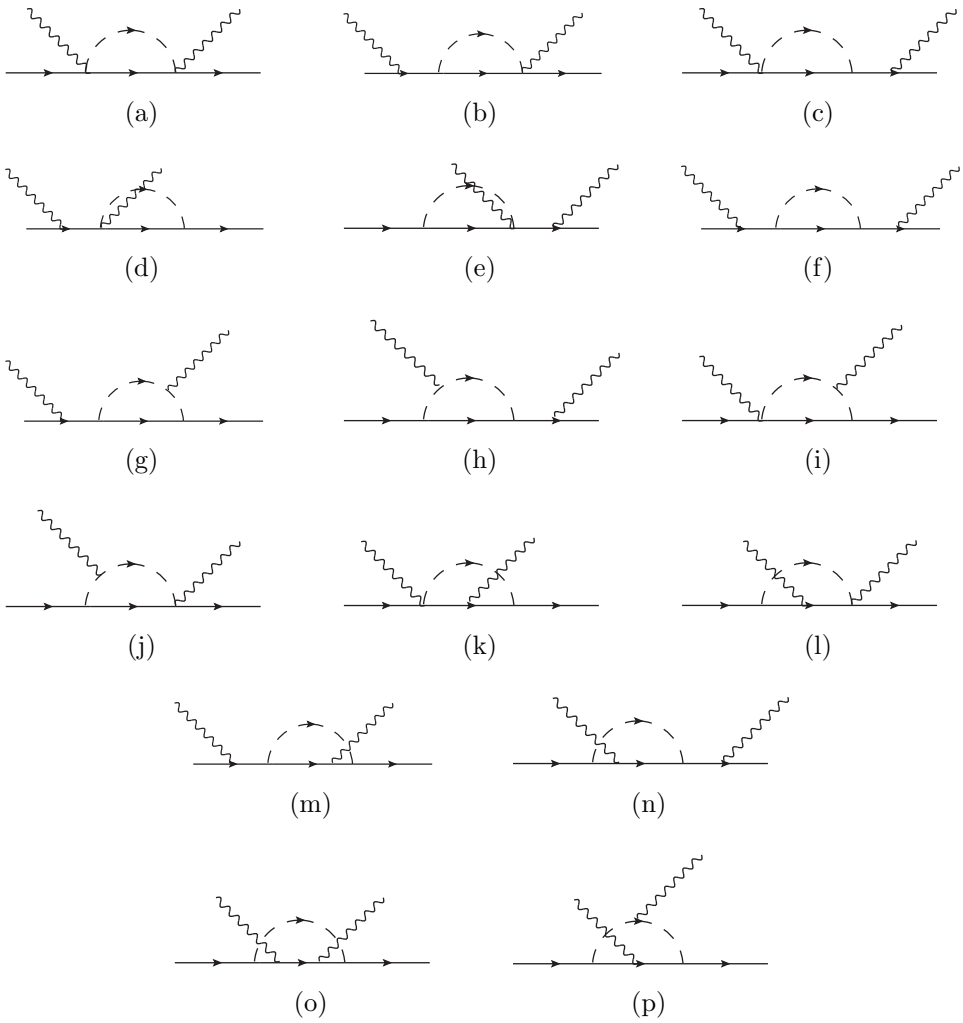

Figure 4.1.: Diagrams contributing to γ_0 with spin-1/2 intermediate states. The crossed diagrams are obtained by the substitutions $\omega \leftrightarrow -\omega$ and $\not{\epsilon} \leftrightarrow \not{\epsilon}^*$. All the vertices that appear are couplings of the lowest-order Lagrangians.

All the terms containing the expression $\not{\epsilon}^* \not{\epsilon}$ contribute to γ_0, as can be seen when comparing Eq. (4.4) with

$$\not{\epsilon}^* \not{\epsilon} = \mathrm{i}\vec{\sigma}(\vec{\epsilon} \times \vec{\epsilon}^{\,*}) - (\vec{\epsilon}\,\vec{\epsilon}^{\,*}). \tag{4.10}$$

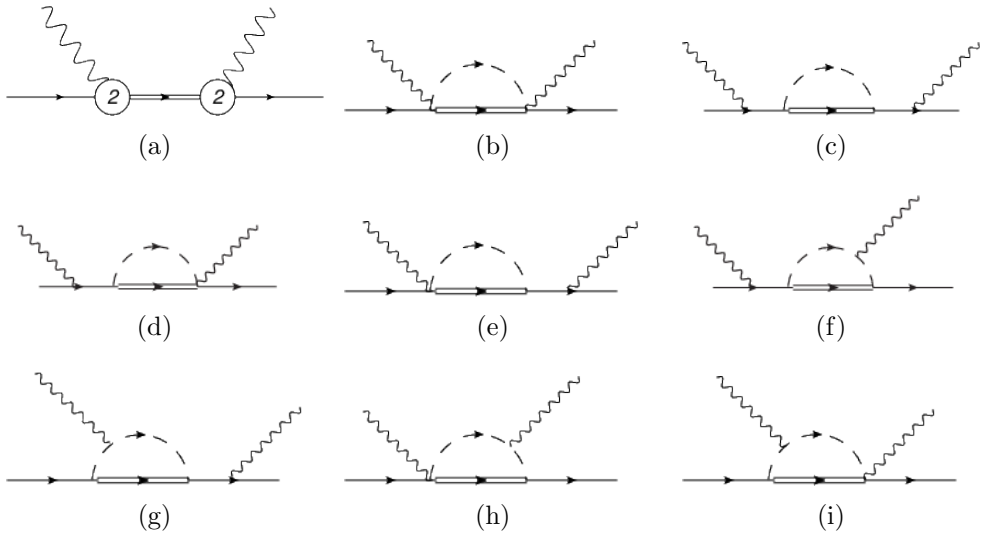

Figure 4.2.: Diagrams contributing to γ_0 with spin-3/2 intermediate states. The crossed diagrams are obtained by the substitutions $\omega \leftrightarrow -\omega$ and $\not{\epsilon} \leftrightarrow \not{\epsilon}^*$. Except for the tree diagram, which has vertices of a second-order Lagrangian, all the vertices that appear are couplings of the lowest-order Lagrangians.

The terms proportional to $\vec{\epsilon}\,\vec{\epsilon}^{\,*}$ are the contributions to the SI piece of the amplitude, as introduced in Eq. (4.1). Terms like $\not{\epsilon}^*\not{q}\not{\epsilon}$ yield a contribution of $-\mathrm{i}\omega\vec{\sigma}(\vec{\epsilon}\times\vec{\epsilon}^{\,*})$ when projected onto the baryon states. All the other expressions that arise can be reduced by applying the Dirac equation to the on-shell baryon states.

While the full set of diagrams in the spin-1/2 sector is gauge invariant, special care has to be taken when including the spin-3/2 states. In order to fully conserve gauge invariance, diagrams which include a minimal coupling of the photon to the $\Delta(1232)$ should be included. Nevertheless, they have two Δ propagators, and therefore they are of higher chiral order. This problem has already been addressed in the context of the proton γ_0 in Ref. [41], and here I follow the same solution. The one-particle-irreducible diagrams of Figs. 4.2(b), 4.2(h) and 4.2(i) are gauge invariant. Therefore, they are calculated normally, summing over all isospin channels. The missing set of one-particle-reducible loop diagrams of Figs. 4.2(c) to 4.2(g) is calculated separately: for the charged-meson channels it is again true that gauge invariance is conserved. It is the neutral channels that are problematic, and therefore their isospin factor is chosen by hand, such that the ratio between the couplings of the one-particle-reducible and the one-particle-irreducible diagrams is the

same as for the charged-meson channels. By doing so, gauge invariance is insured, and the discrepancy with isospin considerations due to this restoration procedure involves higher-order terms only. Indeed, numerically the effects of this correction are negligible.

4.4 Results and discussion

All the values chosen for the constants in this work are given in Tables 4.1 and 4.2. As a first test of the calculations, the goal was to reproduce other works' $SU(2)$ results. This is simply achieved by setting to zero all the channels with strangeness and keeping only those channels involving pions, nucleons and the isospin-3/2 quadruplet of $\Delta(1232)$ states.

		m	M_Δ	M_π	M_K	M_η	F_0
$SU(2)$	chiral limit choice	880	1152	140	$--$	$--$	87
	physical choice	938.9	1232	138.04	$--$	$--$	92.21
$SU(3)$	chiral limit choice	880	1152	140	496	547	87
	physical choice	1149	1381	140	496	547	108

Table 4.1.: Numerical values for the hadron masses and decay constants used in the γ_0 calculations. The values are given in units of MeV. The physical-choice values for $SU(2)$ were taken as in Ref. [119], whereas for the chiral limit and for $SU(3)$ I followed Ref. [19].

4.4.1 $SU(2)$ results revisited

The numerical results when including nucleons, pions and Δ resonances only (hadrons with no strangeness) are given in Table 4.3, where a comparison with the numerical values found by other groups is also given. For the spin-1/2 sector, the agreement with the results of Ref. [119] is complete. I also show how the γ_0 values vary when taking the chiral limit, where the masses are set to the best-fit chiral masses. The results are compared with the HBChPT results from Refs. [101, 118]. The discrepancy between them does not lie in the parameter choice but in the heavy-mass expansion one assumes for HBChPT, which points to the shortcomings of the latter approach.

As for the spin-3/2 sector, the reason for the difference between this thesis' results and those of Ref. [119] is the different counting scheme, and therefore

		g_A	D	F	$\mathcal{C}$	h_A	g_M
$SU(2)$	chiral limit choice	1.27	$--$	$--$	$--$	2.85	3.16
	physical choice	1.27	$--$	$--$	$--$	2.85	3.16
$SU(3)$	chiral limit choice	$--$	0.623	0.441	$-D$	$--$	3.16
	physical choice	$--$	0.8	0.47	-0.85	$--$	3.16

Table 4.2.: Numerical values for the unitless LECs used in the γ_0 calculations. The physical-choice values for $SU(2)$ were taken as in Ref. [119] — notice the difference by a factor 2 in the definition of h_A —, whereas for the chiral limit and for $SU(3)$ Ref. [19] was followed. The value for the coupling g_M is calculated through Eq. (4.8).

the different set of diagrams used. Furthermore, the couplings to the spin-3/2 isobar are introduced with a different Lagrangian, which directly sorts out the spurious spin-1/2 contributions of the RS spin-3/2 spinor. In Ref. [116], the $\Delta(1232)$ was introduced in the same way as in the present work. Nevertheless, there a tree-level diagram of order $p^{9/2}$ was included, which here is left out, in order to keep consistent with the chiral counting. Without this diagram, the numerical results in Ref. [116] are in perfect agreement with the ones presented here. The decomposition of the results for the nucleon polarizabilities of Table 4.3 into their individual parts is listed in Table 4.4. The main correction to the polarizability results comes from the tree-level diagrams with virtual spin-3/2 baryons, while the loop diagrams with Δ intermediate states give only a small contribution.

4.4.2 Extension to the $SU(3)$ sector

The main objective of the work in this chapter is the extension of the calculations to the $SU(3)$ sector, so as to give predictions to the hyperons' γ_0. Again, a distinction is made between the case where the spin-3/2 resonances were included and where only octet baryons were taken into account as intermediate states. Also, the comparison between taking the physical-average values or choosing the chiral limit is made, see Tables 4.1 and 4.2. A full list of the results for the octet baryons is given in Table 4.5 and the decomposition of the results for the nucleons into the single contributing sectors in Table 4.4. A comparison with calculations in HBChPT is given, for which preliminary results were published in Ref. [121]. A complete, improved and corrected analysis is given in our work in Ref. [122].

Model		this work	[119]	[118]	[101]	[116]
proton						
without Δ	HBChPT			4.4		
	covariant chiral limit	2.15				
	covariant physical values	2.07	2.07			
with Δ	HBChPT				1.7	
	covariant chiral limit	-1.59(38)				
	covariant physical values	-0.76(28)	-1.74			-1.0
experiment [110]		$-0.90 \pm 0.08(\text{stat}) \pm 0.11(\text{syst})$				
dispersion relations [112]		-1.1				
neutron						
without Δ	HBChPT			4.4		
	covariant chiral limit	3.24				
	covariant physical values	3.06	3.06			
with Δ	HBChPT				1.7	
	covariant chiral limit	-0.59(38)				
	covariant physical values	0.15(28)	-0.77			
experiment [110]						
dispersion relations [112]		-0.5				

Table 4.3.: Numerical values for γ_0 obtained in the $SU(2)$ sector in this and in other works, in units of 10^{-4} fm^4. The choice of the numerical values for the constants in the present work can be found in Tables 4.1 and 4.2. The error in the results when including the $\Delta(1232)$ resonance arises from the uncertainty in the value of the low-energy constant g_M.

		spin 1/2	spin 3/2 tree level	spin 3/2 loops	total
γ_0^p	$SU(2)$	2.15	-3.62(38)	- 0.13	-1.59
	$SU(3)$	1.53	-3.62(38)	- 0.05	-2.14
γ_0^n	SU(2)	3.24	-3.62(38)	- 0.21	-0.59
	$SU(3)$	2.28	-3.62(38)	- 0.08	-1.43

Table 4.4.: Decomposition of the proton and neutron polarizability results, in units of 10^{-4} fm^4, into the contributions coming from the different sets of diagrams, when using the chiral limit for the masses and low-energy constants. The difference in results when using physical values or the chiral limit can be seen as a systematical uncertainty.

In the HBChPT case, the nucleon values for γ_0 change only slightly when moving from $SU(2)$ to $SU(3)$, which corresponds to including kaon and η loop contributions. The results remain large and positive, in complete disagreement with the experiment or with dispersion-relation analyses. When using the covariant approach, on the other hand, the $SU(3)$ case shows a much better tendency, as it leads to a reduction of the γ_0 results when compared to $SU(2)$, although they remain positive. When additionally including the decuplet contributions, both the $SU(2)$ and the $SU(3)$ cases lead to negative γ_0 values, closer to the empirical value found for the proton, $\gamma_0^p = (-0.90 \pm 0.08(\text{stat}) \pm 0.11(\text{syst})) \cdot 10^{-4}\text{fm}^4$ [110]. It is also interesting to compare the γ_0 results for the nucleons with those from dispersion-relation studies found in Ref. [112] to be $\gamma_0^p = -1.1 \cdot 10^{-4}\text{fm}^4$ and $\gamma_0^n = -0.5 \cdot 10^{-4}\text{fm}^4$. While already having an important effect in HBChPT, the inclusion of spin-3/2 states leads to an even better agreement with the empirical values in the case of fully covariant calculations, both when taking the chiral limit, as well as when taking the average of the physical values for the constants. In fact, the difference between these two parameter sets is of higher chiral order: the chiral and physical masses are the same, up to higher-order corrections.

The main source of uncertainty in the results is the constant g_M, which is not very well known for $SU(3)$, and whose variation is responsible for the error estimates shown. Here, I would like to stress that the results obtained in this chapter are not subject to uncertainties related to renormalization schemes: at the considered order there are no divergences or PCBT entering into the value of γ_0, making it a pure ChPT prediction.

Model	parameters	p	n	Σ^+	Σ^-
no decuplet HBChPT	[121, 122]	4.69	4.53	2.77	2.54
no decuplet covariant	chiral	1.53	2.28	0.90	0.89
	physical	1.68	2.33	0.93	0.91
with decuplet covariant	chiral	-2.14(38)	-1.43(33)	-2.72(33)	0.89
	physical	-1.64(33)	-1.03(33)	-2.30(33)	0.90

Model	parameters	Σ^0	Λ	Ξ^-	Ξ^0
no decuplet HBChPT	[121, 122]	2.44	2.62	0.52	0.68
no decuplet covariant	chiral	1.60	1.09	0.08	0.15
	physical	1.32	1.28	0.15	0.25
with decuplet covariant	chiral	0.67(9)	-1.69(28)	0.07	-3.51(38)
	physical	0.47(8)	-1.25(25)	0.13	-3.02(33)

Table 4.5.: Numerical values for γ_0 obtained in the present calculations, in units of 10^{-4} fm^4 in the $SU(3)$ sector. The choice of the numerical values for the constants in the covariant case can be found in Tables 4.1 and 4.2, both for the chiral limit and for the physical-average case. As for the HBChPT limit, I cite the results in Ref. [121], which were later corrected in our work in Ref. [122]. The errors in the results with the decuplet arise from the uncertainty in the value of the low-energy constant g_M.

As already discussed above, the inclusion of virtual decuplet states is crucial to reproduce the experimental values for the nucleon polarizabilities with ChPT. The dominant contribution arises from the tree-level diagrams, as can be seen in Table 4.4. However, this is not the case for the Σ^- and Ξ^- baryons since the photon transitions to the corresponding decuplet states Σ^{*-} and Ξ^{*-} are forbidden in $SU(3)$-flavour symmetry. Therefore, the tree-level diagrams do not appear. Thus, the polarizabilities are only modified by the decuplet-loop contributions, which are very small. This leads to the conclusion that, for the study of the polarizabilites in baryon ChPT, these two baryons might be better suited than the proton and the neutron, since the uncertainties coming from the inclusion of the decuplet drop out. Naturally, it is not experimentally feasible to measure these polarizabilities, but lattice QCD is a realistic alternative. In fact, first calculations of the nucleon spin polarizabilities on the lattice have been performed, see Refs. [125, 126].

Another point to address is that the main differences between numerical values in $SU(2)$ and $SU(3)$ come from the choice of the parameters in Tables 4.1 and 4.2. All contributions coming from K or η meson loops are negligible. This can be seen when choosing the same masses and constants in $SU(3)$ and in $SU(2)$: the results are then nearly the same, because the only difference is due to these small K and η loop contributions.

4.5 Summary and outlook

In the present chapter, the calculation of the spin polarizability γ_0 for the baryon octet members has been revisited and extended, by using a manifestly Lorentz covariant framework of baryon ChPT. The $SU(2)$ and $SU(3)$ versions were confronted and compared, and the intermediate spin-3/2 states were explicitly included. As expected, and already studied in previous works by other groups in $SU(2)$, it is important to include these states when aiming to reproduce empirical observations which are made at energies close to the resonance's mass.

The main novelties of this work are therefore the $SU(3)$ extension of fully covariant ChPT at order p^3, and also the inclusion of the spin-3/2 decuplet up to the chiral order $p^{7/2}$. Empirical results for the nucleon case confirm that the inclusion of the explicit decuplet states is crucial to find an agreement between the experiment and ChPT, the dominant contribution arising from the tree-level diagram. This observation is also true in the $SU(3)$ case. Interestingly, the contributions from K and η loops resulting from this extension turn out to be negligible, and the main numerical differences arise when taking the different physical-average values of $SU(2)$ and $SU(3)$.

A very interesting outcome of this study concerns the negatively charged

hyperons Σ^- and Ξ^-. Their photon transitions to the corresponding decuplet states Σ^{*-} and Ξ^{*-} are forbidden in $SU(3)$-flavour symmetry, and therefore so are the decuplet tree-level contributions. As a result, their polarizabilities remain nearly unchanged since most of the uncertainties are connected to the decuplet tree-level inclusion, which drops out. Since experimental polarizability measurements for these particular baryons are not feasible, at least a comparison to results from lattice QCD would be very interesting. This would be a test of ChPT, because the forward spin polarizabilities are pure predictions up to the considered chiral order, independent of renormalization schemes, and in this case also of the uncertainty of unknown LECs. The addition of p^4 contributions would be the next step to further refine the calculation.

Following the success of this study, it would be very valuable to extend these calculations to the cases of the electric and magnetic polarizabilities α_E and β_M of the baryon octet, in particular of the Σ^- and the Ξ^-. There, one would expect a similar outcome to be observed as above, and these hyperons would nearly be unsensitive to the decuplet parameters and uncertainties.

CHAPTER **5**

OCTET-BARYON ELECTROMAGNETIC FORM FACTORS

5.1 Introduction

In Chapter 4, the reader was introduced to the value of studying Compton scattering in order to extract information about the inner structure of the hadrons. In the present chapter, I study a different approach of complementary interest, which is elastic electron scattering off baryons for the extraction of electromagnetic form factors. It is straightforward to obtain the latter from the reaction amplitude, which is described by a virtual photon being exchanged between the electron and the baryon. At small momentum transfer, where a Taylor expansion is reliable, the coefficients yield insight about quantities such as the charge radii and the electromagnetic moments. For non-vanishing photon virtualities, one can relate them to the charge and magnetic densities. A good general review on nucleon electromagnetic form factors is given in Refs. [127, 128], both from the theoretical and from the experimental point of view.

The electromagnetic current of spin-1/2 baryons is determined by two form factors: the Dirac and the Pauli form factors or combinations thereof. As is outlined in Chapter 6, where the mechanism of electron scattering is also of importance, if one allows for CP violation, a third form factor appears. At zero momentum transfer, it is related to the EDM. In the present chapter though, I do not consider processes that violate CP.

The first measurements of the nucleon form factors are described in [129–131]. In Ref. [131], it was shown how to extract the form factors from the ratio

between the experimental cross section and the expected Mott cross section of pointlike particles. The separate electric and magnetic form factors were obtained for the first time by the intersecting ellipse method, described by Hofstadter in 1955 [132]. Since then, countless efforts have been made to extract form factors experimentally, at facilities such as the Stanford Linear Accelerator Center (SLAC), the Deutsches Elektronen-Synchrotron (DESY) and the Nationaal Instituut voor Kernfysica en Hoge Energie Fysica (NIKHEF), among many others. More recently, high-precision experiments with electron beams have been performed, e.g., at MAMI.

Of late, the nucleon form factors have received much attention due to apparently conflicting results. Measurements of the proton charge radius r_E^p with electron scattering [133] have shown a disagreement with the results from precise atomic measurements of the muonic hydrogen Lamb shift [134]. This is commonly known as the proton size puzzle. The first method bases on writing the electric form factor G_E as a function of the squared momentum transfer q^2. The charge radius is then obtained from the slope of G_E at vanishing q^2. The second method uses lasers to induce atomic transitions. Here, the charge radius is related to the size of the gap between the levels.

In fact, the mean value reported from electron-scattering experiments is of $r_E^p = 0.8751(61)$ fm [133], while the atomic measurement yielded $r_E^p = 0.84184(67)$ fm [134]. Interestingly, similar measurements on normal instead of muonic hydrogen were compatible with the electron-scattering result. The main difference between the two types of hydrogen is that, since the muon mass is approximately 200 times larger than the electron's, the Bohr radius is two orders of magnitude smaller for the muonic hydrogen. Thus, the muon is much more sensitive to the proton radius, yielding a higher empirical precision. The discrepancy between results leads one to wonder if there might be new physics hiding behind the explanation for the difference between using electrons or muons, such as, e.g., the coupling of the muon to dark matter [135]. The atomic method has been reanalysed in Refs. [135–138], while there has also been an effort to better understand the results from electron scattering [139].

For the latter, an experimental determination of the slope of G_E at the exact point of real photons $q^2 = 0$ is of course not possible. However, one can gather probes of very small virtualities, and extrapolate the value at the physical point. For this extrapolation, one needs to take into account the singularities that appear in the complex plane. The first such point is the two-pion production threshold, where the virtual photon couples to the baryon via two pions. Therefore a polynomial fit for the extrapolation would only be reliable for momentum transfers significantly lower than this cut, where data are scarce. Nevertheless, in Ref. [139] such an analysis has been done, leading to a result compatible with those from the muonic hydrogen Lamb shift, thus

displaying a possible solution for the issue described above.

In order to be able to reproduce the behaviour observed at higher photon virtualities, one needs to find a theoretical approach which describes the complex-plane singularities as well. This question has been studied within dispersion analyses [140, 141], with lattice QCD [142–146] and other approaches. In the present work, the methods of ChPT are focused on. With them, pion loops are effectively described, therefore taking into account the two-pion cut in a consistent manner [8, 16, 147–150]. When moving to yet higher virtualities, kaon loops [12, 38] or even vector-meson exchanges should be considered as well. ChPT does not give a prediction for the leading order of the baryon electric form-factor expansion, since it depends on LECs whose values are not very well known. However, it is possible to predict the analytic structure of higher orders of this expansion at small virtualities. They depend only on known parameters, since there the amplitudes are given by loop diagrams with no unknown LECs.

Other interesting predictive observables to study are the baryon charge and magnetic densities. They are related to the imaginary parts of the form factors, as is explained further below. Therefore, they too appear only at loop level, and they show no dependence on unknown LECs. These densities are the focus of the second part of the present chapter.

Baryonic systems are relativistic, and therefore they are subject to vacuum fluctuations. In order to describe them in a manner in which one can treat the number of particles of the system as being a constant in time, it is convenient to use the light-front formalism [151]. There, at a fixed light-front time [152–154], the densities are real spatial densities with constant parton number. Due to the decoupling from vacuum fluctuations, the matrix elements of current operators can be expressed in the usual non-relativistic picture as overlap integrals of the wave functions in the initial and the final states. Furthermore, in that formulation, the densities are described in the transverse direction, i.e., they represent the cumulative vector current at a specific transverse distance from the center of momentum. This distance corresponds to the impact parameter b of the electrons being scattered.

With dispersion theory, one can relate the transverse densities to the Fourier transform of the imaginary parts of the form factors, i.e., the spectral functions. The imaginary parts of scattering-process amplitudes correspond to particle production. In the particular case of electron scattering, this would mean that the virtual photon that is exchanged between the electron and the target produces intermediate virtual particles, which then couple to the baryon [155, 156]. As mentioned above, the lowest energy required for the creation of virtual hadronic states is that for a pion-pair production. Therefore, the dispersion integral, which corresponds to a Fourier integral over the Mandelstam variable

$t = q^2$, starts at the two-pion cut. Higher-mass states are pseudoscalar-meson pairs such as the kaons, or single neutral vector mesons that couple to the photon directly, the lightest being the ρ, the ω and the ϕ. When moving to yet higher energies, it becomes possible to produce baryon-antibaryon pairs.

Calculations based on dispersion fits of the spectral functions to the experimental data have been done in Ref. [157]. They rely on the fact that the dispersion integral contains the modified Bessel function $K_0(-b\sqrt{t})$, which for large t decreases exponentially as $\exp\left[-b\sqrt{t}\right]$. Therefore, it acts as a filter for the masses of the produced intermediate virtual states: at large b, corresponding to the periphery of the studied baryon, the low-mass hadrons give the dominant contribution; for more central regions, the contributions of higher-mass hadrons start being sizeable too. Thus, the densities' large–distance behaviour is governed by the spectral functions near the two-pion threshold.

In this chapter, the densities I concentrate on are those at the periphery. Hence, the main focus is on the production of intermediate pseudoscalar-meson pairs. Consequently, although the process being studied is high-energy electron scattering, it is nevertheless possible to describe the observables of interest by means of spectral functions at low momentum transfer in ChPT, as has already been done for the $SU(2)$ case in Refs. [16, 158, 159]. One can assume the validity of the chiral prediction up to $t \approx 10m_\pi^2$ [147], and therefore the pseudoscalar dynamics is expected to ensure a model-independent study of the densities for transverse distances beyond 3 fm.

A further advantage of the dispersion representation is that it allows one to combine chiral and non–chiral contributions to the transverse densities in a consistent manner [158, 159]. In this thesis, the latter are modeled phenomenologically by the inclusion of the lightest vector-meson resonance contributions ρ, ω and ϕ, in order to explore the region below 3 fm. It is important to stress that these contributions are model dependent, thus serving only as a guide for the qualitative behaviour and the order of magnitude of the densities up to the peripheral distances of actual interest in this work.

The current chapter is structured as follows: in Sec. 5.2, I introduce the formalism for the calculation of the baryon form factors and the related observables. More precisely, in Sec. 5.2.1, I show the model-independent decomposition of the electron-scattering amplitude into the form factors, and its connection to the charge radii. In Sec. 5.2.2, I discuss the considerations on ChPT needed. The model for the vector-meson contributions is discussed in Sec. 5.2.3. Next, I establish the connection between the form factors and the charge and magnetic densities in Sec. 5.2.4, in the light-front formalism and with dispersion relations. In Sec. 5.3, I review the results. Namely, in Sec. 5.3.1 the results for the predictive piece of the electric form-factor expansion are shown. The spectral functions at low momentum transfer are given

in Sec. 5.3.2, and the resulting peripheral transverse densities are examined in Sec. 5.3.3. Finally, in Sec. 5.4, I present a summary and outlook of this work.

5.2 Formalism

5.2.1 Baryon form factors

The electromagnetic form factors of the octet baryons are given by the Lorentz-invariant decomposition of the matrix element of the vector current J^μ between baryon states:

$$\langle B(p')| J^\mu |B(p)\rangle = \bar{u}(p') \left(\gamma^\mu F_1(Q^2) + \frac{\mathrm{i}\sigma^{\mu\nu} q_\nu}{2m_{B0}} F_2(Q^2) \right) u(p), \tag{5.1}$$

where $u(p)$ is the spinor of the octet baryon with mass m_{B0}, and F_1 and F_2 its electromagnetic form factors. The photon momentum is given by $q = p' - p$, where p' and p are the outgoing and incoming baryon momenta, respectively. The connection to the photon virtuality is given by $q^2 = -Q^2 = t$, with t the Mandelstam variable. As usual, $\sigma^{\mu\nu} = \frac{\mathrm{i}}{2}[\gamma^\mu, \gamma^\nu]$.

The baryon electric form factor is given by

$$G_E(q^2) = F_1(q^2) + \frac{q^2}{4m_{B0}^2} F_2(q^2) = 1 + q^2 \frac{\langle r_E^2 \rangle}{6} + \frac{q^4}{2} \frac{\mathrm{d}^2}{(\mathrm{d}q^2)^2} G_E(q^2)|_{q^2=0} + \mathcal{O}(q^6), \tag{5.2}$$

where r_E is the baryon charge radius, and the pseudoscalar meson-loop contribution to $\frac{\mathrm{d}^2}{(\mathrm{d}q^2)^2} G_E(q^2)$ can be given as a prediction of ChPT. Therefore, the inclusion of this analytical function in the extrapolation of electron-scattering data can be of relevance for obtaining the proton charge radius. Experimental estimates for the value of the proton $\frac{\mathrm{d}^2}{(\mathrm{d}q^2)^2} G_E(q^2)|_{q^2=0}$ were given, for instance, in Refs. [160, 161].

5.2.2 Calculation within chiral perturbation theory

In the following, the ChPT methods for the calculation of the electromagnetic form factors are introduced. As the goal is to determine the predictive contributions to $\frac{\mathrm{d}^2}{(\mathrm{d}q^2)^2} G_E(q^2)$ and to the spectral functions, exclusively loop diagrams are needed. The tree-level diagrams determine the behaviour of $\langle r_E^2 \rangle$ and of the real parts of the form factors, where not so well known LECs from the second and the third-order chiral Lagrangians appear.

The full set of diagrams at leading chiral-loop order, $\mathcal{O}(p^3)$, is shown in Fig. 5.1. The explicit contribution of the decuplet intermediate states is included within the SSE counting scheme [42, 43]. It is important to use this

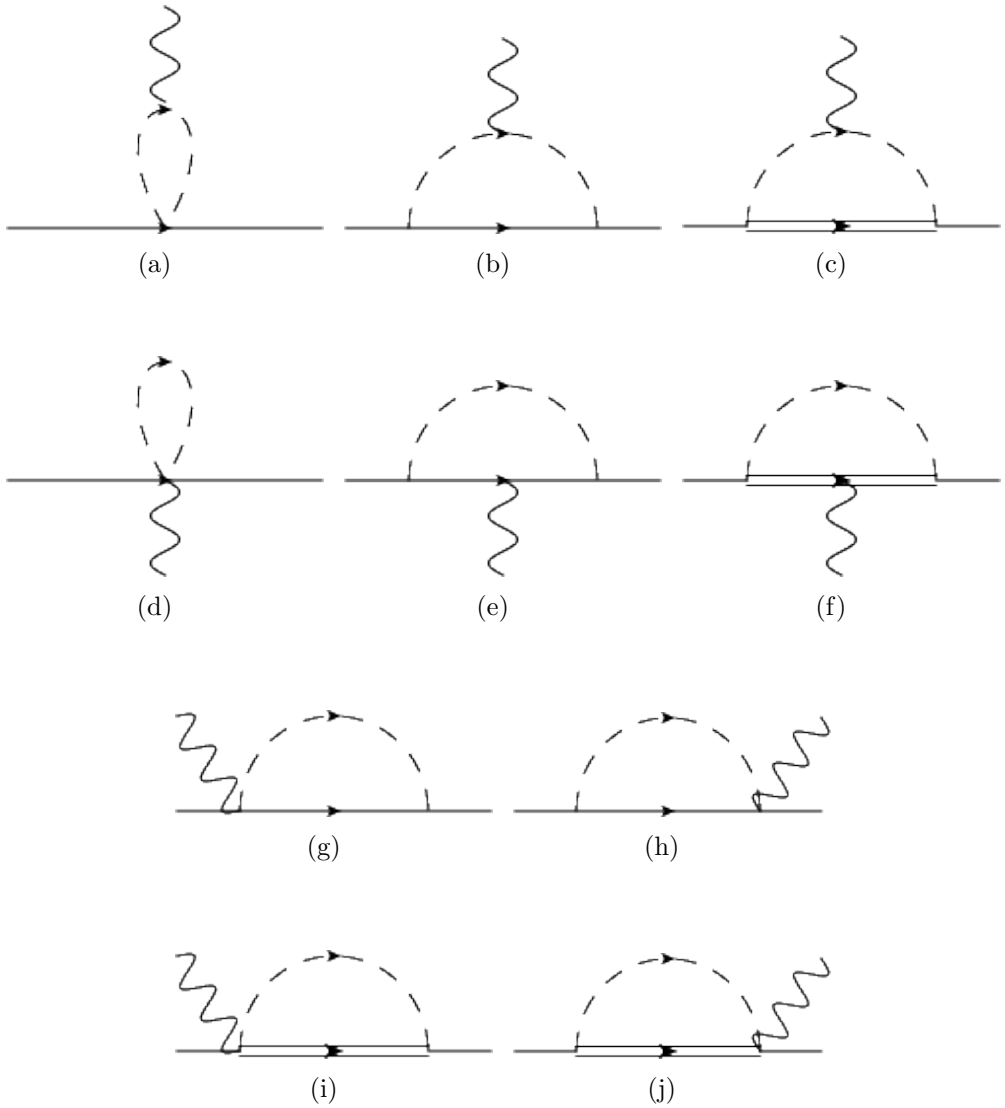

Figure 5.1.: Loop diagrams contributing to the calculation of the electromagnetic form factors at $\mathcal{O}(p^3)$.

counting as one moves towards energies closer to the decuplet mass, as I explain in Sec. 2.2. Otherwise, the effect of the intermediate decuplet states could be underestimated. All the diagrams are calculated in order to ensure gauge invariance, even if only some of them give contributions to the results shown here. The only diagrams that show a q^2 dependence are Figs. 5.1(a) to 5.1(c), 5.1(e) and 5.1(f). The set of diagrams that have imaginary parts at the two-pion cut is further reduced to Figs. 5.1(a) to 5.1(c), where the photon couples directly to the virtual meson. This type of coupling corresponds to a two-meson production in the t-channel. The renormalization of the divergent pieces is performed within the EOMS scheme [7], where the divergent parts of the amplitude are absorbed into the low-energy constants following the $\overline{MS}$ prescription, see also Appendix C. The PCBT have no imaginary parts or q^2 dependence, and therefore they do not modify the considered quantities.

The amplitudes of the diagrams are given in the following, the necessary Lagrangians having been introduced in Chapter 2. I follow the definitions introduced in Appendix B, and furthermore denote the isospin constant of the coupling of two mesons to a baryon at one point as Is_{mm}. Its values for the different baryons are summarized in Tables 5.1 and 5.2. I call the charge

p	n	Σ^+	Σ^0	Σ^-	Λ	Ξ^0	Ξ^-
$-\frac{1}{4}$	$\frac{1}{4}$	$-\frac{1}{2}$	0	$\frac{1}{2}$	0	$-\frac{1}{4}$	$\frac{1}{4}$

Table 5.1.: Values of the isospin constant Is_{mm} for the coupling of two pions to an octet baryon.

p	n	Σ^+	Σ^0	Σ^-	Λ	Ξ^0	Ξ^-
$-\frac{1}{2}$	$-\frac{1}{4}$	$-\frac{1}{4}$	0	$\frac{1}{4}$	0	$\frac{1}{4}$	$\frac{1}{2}$

Table 5.2.: Values of the isospin constant Is_{mm} for the coupling of two kaons to an octet baryon.

of the decuplet baryons c_T. The other constants, c_{DF}, c_m, c_{bi} and Is_m, are as defined in Appendix B.2, and the RS propagator $S_\Delta^{\alpha\beta}(p)$ is introduced in

Eq. (2.41).

$$J^{\mu}_{5.1(a)} = -\frac{\mathrm{i}\ \mathrm{Is_{mm}}}{F_0^2}\int\frac{\mathrm{d}^d k}{(2\pi)^d}\left\{\frac{(2k^\mu+q^\mu)(2\not{k}+\not{q})}{[k^2-m_\pi^2][(k+q)^2-m_\pi^2]}\right\}, \tag{5.3}$$

$$J^{\mu}_{5.1(b)} = \frac{\mathrm{i}\ \mathrm{c_{DF}^2}\ \mathrm{c_m}}{4F_0^2}\int\frac{\mathrm{d}^d k}{(2\pi)^d}\left\{\frac{(\not{k}+\not{q})\gamma_5(2k^\mu+q^\mu)(\not{p}-\not{k}+m_{B0})\not{k}\gamma_5}{[k^2-m_\pi^2][(k+q)^2-m_\pi^2][(p-k)^2-m_{B0}^2]}\right\}, \tag{5.4}$$

$$J^{\mu}_{5.1(c)} = -\frac{2\mathrm{i}\ \mathcal{C}^2\mathrm{Is_m^2}\ \mathrm{c_m}}{F_0^2 M_\Delta^2}\int\frac{\mathrm{d}^d k}{(2\pi)^d}\left\{\frac{(p_\alpha-k_\alpha)(k_\beta+q_\beta)\gamma^{\alpha\delta\beta}(2k^\mu+q^\mu)}{[k^2-m_\pi^2][(k+q)^2-m_\pi^2]}\right.$$
$$\left.\times\, S_\Delta^{\delta\delta'}(p-k)(p_{\alpha'}-k_{\alpha'})k_{\beta'}\gamma^{\alpha'\delta'\beta'}\right\}, \tag{5.5}$$

$$J^{\mu}_{5.1(d)} = \frac{2\mathrm{i}\ \mathrm{Is}_{mm}}{F_0^2}\int\frac{\mathrm{d}^d k}{(2\pi)^d}\frac{\not{\epsilon}}{[k^2-m_\pi^2]},$$

$$J^{\mu}_{5.1(e)} = \frac{\mathrm{i}\ \mathrm{c_{bi}c_{DF}^2}}{4F_0^2}\int\frac{\mathrm{d}^d k}{(2\pi)^d}\left\{\frac{\not{k}\gamma_5(\not{p}+\not{q}-\not{k}+m_{B0})\not{\epsilon}(\not{p}-\not{k}+m_{B0})\not{k}\gamma_5}{[k^2-m_\pi^2][(p-k)^2-m_{B0}^2][(p+q-k)^2-m_{B0}^2]}\right\}, \tag{5.6}$$

$$J^{\mu}_{5.1(f)} = \frac{2\mathrm{i}\ \mathcal{C}^2\mathrm{Is_m^2}\ \mathrm{c_T}}{F_0^2 M_\Delta^2}\int\frac{\mathrm{d}^d k}{(2\pi)^d}\left\{\frac{(p_\alpha+q_\alpha-k_\alpha)k_\beta\gamma^{\alpha\delta\beta}S_\Delta^{\delta\delta'}(p+q-k)\gamma^{\delta'\alpha'\beta'}\epsilon_{\beta'}}{[k^2-m_\pi^2]}\right.$$
$$\left.\times\, S_\Delta^{\alpha'\nu}(p-k)(p_\mu-k_\mu)k_\sigma\gamma^{\mu\nu\sigma}\right\}, \tag{5.7}$$

$$J^{\mu}_{5.1(g)} = -\frac{\mathrm{i}\ \mathrm{c_{DF}^2c_m}}{4F_0^2}\int\frac{\mathrm{d}^d k}{(2\pi)^d}\left\{\frac{\not{k}\gamma_5(\not{p}+\not{q}-\not{k}+m_{B0})\not{\epsilon}\gamma_5}{[k^2-m_\pi^2][(p+q-k)^2-m_{B0}^2]}\right\}, \tag{5.8}$$

$$J^{\mu}_{5.1(h)} = -\frac{\mathrm{i}\ \mathrm{c_{DF}^2c_m}}{4F_0^2}\int\frac{\mathrm{d}^d k}{(2\pi)^d}\left\{\frac{\not{\epsilon}\gamma_5(\not{p}-\not{k}+m)\not{k}\gamma_5}{[k^2-m_\pi^2][(p-k)^2-m_{B0}^2]}\right\}, \tag{5.9}$$

$$J^{\mu}_{5.1(i)} = \frac{2\mathrm{i}\ \mathcal{C}^2\mathrm{Is_m^2c_m}}{F_0^2 M_\Delta^2}\int\frac{\mathrm{d}^d k}{(2\pi)^d}\left\{\frac{(p_\alpha+q_\alpha-k_\alpha)k_\beta\gamma^{\alpha\delta\beta}}{[k^2-m_\pi^2]}\right.$$

$$\times S_{\Delta}^{\delta\delta'}(p+q-k)(p_{\alpha'}+q_{\alpha'}-k_{\alpha'})\epsilon_{\beta'}\gamma^{\alpha'\delta'\beta'}\Bigg\}, \tag{5.10}$$

$$J^{\mu}_{5.1(j)} = \frac{2\mathrm{i}\ \mathcal{C}^2 \mathrm{I}_{\mathrm{m}}^2 \mathrm{c}_{\mathrm{m}}}{F_0^2 M_{\Delta}^2} \int \frac{\mathrm{d}^d k}{(2\pi)^d} \Bigg\{ \frac{(p_{\alpha}-k_{\alpha})\epsilon_{\beta}\gamma^{\alpha\delta\beta}}{[k^2-m_{\pi}^2]}$$

$$\times S_{\Delta}^{\delta\delta'}(p-k)(p_{\alpha'}-k_{\alpha'})k_{\beta'}\gamma^{\alpha'\delta'\beta'}\Bigg\}. \tag{5.11}$$

The following tests were made to ensure the correctness of the calculation. By writing down the form factors in the form introduced in Eq. (5.1), one automatically controls gauge invariance. Furthermore, I verified that the results reproduce the ones of Ref. [16], a work which uses the same approach but within an $SU(2)$ framework. In order to compare the results, I reduced the $SU(3)$ calculations to the $SU(2)$ case. This is straightforwardly obtained by setting to 0 all the contributions coming from K and η loops, and keeping only the π-loop results. Additionally, one has to take into account that in the $SU(2)$ limit the constants g_A and h_A correspond to the $SU(3)$ low-energy constants $D+F$ and $-2\sqrt{2}\mathcal{C}$, respectively. Finally, I performed the calculations with different sets of programmes, FORM [76, 77] and FeynCalc [78, 79]. The two methods were in numerical accord. The computational methods are summarized in Appendix D.

5.2.3 Vector-meson contributions

In order to model the behaviour of the form factors at higher transfer energies, the contributions of the vector mesons are also included. The relevant pieces of the Lagrangians describing the couplings of the vector-meson fields V_μ with momentum q to the octet baryons are [162]

$$\mathcal{L}_{VNN} = \bar{B}\left(g_v\gamma^{\mu} + g_t\frac{\mathrm{i}\sigma^{\mu\nu}q_{\nu}}{2m_{B0}}\right)V_{\mu}B, \tag{5.12}$$

where $g_i \in \{g_v, g_t\}$ are the coupling constants given by

$$g_i = g_i^F\ \mathrm{Tr}(\bar{B}[V_8,B]) + g_i^D\ \mathrm{Tr}(\bar{B}\{V_8,B\}) + g_i^S\ V_1\mathrm{Tr}(\bar{B}B). \tag{5.13}$$

Here, V_8 is the vector-meson field in the octet representation

$$V_8 = \begin{pmatrix} \frac{1}{\sqrt{2}}\rho^0 + \frac{1}{\sqrt{6}}\omega_8 & \rho^+ & K^{*+} \\ \rho^- & -\frac{1}{\sqrt{2}}\rho^0 + \frac{1}{\sqrt{6}}\omega_8 & K^{*0} \\ K^{*-} & \bar{K}^{*0} & -\frac{2}{\sqrt{6}}\omega_8 \end{pmatrix}, \tag{5.14}$$

and the singlet is given by $V_1 = \omega_1$. I assume the case of ideal mixing

$$\omega = \frac{1}{\sqrt{3}}\omega_8 + \sqrt{\frac{2}{3}}\omega_1, \quad \phi = \sqrt{\frac{2}{3}}\omega_8 - \frac{1}{\sqrt{3}}\omega_1. \tag{5.15}$$

The determination of the numerical values for g_i^F, g_i^D and g_i^S is described below. The Lagrangian coupling a photon with 4-polarization ϵ_μ to a neutral vector meson is given by

$$\mathcal{L}_{V\gamma} = \epsilon^\mu \frac{m_V^2}{F_V} V_\mu, \tag{5.16}$$

where the mass and the decay constant of the vector mesons are given by m_V and F_V, respectively. The values are taken from Ref. [124] and tabulated in Table 5.3, bearing in mind that the leptonic decay width of the vector mesons is given by

$$\Gamma_{V\to e^+e^-} = \frac{4\pi\alpha^2}{3}\frac{m_V}{F_V^2}. \tag{5.17}$$

Finally, the propagator of the vector meson with width $\Gamma(t)$ is taken as

$$\frac{1}{q^2 - m_V^2 + \mathrm{i}\sqrt{t}\,\Gamma(t)}\left(-g^{\alpha\beta} + \frac{q^\alpha q^\beta}{m_V^2}\right). \tag{5.18}$$

From Eq. (5.13), one can extract the g_i, e.g., for the proton coupling to the ω and the ρ^0,

$$g_{i,\rho^0 pp} = \frac{1}{\sqrt{2}}(g_i^F + g_i^D), \quad g_{i,\omega pp} = \frac{3g_i^F - g_i^D}{3\sqrt{2}} + \sqrt{\frac{2}{3}}g_i^S, \tag{5.19}$$

and relate them to the empirical couplings from nucleon-nucleon scattering data. In the present chapter, those from the Bonn potential are used [163,

V	m_V [MeV]	$\Gamma_{V\to e^+e^-}$ [keV]
ρ	775	7.0
ω	783	0.6
ϕ	1019	1.3

Table 5.3.: Masses of the vector mesons and their electromagnetic decay widths into e^+e^- pairs.

164]. Note, however, that the values are model dependent and have large uncertainties. They read

$$g_{v,\rho^0pp} = 3.3, \quad g_{v,\omega pp} = 16, \quad g_{t,\rho^0pp} = 20, \quad g_{t,\omega pp} = 0. \tag{5.20}$$

Furthermore, from the baryon electric charges and magnetic moments, one gets

$$\frac{g_v^F}{g_v^F + g_v^D} = 1, \quad \frac{g_v^F + g_t^F}{g_v^F + g_v^D + g_t^F + g_t^D} = \frac{2}{5}, \tag{5.21}$$

respectively [165]. Therefore, one can extract the following information, with the help of which one can obtain all the other couplings between the vector mesons and the octet baryons:

$$g_v^F = 4.6, \quad g_v^D = 0, \quad g_v^S = 15.5,$$

$$g_t^F = 8.4, \quad g_t^D = 19.6, \quad g_t^S = -1.6. \tag{5.22}$$

For the purpose of this work, one can follow the narrow-width approximation [156] for the ω and the ϕ, where $\sqrt{t}\ \Gamma(t)$ is set to an infinitesimally small $\varepsilon > 0$. The spectral functions then yield

$$\text{Im}\ F_{1,2}(t) = \pi\ a_{VBB}^{1,2}\ \delta(m_V^2 - t), \tag{5.23}$$

with

$$a_{VBB}^1 = \frac{g_v m_V^2}{F_V}, \quad a_{VBB}^2 = \frac{g_t m_V^2}{F_V}. \tag{5.24}$$

Furthermore, the real parts of the form factors read

$$\text{Re}\ F_{1,2}(t) = \frac{a_{VBB}^{1,2}}{m_V^2 - t}. \tag{5.25}$$

As for the contribution of the broader ρ^0 to the form factors, one needs to take into account its hadronic width [147]

$$\Gamma(t) = \frac{g_{\rho\pi}^2 (t - 4m_\pi^2)^{3/2}}{48\pi t} \mathcal{H}(t - 4m_\pi^2), \tag{5.26}$$

with $\mathcal{H}$ the Heaviside step function and with $g_{\rho\pi} = 6.03$ determined from the empirical decay width of the ρ into two pions. One obtains

$$\begin{aligned} \text{Im } F_{1,2}(t) &= \frac{\sqrt{t}\ \Gamma(t) a_{VBB}^{1,2}}{(m_V^2 - t)^2 + t\ \Gamma^2(t)} \mathcal{H}(t - 4m_\pi^2), \\ \text{Re } F_{1,2}(t) &= \frac{(m_V^2 - t) a_{VBB}^{1,2}}{(m_V^2 - t)^2 + t\ \Gamma^2(t)} \mathcal{H}(t - 4m_\pi^2) + \frac{a_{VBB}^{1,2}}{m_V^2 - t} \mathcal{H}(4m_\pi^2 - t). \end{aligned} \tag{5.27}$$

Note that this formulation of the broad ρ coupling is equivalent to that in Ref. [147]. In that work, the imaginary parts of the form factors or, to be more precise, the combinations

$$G_E = F_1 + \frac{q^2}{4m_{B0}^2} F_2, \quad G_M = F_1 - F_2 \tag{5.28}$$

are studied. In the present thesis, those results are reproduced up to the size of the vector-meson couplings. As mentioned above, these are not very well known. While in Ref. [147] they are fitted to the size of the ρ peak, here I use the results from the Bonn potential [163, 164].

5.2.4 Transverse electromagnetic densities

Having determined the analytical expressions of the form factors allows one to extract the electromagnetic baryon densities. Here, I give a brief introduction on how to relate these quantities in the light-front picture. A more comprehensive overview can be found in Refs. [151, 159].

One considers the evolution of the relativistic system at fixed light-front time

$$x^+ = x^0 + x^3 = x^0 + z = 0. \tag{5.29}$$

The states are then parameterised by their light-front momentum, transverse momentum and light-front energy, given by

$$p^+ = p^0 + p^z, \quad \vec{p}_T = (p^x, p^y), \quad p^- = p^0 - p^z = \frac{p_T^2 + m_{B0}^2}{p^+}, \tag{5.30}$$

respectively. Independently of the value of p^+, for a transverse momentum transfer to the nucleon $\vec{q}_T$, where $q^\pm = 0$, the light-front current $J^+(\vec{b})$ can be decomposed into a spin-independent and into a spin-dependent part, as follows: for a baryon positioned at the origin and polarized in the y-direction, the SI and SD parts depend on the transverse charge density $\rho_1(b)$ and on $2S^y \cos\phi\, \tilde{\rho}_2(b)$ [159], repectively, where

$$\tilde{\rho}_2(b) = \frac{\partial}{\partial b}\left[\frac{\rho_2(b)}{2m_{B0}}\right] \tag{5.31}$$

and $\rho_2(b)$ is the anomalous magnetization density. The spin projection onto the y-axis is $S^y = \pm 1/2$, and ϕ is the angle of the x-axis with the transverse vector $\vec{b}$ with modulus b.

The distribution of the charge and magnetization is therefore determined by $\rho_1(b)$ and $\tilde{\rho}_2(b)$, and the form factors acquire the simple form of a two-dimensional (transverse) integral over these densities [166–168]

$$F_{1,2}(t = -\vec{q}^{\,2}) = \int \mathrm{d}^2 b \exp\left(\mathrm{i}\vec{q}\vec{b}\right)\rho_{1,2}(b). \tag{5.32}$$

On the other hand, the inverse relation is given by [159]

$$\rho_{1,2}(b) = \int_0^\infty \frac{\mathrm{d}|\vec{q}|}{2\pi}|\vec{q}|J_0(|\vec{q}|b)F_{1,2}(t = -|\vec{q}|^2), \tag{5.33}$$

where J_0 is the Bessel function.

The dispersive representation of the form factors is obtained directly by connecting them to their imaginary parts,

$$F_{1,2}(t) = \int_{4m_\pi^2}^\infty \frac{\mathrm{d}t'}{t' - t - \mathrm{i}\epsilon}\frac{\mathrm{Im}F_{1,2}(t')}{\pi}, \tag{5.34}$$

and therefore with the spectral functions one can also describe the electromagnetic densities as [158]

$$\rho_1(b) = \int_{4m_\pi^2}^\infty \mathrm{d}t\, \frac{K_0(\sqrt{t}b)}{2\pi}\frac{\mathrm{Im}F_1(t)}{\pi},$$

$$\tilde{\rho}_2(b) = -\int_{4m_\pi^2}^\infty \mathrm{d}t\, \frac{\sqrt{t}K_1(\sqrt{t}b)}{4\pi m_{B0}}\frac{\mathrm{Im}F_2(t)}{\pi}, \tag{5.35}$$

where $K_n(z)$ refers to the modified Bessel function of the second kind. Note that the lower integration limit is $t = 4m_\pi^2$, as two pions are the lowest-mass

states that can be created. Therefore, the contributions to the imaginary part of the form factors up to this cut vanish.

It is very instructive to study the analytic behaviour of Eq. (5.35), as some characteristic features of the densities can be inferred from its properties. Due to the weighting of the dispersive integral by $K_n(z)$, the functions are exponentially suppressed for large arguments:

$$K_n(z) \to (2z)^{-1/2}\sqrt{\pi}e^{-z}, \quad z \gg 1. \tag{5.36}$$

The densities are therefore expected to show an exponential fall-off.

As mentioned before, the peripheral densities are determined by diagrams with two-meson cuts. There, the photon couples to the meson directly, and thus only charged mesons give relevant contributions to the densities in the peripheral region. Here, the charged pions and kaons are therefore considered, leading to thresholds at two different positions: one at $t = 4m_\pi^2$ and the other at $t = 4m_K^2$. The spectral function assumes the form

$$\mathrm{Im}F_i(t) = \mathcal{H}(t - 4m_\pi^2)\mathrm{Im}F_i^{2\pi} + \mathcal{H}(t - 4m_K^2)\mathrm{Im}F_i^{2K}, \tag{5.37}$$

where the upper index 2π or $2K$ denotes which cut contributes to the spectral functions. Inserting Eqs. (5.36) and (5.37) into Eq. (5.35), one gets

$$\begin{aligned}\rho_1(b) \approx & \int_{4m_\pi^2}^{\infty} dt\, \frac{e^{-\sqrt{t}b}}{\sqrt{8\pi\sqrt{t}b}} \frac{\mathrm{Im}F_1^{2\pi}(t)}{\pi} + \int_{4m_K^2}^{\infty} dt\, \frac{e^{-\sqrt{t}b}}{\sqrt{8\pi\sqrt{t}b}} \frac{\mathrm{Im}F_1^{2K}(t)}{\pi} \\ =& e^{-2m_\pi b} \int_{4m_\pi^2}^{\infty} dt\, \frac{e^{-(\sqrt{t}-2m_\pi)b}}{\sqrt{8\pi\sqrt{t}b}} \frac{\mathrm{Im}F_1^{2\pi}(t)}{\pi} \\ &+ e^{-2m_K b} \int_{4m_K^2}^{\infty} dt\, \frac{e^{-(\sqrt{t}-2m_K)b}}{\sqrt{8\pi\sqrt{t}b}} \frac{\mathrm{Im}F_1^{2K}(t)}{\pi},\end{aligned} \tag{5.38}$$

which means that the contribution from the $2K$ cut is suppressed with respect to the 2π case by a factor $e^{-2(m_K - m_\pi)b}$. Thus, the kaon cloud is expected to be more central than the pion cloud. In general, for a given value of the impact parameter b, the high-energy modes are exponentially suppressed with respect to the low energy ones. Therefore, even though all the modes should be taken into account in the dispersive integral, for the peripheral regions it does indeed suffice to consider only the low-energy modes from ChPT. These conclusions can be made for $\tilde{\rho}_2$ as well. There, due to the $\sqrt{t}$ factor that results from the derivative of the modified Bessel function of the second kind, the suppression effect will be slightly smaller, but still visible.

5.3 Results and discussion

In the following, I will be showing results for observables that can be extracted from the form factors without any dependence on unknown LECs. That way, the theory is able to give predictions and does not have to be fitted to data. This amounts to observables that can be extracted from the calculation of the loop diagrams alone, not depending on ChPT tree-level contributions. These chiral $\mathcal{O}(p^3)$ loops that depend only on known parameters are shown in Fig. 5.1.

The extraction of baryon charge radii involves tree-level contributions, which depend on little known LECs. Nevertheless, the loop contributions to the quantity $\frac{\mathrm{d}^2}{(\mathrm{d}q^2)^2}G_E$ introduced in Eq. (5.2) involve only known couplings. We assume that the contributions arising from the $\mathcal{O}(p^4)$ chiral Lagrangians are saturated by the vector-meson mechanisms. For the experimental determination, the information on these q^4 coefficients of the $G_E(q^2)$ series is crucial in order to extract the behaviour of the charge radii, which are the q^2 coefficients of the $G_E(q^2)$ series. Therefore, the determination within ChPT, of predictive nature, is of great relevance.

The next point is the main goal of the present chapter: to determine the peripheral transverse electromagnetic densities. They, too, depend only on loop diagrams since, with the dispersive representation introduced in Sec. 5.2.4, only imaginary parts of the form factors give contributions.

For both studies of the present chapter, I want to focus on the extension of $SU(2)$ to $SU(3)$, in order to study the effect of η-loop and kaon-loop contributions on the nucleon observables, and also to be able to study the properties of the hyperons.

5.3.1 Predictive contributions to the electric form factor

As a first result, I want to show the numerical values I obtain for the function $\frac{\mathrm{d}^2}{(\mathrm{d}q^2)^2}G_E|_{q^2=0}$ introduced in Eq. (5.2). In Table 5.4, I present the results for the $SU(2)$ limit. The values for the constants are given in Tables 4.1 and 4.2. These results agree with Ref. [16], which uses exactly the same model[1].

The effect of the vector mesons is also studied, for whose constants the values given in Sec. 5.2.3 are taken. As one can see, the vector mesons give large contributions, and in the proton case they are much larger than those from the ChPT loops. In fact, it is with their inclusion that one achieves a

[1] A minor error has been detected in the evaluation of diagram Fig. 5.1(f), in Ref. [16]. Furthermore, in that work, the inclusion of additional higher-order terms was also explored. They are called non-minimal couplings, for the $\Delta\gamma\Delta$ vertex.

		Nucleon	$\Delta(1232)$	Vector mesons	Total
Proton	chiral limit	5.2	0.9	12.5	18.6
	experiment [160]	—	—	—	11.7 – 16.6
	physical average	4.9	0.6	12.0	17.5
Neutron	chiral limit	-5.2	0.1	-3.5	-8.6
	physical average	-4.9	0.1	-3.0	-7.8

Table 5.4.: Numerical values for the nucleon $\frac{\mathrm{d}^2}{(\mathrm{d}q^2)^2} G_E(q^2)|_{q^2=0}$ in units of GeV^{-4}, in an $SU(2)$ framework. The contributions coming from the diagrams with nucleon intermediate states, Figs. 5.1(a), 5.1(b), 5.1(d), 5.1(e), 5.1(g) and 5.1(h), and those with spin-3/2 intermediate states, Figs. 5.1(c), 5.1(f), 5.1(i) and 5.1(j), are shown separately. Furthermore, the contributions of the vector mesons ω, ρ and ϕ are listed. The values are shown both when taking the chiral limit of masses and LECs, and when taking the physical-average values of $SU(2)$.

better agreement with the experimental estimates [160]. There, polynomial fits to the proton electric form factor at very low Q^2 were made. The values range between 11.7 GeV^{-4} and 16.6 GeV^{-4}, depending on the grade of the polynomial that was taken. Substantially higher values of $\frac{\mathrm{d}^2}{(\mathrm{d}q^2)^2} G_E(q^2)|_{q^2=0} =$ 29.1 GeV^{-4} had been previously obtained in Ref. [161], also in a polynomial fit, but including larger Q^2 values.

With the framework introduced in the present thesis, I now analyse two new aspects: on the one hand, I study the influence of kaon and η loops on the results for the nucleons, by the extension of the symmetry to $SU(3)$. On the other hand, I give predictions for the hyperon values. The results are shown in Table 5.5. Concerning the nucleons, one can see that the values calculated in $SU(3)$ are slightly different from $SU(2)$. When separating the contributions of the pion loops from those of the η and the kaons, though, one sees that this is not due to the contributions of the latter heavier mesons, which turn out to give corrections of less than 10%. The numerical differences in the results when extending the symmetry to $SU(3)$ are mainly due to the different values taken for the masses and the LECs in the two approaches.

While the chiral-loop contributions to the neutron and to the proton are almost identical, but with opposite sign, this symmetry vanishes when introducing the vector-meson contributions. A similar effect can be seen for the charged Σ doublet. It is interesting to see that the other four members of the baryon octet show much smaller values of $\frac{\mathrm{d}^2}{(\mathrm{d}q^2)^2} G_E|_{q^2=0}$.

The fact that the loops of mesons with strange content give only small contributions is to be expected. Due to the higher masses, their effect becomes sizable at higher momentum transfers. Therefore, the extraction of the electric form factors at small virtualities should only be slightly affected by their contributions. The inclusion of the decuplet states, on the other hand, is again important when considering the chiral regime only. There, they give corrections to the slope's behaviour up to around 20% for the nucleons and the charged Σ hyperons. For the other hyperons, where the octet contributions are small, it might be of even more importance to include the decuplet contributions, as they become comparable in size. Of course, these effects are subdominant when compared to the vector-meson contributions, which are predominantly of larger size than those obtained from chiral loops.

It is interesting to draw the behaviour of the function $G_E(Q^2)$ compared to the experimental data separated with the Rosenbluth technique [161], which is shown in Fig. 5.2. When plotting a line of the type

$$1 + q^2 \frac{\langle r_E^2 \rangle}{6}, \tag{5.39}$$

one sees that the description is good only up to around $Q^2 = 0.03$ GeV^2, being

		Octet	Decuplet	Vector mesons	Total
Proton	chiral limit	4.0	0.4	12.5	16.9
	experiment [160]	—	—	—	11.7 – 16.6
	physical average	3.9	-0.1	10.7	14.5
Neutron	chiral limit	-3.8	-0.0	-3.5	-7.3
	physical average	-3.7	0.3	-1.7	-5.1
Σ^+	chiral limit	3.4	0.7	13.8	17.9
	physical average	2.8	0.4	12.3	15.5
Σ^-	chiral limit	-3.3	-0.4	-5.9	-9.6
	physical average	-2.7	-0.3	-5.3	-8.3
Σ^0	chiral limit	-1.0	0.1	4.0	3.1
	physical average	-0.8	0.1	3.5	2.8
Λ	chiral limit	-0.8	-0.1	1.6	0.7
	physical average	-0.9	-0.1	2.1	1.1
Ξ^-	chiral limit	-1.0	-0.5	-2.3	-3.8
	physical average	-0.8	-0.4	-2.5	-3.7
Ξ^0	chiral limit	0.7	-0.2	1.6	2.1
	physical average	0.5	0.1	2.9	3.5

Table 5.5.: Numerical values for the octet-baryon $\frac{\mathrm{d}^2}{(\mathrm{d}q^2)^2} G_E|_{q^2=0}$ in units of GeV^{-4}, in an $SU(3)$ framework. The values are shown both when taking the chiral limit of masses and LECs, and when taking the physical-average values of $SU(3)$. The further explanations are as in Table 5.4.

slighlty better when taking the radius obtained from muonic hydrogen atomic experiments [134] instead of the average radius reported for electron-scattering experiments [133]. The former leads to a slope that describes the data up to higher Q^2. One can see, though, that at least a quadratical description is needed in order to reproduce the data at even larger Q^2, of the type

$$1 + q^2 \frac{\langle r_E^2 \rangle}{6} + \frac{q^4}{2} \frac{\mathrm{d}^2}{(\mathrm{d}q^2)^2} G_E(q^2)|_{q^2=0}. \tag{5.40}$$

Two cases are compared: when including only chiral-loop contributions in the function $\frac{\mathrm{d}^2}{(\mathrm{d}q^2)^2} G_E(q^2)$, and when additionally including the vector mesons. For both these cases the proton charge radius r_E^p obtained from electron scattering was used. One can see that the inclusion of the chiral-loop contributions slightly improves the description of the data, leading to a similar effect as the linear description with the radius from muonic hydrogen experiments. The effects of the vector mesons are, as discussed above, even larger, and one can see that they lead to a good agreement up to around $Q^2 = 0.07$ GeV^2, where the quadratic description starts diverging from the data. Of course, since in the present work no fit was performed, this is to be seen as a qualitative study of the mentioned effects. Nevertheless, the behaviour seen is very promising for a better understanding of the discrepancies between the proton-radius results from different experiments.

5.3.2 Spectral functions

In the following, the results for the spectral functions of the baryon octet are shown, as functions of the squared momentum transfer. A range of values for baryon masses, meson-decay constants and couplings is considered, from the chiral limit up to the average physical values. This is depicted as bands in the plots. These sets of values have also been used in Chapter 4, and can be found in Tables 4.1 and 4.2. Note that the η loops do not contribute to diagrams relevant to the spectral function, due to this meson's vanishing charge.

In Figs. 5.3 and 5.4, the contributions to the spectral functions $\mathrm{Im}(F_1)$ and $\mathrm{Im}(F_2)$ from the meson loops are shown for the proton and the neutron, as a base of comparison with previous works on nucleon form factors. First of all, it is important to see that for most of the energy region depicted here, only the pion loops are relevant. The kaon cut starts at $t > 1$ GeV^2, giving some small corrections to the form factors at higher momentum transfers. Only at much higher energies, not shown here, the kaon and the pion loops become comparable in size. This confirms the reliability of the results calculated in previous works, in the framework of $SU(2)$.

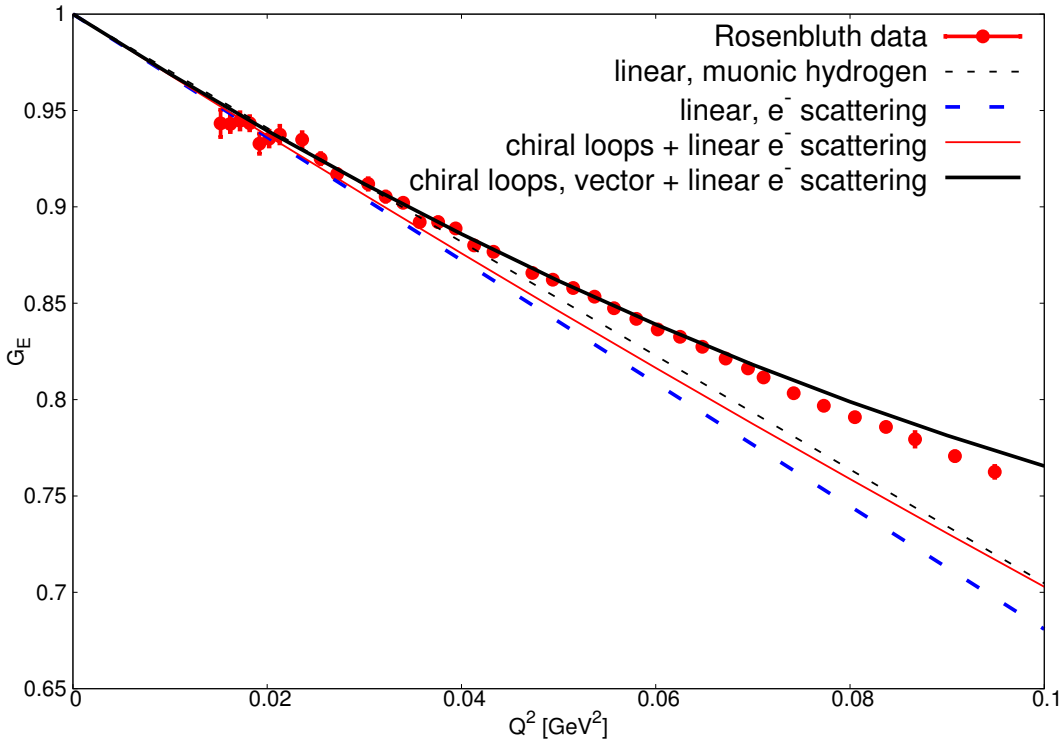

Figure 5.2.: Proton $G_E(Q^2)$ data [161] (red points) compared with the theoretical models: descriptions linear in q^2, with r_E^p from the muonic hydrogen lamb shift (short black dashes) or from the electron-scattering data (long blue dashes), as well as additional q^4 contributions from chiral loops (red thin line) and from the combination of the chiral-loop and vector-meson contributions (broad black line).

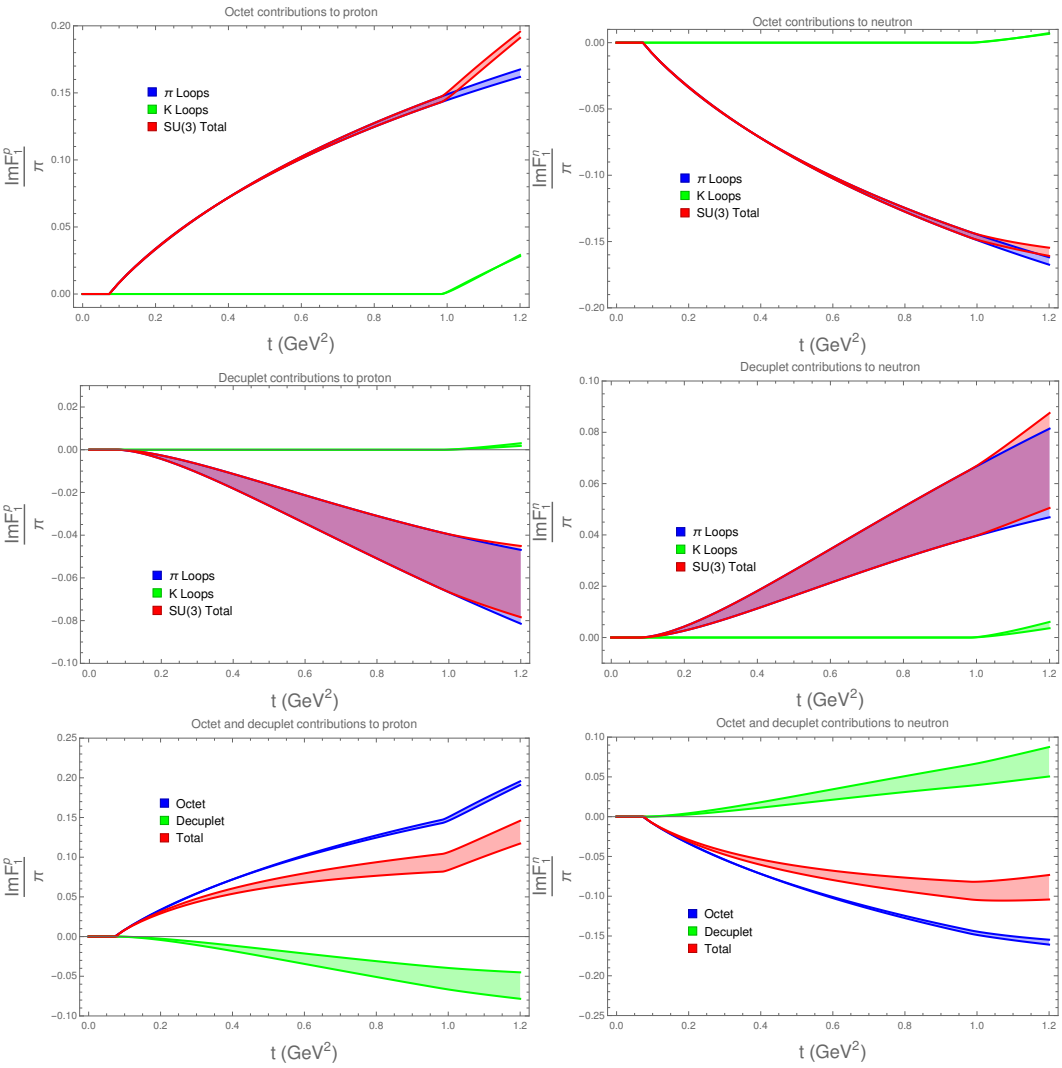

Figure 5.3.: Meson-loop contributions to the spectral function $\mathrm{Im}(F_1)$ for the nucleons. The left column is dedicated to the proton, while the neutron results are shown on the right side. The first two rows show the contributions of the octet and decuplet intermediate states, respectively. The blue band corresponds to the π-loop contributions, the green band to the K-loop contributions, and the red one shows their combination. The bands are obtained by varying the values of the constants used between the physical $SU(3)$ average and the chiral limit. The last row shows the combination (red) of octet (blue) and decuplet contributions (green).

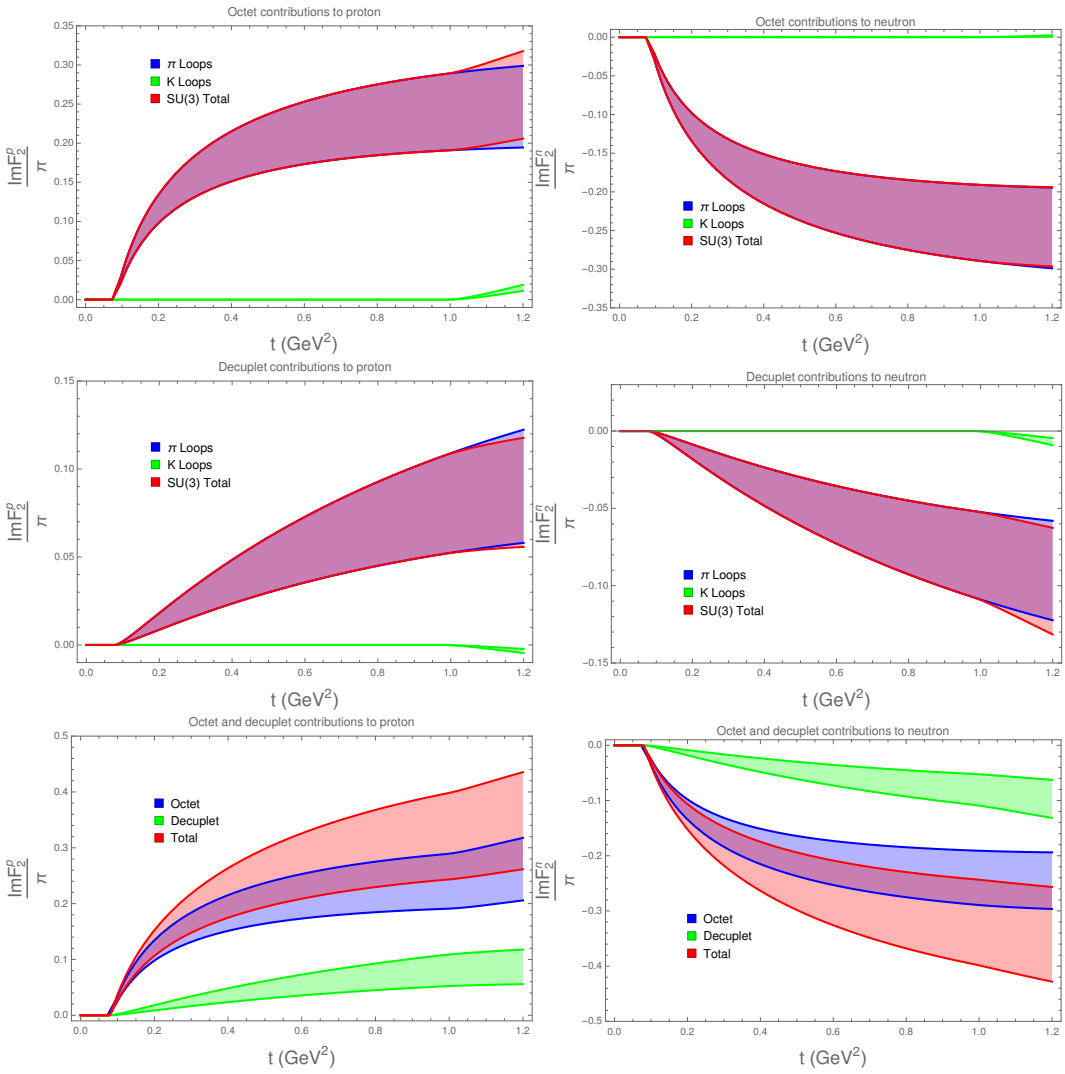

Figure 5.4.: Meson-loop contributions to the spectral function $\mathrm{Im}(F_2)$ for the nucleons. The explanation of the figures and colors is as in Fig. 5.3.

Furthermore, it is important to note that the decuplet contributions give sizeable cancellations to those of the octet. This comes as no surprise, after having studied the behaviour of $G_E(q^2)$ in the previous subsection. There, it could be seen that the decuplet contributions give important corrections in the chiral region, for which reason it is to be expected that their effect is clearly visible in the spectral functions, as well.

In total, for both the nucleons, one obtains a spectral function which is slightly decreased in magnitude when compared to the case without the decuplet inclusion. Furthermore, it shows a clear cusp at the opening of the kaon channels. The total behaviour of the two nucleons is almost identical, with a difference in the overall sign. Other small numerical differences arise from the interference behaviour between the kaon and the pion loops. For $\mathrm{Im}(F_1)$, it is in total constructive for the proton, but destructive for the neutron. Concerning $\mathrm{Im}(F_2)$, the effect of the kaon contributions is smoother and almost not visible in the momentum-transfer region considered here.

In Figs. 5.5 and 5.6, the contributions to the spectral functions $\mathrm{Im}(F_1)$ and $\mathrm{Im}(F_2)$ from the meson loops are shown for all the octet members. One can see that they can be clearly grouped in pairs with similar behaviour. Both the Ξ and the charged Σ hyperons exhibit a constructive intereference between the decuplet and the octet contributions, where the importance of the former is very strong for the Ξ. In fact, contrary to the other baryon-octet members, there the decuplet and octet contributions are of a similar size, even for small energies. This is a very important result, which shows that it is crucial to include the spin-3/2 states in the theory.

Concerning the Σ^0 and the Λ, their behaviour is of major interest as well. In the isospin limit, where the charged and the neutral pions have the same masses, the pion loops cancel exactly. As one can see, one only obtains non-zero contributions to the spectral functions at the two-kaon cusp. Since the isospin-breaking corrections are small, they are normally neglected. However, these effects become dominant when calculating quantities suppressed by isospin symmetry, i.e., when the isospin-symmetric result cancels out exactly, as is the case of the Λ and the Σ^0. The effect in the spectral functions is small, though.

For the following section, where the charge and magnetic densities are to be extracted from the spectral functions, it is important to include also the vector-meson contributions, as introduced in Sec. 5.2.3. These model the behaviour of the densities at small transverse distances, closer to the baryons' core. Therefore, one can estimate the size and the qualitative behaviour of the transition region between the chiral periphery and the more central regions.

The vector-meson contributions to the spectral functions are shown in Fig. 5.7 for the case of the nucleon. The broad ρ starts to be significant at relatively

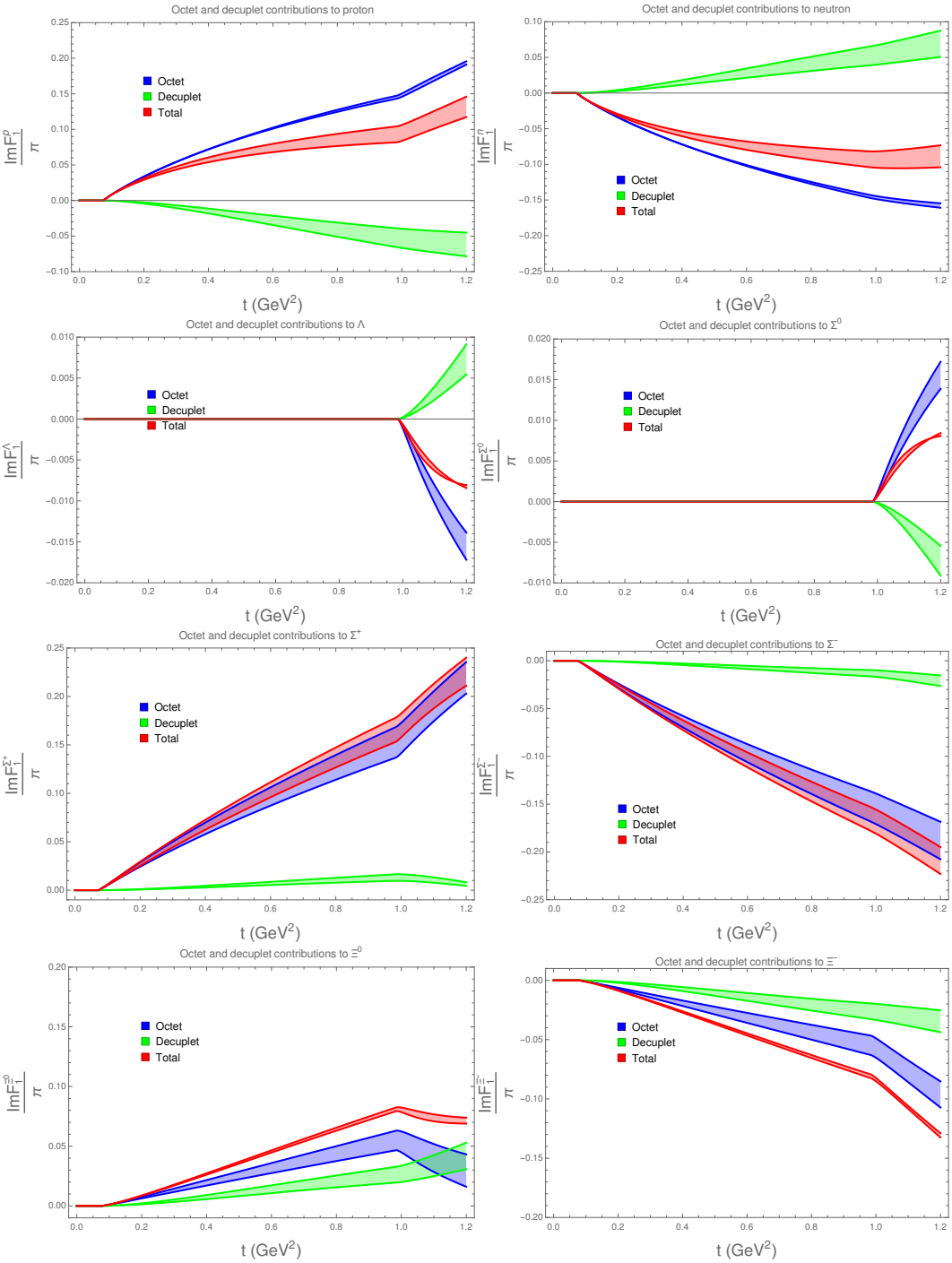

Figure 5.5.: Meson-loop contributions to the spectral function $\mathrm{Im}(F_1)$ for all the octet members. The combination (red) of octet (blue) and decuplet (green) contributions is shown. The bands are obtained by varying the values of the constants used between the physical $SU(3)$ average and the chiral limit.

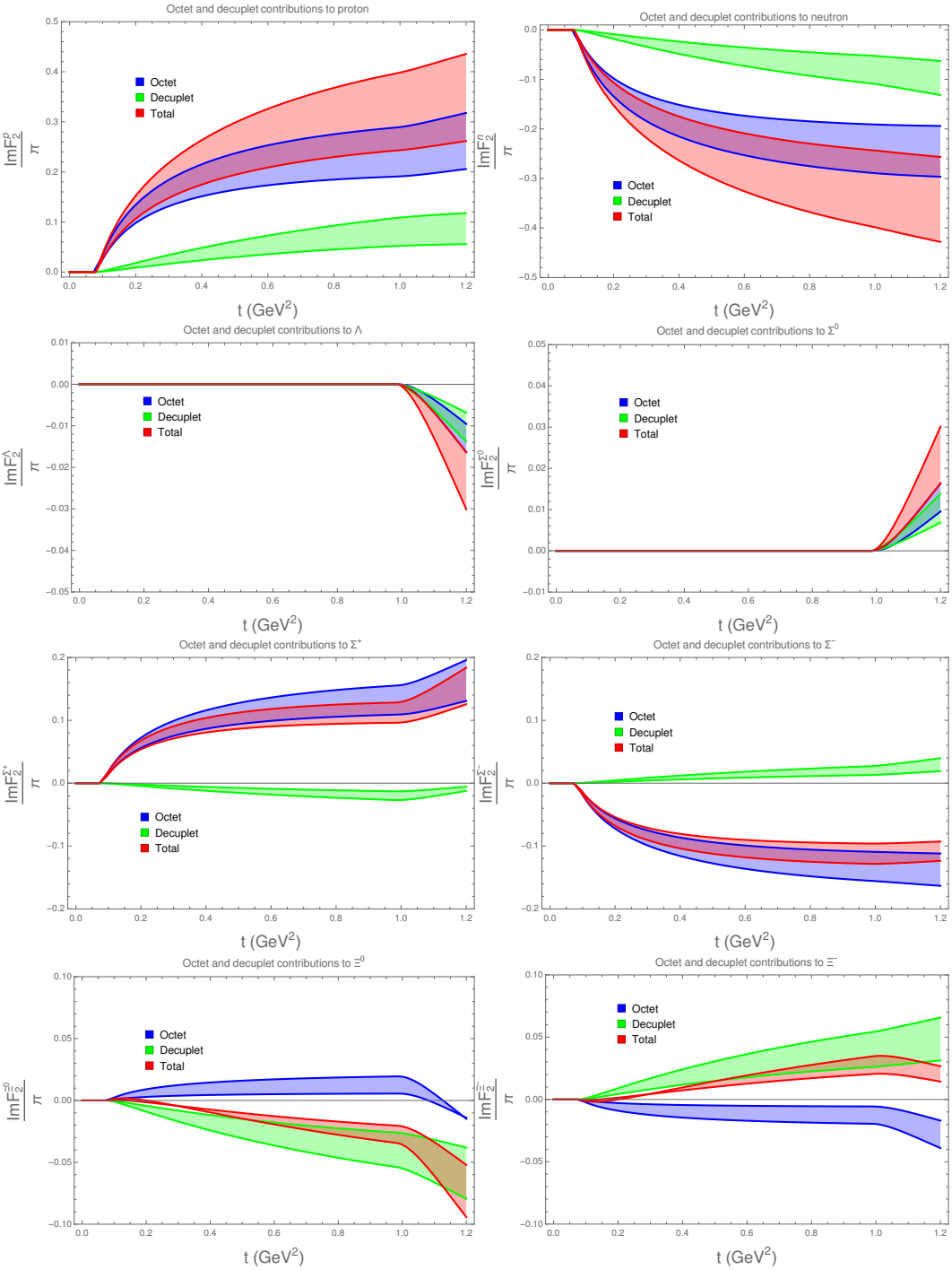

Figure 5.6.: Meson-loop contributions to the spectral function $\mathrm{Im}(F_2)$ for all the octet members. The explanation is as in Fig. 5.5.

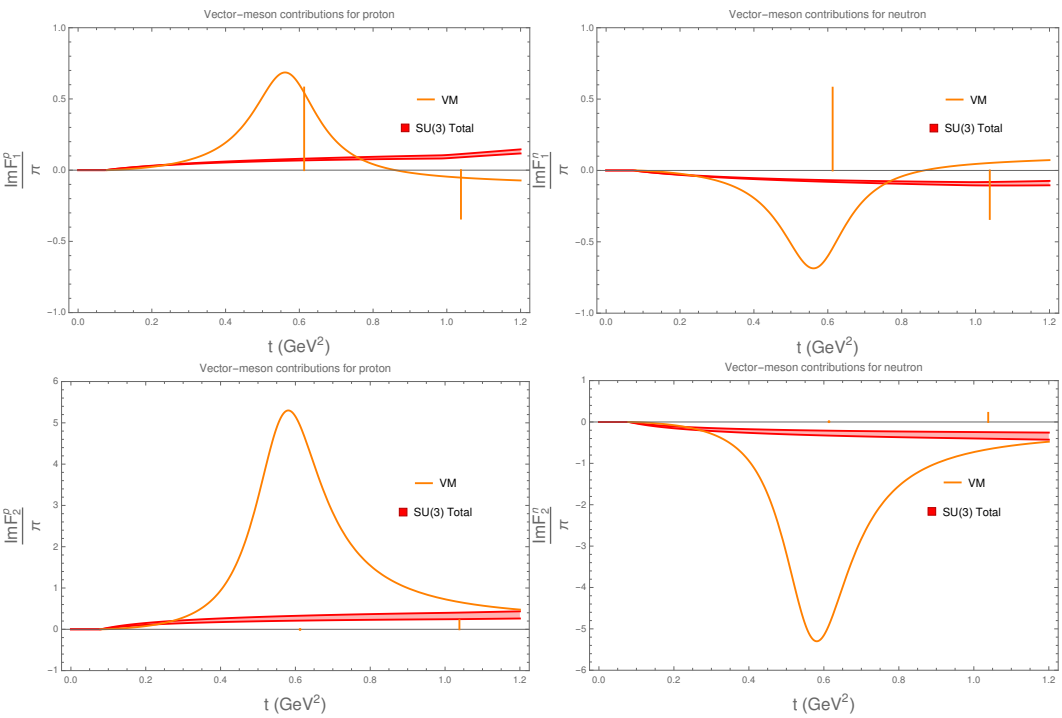

Figure 5.7.: Spectral functions of the nucleons, with vector-meson contributions. The left column shows the proton and the neutron is on the right. The upper panels show $\mathrm{Im}(F_1)$ and the lower ones $\mathrm{Im}(F_2)$. The red band shows the total $SU(3)$ chiral-loop contributions, while the orange lines show the vector-meson contributions.

low momentum transfers, $t \approx 0.3$ GeV^2. This means that it is sizeable even for energies that are still in the chiral domain. For $\mathrm{Im}(F_1)$, the higher-mass poles ω and ϕ play an important role at higher transfer energies. In fact, there is an interesting interplay between the ρ and the ω, which in the case of the neutron partially cancel each other, while for the proton they add up. This promises interesting results for the charge densities, shown in Sec. 5.3.3. The case of $\mathrm{Im}(F_2)$ is different, where the ω and ϕ contributions are zero or negligible, respectively.

5.3.3 Charge and magnetic transverse densities

Finally, I discuss the results for the charge and magnetic densities, extracted via the Fourier integral over the spectral functions, as explained in Sec. 5.2.4. They are shown for all the octet baryons, in Figs. 5.8 and 5.9. The vector-meson contributions are already included. The uncertainty-bands in the plots are again given by the variation of the parameters used between the chiral limit and the physical average. Furthermore, they are now additionally associated with the low-energy representation of the spectral functions in the dispersive integral: by varying its upper limit from $t = 10m_\pi^2$ to infinity, one can estimate the error that arises from the assumption that higher-mass states need not be included.

An $SU(2)$ calculation for the nucleon isovector combination has already been presented in Ref. [159], but using a different formulation for the spin-3/2 resonances. In the present work, the study is extended to the hyperons. As expected from the spectral functions, the chiral contributions to the peripheral density of the nucleons are mainly given by the loops of pions and octet baryons, while only at very short distances, not shown here, the kaon cloud and the decuplet become sizeable. Therefore, in the peripheral region, the differences between the proton and the neutron behaviour are negligible, as they are solely given by these kaon and decuplet contributions.

Concerning the vector-meson effects, it is interesting to see that, due to the identical sign of the ρ and the ω in the spectral function $\mathrm{Im}(F_1)$ of the proton, the charge density's final result is increased for peripheral distances $b > 1$ fm. In fact, the calculations yield that the ρ gains the same importance as the two-pion cut at distances $b \approx 3$ fm, and that it increases with smaller b. This effect of the vector mesons on the charge-density profile is still present when adding the negative ϕ contribution. Due to its higher mass, it has less weight in the dispersive integral.

For the neutron, the situation is different. Since the ρ contribution is reversed in sign, there is an interesting interplay between the contributions of this negative resonance and the positive ω. At large transverse distances, the

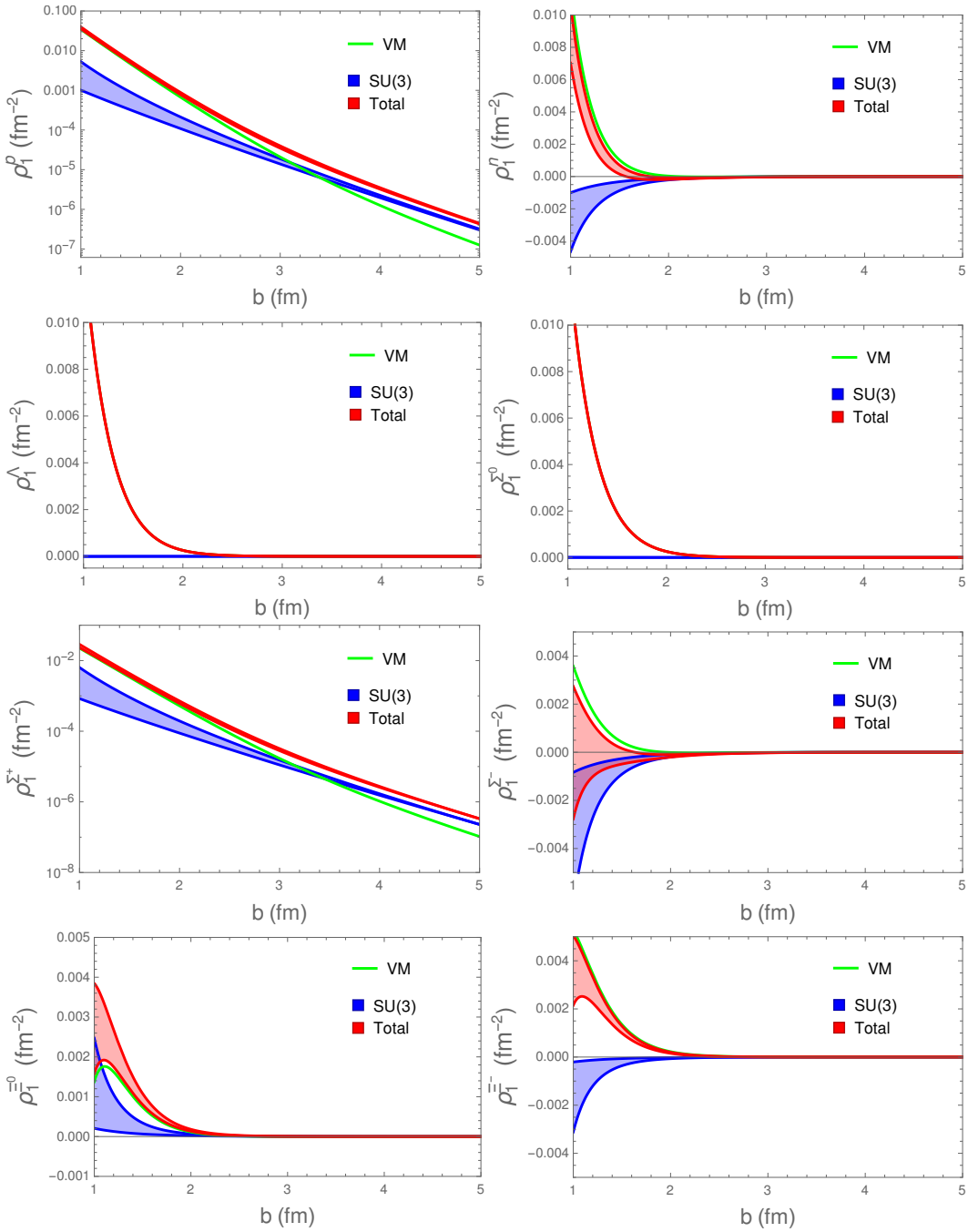

Figure 5.8.: Charge densities ρ_1 for all the octet members as functions of the transverse distance b. The combination (red) of chiral-loop (blue) and vector-meson (green) contributions is shown. The bands are obtained by varying the values of the constants used between the physical $SU(3)$ average and the chiral limit, in combination with varying the cut of the upper limit in the dispersive integral.

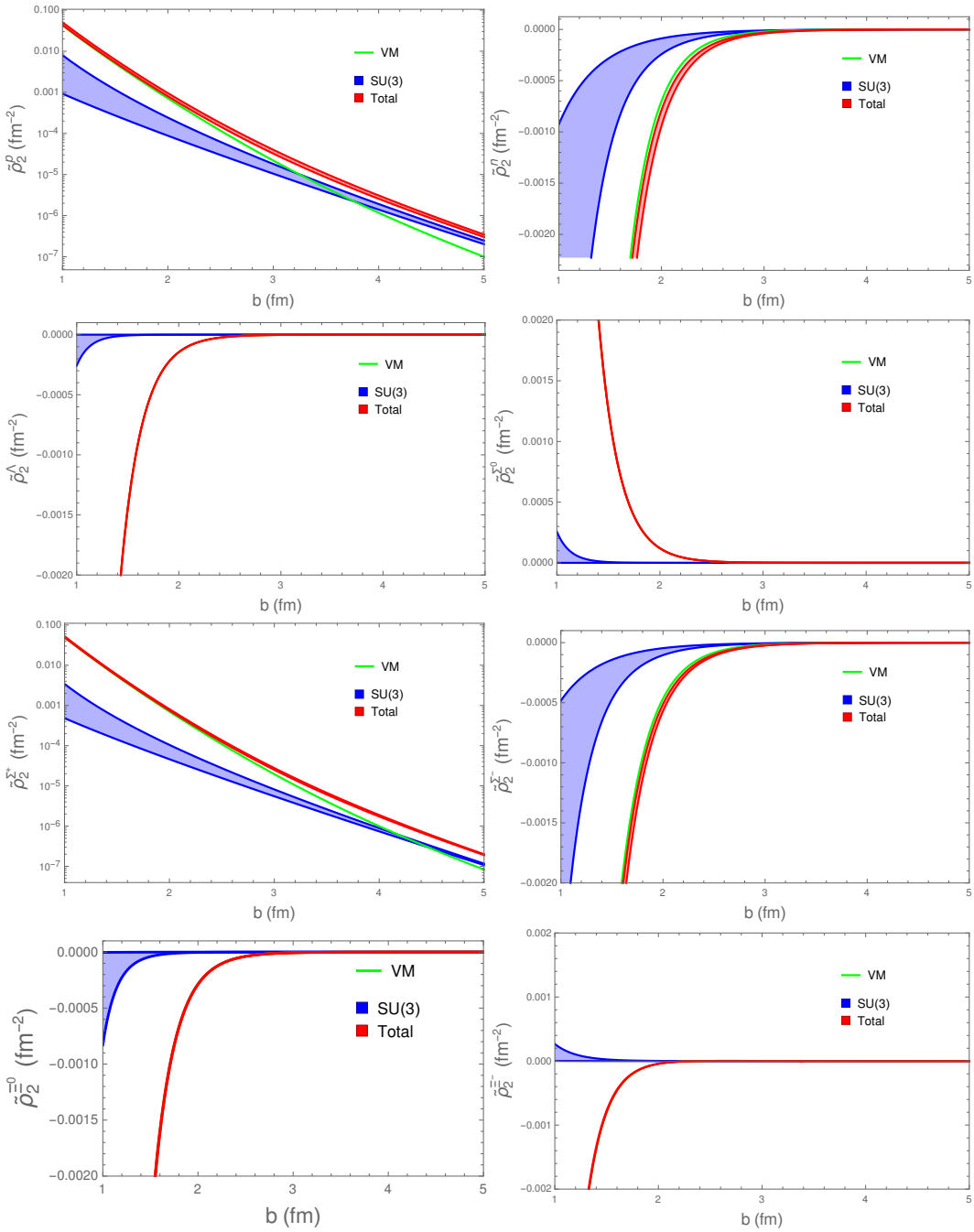

Figure 5.9.: Magnetic densities $\tilde{\rho}_2$ for all the octet members as functions of the transverse distance b. The explanation is as in Fig. 5.8.

ρ dominates the vector-meson contributions but, at distances between 1 fm and 2 fm, the dominant role is played by the ω, therefore compensating the negative contribution of the two-pion cut. Thus, the behaviour of the two nucleons' charge densities is quite different, especially when considering the more central regions.

As for the nucleon magnetic densities, in Sec. 5.3.2 it was discussed that the relevant vector-meson contribution to $\mathrm{Im}(F_2)$ stems from the ρ, the others being of vanishing or negligible size. Therefore, while the qualitative behaviour of the proton magnetic density is similar to that of its charge density — with the difference being that the vector-meson contributions obtain the same importance as the pseudoscalar mesons' closer to the periphery —, the case of the neutron is different. There are no cancellations of the negative ρ contributions with the ω, thus leading to a total negative magnetic density in the whole range considered.

As discussed in Sec. 5.3.2, for the Σ^0 and the Λ the pion-loop contributions cancel out exactly in the isospin-symmetric case. This means that only the $2K$ cut contributes to the peripheral densities. Since the suppression factor for this cut is $e^{-2m_K b}$ (see Sec. 5.2.4), its contribution only starts to be relevant at smaller transverse distances, and therefore these baryons are rather compact objects with respect to the charge distribution. Moreover, even for the two-kaon cut there is a significant cancellation between the loop contributions of the octet and the decuplet intermediate states. In fact, the isospin-breaking effects of the pion cloud generate much larger contributions in the peripheral region than the kaon loops. Again, the reason for this is the weighting function in the dispersive representation of the densities, which turns the pion contributions dominant when compared to the kaon contributions. Combining the results, one sees that the charge densities of the Λ and Σ^0 baryons are up to five orders of magnitude smaller than for the other baryon-octet members for distances $b > 3$ fm. Thus, the effect of the vector mesons, especially the ω, is dominant along the full b range considered here.

The conclusions are also valid for the magnetic densities of these two hyperons. In fact, the kaon-loop effects are slightly more sizeable than for the charge densities due to the analytical structure of the dispersive integral discussed in Sec. 5.2.4. Nevertheless, it remains true that they are negligible when compared to the vector-meson contributions.

The charged Σ hyperons show a behaviour very similar to the that of the nucleons, although in the peripheral region the charge density is given almost entirely by the octet intermediate states. The decuplet contribution is an order of magnitude smaller. The pion-cloud contributions to Σ^- are the same as to Σ^+, but of opposite sign, as was the case of the nucleon doublet. When including the vector mesons, one sees that the ρ, the ω and the two-pion

continuum give positive contributions to the charge density of the Σ^+. The vector-meson contribution becomes comparable to the two-pion cut at $b \approx 3$ fm. On the other hand, the effect of the negative contribution from the ϕ is visible only at shorter distances than the ones considered here, similar to what was seen for the proton. The contribution of the ω and of the ϕ is the same for the Σ^+ and for the Σ^-. However, the two-pion continuum and the ρ contributions to the Σ^- are reversed in sign, producing a scenario that reminds one of the neutron. The effects produced in the magnetic densities are of the same qualitative behaviour as for the nucleons, too.

The last hyperons to be considered are the Ξ. Their peripheral densities turn out to be larger than for many of the other members of the octet, due to the relative size of the decuplet contributions, which gain a similar importance to those of the octet. Concerning the vector mesons, the ϕ contribution to the Ξ charge densities dominates over the others. Its large negative value decreases the other positive effects very quickly, although it only leads to a total negative contribution at transverse distances $b < 1$ fm. As for the magnetic densities, both the two-meson continuum and the vector mesons give negative contributions to the Ξ^0. For the Ξ^-, there is an interplay between the negative ρ contribution and the other positive contributions, which produce a total positive effect at larger distances, $b > 2.5$ fm.

In general, it is important to comment that the decuplet and vector-meson contributions start being important at more peripheral regions for the magnetic than for the charge densities. This is due to the larger weight of the high-t region in the dispersive representation of the magnetic densities, as commented in Sec. 5.2.4.

5.4 Summary and outlook

In this chapter, I presented the study of the electromagnetic form factors of the baryon octet. In particular, I focused on the contributions of the chiral loops of $\mathcal{O}(p^3)$. I included the spin-3/2 degrees of freedom explicitly, in the SSE counting scheme. The renormalization was performed with EOMS. The contributions considered here are not dependent on any unknown LECs, therefore giving real predictions of ChPT. These were applied to two main studies.

On the one hand, I studied the contributions to $\frac{\mathrm{d}^2}{(\mathrm{d}q^2)^2} G_E(q^2)$. When extracting the baryon charge radii from the experiment, it does not suffice to make a polynomial fit to the form factors, because of the poles that appear, e.g., at the two-pion cut. By taking them into account in the quantity $\frac{\mathrm{d}^2}{(\mathrm{d}q^2)^2} G_E(q^2)$, the expansion of the electric form factor around small q^2 might lead to a better extraction of the charge radii.

The present chapter showed that for the nucleon there are some differences

arising when extending the $SU(2)$ framework to $SU(3)$. Although the kaon and the η contributions are very small when compared to those of the pion, the parameters for masses and LECs are different, and they therefore lead to corrections. For all the octet members, it was shown that, concerning the chiral-loop contributions, those arising from the decuplet are sizeable and need to be included. Furthermore, the model dependent vector-meson effects on the results are in general larger than those from the meson cloud. In fact, when including them, the experimental expectations for the proton are better met.

On the other hand, the spectral functions and their role in determining the charge and magnetic density profiles was studied. This was done for all the baryon-octet members, for transverse distances $b > 1$ fm. The results are based on the combination of the chiral EFT predictions for the octet spectral functions with decuplet intermediate states and the presented model for the vector-meson contributions. In general, the latter is only relevant for short transverse distances, while the peripheral behaviour is predicted in a model-independent fashion with ChPT. To be more precise, it is the loop diagrams with imaginary parts at the two-meson cut that give contributions.

When studying the spectral functions, the imaginary parts of the form factors, as functions of the squared momentum transfer, one can obtain information about the charge and magnetic densities. It could be seen that for most cases the pion-octet loops dictated the analytical behaviour of the peripheral transverse densities. However, for the Λ and the Σ^0, the rest of the contributions becomes relevant, because there are strong cancellations in the pion cloud. Isospin-breaking effects and the contribution of vector mesons become dominant, even at the periphery. Another relevant case is that of the Ξ baryons, where the pion-decuplet intermediate state gains a similar importance to the pion-octet contribution, already at the periphery.

The results obtained here define a hierarchy of contributions to the form factors of all the members of the octet, and they also establish the region of dominance of the vector mesons for these baryons. Although one would always expect the lower-mass intermediate states to give the relevant contributions at low energies, i.e., at high transverse distances, it was found that the higher-mass states are not negligible. They turn out to be even more dominant for some of the baryon-octet members for which there are strong cancellations between lower-mass states.

Following this extensive study, in the future one could investigate more deeply the effects of isospin breaking. Furthermore, it would be interesting to analyse the form factors of the spin-3/2 decuplet members, about which the experimental data are scarce, within the same framework, and focusing on the question if there are anomalous thresholds appearing below the two-pion cut. Last but not least, it is important to apply the present theory to

the extraction of the proton electromagnetic form factors in the experiment, for a better understanding of its properties and of the discrepancies between different empirical approaches.

CHAPTER **6**

CP-VIOLATING η AND η' DECAYS: RELATION WITH THE NEUTRON ELECTRIC DIPOLE MOMENT

6.1 Introduction

The investigation of the CP-symmetry violation is strongly connected to the question as to why matter and antimatter in our vicinity of the universe show such a large asymmetry. In 1967, Sakharov postulated three principles that should be fulfilled to explain this observation [169]: the violation of the baryon number conservation, a thermal disequilibrium and the violation of the C and CP symmetries. The first would allow for a different number of baryons and antibaryons, which is a necessity if the asymmetry is to be explained. The second would explain why there are more reactions in one direction than in the other, so that the net amount of matter is larger than that of antimatter. Finally, the symmetry violations would lead particles and antiparticles to have different reaction rates.

All these postulates can be described qualitatively in the Standard Model (SM). For instance, a source of CP violation comes from the complex phases in the quark-mixing matrix. In fact, these are the only experimentally confirmed CP-violating processes up to date. But the theoretical description of the CP violation in the SM turns out to be many orders of magnitude smaller than necessary to produce the observed baryon asymmetry [170, 171].

The SM predicts some CP violation, already confirmed in the experiment, in the electroweak sector. There, C and P are maximally violated, and, though smaller, there is also a CP violation due to the complex phases in the quark and lepton mixing matrices. On the other hand, the standard version of QCD

does not contain any term violating CP, and at the moment there is no experimentally known CP violation in purely strong processes. However, the gauge symmetry allows for additional pieces of the QCD Lagrangian that break CP, and there is no good reason why they should not be there. This is known as the strong CP problem.

Moreover, the addition to the Lagrangian of and odd term with respect to the CP transformation [172–174] would lead to a sizeable permanent neutron electric dipole moment. Thus, it would have an asymmetric distribution of positive and negative charges. Furthermore, if it is to be sizeable, it is a clear sign of physics beyond the SM, since otherwise the CP violation would only account for a neutron EDM of the order of magnitude $10^{-32}e$ cm [175]. This is much too low to be brought in connection with the baryon asymmetry that can be observed in the universe. While such a result is far from the precision experimentally reachable today, of all the baryons the neutron remains the most convenient object for precision measurements of the EDM, owing to its vanishing charge and its stability. The current experimental upper limit for its value is $d_n^{\text{exp}} = 2.9 \times 10^{-26} e$ cm [124] at a confidence level (CL) of 90%, which still allows for some CP violation from the QCD sector.

Previous studies of the relation between the CP violation and the neutron EDM have been made in Refs. [175–178], among others. There is also an extensive experimental programme looking for rare decays which violate CP. For instance, as is the purpose of the present chapter to show, if the explicitly CP-violating decay $\eta^{(\prime)} \to \pi\pi$ exists, then the coupling of the $\eta^{(\prime)}$ to two pions automatically generates a non-vanishing EDM of the neutron.

The branching ratios of the $\eta^{(\prime)}$ decays into two pions have the current experimental upper limits [124]:

$$\frac{\Gamma(\eta \to \pi\pi)}{\Gamma_\eta^{\text{full}}} < \begin{cases} 1.3 \times 10^{-5} \text{ for } \pi^+\pi^- \\ 3.5 \times 10^{-4} \text{ for } \pi^0\pi^0 \end{cases},$$

$$\frac{\Gamma(\eta' \to \pi\pi)}{\Gamma_{\eta'}^{\text{full}}} < \begin{cases} 6 \times 10^{-5} \text{ for } \pi^+\pi^- \\ 4 \times 10^{-4} \text{ for } \pi^0\pi^0 \end{cases}, \tag{6.1}$$

with a CL of 90%, and where $\Gamma_\eta^{\text{full}} = (1.31 \pm 0.05)$keV and $\Gamma_{\eta'}^{\text{full}} = (0.198 \pm 0.009)$MeV. Recently, the LHCb collaboration reported a smaller upper limit for the $\eta' \to \pi^+\pi^-$ branching ratio of 1.8×10^{-5} [179]. If the values of the branching ratios were known exactly, one could estimate the contributions of these CP-violating decays to the neutron EDM. Together with the decay of the η into four pions, which currently has an upper limit for the branching ratio

two orders of magnitude smaller in size, these are the only flavour-conserving CP-violating decays measured so far. In return, one can treat this problem from the opposite perspective: by knowing the size of the neutron EDM, one can set an upper limit for the branching ratios. This is the goal of the present work, because the neutron EDM is better experimentally constrained than the CP-violating decays.

In Ref. [176], the size of the neutron EDM was estimated from the construction of a CP-violating chiral Lagrangian that couples the light pseudoscalars to the neutron, modulo the size of the phase of CP violation θ. At leading chiral order, only the contributions of the charged mesons survive, for which there is no experimental input on the size of the CP-violating couplings. In order to relate the neutron EDM to the couplings with the $\eta^{(\prime)}$, next-to-leading order chiral Lagrangians must be taken into account.

As mentioned, this is precisely the aim of the present chapter. Here, I give a theoretical upper limit for the CP-violating $\eta^{(\prime)}$ branching ratios, to a higher precision than possible in experiments up to date, by calculating the size of the empirically well-constrained neutron EDM that arises from these contributions. The approach is as follows: in Sec. 6.2, I construct the Lagrangian for the CP-violating coupling of the $\eta^{(\prime)}$ to the pions, in order to connect it to the branching ratio. In Sec. 6.3, I use this input to construct the CP-violating coupling of the $\eta^{(\prime)}$ to the nucleon. The CP-conserving coupling is discussed in Sec. 6.4, with the usual $SU(3)$ considerations. In Sec. 6.5, I give a brief overview on the couplings with vector mesons. The calculation of an estimate for the neutron EDM is shown in Sec. 6.6. By constraining this result by the experimental upper limit for the neutron EDM, I extract an estimate for the upper limit of the $\eta^{(\prime)} \to \pi\pi$ branching ratios. In Sec. 6.7, I summarize the chapter and give my conclusions.

6.2 The CP violating $\eta^{(\prime)} \to \pi\pi$ decay

I closely follow the arguments presented in Ref. [177]. The effective Lagrangian describing the CP-violating $\eta\pi\pi$ coupling is given by

$$\mathcal{L}^{\mathrm{CP}}_{\eta\pi\pi} = f_{\eta\pi\pi} m_\eta \eta \vec{\pi}^2, \tag{6.2}$$

with m_η the mass of the η field and $f_{\eta\pi\pi}$ its coupling to the $\vec{\pi}$ with mass M_π. The Lagrangian is analogous for the η'.

In order to obtain information about the coupling constant, I calculate the decay width of the $\eta^{(\prime)}$ into two pions from the squared reaction amplitude $\left|\mathcal{M}_{\eta^{(\prime)}\pi\pi}\right|^2 = 4|f_{\eta^{(\prime)}\pi\pi}|^2 m^2_{\eta^{(\prime)}}$ directly obtained from Eq. (6.2). Since the decay

products have the same mass, the following relation for the width holds [124]:

$$\Gamma = \frac{S|\vec{p}_\pi|}{8\pi m^2_{\eta^{(\prime)}}} \left|\mathcal{M}_{\eta^{(\prime)}\pi\pi}\right|^2 = \frac{\sqrt{m^2_{\eta^{(\prime)}} - 4M^2_\pi}}{4\pi} |f_{\eta^{(\prime)}\pi\pi}|^2 S, \tag{6.3}$$

where $S = \frac{1}{2}$ if the two final particles are identical ($\pi^0\pi^0$ channel) and $S = 1$ otherwise ($\pi^+\pi^-$). The momentum $|\vec{p}_\pi|$ for the final particles in the center-of-mass frame is easily obtained from energy-conservation considerations:

$$\begin{cases} M^2_\pi &= E^2_\pi - |\vec{p}_\pi|^2 \\ m_{\eta^{(\prime)}} &= 2E_\pi \end{cases} \Rightarrow |\vec{p}_\pi|^2 = \frac{m^2_{\eta^{(\prime)}} - 4M^2_\pi}{4}. \tag{6.4}$$

With the numerical values for the masses [124]

$$M_{\pi^\pm} = 139.57\text{MeV}, M_{\pi^0} = 134.98\text{MeV},$$

$$m_\eta = 547.86\text{MeV}, m_{\eta'} = 957.78\text{MeV}, \tag{6.5}$$

and Eq. (6.1), one obtains the upper limits for the coupling constants. Here I choose to calculate the charged and neutral channels separately, and to keep only the lower result as the global upper limit:

$$\begin{aligned} |f_{\eta\pi\pi}| &< 2.13 \times 10^{-5}, \\ |f_{\eta'\pi\pi}| &< 4.04 \times 10^{-4}. \end{aligned} \tag{6.6}$$

6.3 The CP-violating coupling of the η and the η' to the nucleon

With the previous considerations, one can obtain an estimate for the CP-violating coupling of the $\eta^{(\prime)}$ to the nucleon

$$\mathcal{L}^{CP}_{\eta^{(\prime)}NN} = g^{CP}_{\eta^{(\prime)}NN} \bar{N} N \eta^{(\prime)}, \tag{6.7}$$

the ansatz being via pion loops as shown in Fig. 6.1. Isospin considerations make it clear that there is no contribution from Fig. 6.1(c), due to the cancellation between the π^+ and the π^- loops. The method for the calculation of Figs. 6.1(a) and 6.1(b) is fully covariant ChPT with the $SU(2)$ Lagrangians introduced in Eqs. (2.10) and (2.18), together with the vertex from Eq. (6.2). Fig. 6.1(a) then reads

$$g^{CP}_{\eta^{(\prime)}NN} = -\mathrm{i} I^2_{N\pi} \frac{g^2_A f_{\eta^{(\prime)}\pi\pi} m_{\eta^{(\prime)}}}{F^2_\pi} \int \frac{\mathrm{d}^d z}{(2\pi)^d} \frac{(\not{z} + \not{k})\gamma_5(\not{p} - \not{z} + m)\not{z}\gamma_5}{[(k+z)^2 - M^2_\pi][z^2 - M^2_\pi][(p-z)^2 - m^2]}, \tag{6.8}$$

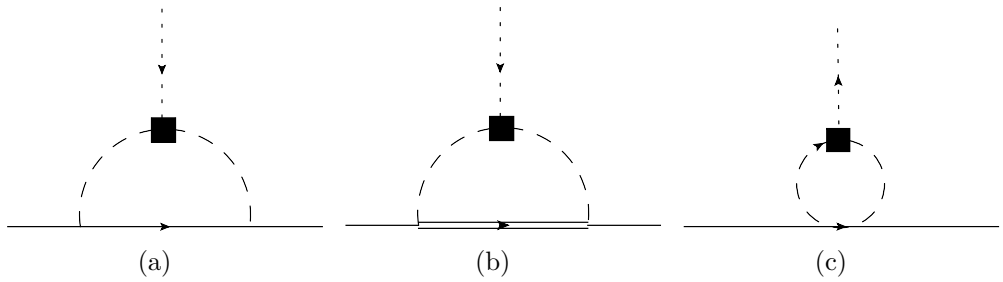

Figure 6.1.: Loops that can contribute to the CP-violating coupling of $\eta^{(\prime)}$ to the nucleon. The single solid lines stand for nucleons, the double lines for the Δ, the dashes for pions and the dotted lines for the $\eta^{(\prime)}$. The black box at the $\eta^{(\prime)}\pi\pi$ vertex indicates the CP violation.

where k is the momentum of the $\eta^{(\prime)}$ and $I_{N\pi}$ is the isospin factor. It reads $I_{N\pi} = 1/2$ for the $\pi^0 n$ loop and $I_{N\pi} = \sqrt{2}/2$ for $\pi^- p$. The incoming nucleon momentum is given by p, M_π is the pion mass, and m the nucleon mass within the loop. To estimate the coupling, I use the approximation where the external nucleon legs are on shell. When simplifying this integral with the help of the Feynman parameterisation and the dimensional regularization, I obtain the result:

$$\begin{aligned} g^{CP}_{\eta^{(\prime)}NN} =& \frac{g_A^2 I_{N\pi}^2}{F_\pi^2} f_{\eta^{(\prime)}\pi\pi} m_{\eta^{(\prime)}} \int_0^1 \mathrm{d}f_a \int_0^{1-f_a} \mathrm{d}f_b \Bigg[-(3f_b m_n + m_n + 2m)\lambda_2(\Delta_{\eta NN}) \\ &+ \frac{m_n + m + f_b m_n}{2} \rho_2(\Delta_{\eta NN}) \\ &+ \Bigg(f_a^2 k^2 (f_b m_n + m + m_n) + f_a (f_b - 1) k^2 (f_b m_n + m + m_n) \\ &+ f_b^2 m_n^2 ((f_b - 1) m_n + m) \Bigg) \lambda_3(\Delta_{\eta NN}) \Bigg], \end{aligned} \tag{6.9}$$

where f_a and f_b are the Feynman parameters and m_n is the external nucleon mass. Furthermore (see also Appendix C),

$$\lambda_2(\Delta) = \frac{1}{16\pi^2} \left[\frac{2}{\epsilon} - \log\left(\frac{\Delta}{\mu^2}\right) + \log(4\pi) - \gamma_E \right],$$

$$\rho_2(\Delta) = \frac{2}{16\pi^2},$$

$$\lambda_3(\Delta) = \frac{1}{16\pi^2\Delta}, \tag{6.10}$$

with $\epsilon = 4 - d$, and where μ is the renormalization scale for which I take the nucleon mass. For the considered diagram,

$$\Delta_{\eta NN} = M_\pi^2(1 - f_b) - f_a k^2(1 - f_a - f_b) - m_n^2 f_b \left(1 - f_b - \frac{m^2}{m_n^2}\right). \tag{6.11}$$

For the purpose of comparison, I extract the heavy-baryon limit from Eq. (6.9) by taking the leading order of the Taylor expansion around the small parameters m^{-1} and m_n^{-1}. In the isospin limit of equal pion masses and of equal nucleon masses, and when choosing a vanishing $k^2 = 0$ for the $\eta^{(\prime)}$, the result has the compact form

$$g^{CP,\,HB}_{\eta^{(\prime)}NN} = \frac{3 f_{\eta^{(\prime)}\pi\pi} g_A^2 m\; m_{\eta^{(\prime)}}(\gamma_E - 2 - \log(4\pi) - \frac{2}{\epsilon})}{32\pi^2 F_\pi^2}. \tag{6.12}$$

This is in agreement with the previous calculations in Ref. [177] after some typos are corrected.

For the relativistic calculation, I use the EOMS renormalization scheme, where the divergences are absorbed with the $\overline{MS}$ prescription: terms proportional to $\frac{2}{\epsilon} + \log(4\pi) - \gamma_E$ are subtracted, see also Appendix C. Again taking the mass isospin limit and setting $k^2 = 0$, I obtain the compact result for Eq. (6.9):

$$g^{CP}_{\eta^{(\prime)}NN} = -\frac{3 f_{\eta^{(\prime)}\pi\pi} g_A^2 m_{\eta^{(\prime)}}}{16\pi^2 F_\pi^2 m}\left\{ M_\pi^2 \log\left(\frac{m}{M_\pi}\right) + m^2 + \frac{M_\pi\,(M_\pi^2 - 3m^2)}{\sqrt{4m^2 - M_\pi^2}}\right.$$

$$\left.\times\left[\arctan\left(\frac{M_\pi}{\sqrt{4m^2 - M_\pi^2}}\right) + \arctan\left(\frac{2m^2 - M_\pi^2}{\sqrt{4m^2 M_\pi^2 - M_\pi^4}}\right)\right]\right\}. \tag{6.13}$$

As for Fig. 6.1(b), with a Δ intermediate state, it reads

$$g^{CP}_{\eta^{(\prime)}NN,\,\Delta} = \mathrm{i} I^2_{N\Delta\pi} \frac{h_A^2 f_{\eta^{(\prime)}\pi\pi} m_{\eta^{(\prime)}}}{F_\pi^2 M_\Delta^2} \int \frac{\mathrm{d}^d z}{(2\pi)^d}$$

$$\times \frac{(p^\alpha - z^\alpha) z^\delta \gamma_{\alpha\beta\delta} S_\Delta^{\beta\beta'}(p - z)(p^{\alpha'} - z^{\alpha'})(z^{\delta'} + k^{\delta'})\gamma_{\alpha'\beta'\delta'}}{[(k + z)^2 - M_\pi^2][z^2 - M_\pi^2][(p - z)^2 - M_\Delta^2]}, \tag{6.14}$$

where $I_{N\Delta\pi}$ is the isospin factor for the hadronic transition, via a pion, between the nucleon and the Δ with mass M_Δ. It reads $I_{N\Delta\pi} = 1/6$ for the $\pi^0\Delta^0$ loop and $I_{N\Delta\pi} = 1/3$ for the combination of $\pi^-\Delta^+$ and $\pi^+\Delta^-$. The definition of the RS propagator $S_\Delta^{\alpha\beta}(p)$ is given in Eq. (2.41). When setting the external nucleon legs on shell, choosing $k^2 = 0$ and taking the isospin limit, one obtains:

$$
\begin{aligned}
g^{CP}_{\eta^{(\prime)}NN,\Delta} = \frac{f_{\eta^{(\prime)}\pi\pi} h_A^2 m^2 m_{\eta^{(\prime)}}}{1152\pi^2 F_\pi^2 M_\Delta^2} \Bigg\{ & -\frac{6\left(m^2 + M_\pi^2 - M_\Delta^2\right)}{m} + 6(2m + 3M_\Delta)\log\left(\frac{M_\Delta^2}{m^2}\right) \\
& - \frac{6\left(2m^4 + 3m^3 M_\Delta + m^2\left(2M_\Delta^2 - 6M_\pi^2\right) + m\left(3M_\Delta^3 - 3M_\pi^2 M_\Delta\right) + 2\left(M_\pi^2 - M_\Delta^2\right)^2\right)}{m^3} \\
& + 4m + \frac{1}{m^5\sqrt{-m^4 + 2m^2\left(M_\pi^2 + M_\Delta^2\right) - \left(M_\pi^2 - M_\Delta^2\right)^2}} \\
& \times \Bigg[6\left(2m^4 - 5m^3 M_\Delta + m^2\left(6M_\Delta^2 - 4M_\pi^2\right) + 5mM_\Delta\left(M_\pi^2 - M_\Delta^2\right) + 2\left(M_\pi^2 - M_\Delta^2\right)^2\right) \\
& \times \left(m^2 + 2mM_\Delta - M_\pi^2 + M_\Delta^2\right)^2 \Bigg] \\
& \times \Bigg[\arctan\left(\frac{-m^2 - M_\pi^2 + M_\Delta^2}{\sqrt{-m^4 + 2m^2\left(M_\pi^2 + M_\Delta^2\right) - \left(M_\pi^2 - M_\Delta^2\right)^2}}\right) \\
& - \arctan\left(\frac{m^2 - M_\pi^2 + M_\Delta^2}{\sqrt{-m^4 + 2m^2\left(M_\pi^2 + M_\Delta^2\right) - \left(M_\pi^2 - M_\Delta^2\right)^2}}\right) \Bigg] \\
& + \frac{3\log\left(\frac{M_\pi^2}{M_\Delta^2}\right)}{m^5} \Bigg[2m^6 + 3m^5 M_\Delta + 6m^4 M_\pi^2 + 6m^3 M_\pi^2 M_\Delta + 6m^2 M_\pi^2\left(M_\Delta^2 - M_\pi^2\right) \\
& - 3mM_\Delta\left(M_\pi^2 - M_\Delta^2\right)^2 + 2\left(M_\pi^2 - M_\Delta^2\right)^3 \Bigg] \Bigg\}. \qquad (6.15)
\end{aligned}
$$

In the following, I use the physical-average $SU(2)$ values given in Tables 4.1 and 4.2. Furthermore, the η and η' masses are given Eq. (6.5). Taking the

upper limits for the $\eta^{(\prime)}\pi\pi$ couplings as introduced in Sec. 6.2, one obtains the following upper limits for the CP-violating $\eta^{(\prime)}NN$ couplings:

$$|g^{CP}_{\eta NN}| = 2.8 \cdot 10^{-5},\ |g^{CP}_{\eta' NN}| = 9.4 \cdot 10^{-4},$$

$$|g^{CP,HB}_{\eta NN}| = 3.9 \cdot 10^{-5},\ |g^{CP,HB}_{\eta' NN}| = 1.3 \cdot 10^{-3},$$

$$|g^{CP}_{\eta NN,\Delta}| = 7.9 \cdot 10^{-6},\ |g^{CP}_{\eta' NN,\Delta}| = 2.6 \cdot 10^{-4}. \tag{6.16}$$

One can see from the numerical result that it is important to take the Δ loop into account, as its contribution is larger than 20% of that from the nucleon intermediate state. Furthermore, although the magnitude of the heavy-baryon calculation is similar in size to the fully covariant one, one can see that there is a sizeable change of around 30% in the numerical value due to this non-relativistic approximation.

These couplings had been calculated previously in the HBChPT approach, in Ref. [177], whithout the Δ contribution. A direct comparison between the numerical results has little meaning because of some errors in the formulas and the now experimentally better constrained values for the branching ratios in Eq. (6.1) [124].

6.4 The CP-conserving coupling of the η and the η' to the nucleon

The CP-conserving coupling of the $\eta^{(\prime)}$ to the nucleon is most commonly given by

$$\mathcal{L}_{\eta^{(\prime)}NN} = -\mathrm{i}\frac{g_{\eta^{(\prime)}NN}}{2F_{\eta^{(\prime)}}}\bar{N}\not{k}\gamma_5 N\eta^{(\prime)}, \tag{6.17}$$

with k the $\eta^{(\prime)}$ momentum, and where $\bar{N}$ and N are the outgoing and incoming nucleon states with mass m, respectively. This is nothing else than the reduction of the $SU(3)$ Lagrangian in Eq. (2.25) to this particular case, with the difference that the mixing with the pseudoscalar singlet η' is considered as well. Therefore one is now working with the extension of the pseudoscalar meson octet to the nonet. In the present calculation, I set the decay constant $F_{\eta^{(\prime)}}$ to the $SU(3)$ physical average 108 MeV, as in Chapter 4.

When considering only the octet of mesons, the $\pi^0 nn$ coupling is given by $-g_A = -(F+D)$, while the ηnn vertex has the coupling $g_{\eta nn} = \frac{3F-D}{\sqrt{3}}$. The

representation of the nonet, on the other side, is given by

$$\frac{\lambda_a}{\sqrt{2}}\phi^a = \begin{pmatrix} \frac{\phi_u}{\sqrt{2}} & \pi^+ & K^+ \\ \pi^- & \frac{\phi_d}{\sqrt{2}} & K^0 \\ K^- & \bar{K}^0 & \frac{\phi_s}{\sqrt{2}} \end{pmatrix}, \tag{6.18}$$

where the physical states π^0, η and η' are related to the fields ϕ_u, ϕ_d and ϕ_s via

$$\begin{aligned} \phi_u &= \pi_0 + \eta_{ns}, \\ \phi_d &= -\pi_0 + \eta_{ns}, \\ \phi_s &= \sqrt{2}\eta_s. \end{aligned} \tag{6.19}$$

In the isospin limit, the π^0 does not mix with the η or the η'. The strange and non-strange fields are given by $\eta_s = \eta' \cos\psi - \eta \sin\psi$ and $\eta_{ns} = \eta \cos\psi + \eta' \sin\psi$, respectively. The mixing angle ψ between the η and the η' has been estimated in many works [180–186] to be in a range between 38° [185] from the $\eta \to e^+e^-\gamma$ decay data and 45° [181] in a ChPT analysis. The more recent results tend to values close to 40°, which I use in the following. For F and D, I also take the physical-average values shown in Table 4.2.

6.5 Couplings with vector mesons

As in the previous chapter, here I also study the effects of the couplings with vector mesons. The Lagrangian coupling vector mesons to octet baryons was already introduced in Chapter 5. Here, I reduce the Lagrangian to the relevant couplings with the nucleon. Furthermore, the electromagnetic transition between the vector mesons and the $\eta^{(\prime)}$ is needed. Therefore, the relevant pieces of the Lagrangian are [162, 187, 188]

$$\mathcal{L}_{\gamma\eta^{(\prime)}V} = \frac{e\lambda_V}{4m_{\eta^{(\prime)}}}\epsilon_{\mu\nu\alpha\beta}F^{\mu\nu}V^{\alpha\beta}\eta^{(\prime)}, \tag{6.20}$$

$$\mathcal{L}_{VNN} = \bar{N}\left(g_v\gamma^\mu + \mathrm{i}g_t\frac{\sigma^{\mu\nu}}{2m}q_\nu\right)V_\mu\tau_V N, \tag{6.21}$$

where the numerical values for the masses [124] and the results for the coupling constants [177, 188] are summarized in Table 6.1 for the cases relevant here.

Note that the coupling of the ρ to the nucleon is poorly known, and here, for comparison purposes, I use the values from Ref. [177]. The electromagnetic

V	m_V (MeV)	g_v^V	$\frac{g_t^V}{g_v^V}$	λ_V	λ'_V	τ_V
ρ	775.8	2.4	6.1	0.9	1.18	σ_3
ω	782.6	16	0	0.25	0.43	1

Table 6.1.: Parameters for the Lagrangians that involve vector mesons.

field couples with the usual definition for $F^{\mu\nu}$ introduced in Chapter 2, and the tensor field for the vector meson V^μ is given by $V^{\mu\nu} = \partial^\mu V^\nu - \partial^\nu V^\mu$.

Due to the fact that the values for the couplings are poorly known, they are an important source of uncertainty in the results. Furthermore, in higher orders they have a dependency on the virtuality of the vector meson, which I ignore in the calculations that follow.

6.6 Calculation of the nucleon EDM

The EDM is extracted from the amplitude that describes the photon coupling to the nucleon. This amplitude can generically be written in terms of form factors, as I already introduced in Chapter 5. There, the structures could be reduced to two form factors, F_1 and F_2, see Eq. (5.1). In the study of the present chapter, as CP-violating vertices are taken into account, an additional form factor is needed. This is exactly the form factor corresponding to the EDM, which I call F_{EDM}. Therefore the vector current J^μ between baryon states now reads:

$$\begin{aligned}&\langle B(p')|\, J^\mu \,|B(p)\rangle \\ =&\bar{u}(p')\left(\gamma^\mu F_1(Q^2) + \frac{\mathrm{i}\sigma^{\mu\nu}q_\nu}{2m}F_2(Q^2) + \frac{\mathrm{i}\sigma^{\mu\nu}\gamma_5 q_\nu}{2m}F_{\text{EDM}}(Q^2)\right)u(p),\end{aligned} \tag{6.22}$$

where q_ν is the photon momentum, ϵ_μ its polarization, and $\sigma^{\mu\nu} = \frac{\mathrm{i}}{2}[\gamma^\mu, \gamma^\nu]$. At the physical point, where $q^2 = -Q^2 = 0$, the structure functions reduce to

$$F_1(0) = e_N, \quad F_2(0) = \kappa_N, \quad F_{\text{EDM}}(0) = \tilde{d}_N. \tag{6.23}$$

The charge e_N is given in units of the elementary charge e, while the anomalous magnetic moment κ_N and the EDM $\tilde{d}_N$ are given in units of $\frac{e}{2m}$. For the kind

of structure that multiplies F_{EDM} to appear, the photon has to couple to the nucleon via a CP-violating loop, as otherwise the amplitude would not be proportional to γ_5. The loops I consider in the present chapter are shown in Fig. 6.2.

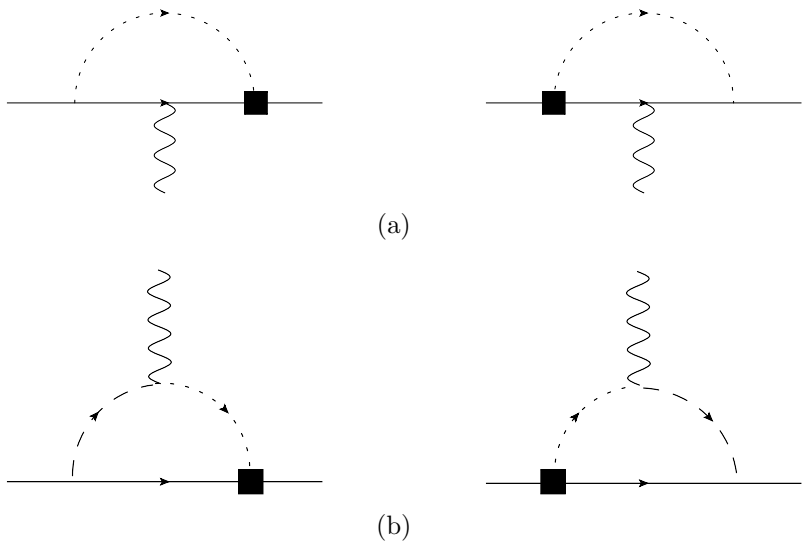

Figure 6.2.: Considered loops that can contribute to the neutron EDM. The solid line represents the neutron, the dotted line the $\eta^{(\prime)}$, the dashed lines are vector-meson contributions and the wavy line corresponds to the photon. The black box stands for a CP-violating vertex.

In Fig. 6.2(a), the photon couples to the nucleon that propagates inside the loop. For this kind of loop, all the tools necessary for the calculation are introduced in the Secs. 6.3 and 6.4, and in the Lagrangians of Chapter 2. In the particular case of the neutron, the leading-order coupling to the photon vanishes, for which reason only the next-to-leading order term contributes. The second-order nucleon Lagrangian of Eq. (2.13) is needed to describe such a vertex at lowest non-vanishing order for the neutron, which reduces to:

$$\mathcal{L}^{(2)}_{\gamma nn} = e\kappa_n \mathrm{i}\sigma^{\mu\nu}\frac{\epsilon_\mu q_\nu}{2m}, \tag{6.24}$$

where $\kappa_n = -1.913$ is the neutron magnetic moment in units of $\frac{e}{2m}$. Note that, at the considered order, $\kappa_n = c_7$ in the notation used in the present work, and for the proton magnetic moment the relation $\kappa_p = c_6 + c_7$ holds.

A direct coupling of the photon to an $\eta^{(\prime)}$ is not possible, due to this meson's vanishing charge. Nevertheless, as is depicted in Fig. 6.2(b), it is possible to achieve a coupling via a vector-meson exchange, which here I also perform for

the sake of comparison with Ref. [177], and for an estimate of the importance of its effect.

The analytical calculations are done with the help of the program *Form*, see Appendix D, with which it is easy to obtain the coefficient F_{EDM} by isolating the pieces that have the needed structure $\mathrm{i}\sigma^{\mu\nu}\gamma_5 q_\nu/(2m)$. In fact, precisely due to the CP-violating coupling that was inserted into these diagrams, these loops only have structures of this kind, while $F_1(0) = F_2(0) = 0$.

For the η, the amplitude of Fig. 6.2(a) reads

$$\frac{e\kappa_N g_{\eta NN}\bar{g}_{\eta NN}}{8mF_\eta}\int\frac{\mathrm{d}^d z}{(2\pi)^d}\frac{1}{[z^2-m_\eta^2][(p-z)^2-m^2][(p+q-z)^2-m^2]}$$
$$\times\left[(\not p+\not q-\not z+m)(\not q\not\epsilon-\not\epsilon\not q)(\not p-\not z+m)\not z\gamma_5\right.$$
$$\left.-\not z\gamma_5(\not p+\not q-\not z+m)(\not q\not\epsilon-\not\epsilon\not q)(\not p-\not z+m)\right], \quad (6.25)$$

which for the EDM $\tilde{d}_n$ in units of $\frac{e}{2m}$ at $q^2=0$ leads to

$$\tilde{d}_{n,a} = \frac{\bar{g}_{\eta NN}g_{\eta NN}m\kappa_n}{F_\eta}\int_0^1\mathrm{d}f_b\int_0^{1-f_b}\mathrm{d}f_a\Big\{(6f_a-5)\lambda_2(\Delta_{\mathrm{EDM,a}})+(2-f_a)\rho_2(\Delta_{\mathrm{EDM,a}})$$
$$-2m^2\left[f_a(f_a^2-2)+2(1+(f_a-1)f_a)f_b+(f_a-2)f_b^2\right]\lambda_3(\Delta_{\mathrm{EDM,a}})\Big\}, \quad (6.26)$$

where, with the definitions in Eq. (6.10),

$$\Delta_{\mathrm{EDM,a}} = m_\eta^2(1-f_a-f_b)+m^2(f_a+f_b^2). \quad (6.27)$$

After integration, the analytical expression is also quite compact:

$$\tilde{d}_{n,a} = \frac{\bar{g}_{\eta NN}g_{\eta NN}\kappa_N}{32\pi^2\mathrm{F}\eta m^3}\Bigg\{m^4-3m^2m_\eta^2+\left(3m_\eta^4-6m^2m_\eta^2\right)\log\left(\frac{m_\eta}{m}\right)$$
$$-\frac{3m_\eta^3}{\sqrt{4m^2-m_\eta^2}}\left(m_\eta^2-4m^2\right)$$
$$\times\left[\arctan\left(\frac{m_\eta}{\sqrt{4m^2-m_\eta^2}}\right)+\arctan\left(\frac{2m^2-m_\eta^2}{m_\eta\sqrt{4m^2-m_\eta^2}}\right)\right]\Bigg\}. \quad (6.28)$$

As for the amplitude in Fig. 6.2(b), it is given by

$$
\begin{aligned}
&-\frac{e\lambda_V\tau_V\bar{g}_{\eta NN}}{m_\eta}\int\frac{\mathrm{d}^d z}{(2\pi)^d}\Bigg\{\frac{(\not{z}+m)}{[(p-z)^2-m_V^2][z^2-m^2][(p'-z)^2-m_\eta^2]}\\
&\times q_\mu\epsilon_\nu(p-z)_\alpha \mathrm{i}\epsilon^{\mu\nu\alpha\beta}\left(-g_{\beta\beta'}+\frac{(p-z)_\beta(p-z)_{\beta'}}{m_V^2}\right)\left(g_v^V\gamma^{\beta'}+\frac{g_t^V}{4m}(p-z)^{\alpha'}[\gamma^{\beta'},\gamma^{\alpha'}]\right)\\
&-\frac{\left(g_v^V\gamma^{\beta'}-\frac{g_t^V}{4m}(p'-z)^{\alpha'}[\gamma^{\beta'},\gamma^{\alpha'}]\right)\left(-g_{\beta'\beta}+\frac{(p'-z)_{\beta'}(p'-z)_\beta}{m_V^2}\right)}{[(p-z)^2-m_\eta^2][z^2-m^2][(p'-z)^2-m_V^2]}\\
&\times q_\mu\epsilon_\nu(p'-z)_\alpha \mathrm{i}\epsilon^{\mu\nu\alpha\beta}(\not{z}+m)\Bigg\}. \qquad (6.29)
\end{aligned}
$$

For this loop, the analytical result has the very simple form

$$
\tilde{d}_{n,b}=-2\frac{\bar{g}_{\eta\mathrm{NN}}\lambda_V\tau_V m}{m_\eta}\int_0^1\mathrm{d}f_b\int_0^{1-f_b}\mathrm{d}f_a\left\{(g_v^V+g_t^V)(2\lambda_2(\Delta_{\mathrm{EDM,b}})+3\rho_2(\Delta_{\mathrm{EDM,b}}))\right\},
$$

where

$$
\Delta_{\mathrm{EDM,b}}=m^2(1-f_a-f_b)^2+m_\eta^2 f_b+m_V^2 f_a.
$$

Note that for each of the two diagrams in Fig. 6.2(b) there are also pieces of the type $\lambda_3(\Delta_{\mathrm{EDM,b}})$, but they cancel. Integrating over the Feynman parameters yields

$$
\begin{aligned}
\tilde{d}_{n,b}=&\frac{\bar{g}_{\eta NN}(g_t^V+g_v^V)\lambda_V\tau_V}{24\pi^2 m^3 m_\eta(m_\eta^2-m_V^2)}\Bigg\{m^2(m_\eta^4-m_V^4)\\
&+m_\eta^3(4m^2-m_\eta^2)^{3/2}\left[\arctan\left(\frac{m_\eta}{\sqrt{4m^2-m_\eta^2}}\right)-\arctan\left(\frac{m_\eta^2-2m^2}{m_\eta\sqrt{4m^2-m_\eta^2}}\right)\right]\\
&-m_V^3(4m^2-m_V^2)^{3/2}\left[\arctan\left(\frac{m_V}{\sqrt{4m^2-m_V^2}}\right)-\arctan\left(\frac{m_V^2-2m^2}{m_V\sqrt{4m^2-m_V^2}}\right)\right]\\
&+m_\eta^4(6m^2-m_\eta^2)\log\left(\frac{m_\eta}{m}\right)-m_V^4(6m^2-m_V^2)\log\left(\frac{m_V}{m}\right)\Bigg\}. \qquad (6.30)
\end{aligned}
$$

The expressions are analogous for the η'.

At this point, I want to discuss the numerical results, which are summarized in Table 6.2. The vector-meson contributions of Fig. 6.2(b) turn out to be of the same order of magnitude as the loops in Fig. 6.2(a), or slightly larger. This is to be expected, even though the vector mesons are higher-mass states. For Fig. 6.2(a), the Lagrangian of first chiral order does not allow a coupling of the photon to the neutron. Therefore, that contribution is suppressed, and the vector-meson contributions become equally important. The sum of all the contributions yields a total $d_n^{\text{tot}} < 7.7 \cdot 10^{-18} e$ cm.

Considering the experimental upper limit of $d_n^{\text{exp}} = 2.9 \cdot 10^{-26} e$ cm, the ratio between the theoretical expectation and the measurement is of the order of magnitude 10^8. This means that the upper limit for the decay ratio of the $\eta^{(\prime)}$ into two pions gives a large overestimation of the CP-violating coupling constant. In fact, in order for the results to be compatible with the experimental constraint on the neutron EDM, the branching ratio would have to be at least eight orders of magnitude smaller. This is a very important result, as it leads to a magnitude of CP violation which, due to its small size, has not been possible to extract experimentally so far. Note that the recent experimental report on the $\eta' \to \pi^+\pi^-$ decay ratio [179] is approximately three times smaller than the values used here [124]. Therefore, when taking this new value the η' contributions to the neutron EDM would be reduced by a factor $\approx \sqrt{3}$. As they are the dominant contributions, so would also the the value for d_n^{tot}.

	η	η'
Fig. 6.2(a)	$3.1 \cdot 10^{-20}$	$2.7 \cdot 10^{-18}$
Fig. 6.2(b)	$2.1 \cdot 10^{-19}$	$4.8 \cdot 10^{-18}$

Table 6.2.: Contributions to the upper limit of the neutron EDM from the current experimental upper limits of the η and η' branching ratios into two pions. The units are e cm.

It is interesting to confront these results with those in Ref. [176]. There, as mentioned, the size of the neutron EDM was estimated within a similar framework as presented here, but taking into account the charged-meson contributions of leading chiral order. There, up to the unknown CP-violating phase θ, the EDM was estimated to be of the order of magnitude $10^{-16} e$ cm. The fact that in the present chapter the estimate is smaller is in good agreement with that calculation, knowing that for the neutral mesons considered

here the diagrams that contribute are of the next chiral order.

It is important to keep in mind that the values shown in Table 6.2 are not to be seen as predictions for the neutron EDM, but as estimates for the order of magnitude of the $\eta^{(\prime)}$ branching ratios into two pions. Other processes beyond the scope of this thesis give additional contributions to the neutron EDM. E.g., these are pieces obtained from the CP-violating decay of the $\eta^{(\prime)}$ into four pions, or processes that do not conserve flavour, via the quark-mixing matrix. Furthermore, as mentioned in Sec. 6.5, some of the coupling constants used here are poorly known, and the results depend on the renormalization scheme used. Nevertheless, due to the very large discrepancy between the experimental constraint of the EDM and the one calculated from the current upper limits for the CP-violating branching ratios, the results are still rigorous enough to be instructive. The conclusions made here remain, even if other processes are to be additionally considered, or if the coupling constants are to have different sizes.

6.7 Summary and outlook

In the present chapter, I calculated the nucleon EDM originated by a CP violating coupling to the $\eta^{(\prime)}$ meson. In particular, I focused on the result for the neutron, as its experimental upper limit is very small, $d_n^{\text{exp}} = 2.9 \cdot 10^{-26} e$ cm. This gives a very strong constraint on observables related to it. More specifically, if a neutron EDM is to exist, then CP violation has to occur. Therefore, here the goal was to give an estimate for the size of this violation.

This was achieved by constructing a CP-violating coupling of the η to the nucleon, via loops that include an $\eta^{(\prime)}\pi\pi$ vertex. While there are experimental results for the upper limit of the $\eta^{(\prime)} \to \pi\pi$ decay ratio, here I wanted to test if indeed this constraint is compatible with the size of the neutron EDM. As in the previous chapters of this thesis, the Δ contributions were taken into account as well, leading to a correction to the CP-violating $\eta^{(\prime)}NN$ vertex larger than 20%.

I considered two possible sources for the neutron EDM. In one case, the photon coupled to the neutron in a loop with a CP-violating ηNN vertex. In the other, vector-meson contributions within the loop were considered as well. The two contributions turned out to be of a similar size.

In total, I obtained a constraint on the CP-violating $\eta^{(\prime)} \to \pi\pi$ decay ratio roughly eight orders of magnitude smaller than measured in the experiment so far. This is a very instructive result, since it gives an estimate on symmetry violations in nature, where experimental results are not yet achievable. Of course, additional processes that have not been taken into account in the present chapter might give contributions to the neutron EDM with a differ-

ent relative sign to those considered here, possibly leading to cancellations. Nevertheless, in order to make up for the eight orders of magnitude, these cancellations would have to be extremely precise, which is not justified by any known symmetries so far. The conclusions above are therefore expected to hold even when including the contributions of other CP-violating processes.

CHAPTER **7**

SUMMARY AND CONCLUSIONS

In this work, I have studied the low-energy behaviour of baryons subjected to external electromagnetic fields. I used the framework of fully covariant Chiral Perturbation Theory for light hadrons, with the explicit inclusion of spin-3/2 degrees of freedom. The renormalization used was the Extended On Mass Shell scheme, with which the fully analytical expressions of divergences and power-counting breaking terms are absorbed into the chiral Lagrangian's low-energy constants.

The work is divided into four main chapters, each of them treating a different low-energy process or observable. In Chapter 3, the photoproduction of neutral pions off proton targets was studied, with a focus on the comparison with experimental data on differential cross sections, photon asymmetries, s-wave and p-wave multipoles. The observed photon energies ranged from the production threshold up to slightly above 200 MeV in the laboratory frame. While I started with the description of the interactions between nucleons and pions, the framework used sets an excellent basis for the calculation of low-energy processes involving baryons, mesons and photons, in general. Thus, in Chapter 4, I studied the forward spin polarizabilities of the nucleons and the hyperons, which can be extracted from Compton scattering. There are no data for hyperons yet — although it would be possible to obtain information from lattice QCD —, and therefore the goal was to give predictions for their values. This is especially interesting for this specific polarizability, as it turns out to be renormalization-scheme independent, and only well-known LECs are involved. Similarly, in Chapter 5, the electromagnetic form factors of the nucleons and the hyperons were calculated. In particular, the connection to the low momentum-transfer expansion of the electric form factor and to the peripheral transverse charge and magnetic densities of these baryons was made. The results are also predictive, although dependent on the renormalization

scheme used. For the hyperons, it should be possible to confirm them with lattice QCD calculations in the near future. For the nucleons, the form factors are extracted from the elastic electron scattering. With the help of the same process, one can gather information about the neutron electric dipole moment at vanishing photon virtuality. In Chapter 6, I concentrated on this point, with the aim of relating this quantity to the size of some possible CP-violating meson decays in nature. From the experimental constraint on the neutron EDM, I gave an estimate for the upper limit of the branching ratios of some of these decays. I discuss these four projects in more detail in the following.

In Chapter 3, the process of neutral pion photoproduction off proton targets has been extensively studied. This was motivated by the new high-precision differential cross-section and photon-asymmetry data recently obtained by the Mainz Microtron. These were the first to provide access to a wide range of scattering angles and a narrow binning in photon energies, from pion production threshold up to over 200 MeV in the laboratory frame. With this new information, previous work by other theoretical groups has been shown to reproduce data up to not more than 20 MeV above threshold. The most successful approaches had been ChPT calculations to fourth chiral order, both in covariant and nonrelativistic approaches. These $\mathcal{O}(p^4)$ calculations imply the appearance of many unknown LECs, which in principle mean the existence of additional degrees of freedom for the fitting procedures. Unfortunately, despite this, the agreement between the data and the theory turned out not to be significantly better than in previous lower-order calculations. Even including the vector-meson resonances explicitly did not improve the situation.

Here, we tested an alternative approach: the explicit inclusion of spin-3/2 degrees of freedom. These are related to the experimental observation of nucleon-excitations to the $\Delta(1232)$ resonance. In fact, the coupling of these states to the nucleons is quite strong, so their contributions should be significant at energies close to their mass. Nevertheless, previous works done in the nonrelativistic heavy-baryon ChPT did not succeed in describing the data, either. The reason for this could be that, due to the static nature of the framework used in those calculations, the energy dependence of the Δ propagator could not be fully taken into account. However, it is exactly this dependence that is crucial to describe the steep rise of the cross sections with the photon energy. Therefore, we revisited the calculations, now in fully relativistic ChPT.

The first step was to include the $\Delta(1232)$ at tree level, in addition to tree and loop-level diagrams with nucleon propagators. Unlike previous calculations, we stayed at $\mathcal{O}(p^3)$, avoiding a too large number of unknown LECs. In addition to the high number of data points the fits were made to, this too leads to more predictive results. The outcome was highly satisfactory, as the theory was in agreement with the data in the whole range of energies considered. We then

additionally included the lowest-order loop diagrams with Δ propagators, in order to test the convergence of the theory at higher orders. In the counting scheme chosen in Chapter 3, this inclusion amounts to a calculation at chiral $\mathcal{O}(p^{7/2})$. These extensive calculations had the advantage of being a nontrivial test of the convergence of the chiral series, as the agreement between data and theory was nearly the same as at $\mathcal{O}(p^3)$. Furthermore, they allowed to better study the dependence of the LECs on the Δ-loop inclusion, and might lead to a good agreement between data and theory at energies even higher than those considered here. Finally, a study of the lowest (s-wave and p-wave) multipoles confirmed the indispensability of taking into account the Δ degrees of freedom.

In Chapter 4, I calculated the ChPT prediction for the forward spin polarizabilities of the baryon octet from Compton-scattering amplitudes. Here, too, the values were extracted in the framework of a fully covariant calculation with the explicit inclusion of spin-3/2 degrees of freedom, at $\mathcal{O}(p^{7/2})$. Calculations with the same approach had already been done for the nucleons, by studying the effects of pion loops in $SU(2)$, i.e., by taking into account baryons composed of u and d quarks. The results agreed very well with the experiment, which is particularly striking as no fits to data had to be made: the LECs appearing at the order considered had already been well determined in the course of the past few decades through the study of other processes. The calculation therefore presented a non-trivial and successful test of baryon ChPT.

For this reason it is promising to extend the calculations to include the s quarks, which amounts to studying not only nucleons with pion-loop contributions, but also hyperons, with kaon and η loops. In the present work, I described my calculations related to this topic. The study of the hyperons' forward spin polarizabilities had previously been performed in HBChPT, without the inclusion of the spin-3/2 degrees of freedom. However, since this approach was shown to be insufficient even in the nucleon sector, the reliability of the hyperon results is questionable. Instead, to extract the baryon polarizabilities that have not been measured yet, here we chose to apply the framework that reproduced the empirical observations for the nucleons. In fact, due to the short lifetimes of the hyperons, an experimental confirmation of these results is not to be expected in the near future. Calculations on the lattice are a possibility though, and they would provide a welcome test for ChPT predictions.

In Chapter 5, I presented the calculations on the electromagnetic form factors of the octet baryons. The process considered is electron scattering off the baryon with the exchange of a virtual photon. With these form factors, one has access to information about many observables related to the electromagnetic structure and behaviour of these hadrons. In this particular work, the goal was to obtain information about the electric form factor and about the

distributions of charge and magnetic densities. For both these quantities, only those analyses were considered that have predictive power in ChPT, i.e., no dependence on unknown LECs. We started with the calculation of the second derivative of the electric form factor. While it is not directly related to the charge radius, which is fixed by the slope of that form factor, it does allow one to better extract it from data. The behaviour of the second derivative within ChPT calculations gives insight about the analytic structure of the electric form factor in an energy region close to the two-pion production cut. There, due to the poles in the complex plane, a polynomial fit for the extraction of the charge radii is not viable, for which reason an understanding of these poles in ChPT is very instructive.

Dispersive analyses link the charge and magnetic densities to the imaginary parts of the form factors, the spectral functions, via a Fourier transformation. If in electron scattering the exchanged virtual photon couples to the baryon target via the creation of an intermediate hadronic state, an imaginary part is generated in the amplitude. Using the light-front formalism, one can associate two quantities as they decouple from vacuum fluctuations: the density at a specific transverse distance from the baryon center-of-momentum, and the particular energy region of the form-factor calculation. At high transverse distances, i.e., in the baryon's periphery, low-energy contributions suffice to describe the density behaviour, as higher-energy cuts have vanishing imaginary parts. For smaller transverse distances, the higher-mass contributions start being sizeable too.

Nucleon form factors have been extensively studied in the literature. Among others, the low-energy peripheral region has been calculated with covariant ChPT approaches that include the $\Delta(1232)$ as an explicit intermediate state. Here, we extended the form-factor calculations to $SU(3)$, therefore taking into account kaon-loop and η-loop contributions to the nucleons, as well as enabling the study of hyperon properties. While for the charge radii an expansion around small momentum transfers is needed, the spectral functions start contributing at the two-pion cut, i.e., where the virtual photon couples to the baryon target via a pion loop. Kaon-loop contributions appear at slightly higher energies. The effect of taking into account the contributions of vector mesons has also been studied, in a model-dependent manner.

The results gave insight into several new aspects of the baryon densities, and about the extraction of charge radii. The behaviour of the second derivative of the electric form factor seems to be dominated by the vector-meson exchange. It was found that the chiral-loop contributions, including the spin-3/2 states, are important, but that they alone do not suffice to reproduce the experimental estimates. When adding the vector mesons, the results lie in the expected range, and the empirically determined nucleon electric form factor is

reproduced up to higher momentum transfers.

On the other hand, for the electromagnetic densities the vector mesons are mainly important to determine the qualitative behaviour of the transition between the chiral (peripheral) region and higher energies (more central distances). While indeed the periphery region is usually dominated by ChPT-loop contributions, the particular cases of the Λ and the Σ^0 are special. Here, the pion loops cancel exactly, and the kaon loops give very small contributions due to partial cancellations. Therefore, the periphery region of these hyperons has nearly vanishing densities, and the vector-meson contributions start to be relevant at higher transverse densities than for the other octet members. These objects can thus be interpreted as very compact in terms of charge and magnetic distributions. In Chapter 5, it was shown that this is true even when breaking the isospin symmetry, i.e., when giving different masses to the baryons instead of setting them all to the limit of equal masses. The pion contributions are then nonzero, but negligible. The particularity of the Ξ hyperons is that there the spin-3/2 decuplet contributions have a similar size to the spin-1/2 contributions even at the periphery, in spite of their higher mass. This again showed the importance of taking the explicit decuplet degrees of freedom into account, confirming the discussion in Chapters 3 and 4. Finally, returning to the nucleons, I would like to stress that although the pion loops give the main periphery contributions, an extension to $SU(3)$ with the kaon-loop inclusion did indeed give new insight regarding these baryons. This is especially the case for the transition between the periphery and the vector-meson dominated region.

The final study within the present thesis is described in Chapter 6. There, I give an estimate for the upper limits of the branching ratios for the CP-violating decays of the η and η' pseudoscalars into two pions. This was done by connecting the size of the upper limit of the neutron EDM to the magnitude of the CP violation. More precisely, taking the decay of the η and η' mesons into two pions as a starting point, we postulated the Lagrangian that describes the CP-violating coupling of these mesons to the nucleon. Having constructed such a vertex, it is then straightforward to calculate the CP-violating contributions to the electron-scattering amplitudes off nucleons. At the $q^2 = 0$ limit, where the exchanged photon is real, this amplitude can be connected to the EDM of the target. In fact, from a theoretical perspective, the only possibility to obtain a non-vanishing EDM is the presence of such CP-violating structures in the amplitude.

In this chapter too, the calculations were performed in fully covariant ChPT with the inclusion of the Δ contributions. The renormalization scheme used was EOMS. Due to the fact that the coupling of the photon to the neutron vanishes at leading chiral order, we also included vector-meson contributions,

which can in this case be sizeable.

This framework was not meant to estimate the size of the neutron EDM: there are uncertainties in some coupling constants, as well as a dependence on the renormalization scheme. Furthermore, only a few of the many processes that can contribute to the existence of an EDM are considered. Nevertheless, the results are of striking interest. In order to be consistent with the very small upper limit of the empirically extracted neutron EDM, we obtained a tight constraint for the CP-violating decay branching ratios of the η and the η' as well. In fact, they would have to be at least eight orders of magnitude smaller than what has been experimentally possible to determine so far. Even with the large uncertainties mentioned above, and even when considering the possible partial cancellations with other contributing processes, this qualitative behaviour and conclusion remains true, and a further step towards the understanding of the size of CP violation could be made.

In the following, I will discuss the questions that may be treated in follow-up studies to this thesis. In the case of the pion photoproduction, discussed in Chapter 3, the natural extension is to study isospin-breaking effects due to the mass splittings between the charged and neutral pions, and between protons and neutrons. Only when taking these into account one can reproduce the observation of the cusp effect close to the threshold. Furthermore, it would be interesting to test up to which energies the model introduced here applies. A breakdown is expected when approaching energies too close to the $\Delta(1232)$ mass. Finally, also the other channels of pion production should be studied with this approach, as well as the dependence on the photon virtuality in electroproduction processes, in order to obtain further constraints on the LECs.

The framework used to extract the results in Chapter 4 can be applied to the extraction of other hyperon properties related to Compton-scattering observables, such as the spin-independent electric and magnetic polarizabilities, and the four separate spin polarizabilities. Also in this case, the dependence on the photon virtuality could be studied. Furthermore, it would be interesting to test the convergence of the chiral series. This could be done by employing the counting scheme used in Chapter 5 for the inclusion of the decuplet baryons. This amounts to an additional set of loop diagrams without the appearance of unknown LECs. The predictive power would therefore be maintained, and the results would be valid up to higher virtualities.

As for the calculations of Chapter 5, a next step is to extend them to the extraction of the decuplet-baryon form factors, as well as the transition form factors between the octet and decuplet members. For the decuplet, it is interesting to study the impact of anomalous thresholds on the observables considered. In some cases, the intermediate baryon-pion loop might be put on shell below the two-pion cut, promising an interesting interplay between this

anomalous threshold and that of the two-pion production.

Lastly, Chapter 6 can be expanded by taking into consideration additional CP-violating decays that might contribute to the neutron EDM. For example, tensor-meson contributions have not been taken into account within the present work, nor the decay of the η and of the η' into four pions. Furthermore, it would be important to study the dependence on the renormalization scheme used, in order to extract information about the counterterms applied.

In summary, in this work I presented detailed studies of low-energy electromagnetic interactions with baryons, focusing on the importance of the explicit inclusion of the spin-3/2 contributions and of a proper covariant treatment in all the projects presented here. We started with a framework of $SU(2)$ ChPT for the description of interactions between pions, nucleons, and the Δ resonance. We compared and fitted the results to new data on threshold neutral pion photoproduction. Because of their sensitivity to higher-order terms, the results were a good test of ChPT.

Building on this basis, we extended the framework to $SU(3)$, including hadrons with strange content. With this setup, we studied Compton scattering and electron scattering off baryon targets. The main observables were the forward spin polarizability, the electromagnetic form factors, the charge and magnetic densities and the EDM.

The theoretical description has successfully reproduced the experimental findings for the nucleon forward spin polarizabilities. Therefore, in the present work, the hyperon polarizabilities were predicted within the same framework. The study of the electric form factors allowed a better understanding on the extraction of the charge radii from data and on the transverse baryon densities. Finally, the calculation of the neutron EDM was not meant as a prediction, but as an estimate of the size of the strong CP violation in some meson decays.

While the calculations are stringent tests of ChPT, giving nontrivial fits and predictive results, there is room for many interesting follow-up studies, which are discussed above. The analysis of the isospin-breaking effects, the test of the convergence at higher energies, as well as the study of other observables and channels of the processes considered are only a few examples. There is a constant interplay between the theoretical predictions and the empirical findings. The appearance of new experimental and lattice QCD results will always call for the improvement and extension of the calculations to phenomenological regions that had not been accessible so far. On the other hand, theories want to be confirmed, and the promise of tests on the predictions made is exciting. The deeper experimentalists and theoreticians dig into specific subjects, the more we will learn about the broader picture within which these objects of study are inserted, and connections might be made that had never been planned to be established.

CHAPTER 8

RESUMEN EN ESPAÑOL

8.1 Objetivos

Las interacciones entre hadrones ligeros y campos de fotones son importantes para el estudio de la estructura de la materia y de la interacción fuerte. Sus propiedades fundamentales son descritas por la cromodinámica quántica (QCD). A energías elevadas, esta teoría ya ha sido bien comprobada con métodos perturbativos que tienen los quarks y gluones como grados de libertad. Sin embargo, a bajas energías, QCD es no-perturbativa y quedan muchos detalles por entender. Estas son precisamente las energías necesarias para describir interacciones entre hadrones a distancias superiores a su tamaño.

Procesos que involucran interacciones con hadrones han sido extensamente estudiados a lo largo de las décadas, tanto en instalaciones experimentales, así como desde el punto de vista teórico. Aquí me concentraré en el límite de bajas energías de algunos de estos procesos: la fotoproducción de piones neutros, la dispersión Compton y dispersiones elásticas de electrones en blancos bariónicos. En particular, esta tesis contiene los siguientes estudios principales en QCD no-perturbativa: la determinación de secciones eficaces de la fotoproducción de piones, el estudio de polarizabilidades y factores de forma electromagnéticos de bariones y un cálculo del momento dipolar eléctrico del neutrón. Estos estudios dan información sobre la estructura interna de los bariones, sobre sus densidades y, por lo tanto, indirectamente también sobre sus distribuciones partónicas. Además, llevan a un mejor conocimiento de las interacciones, tanto entre hadrones como dentro de ellos. Al estudiar secciones eficaces, uno obtiene también información sobre estados resonantes que surgen debido a la excitación de hadrones ligeros. Aparecen como polos en las amplitudes de las interacciones electromagnéticas estudiadas, afectando considerablemente el comportamiento de los observables.

Con el fin de motivar el cuadro teórico en que se enmarca esta tesis, la teoría quiral de perturbaciones (ChPT), es importante entender primero QCD, la teoría sobre la cual está construido. Como se ha mencionado, esta teoría de gauge describe con éxito interacciones fuertes a altas energías, con los grados de libertad quarks y gluones para campos de materia y de partículas que median la interacción, respectivamente. A energías de algunos GeV y superiores, los quarks confinados dentro de hadrones pueden ser tratados como asintóticamente libres, siendo así posible usar los métodos de QCD perturbativa como una expansión en términos de la constante de acoplamiento fuerte $\alpha_s \ll 1$. El grupo de simetría correspondiente, $SU(3)$ (color), es no-Abeliano. Esto lleva a auto-interacciones de campos de gluones, afectando el comportamiento del acoplamiento fuerte en función de la energía: a bajas energías o, de modo equivalente, a distancias elevadas, α_s se hace más grande. A una escala de $\Lambda \approx 1$ GeV, la constante de acoplamiento fuerte α_s se vuelve demasiado grande para cálculos perturbativos de QCD. Esta escala corresponde a distancias superiores al tamaño del nucleón, pudiendo así ser entendida como una escala de confinamiento de los quarks que lo componen.

Los procesos en esta tesis son descritos para energías de centro de masa bastante inferiores a Λ. Por causa de la divergencia de la serie perturbativa de QCD en esta zona energética, uno necesita de un método alternativo. Se han usado muchos modelos que cumplen teoremas de bajas energías a lo largo de las décadas pasadas, la mayor parte de ellos puramente fenomenológicos. Sería ventajoso encontrar una teoría que mantenga las simetrías de QCD y que además sea aplicable al estudio combinado de estos procesos de baja energía. A lo largo de los capítulos de esta tesis, me concentro en hadrones ligeros, i.e., aquellos que están compuestos solamente por los quarks u, d y s, por lo cual pueden ser descritos por una simetría $SU(3)$ (sabor). En el límite relativista de quarks ligeros sin masa, los campos dextrógiros q_R y levógiros q_L se desacoplan unos de los otros, llevando a una teoría invariante bajo transformaciones quirales. Hay dos observaciones que sugieren la rotura espontánea de esta simetría del límite quiral de QCD. Por un lado, en la naturaleza los miembros del octete seudoescalar de mesones tienen una masa pequeña en relación a la escala Λ. Estos mesones son, por lo tanto, buenos candidatos para bosones Goldstone provenientes de la rotura espontánea de una simetría. Por otro lado, el octete ligero de bariones tiene paridad positiva y no existen compañeros de masas similares y con paridad negativa, como requeriría una simetría exacta. De hecho, en el sector fermiónico, la rotura espontánea de la simetría quiral genera las masas del octete de bariones $SU(3)$ (sabor), las cuales en el límite quiral son degeneradas. Adicionalmente, las masas de los bosones seudo-Goldstone son interpretadas como consecuencia de una rotura explícita de la simetría por causa del hecho de que los quarks tienen masa. Los

términos resultantes del lagrangiano mezclan q_L y q_R por medio de términos de la masa de los quarks.

De hecho, en el marco de ChPT, estas simetrías espontánea y explícitamente rotas son usadas como base para contruir los lagrangianos de interacción, llevando a una teoría efectiva (EFT) de QCD. En lugar de usar α_s como parámetro perturbativo, ahora se hace una expansión quiral simultánea en potencias de momentos externos y de las masas de los mesones Goldstone. Ambos parámetros son pequeños comparados con la escala de confinamiento. Se integra sobre los grados de libertad de QCD, los quarks y los gluones, así que las interacciones son descritas directamente entre los estados compuestos, los bariones y los mesones. Esta EFT es válida para rangos de energía significativamente más bajos que $\Lambda \approx 1$ GeV, lo que corresponde a distancias superiores al tamaño del barión.

La masa corriente de los quarks u y d es mucho menor que la escala hadrónica, garantizando así una convergencia rápida de la serie quiral cuando uno trabaja únicamente con interacciones entre piones, i.e., cuando uno considera una simetría $SU(2)$ de sabor. La extensión de ChPT a $SU(3)$ con el fin de acomodar el quark s, y como tal el octete completo de mesones seudoescalares, requiere mucho cuidado, ya que la masa corriente de este quark está cerca del orden de magnitud de la escala Λ. Asimismo, la inclusión de los bariones en ChPT también introduce una escala adicional, la masa del barión en el límite quiral.

El rigor de ChPT depende mucho de los grados de libertad incluidos. En el presente trabajo, no solo consideré las interacciones con el octete de bariones de espín-1/2 — los nucleones y los hiperones—, sino también las resonancias de espín-3/2. Estas consisten en un quadruplete de isospín en $SU(2)$ y en un decuplete en $SU(3)$, respectivamente. El acoplamiento con el octete de bariones es fuerte y por consiguiente los bariones de espín-3/2 aparecen muy fácilmente como estados excitados, o resonancias, de los estados de espín-1/2. Teniendo esto en cuenta, es evidente que se esperan contribuciones importantes por parte de estos estados a procesos que tengan lugar en un rango de energías cercano a sus masas. Este es efectivamente el caso de las reacciones estudiadas a lo largo de los siguientes capítulos. Desde luego, las masas de las resonancias también son superiores a Λ. En efecto, al introducir estos estados en el marco de ChPT, aparte las masas mesónicas y los momentos externos, uno obtiene un parámetro pequeño adicional: la diferencia entre las masas del decuplete y del octete de bariones.

La renormalización de divergencias en ChPT se hace orden por orden, absorbiéndolas en coeficientes del lagrangiano más general. Este procedimiento lleva al aparecimiento de constantes de baja energía (LECs), las cuales tienen que ser determinadas por medio de ajustes a datos experimentales. Esto reduce

la calidad predictiva de la teoría. No obstante, muchas de estas constantes ya han sido determinadas a lo largo de las últimas décadas y uno puede usar los valores de la literatura para hacer nuevas predicciones.

Al incluir bariones en ChPT, el contaje quiral de potencias en términos de masas y momentos se rompe, ya que sus masas son del orden de Λ. Por consiguiente, a priori no hay una manera clara de como asociar un orden quiral específico a un número definido de loops. Esto inicialmente se ha resuelto tratando los bariones en el límite no-relativista de ChPT de bariones pesados (HBChPT) [1, 2]. Una alternativa relativista para evaluar las correcciones de loop fue propuesta a finales de los años 1990 [3–5]. Esta llamada regularización infrarroja (IR) aisla la parte regular de las singularidades en cálculos de un loop. Las partes singulares satisfacen el contaje de potencias, mientras que las regulares pueden ser absorbidas en términos locales del lagrangiano que las cancelan. Esta técnica soluciona el problema de contaje de potencias de ChPT de bariones relativista, a un loop. Adicionalmente, aisla las singularidades infrarrojas.

En el marco de esta tesis, los cálculos se hicieron en otro esquema relativista de renormalización, el esquema Extended On Mass Shell (EOMS) [6, 7]. Este satisface por completo la analiticidad y normalmente converge más rápidamente que métodos no-relativistas. Las divergencias y los términos que rompen el esquema de contaje (PCBT) tienen expresiones que son por entero analíticas. Por lo tanto estas pueden ser identificadas con términos del lagrangiano y absorbidas dentro de las LECs correspondientes. Este esquema se ha manifestado exitoso en muchos trabajos [8–20] y puede ser implementado de forma sencilla.

Esta tesis contiene cuatro estudios principales. Un capítulo está dedicado a cada uno de ellos, por lo que escojo dar introducciones y sumarios separados en las respectivas secciones. Sin embargo, una descripción global del formalismo de ChPT que se aplica a todas ellas es dada en el capítulo 2. En el capítulo 3, enseño mi trabajo sobre el estudio de la fotoproducción de piones neutros a partir de blancos protónicos, que se radica en un marco $SU(2)$. Este es extendido a $SU(3)$ en el capítulo 4, con el objetivo de incluir el quark s. Ahí se estudia la polarizabilidad de espín de dirección hacia delante de los nucleones y hiperones, con la ayuda de la dispersión Compton. También en el enfoque de $SU(3)$, el capítulo 5 estudia la dispersión elástica de electrones para la extracción de los factores de forma electromagnéticos de los bariones. Luego estos se relacionan con densidades magnéticas y de carga por medio de un análisis dispersivo. El capítulo 6 muestra un estudio del momento dipolar eléctrico del nucleón y su conexión con la violación fuerte de CP. Finalmente, en el capítulo 7, presento las conclusiones del trabajo y las perspectivas de posibles ampliaciones de los procesos estudiados.

8.2 Metodología

En el capítulo 3, se introduce el estudio de la fotoproducción del pión neutro desde el protón, a bajas energías. Se usa ChPT covariante, con la inclusión explícita de la resonancia $\Delta(1232)$. En $SU(2)$, esta teoría describe además las interacciones entre piones, nucleones y fotones. Hice un cálculo completo hasta el orden quiral $p^{7/2}$ en el contaje llamado δ counting. Esto consiste en tener en cuenta todas las contribuciones de diagramas árbol que provienen de lagrangianos hasta el orden p^3 y los diagramas loop del orden más bajo. En efecto, los diagramas loop con estados intermedios nucleónicos empiezan al orden p^3, mientras que los que incluyen la Δ empiezan al orden $p^{7/2}$. Para renormalizar las divergencias y los PCBT, he usado el esquema de renormalización EOMS, con el cual se sustraen estos términos analíticos a través de una redefinición de las LECs en el lagrangiano. He comparado y ajustado el modelo a datos experimentales de secciones eficaces diferenciales y asimetrías de fotones de la Ref. [55], desde el umbral hasta energías superiores a 200 MeV, en el sistema de referencia de laboratorio. Las LECs son mayoritáriamente restringidas por otros observables. En particular, g_0, $\tilde{c}_{67}$, h_A y g_M son fijadas por el acoplamiento de vector axial al nucleón, por el momento magnético del protón y por las desintegraciones fuerte y electromagnética de la $\Delta(1232)$, respectivamente. Los ajustes que se enseñan en el presente trabajo son compatibles con estas restricciones. Las LECs $\tilde{d}_{168}$ y g_E, que aparecen en lagrangianos de orden superior, están también parcialmente restringidas por la relación Goldberger-Treiman y la razón de multipolos $R_{EM} = E_2/M_1$ del nucleón a la Δ, respectivamente. Sin embargo, resulta que estas constantes son sensibles a correcciones de orden superior, fuera del marco de esta tesis.

En el capítulo 4, se ha calculado la polarizabilidad de espín γ_0 del octete de bariones, usando también ChPT de bariones con covariancia Lorentz manifiesta. Como el octete de bariones incluye miembros compuestos por quarks s, se extiende la teoría a la simetría $SU(3)$, confrontándola con la versión $SU(2)$ de quarks u y d. Se incluyen explícitamente los estados intermedios de espín-3/2, en este caso el decuplete de bariones, ya que la inclusión de estos estados es importante para reproducir las observaciones empíricas que se hacen a energías cercanas a sus masas. Las contribuciones del octete de bariones provienen exclusivamente de los diagramas de loop de orden p^3 y superiores. En cuanto a las contribuciones del decuplete, estas consisten en un diagrama del tipo árbol, dominante, y en diagramas de loop que empiezan a orden $p^{7/2}$. En el presente trabajo, hice un estudio completo hasta ese orden. Al usar un marco $SU(3)$, se tienen también en cuenta las contribuciones de loops de K y η, aunque se espera que sus efectos sean menos relevantes que los de los piones. Las polarizabilidades son independientes de esquemas de renormal-

ización hasta el orden quiral considerado, llevando a una capacidad altamente predictiva de la teoría. La incertidumbre proviene únicamente de la constante g_M de acoplamiento del fotón al decuplete, que en $SU(3)$ todavía no se conoce muy bien. Aquí se da una estimación de su valor a partir de la desintegración electromagnética de bariones de espín-3/2 a bariones de espín-1/2.

Como continuación de este estudio, en el capítulo 5 he presentado el cálculo de los factores de forma del octete de bariones. Esto se hizo en ChPT, con el esquema de renormalización EOMS, para describir la zona de bajas energías, con virtualidades fotónicas desde cero hasta por encima del corte de dos kaones. Estas predicciones en EFT quiral se hicieron con estados intermedios del octete y del decuplete, este último habiendo sido introducido en el esquema de contaje expansión de escala pequeña (SSE). Con estos factores de forma se puede extraer información sobre el radio de carga de los bariones. Con las partes imaginarias, las funciones espectrales, se extraen además las densidades electromagnéticas. Introduje también la contribución de mesones vectoriales. Los últimos son relevantes para la descripción correcta del comportamiento analítico de los factores de forma. Son importantes en el caso de las densidades elctromagnéticas a distancias transversales cortas, mientras que el comportamiento periférico se predice de manera independiente de modelos, con ChPT.

En el capítulo 6, he calculado la contribución al momento dipolar eléctrico (EDM) del nucleón originada por un acoplamiento al mesón $\eta(')$ que viola CP. En particular, focalicé el estudio en el resultado para el neutrón, ya que su límite superior experimental es muy pequeño, $2.9 \cdot 10^{-26} e$ cm. Esto lleva a una restricción muy fuerte de los observables a él relacionados. Específicamente, si existe un EDM del neutrón, entonces necesariamente tiene que haber violación CP. Por lo tanto, el objetivo fue dar una estimación al valor del tamaño de esta violación. Esto se ha logrado al construir un acoplamiento de la $\eta(')$ al nucleón que viola CP, a través de loops que incluyen un vértice $\eta(')\pi\pi$. Existen resultados experimentales para el límite superior del ratio de desintegración $\eta(') \to \pi\pi$ y aquí yo quería examinar si realmente esta condición es compatible con el tamaño del EDM del neutrón. Como fue el caso de los otros proyectos descritos en esta tesis, se han considerado también las contribuciones de la Δ, las cuales llevaron a una corrección superior a 20% del vértice $\eta(')NN$ que viola CP. El esquema de renormalización usado fue de nuevo EOMS. He tenido en cuenta dos posibles fuentes para el EDM del neutrón. En un caso, el fotón se acopla al neutrón dentro de un loop con vértice ηNN que rompe CP. En el otro, se consideran también contribuciones de mesones vectoriales dentro del loop. Las dos contribuciones resultaron tener tamaños similares.

8.3 Resultados

En este trabajo, he estudiado el comportamiento a bajas energías de bariones bajo la influencia de campos electromagnéticos externos. He usado el marco de ChPT covariante para hadrones ligeros, con la inclusión explícita de grados de libertad de espín-3/2. El esquema de renormalización utilizado fue EOMS, en el cual las expresiones analíticas de divergencias y PCBT son absorbidas en LECs del lagrangiano quiral.

El trabajo está dividido en cuatro capítulos principales, cada uno tratando un proceso u observable distinto, a bajas energías. En el capítulo 3, fue estudiada la fotoproducción de piones neutros a partir de blancos protónicos, centrando el interés en la comparación con los datos experimentales de secciones eficaces, asimetrías fotónicas y multipolos de onda-s y de onda-p. El rango de energías observado fue desde el umbral de producción hasta más de 200 MeV. He empezado con una descripción de interacciones electromagnéticas entre nucleones y piones, pero este marco es una base excelente para la descripción de procesos a bajas energías con bariones, mesones y fotones en general.

Así, en el capítulo 4, he estudiado la polarizabilidad de espín en dirección hacia delante, la cual puede ser extraída a partir de la dispersión Compton. Todavía no existen datos — aunque sería posible obtener información de lattice QCD —, y por lo tanto el objetivo era dar predicciones para sus valores. Esto es especialmente interesante para esta polarizabilidad en particular, ya que no depende de esquemas de renormalización. Asimismo, en el capítulo 5, se han calculado los factores de forma electromagnéticos de nucleones e hiperones. En particular, se hizo la conexión con las densidades de carga y magnéticas en la periferia y con el radio de carga. Estos resultados también son predictivos, aunque dependan del esquema de renormalización usado. Sería posible confirmarlos en cálculos de lattice QCD en el futuro próximo. La extracción experimental, por otro lado, se hace a partir de la dispersión de electrones en bariones. Con la ayuda del mismo proceso, uno puede también obtener información sobre el EDM del neutrón, en el punto en que la virtualidad del fotón es nula. En el capítulo 6, me he concentrado en este punto, con el objetivo de relacionarlo al tamaño de desintegraciones que violan CP en la naturaleza. A partir de la restricción experimental del EDM del neutrón, he podido dar una estimación del límite superior de los ratios de algunas de estas desintegraciones. A continuación, discuto estos cuatro proyectos en más detalle.

En el capítulo 3, fue extensamente estudiado el proceso de la fotoproducción del pión neutro a partir de blancos protónicos. Esto fue motivado por los nuevos datos de alta precisión de secciones eficaces diferenciales y asimetrías fotónicas obtenidos recientemente por el Mainz Microtron (MAMI). Estos resultados han sido los primeros en dar acceso a un amplio rango de ángulos de

dispersión, con pasos de energía fotónica muy estrechos, desde el umbral hasta energías superiores a 200 MeV en el sistema de referencia de laboratorio. Con esta nueva información, fue demostrado que trabajos previos por otros grupos teóricos solamente han podido reproducir los datos experimentales hasta no más de 20 MeV por encima del umbral. Los métodos con más éxito habían sido cálculos en ChPT hasta el cuarto orden quiral, tanto de modo covariante, como no-relativista. Estos cálculos de $\mathcal{O}(p^4)$ implican la aparición de muchas LECs, lo que en principio significa la existencia de muchos grados de libertad adicionales para los procedimientos de ajuste. Desafortunadamente, no obstante, el acuerdo entre los datos y la teoría no se mostró significativamente mejor que en cálculos previos, a órdenes más bajos. Hasta la inclusión explícita de resonancias de mesones vectoriales no ha mejorado la situación.

Aquí, probamos una idea alternativa: la inclusión explícita de grados de libertad de espín-3/2, la resonancia $\Delta(1232)$. De hecho, el acoplamiento de este estado a los nucleones es bastante fuerte, llevando a que las contribuciones sean significativas a energías que están cerca de su masa. Sin embargo, trabajos previos hechos en HBChPT no-relativista tampoco han logrado describir los datos pese a incluir esta resonancia. La razón podría ser que, debido a la naturaleza estática del marco usado en esos cálculos, la dependencia energética del propagador de la Δ no ha podido ser tenida en cuenta por completo. No obstante, justamente esta dependencia es crucial para describir el aumento drástico de las secciones eficaces con la energía del fotón. Por lo tanto, hemos reanudado los cálculos, ahora en ChPT íntegramente relativista.

El primer paso ha sido incluir la $\Delta(1232)$ a nível árbol, en adición a los diagramas con nucleones del tipo árbol y loop. En contraposición a cálculos previos, me mantuve a $\mathcal{O}(p^3)$, evitando así un número demasiado grande de LECs desconocidas. Adicionalmente al número elevado de datos a los cuales fueron hechos los ajustes, esto también lleva a resultados más fiables. Los resultados han sido muy satisfactorios, ya que los cálculos acordaron con los datos en el rango completo de energías consideradas. Además, he añadido el siguiente orden de diagramas del tipo loop con propagadores de Δ, para hacer una prueba de la convergencia de la teoría a órdenes más altos. En el esquema de contaje escogido en el capítulo 3, esta inclusión significa un cálculo a $\mathcal{O}(p^{7/2})$ quiral. Estos extensos cálculos han tenido la ventaja de ser una buena prueba no-trivial de la convergencia de la serie quiral, ya que el acuerdo entre los datos y la teoría resultó casi igual al cálculo a $\mathcal{O}(p^3)$. Permitió además estudiar mejor como dependen las LECs de la inclusión de los loops de Δ, pudiendo llevar a un buen acuerdo entre datos y teoría a energías aún superiores que las aquí consideradas. Finalmente, un estudio de los multipolos más bajos (ondas s y p) confirmó la indispensabilidad de tener en cuenta los grados de libertad de la Δ.

En el capítulo 4, he calculado la predicción de ChPT para la polarizabilidad de espín en dirección hacia delante de los hiperones a partir de amplitudes de la dispersión Compton. Aquí también, los valores fueron extraídos en un marco covariante con la inclusión explícita de grados de libertad de espín-3/2, a $\mathcal{O}(p^{7/2})$. Cálculos con el mismo método han sido hechos para el nucleón, estudiando los efectos de loops piónicos en $SU(2)$, i.e., teniendo en cuenta bariones compuestos de quarks u y d. Los resultados estaban en muy buen acuerdo con el experimento, lo que es particularmente notable por el hecho de que no hayan sido necesarios ajustes a datos: las LECs que aparecen al orden considerado ya habían sido bien determinadas a lo largo de las pasadas décadas, a través del estudio de otros procesos. Este cálculo ha por lo tanto presentado una prueba no-trivial y exitosa de los métodos de ChPT.

Por este motivo, es prometedor extender los cálculos para incluir los quarks s, lo que consiste en estudiar no solo nucleones con contribuciones de loops de piones, sino también los hiperones, con loops de kaones y de la η. En la presente tesis, he descrito mis cálculos relacionados con este tema. El estudio de la polarizabilidad de espín en dirección hacia delante de los hiperones ha sido hecho previamente en HBChPT, sin la inclusión de los grados de libertad de espín-3/2. Sin embargo, como ese método se mostró insuficiente para nucleones, la fiabilidad para los resultados de hiperones también es dudosa. Por eso, aquí escojo aplicar el mismo marco que ha logrado reproducir las observaciones empíricas para los nucleones para extraer la polarizabilidad de bariones que no hayan todavía sido medidas. De hecho, debido a los cortos tiempos de vida de los hiperones, no se espera una confirmación experimental de estos resultados en el futuro próximo. Pero es posible hacer cálculos en el lattice, los cuales facilitarían una prueba bienvenida de las predicciones en ChPT.

En el capítulo 5, he presentado los cálculos de los factores de forma electromagnéticos del octete de bariones. El proceso considerado es dispersión de electrones en el nucleón, con el intercambio de un fotón virtual. Con estos factores de forma, uno puede acceder a información sobre muchos observables relacionados con la estructura y el comportamiento electromagnético de estos hadrones. En este trabajo en particular, el objetivo era obtener información sobre las distribuciones de las densidades de carga y magnéticas. Para estos observables, únicamente se consideraron aquellos análisis que son predictivos en ChPT, no dependiendo de LECs desconocidas. En respecto a los radios de carga, esto significa el cálculo de la segunda derivada del factor de forma eléctrico. Esta no está directamente relacionada con el radio de carga, el cual se fija a través de la pendiente de ese factor de forma, pero posibilita una mejor extracción a partir de los datos experimentales. El comportamiento de la segunda derivada en cálculos de ChPT ofrece información sobre la estructura analítica del factor de forma eléctrico en una zona de energías cercanas

al corte de producción de dos piones. Ahí, debido a los polos en el plano complejo, un ajuste polinómico para la extracción de los radios de carga no es viable, por lo cual un mejor entendimiento de estos polos en ChPT es muy instructivo. En cuanto a las distribuciones de carga y magnéticas, análisis dispersivos las conectan a las partes imaginarias de los factores de forma, las funciones espectrales, via transformaciones de Fourier. Si el fotón se acopla al nucleón a través de la creación de un estado hadrónico intermedio, se genera una parte imaginaria de la amplitud. Usando el formalismo light-front, uno puede asociar dos variables: la densidad a una distancia transversal específica del centro de momento del nucleón y la región particular de energía del cálculo de los factores de forma. A distancias transversales elevadas, i.e., en la periferia del nucleón, las contribuciones de baja energía son suficientes para describir el comportamiento de la densidad, ya que los cortes a energías más elevadas tienen partes imaginarias nulas. Por otro lado, para distancias transversales menores, los cortes de energía bajos son exponencialmente suprimidos en la integración dispersiva, siendo las contribuciones de cortes de energías más elevadas las que se vuelven dominantes.

Los factores de forma de nucleones han sido extensamente estudiados en la literatura. Entre otros, la región periférica de bajas energías fue calculada en cálculos covariantes de ChPT que incluyen la $\Delta(1232)$ como estado intermedio explícito. Aquí, extendí los cálculos de factores de forma a $SU(3)$, teniendo en cuenta así las contribuciones de loops de kaones a las densidades nucleares y posibilitando también el estudio de las densidades transversales de los hiperones. Para los radios de carga, hace falta un desarrollo en torno a pequeños momentos transferidos, mientras que las funciones espectrales empiezan a contribuir en el corte de dos piones, i.e., donde el fotón virtual se acopla al blanco bariónico a través de un loop piónico. Contribuciones de loops de kaones aparecen a energías ligeramente superiores. También se estudiaron los efectos de la inclusión de mesones vectoriales.

Los resultados han aportado información sobre varios aspectos de las densidades de los bariones y sobre la extracción de los radios de carga. El comportamiento de la segunda derivada del factor de forma eléctrico parece ser dominado por el intercambio de mesones vectoriales. Se encontró que las contribuciones de loops quirales, incluyendo los estados de espín-3/2, son importantes, pero que solo ellas no bastan para reproducir las estimaciones experimentales. Al incluir los mesones vectoriales, los resultados se encuentran en el intervalo esperado y el factor de forma eléctrico del protón determinado experimentalmente se reproduce hasta momentos transferidos más altos.

Por otro lado, para las densidades electromagnéticas, los mesones vectoriales son importantes principalmente para determinar cualitativamente el comportamiento de transición entre la zona quiral (periférica) y energías más elevadas

(densidades más centrales). Mientras que la región periférica es de hecho normalmente dominada por contribuciones de loops de ChPT, el caso particular de la Λ y de la Σ^0 es especial. Aquí los loops de piones se cancelan exactamente y los loops de kaones dan contribuciones muy pequeñas debido a cancelaciones parciales. Por lo tanto, la zona periférica tiene densidades casi nulas y las contribuciones de mesones vectoriales empiezan a ser relevantes a distancias transversales más elevadas que para los otros miembros del octete. Estos objetos pueden por eso ser interpretados como siendo muy compactos en respecto a las distribuciones de carga y magnéticas. En el capítulo 5, muestro que esto sigue siendo correcto hasta cuando se rompe la simetría isospín, i.e., cuando se toman masas distintas para los bariones en lugar de ponerlas todas en el límite quiral de masas iguales, o a una sola masa física media. Las contribuciones de piones no son nulas, pero negligibles. Por razones similares, la particularidad de los hiperones Ξ es que ahí el decuplete de espín-3/2 da contribuciones similares en tamaño a los de espín-1/2, hasta en la periferia, a pesar de su masa más elevada. Esto ha demostrado de nuevo la importancia de tener en cuenta los grados de libertad explícitos del decuplete, confirmando la discusión de los capítulos 3 and 4. Por último, volviendo a los nucleones, me gustaría poner el énfasis en que, aunque sean los loops de piones los que dan las contribuciones principales a la periferia, una extensión a $SU(3)$ con la inclusión de loops de kaones ha de hecho dado conocimiento nuevo sobre estos bariones. Esto es particularmente cierto para la zona de transición entre la periferia y la región de mesones vectoriales.

El estudio final de la presente tesis está descrito en el capítulo 6. Ahí doy un valor estimado de los límites superiores de los ratios de desintegración que violan CP de los seudoescalares η y η' a dos piones. Lo he hecho conectando el tamaño del EDM del neutrón a la magnitud de la violación CP. Para ser más precisa, al tomar como punto de partida la desintegración de los mesones η y η' a dos piones, he calculado el lagrangiano que describe los acoplamientos que violan CP de estos mesones al nucleón. La construcción de tal vértice lleva a que sea directamente posible calcular las contribuciones que violan CP en la amplitud de dispersión de electrones en nucleones. Para el caso de fotones reales, piezas de la amplitud pueden ser conectadas al EDM del blanco. De hecho, desde la perspectiva teórica, la única posibilidad de obtener un EDM es justamente la presencia en la amplitud de una estructura de este tipo que viola CP.

Aquí también, los cálculos se hicieron en ChPT covariante, incluyendo las contribuciones de la Δ. El marco necesario es mayoritariamente $SU(2)$, ya que el enfoque es sobre el neutrón. Donde necesario, términos de $SU(3)$ que describen el acoplamiento de la η fueron introducidos, en analogía a los de los capítulos 4 y 5. El esquema de renormalización usado fue EOMS. Debido

al hecho de que el acoplamiento del fotón al neutrón es nulo en el primer orden quiral, he también incluido las contribuciones de mesones vectoriales, que pueden en este caso ser relevantes.

Este marco solamente puede dar una estimación del tamaño del EDM del neutrón: hay incertidumbres en algunas constantes de acoplamiento y también una dependencia del esquema de renormalización. Además, se han considerado solamente algunos de los procesos que pueden contribuír a la existencia de un EDM. No obstante, los resultados son de interés notable. Para ser consistente con el límite superior tan pequeño que ha sido extraído experimentalmente para el EDM del neutrón, obtuve también unos límites muy fuertes para los ratios de desintegración que violan CP. De hecho, tendrían que ser por lo menos ocho órdenes de magnitud menores que lo que fue experimentalmente posible de determinar hasta hoy. Este comportamiento cualitativo se mantiene, hasta teniendo en cuenta las grandes incertidumbres mencionadas. Ello permite dar un paso adicional en dirección a entender el tamaño de las violaciones de la simetría CP.

En lo siguiente, discutiré las cuestiones que podrían ser abordadas como continuación de este trabajo. En el caso de la fotoproducción de piones, discutida en el capítulo 3, la extensión natural sería estudiar efectos de la rotura de la simetría de isospín debido a la diferencia entre las masas de los piones cargados y neutros en la naturaleza. Solamente al tener esto en cuenta, uno puede reproducir la observación del efecto de cúspide cerca del umbral. Sería además interesante comprobar hasta qué energías el modelo aquí introducido puede ser aplicado. Se espera una quiebra del modelo al llegar a energías demasiado cercanas a la masa de la $\Delta(1232)$. Por último, con este enfoque deberían de ser estudiados otros canales de producción de piones y también la dependencia de la virtualidad del fotón en procesos de electroproducción, con el fin de obtener más información sobre las LECs.

El marco usado para extraer los resultados en el capítulo 4 se puede aplicar a la extracción de otras propiedades de hiperones relacionadas a observables de la dispersión Compton, tal como las polarizabilidades eléctrica y magnética que no dependen del espín y también las cuatro polarizabilidades de espín por separado. Se podría estudiar la dependencia de la virtualidad del fotón. Por fin, sería interesante hacer la prueba de la convergencia de la serie quiral. Esto se puede hacer usando el esquema de contaje que fue usado en el capítulo 5 para la inclusión del decuplete de bariones. Esto consiste en la inclusión adicional de diagramas sin que aparezcan LECs desconocidas. Se mantendría por lo tanto el poder predictivo y los resultados serían consistentes hasta virtualidades más elevadas. Además, los problemas de invariancia gauge discutidos en el capítulo 4 serían automáticamente resueltos.

En cuanto a los cálculos del capítulo 5, el paso siguiente sería usarlos para

extraer también los factores de forma del decuplete de bariones y de la transición entre el octete y el decuplete. Asimismo, sería interesante estudiar la influencia de umbrales anómalos sobre el comportamiento del umbral de dos piones. Por ejemplo, para factores de forma del decuplete, en algunos casos el loop barión-pión puede ser puesto on shell por debajo del corte de dos piones. Es importante estudiar el impacto que esto pueda tener sobre los observables.

Finalmente, el capítulo 6 puede ser ampliado al considerar contribuciones adicionales al EDM del neutrón, aparte de las de ChPT. Por ejemplo no fueron tenidas en cuenta en el presente trabajo las contribuciones de mesones tensoriales o de las desintegraciones de la η y de la η' a cuatro piones. Además, sería importante estudiar la dependencia de esquemas de renormalización usados, para obtener información sobre los términos de sustracción aplicados.

En sumario, en este trabajo he realizado varios estudios detallados de interacciones electromagnéticas de los bariones a bajas energías, dedicando especial atención a la inclusión explícita de las contribuciones de los bariones de espín-3/2.

Comencé utilizando $SU(2)$ ChPT para describir sistemas donde los grados de libertad relevantes eran piones, nucleones y la resonancia Δ. El esquema de renormalización usado ha sido EOMS que presenta varias ventajas sobre las aproximaciones no relativistas de HBChPT y sobre otros esquemas covariantes como la IR.

En este marco, he comparado y ajustado los resultados a datos recientes y muy precisos de la fotoproducción de piones neutros cerca del umbral. Los resultados han sido un buen test de ChPT, ya que las secciones eficaces diferenciales de este proceso en particular son muy pequeñas, debido a las cancelaciones en el orden quiral más bajo. Ello permite ser más sensible a los términos de orden superior.

Puesta esta base, he extendido el marco a $SU(3)$, con el objetivo de incluir hadrones con contenido extraño. Asimismo, he estudiado dos procesos: la dispersión Compton y la de electrones en blancos bariónicos. En particular, los observables que he estudiado fueron la polarizabilidad de espín hacia delante, las densidades de carga y magnética y el momento dipolar eléctrico. El primero de estos observables pudo ser extraído de manera totalmente predictiva, mientras que los otros dependen del esquema de renormalización. Los cálculos de la polarizabilidad han sido muy exitosos en la descripción de los observables nucleónicos, que pueden ser comparados con resultados experimentales. Por tanto, esperamos que las predicciones de las polarizabilidades de los hiperones sean igualmente fiables.

El estudio de los factores de forma eléctricos permite entender mejor como extraer los radios de carga de los bariones a partir del experimento. En cuanto a las densidades transversales de los bariones del octete, esperamos que existan

resultados de lattice en el futuro próximo. La confirmación de los resultados aquí presentados sería de gran interés.

En contraste, el cálculo del EDM del neutrón no tenía como objetivo obtener una predicción, sino una estimación del tamaño y relación entre varios observables que dependen de la violación de la simetría CP en la interacción fuerte. Incluso con estos caveats, las incertidumbres presentes en los cálculos son mucho mayores que en los otros procesos estudiados, debido a algunas constantes de acoplamiento cuyos valores numéricos no se conocen muy bien y a la necesidad de incluir procesos adicionales a los del marco de esta tesis. No obstante, hay resultados interesantes como las cotas a los branching ratios de desintegración de $\eta(')$ a dos piones obtenidas a partir del EDM del neutrón. Estas cotas son muchos órdenes de magnitud inferiores a las determinadas experimentalmente hasta la fecha.

Los cálculos de esta tesis, obteniendo ajustes y predicciones nada triviales, constituyen un exigente test para ChPT en el sector de los bariones. Además, hay espacio para varias líneas de investigación que son continuación natural y han sido discutidas previamente. El análisis de la convergencia de la serie quiral a energías más elevadas y el estudio de otros observables y canales de los procesos considerados son algunos de los muchos ejemplos. Hay un constante juego entre predicciones teóricas y logros experimentales. La aparición de nuevos resultados empíricos y de lattice QCD inducirá siempre que se mejoren y extiendan los cálculos hacia regiones fenomenológicas que hasta ahora no habían sido accesibles. Por otro lado, las teorías requieren confirmación y la expectativa de posibles tests a las predicciones que se hacen es siempre excitante. Cuanto más al fondo de los temas van experimento y teoría, más aprenderemos sobre el cuadro general en el cual se insertan nuestros objetos de estudio y se pueden establecer vínculos que nunca habían sido planeados.

APPENDIX **A**

MULTIPOLE DECOMPOSITION OF AMPLITUDES

The pion photoproduction amplitudes $\mathcal{F}_i$ defined in Eq. (3.9) can be written in terms of multipoles as [189]

$$\begin{aligned}
\mathcal{F}_1 &= \sum_{l=0}^{\infty}[lM_l^+ + E_l^+]P'_{l+1}(x) + \sum_{l=2}^{\infty}[(l+1)M_l^- + E_l^-]P'_{l-1}(x),\\
\mathcal{F}_2 &= \sum_{l=1}^{\infty}[(l+1)M_l^+ + lM_l^-]P'_l(x),\\
\mathcal{F}_3 &= \sum_{l=1}^{\infty}[E_l^+ - M_l^+]P''_{l+1}(x) + \sum_{l=3}^{\infty}[E_l^- + M_l^-]P''_{l-1}(x),\\
\mathcal{F}_4 &= \sum_{l=2}^{\infty}[M_l^+ - E_l^+ - M_l^- - E_l^-]P''_l(x),
\end{aligned} \tag{A.1}$$

where $x = \cos(\theta)$ is the center-of-mass production angle, and P_l are the Legendre polynomials for an angular momentum l. One can extract the expressions for the multipoles in terms of these amplitudes:

$$E_l^+ = \int_{-1}^{1}\frac{\mathrm{d}x}{2(l+1)}\left[P_l\mathcal{F}_1 - P_{l+1}\mathcal{F}_2 + \frac{l}{2l+1}(P_{l-1}-P_{l+1})\mathcal{F}_3 + \frac{l+1}{2l+3}(P_l - P_{l+2})\mathcal{F}_4\right],$$

$$E_l^- = \int_{-1}^{1}\frac{\mathrm{d}x}{2l}\left[P_l\mathcal{F}_1 - P_{l-1}\mathcal{F}_2 - \frac{l+1}{2l+1}(P_{l-1}-P_{l+1})\mathcal{F}_3 + \frac{l}{2l-1}(P_l - P_{l-2})\mathcal{F}_4\right],$$

$$M_l^+ = \int_{-1}^{1}\frac{\mathrm{d}x}{2(l+1)}\left[P_l\mathcal{F}_1 - P_{l+1}\mathcal{F}_2 + \frac{1}{2l+1}(P_{l-1}-P_{l+1})\mathcal{F}_3\right],$$

$$M_l^- = \int_{-1}^{1} \frac{\mathrm{d}x}{2l} \left[-P_l \mathcal{F}_1 + P_{l-1}\mathcal{F}_2 + \frac{1}{2l+1}(P_{l-1} - P_{l+1})\mathcal{F}_3 \right], \tag{A.2}$$

where P_l should be set to 0 for negative values of l.

When using only the s and p-waves, the observables of interest (the differential cross section $\frac{\mathrm{d}\sigma}{\mathrm{d}\Omega_\pi}$ and the photon asymmetry Σ) can be written as follows:

$$\frac{\mathrm{d}\sigma}{\mathrm{d}\Omega_\pi} = \frac{|\vec{q}|}{|\vec{k}|}[A + B\cos(\theta) + C\cos^2(\theta)],$$

$$\Sigma = \frac{|\vec{q}|\sin^2(\theta)}{2|\vec{k}|\frac{\mathrm{d}\sigma}{\mathrm{d}\Omega_\pi}}[|\mathcal{P}_3|^2 - |\mathcal{P}_2|^2], \tag{A.3}$$

with the definitions

$$A = |E_0^+|^2 + \frac{1}{2}[|\mathcal{P}_2|^2 + |\mathcal{P}_3|^2],$$

$$B = 2\mathrm{Re}(E_0^+ \mathcal{P}_1^*),$$

$$C = |\mathcal{P}_1|^2 - \frac{1}{2}[|\mathcal{P}_2|^2 + |\mathcal{P}_3|^2],$$

$$\mathcal{P}_1 = 3E_1^+ + M_1^+ - M_1^-,$$

$$\mathcal{P}_2 = 3E_1^+ - M_1^+ + M_1^-,$$

$$\mathcal{P}_3 = 2M_1^+ + M_1^-. \tag{A.4}$$

Furthermore, q and k are the pion and the photon momenta, respectively.

As discussed in Chapter 3, although customary in both theoretical and experimental analyses, it is not sufficient to include the s and p-waves only, especially the higher one gets in energies. Therefore here I also give the expressions up to $l = 2$, in order to take the d-waves into account:

$$\mathcal{F}_1 = E_2^- + E_0^+ + \frac{3}{2}[-E_2^+ + 2M_2^- + 2x(E_1^+ + M_1^+) - 2M_2^+ + 5x^2(E_2^+ + 2M_2^+)],$$

$$\mathcal{F}_2 = M_1^- + 6xM_2^- + 2M_1^+ + 9xM_2^+,$$

$$\mathcal{F}_3 = 3[E_1^+ - M_1^+ + 5x(E_2^+ - M_2^+)],$$

$$\mathcal{F}_4 = -3[E_2^- + E_2^+ + M_2^- - M_2^+]. \tag{A.5}$$

With the help of Eqs. (3.12) to (3.14) one can connect these to the measured observables.

APPENDIX **B**

LIST OF DIAGRAMS AND AMPLITUDES

B.1 Amplitudes of pion photoproduction

The tree-level diagrams of Fig. 3.3 have the following amplitude expressions:

$$\begin{aligned}\mathcal{M}_{3.3(a),p^1} =& -\mathrm{i}\frac{eg_0}{2F}\Bigg[\left(\frac{m+m_2}{m^2+2p\cdot k-m_2^2}+\frac{m+m_2}{m^2-2p'\cdot k-m_2^2}\right)\not{\epsilon}\not{k}\gamma_5 \\ &+\left(\frac{2p\cdot k}{m^2+2p\cdot k-m_2^2}+\frac{2p'\cdot k}{m^2-2p'\cdot k-m_2^2}\right)\not{\epsilon}\gamma_5 \\ &+\frac{2(m+m_2)}{m^2-2p'\cdot k-m_2^2}\epsilon\cdot q\gamma_5\Bigg],\end{aligned} \tag{B.1}$$

$$\begin{aligned}\mathcal{M}_{3.3(a),p^2} =& -\mathrm{i}\frac{eg_A}{8mF_\pi}(c_6+c_7)\Bigg[\left(4+4m^2\left(\frac{1}{p\cdot k}-\frac{1}{p'\cdot k}\right)\right)\not{\epsilon}\not{k}\gamma_5 \\ &-\frac{4m}{p'\cdot k}\epsilon\cdot q\not{k}\gamma_5\Bigg],\end{aligned} \tag{B.2}$$

$$\begin{aligned}\mathcal{M}_{3.3(a),p^3} =& \frac{\mathrm{i}e(2d_{16}-d_{18})m\ m_\pi^2}{F_\pi}\Bigg[\left(\frac{1}{p'\cdot k}-\frac{1}{p\cdot k}\right)\not{\epsilon}\not{k}\gamma_5 \\ &+\frac{2}{p'\cdot k}\epsilon\cdot q\gamma_5\Bigg],\end{aligned} \tag{B.3}$$

$$\mathcal{M}_{3.3(b)} = \frac{4\mathrm{i}e(d_8+d_9)}{F_\pi}\left[\frac{1}{m}\left(m^2+p\cdot p'\right)\not{\epsilon}\not{k}\gamma_5 + \frac{1}{m}p\cdot k\epsilon\cdot q\gamma_5 \right.$$
$$\left. + (p+p')\cdot k\not{\epsilon}\gamma_5 + \epsilon\cdot q\not{k}\gamma_5\right]. \tag{B.4}$$

Note that the nucleon mass m is set to the physical nucleon mass m_N everywhere except in the propagator of the $\mathcal{O}(p^1)$ amplitude, where I perform the correction shown in Eq. (3.25).

The amplitudes of the diagrams of Figs. 3.5(a) to 3.5(c) combined have the following simple expression (the sum over the isospin channels has already been performed):

$$\mathcal{M}_{3.5(a),3.5(b),3.5(c)} = \frac{\mathrm{i}e\, m\, m_\pi^2 g_A}{96\pi^2 F_\pi^3}\left(\lambda - \log\left[\frac{m_\pi^2}{m^2}\right]\right)$$
$$\times\left[\left(\frac{1}{p'\cdot k} - \frac{1}{p\cdot k}\right)\not{\epsilon}\not{k}\gamma_5 + \frac{2}{p'\cdot k}\epsilon\cdot q\gamma_5\right], \tag{B.5}$$

where $\lambda = \frac{2}{\epsilon} + \log(4\pi) - \gamma_E + 1 + \mathcal{O}(\epsilon)$ is the piece that is EOMS-renormalized according to the $\widetilde{MS}$ prescription, see also Appendix C. Note that I am using the nucleon mass m as the chiral-symmetry breaking scale. As for the other diagrams in Fig. 3.5, their expressions are listed here before being integrated, as after evaluation they are rather large:

$$\mathcal{M}_{3.5(d)} = \frac{eg_A}{4F_\pi^3}\int\frac{\mathrm{d}^d z}{(2\pi)^d}\left[\frac{(\not{z}+\not{q})(\not{p}+\not{k}-\not{z}+m)\not{\epsilon}\gamma_5}{[z^2-m_\pi^2][(z-p-k)^2-m^2]}\right.$$
$$\left. - \frac{\not{\epsilon}\gamma_5(\not{p}-\not{q}-\not{z}+m)(\not{z}-\not{q})}{[z^2-m_\pi^2][(z-p+q)^2-m^2]}\right]. \tag{B.6}$$

The contributions of the direct and crossed diagrams in Fig. 3.5(e) exactly cancel each other.

$$\mathcal{M}_{3.5(f)} = \frac{eg_A}{4F_\pi^3}\int\frac{\mathrm{d}^d z}{(2\pi)^d}$$
$$\times\left[-\frac{(\not{z}+\not{q})(\not{p}+\not{k}-\not{z}+m)\not{z}\gamma_5(\not{p}+\not{k}+m)\not{\epsilon}}{[z^2-m_\pi^2][(z-p-k)^2-m^2]2p\cdot k}\right.$$
$$+\frac{\not{z}\gamma_5(\not{p}'-\not{z}+m)(\not{z}-\not{q})(\not{p}+\not{k}+m)\not{\epsilon}}{[z^2-m_\pi^2][(z-p')^2-m^2]2p\cdot k}$$

$$
\begin{aligned}
&- \frac{\not\epsilon(\not p' - \not k + m)\not z\gamma_5(\not p' - \not k - \not z + m)(\not z - \not q)}{[z^2 - m_\pi^2][(z - p' + k)^2 - m^2]2p' \cdot k} \\
&+ \frac{\not\epsilon(\not p' - \not k + m)(\not z + \not q)(\not p - \not z + m)\not z\gamma_5}{[z^2 - m_\pi^2][(z - p)^2 - m^2]2p' \cdot k}\Bigg], \qquad \text{(B.7)}
\end{aligned}
$$

$$
\begin{aligned}
\mathcal{M}_{3.5(g)} =& \frac{eg_A^3}{4F_\pi^3}\int \frac{\mathrm{d}^d z}{(2\pi)^d} \\
&\times\Bigg[- \frac{\not q\gamma_5(\not p + \not k + m)\not z\gamma_5(\not p + \not k - \not z + m)\not\epsilon\gamma_5}{[z^2 - m_\pi^2][(z - p - k)^2 - m^2]2p \cdot k} \\
&+ \frac{\not z\gamma_5(\not p' - \not z + m)\not\epsilon\gamma_5(\not p' - \not k + m)\not q\gamma_5}{[z^2 - m_\pi^2][(z - p')^2 - m^2]2p' \cdot k} \\
&+ \frac{\not\epsilon\gamma_5(\not p' - \not k - \not z + m)\not z\gamma_5(\not p' - \not k + m)\not q\gamma_5}{[z^2 - m_\pi^2][(z - p' + k)^2 - m^2]2p' \cdot k} \\
&- \frac{\not q\gamma_5(\not p + \not k + m)\not\epsilon\gamma_5(\not p - \not z + m)\not z\gamma_5}{[z^2 - m_\pi^2][(z - p)^2 - m^2]2p \cdot k}\Bigg], \qquad \text{(B.8)}
\end{aligned}
$$

$$
\begin{aligned}
\mathcal{M}_{3.5(h)} =& \frac{3eg_A^3}{8F_\pi^3}\int \frac{\mathrm{d}^d z}{(2\pi)^d} \\
&\times\Bigg[\frac{\not q\gamma_5(\not p + \not k + m)\not z\gamma_5(\not p + \not k - \not z + m)\not z\gamma_5(\not p + \not k + m)\not\epsilon}{[z^2 - m_\pi^2][(z - p - k)^2 - m^2]4(p \cdot k)^2} \\
&+ \frac{\not\epsilon(\not p' - \not k + m)\not z\gamma_5(\not p' - \not k - \not z + m)\not z\gamma_5(\not p' - \not k + m)\not q\gamma_5}{[z^2 - m_\pi^2][(z - p' + k)^2 - m^2]4(p' \cdot k)^2}\Bigg], \qquad \text{(B.9)}
\end{aligned}
$$

$$
\begin{aligned}
\mathcal{M}_{3.5(i)} =& \frac{eg_A}{2F_\pi^3}\int \frac{\mathrm{d}^d z}{(2\pi)^d} \\
&\times\Bigg[- \frac{(\not z + \not q + \not k)\epsilon \cdot z(\not p - \not z + m)\not z\gamma_5}{[z^2 - m_\pi^2][(z - p)^2 - m^2][(z + k)^2 - m_\pi^2]}
\end{aligned}
$$

$$+\frac{(\not{z}+\not{k})\gamma_5\epsilon\cdot z(\not{p}'-\not{k}-\not{z}+m)(\not{z}-\not{q})}{[z^2-m_\pi^2][(z-p'+k)^2-m^2][(z+k)^2-m_\pi^2]}\Bigg], \tag{B.10}$$

$$\mathcal{M}_{3.5(j)}=\frac{eg_A^3}{2F_\pi^3}\int\frac{\mathrm{d}^dz}{(2\pi)^d}$$

$$\times\Bigg[\frac{\not{q}\gamma_5(\not{p}+\not{k}+m)(\not{z}+\not{k})\gamma_5\epsilon\cdot z(\not{p}-\not{z}+m)\not{z}\gamma_5}{[z^2-m_\pi^2][(z-p)^2-m^2][(z+k)^2-m_\pi^2]2p\cdot k}$$

$$-\frac{(\not{z}+\not{k})\gamma_5\epsilon\cdot z(\not{p}'-\not{k}-\not{z}+m)\not{z}\gamma_5(\not{p}'-\not{k}+m)\not{q}\gamma_5}{[z^2-m_\pi^2][(z-p'+k)^2-m^2][(z+k)^2-m_\pi^2]2p'\cdot k}\Bigg], \tag{B.11}$$

$$\mathcal{M}_{3.5(k)}=\frac{eg_A^3}{8F_\pi^3}\int\frac{\mathrm{d}^dz}{(2\pi)^d}$$

$$\times\Bigg[-\frac{\not{z}\gamma_5(\not{p}'-\not{z}+m)\not{q}\gamma_5(\not{p}+\not{k}-\not{z}+m)\not{z}\gamma_5(\not{p}+\not{k}+m)\not{\epsilon}}{[z^2-m_\pi^2][(z-p')^2-m^2][(z-p-k)^2-m^2]2p\cdot k}$$

$$+\frac{\not{\epsilon}(\not{p}'-\not{k}+m)\not{z}\gamma_5(\not{p}'-\not{k}-\not{z}+m)\not{q}\gamma_5(\not{p}-\not{z}+m)\not{z}\gamma_5}{[z^2-m_\pi^2][(z-p'+k)^2-m^2][(z-p)^2-m^2]2p'\cdot k}\Bigg], \tag{B.12}$$

$$\mathcal{M}_{3.5(l)}=\frac{eg_A^3}{4F_\pi^3}\int\frac{\mathrm{d}^dz}{(2\pi)^d}$$

$$\times\Bigg[\frac{\not{z}\gamma_5(\not{p}'-\not{z}+m)\not{q}\gamma_5(\not{p}+\not{k}-\not{z}+m)\not{\epsilon}\gamma_5}{[z^2-m_\pi^2][(z-p')^2-m^2][(z-p-k)^2-m^2]}$$

$$+\frac{\not{\epsilon}\gamma_5(\not{p}'-\not{k}-\not{z}+m)\not{q}\gamma_5(\not{p}-\not{z}+m)\not{z}\gamma_5}{[z^2-m_\pi^2][(z-p'+k)^2-m^2][(z-p)^2-m^2]}\Bigg], \tag{B.13}$$

$$\mathcal{M}_{3.5(m)}=\frac{eg_A^3}{8F_\pi^3}\int\frac{\mathrm{d}^dz}{(2\pi)^d}$$

$$\times\Bigg[\frac{\not{q}\gamma_5(\not{p}+\not{k}+m)\not{z}\gamma_5(\not{p}+\not{k}-\not{z}+m)\not{\epsilon}(\not{p}-\not{z}+m)\not{z}\gamma_5}{[z^2-m_\pi^2][(z-p)^2-m^2][(z-p-k)^2-m^2]2p\cdot k}$$

$$- \frac{\not{z}\gamma_5(\not{p}' - \not{z} + m)\not{\epsilon}(\not{p}' - \not{k} - \not{z} + m)\not{z}\gamma_5(\not{p}' - \not{k} + m)\not{q}\gamma_5}{[z^2 - m_\pi^2][(z-p'+k)^2 - m^2][(z-p')^2 - m^2]2p'\cdot k}\Bigg], \quad \text{(B.14)}$$

$$\mathcal{M}_{3.5(n)} = \frac{eg_A^3}{8F_\pi^3}\int \frac{\mathrm{d}^d z}{(2\pi)^d}$$

$$\times\Bigg[\frac{\not{z}\gamma_5(\not{p}' - \not{z} + m)\not{q}\gamma_5(\not{p} + \not{k} - \not{z} + m)\not{\epsilon}(\not{p} - \not{z} + m)\not{z}\gamma_5}{[z^2 - m_\pi^2][(z-p')^2 - m^2][(z-p-k)^2 - m^2][(z-p)^2 - m^2]}$$

$$+ \frac{\not{z}\gamma_5(\not{p}' - \not{z} + m)\not{\epsilon}(\not{p}' - \not{k} - \not{z} + m)\not{q}\gamma_5(\not{p} - \not{z} + m)\not{z}\gamma_5}{[z^2 - m_\pi^2][(z-p')^2 - m^2][(z-p'+k)^2 - m^2][(z-p)^2 - m^2]}\Bigg], \quad \text{(B.15)}$$

$$\mathcal{M}_{3.5(o)} = -\frac{eg_A^3}{2F_\pi^3}\int \frac{\mathrm{d}^d z}{(2\pi)^d}$$

$$\times\Bigg[\frac{(\not{z} + \not{k})\gamma_5\epsilon\cdot z(\not{p}' - \not{k} - \not{z} + m)\not{q}\gamma_5(\not{p} - \not{z} + m)\not{z}\gamma_5}{[z^2 - m_\pi^2][(z+k)^2 - m_\pi^2][(z-p)^2 - m^2][(z-p'+k)^2 - m^2]}\Bigg]. \quad \text{(B.16)}$$

As for the diagrams including the RS Δ propagators, I use the definition $S_\Delta^{\alpha\beta}(p)$ introduced in Eq. (2.41). The tree-level amplitudes of Fig. 3.4 then read:

$$\mathcal{M}_{3.4,p^2} = -\frac{eh_A g_M}{2mM_\Delta(m+M_\Delta)F_\pi}$$

$$\times\Big[(p_\mu + k_\mu)q_\lambda\gamma^{\mu\nu\lambda}S_\Delta^{\nu\beta}(p+k)(p_\alpha + k_\alpha)k_\delta\epsilon_\rho\epsilon^{\alpha\beta\delta\rho}$$

$$-(p'_\alpha - k_\alpha)k_\delta\epsilon_\rho\epsilon^{\alpha\beta\delta\rho}S_\Delta^{\beta\nu}(p'-k)(p'_\mu - k_\mu)q_\lambda\gamma^{\mu\nu\lambda}\Big], \quad \text{(B.17)}$$

$$\mathcal{M}_{3.4,p^3} = -\mathrm{i}\frac{eh_A g_E}{2mM_\Delta(m+M_\Delta)F_\pi}$$

$$\times\Big[(p_\mu + k_\mu)q_\lambda\gamma^{\mu\nu\lambda}S_\Delta^{\nu\beta}(p+k)(p_\alpha + k_\alpha)(k^\alpha\epsilon^\beta - k^\beta\epsilon^\alpha)\gamma_5$$

$$-(p'_\alpha - k_\alpha)(k^\alpha\epsilon^\beta - k^\beta\epsilon^\alpha)\gamma_5 S_\Delta^{\beta\nu}(p'-k)(p'_\mu - k_\mu)q_\lambda\gamma^{\mu\nu\lambda}\Big]. \quad \text{(B.18)}$$

The loop diagrams of Fig. 3.6 also have very large expressions after evaluation, and therefore I opt to show the expressions before the momentum integration or the action of the Dirac equation. The sum over the isospin channels was already performed:

$$\begin{aligned}
\mathcal{M}_{3.6(a)} = &- \frac{e g_A h_A^2}{16 F_\pi^3 M_\Delta^2} \int \frac{\mathrm{d}^d z}{(2\pi)^d} \frac{1}{z^2 - m_\pi^2} \\
&\times \Bigg\{ \not{q} \gamma_5 (\not{p} + \not{k} + m)(p + k - z)_\alpha z_\delta \gamma^{\alpha\beta\delta} \\
&\times \frac{S_\Delta^{\beta\nu}(p + k - z)(p + k - z)_\mu z_\lambda \gamma^{\mu\nu\lambda} (\not{p} + \not{k} + m) \not{\epsilon}}{(p \cdot k)^2} \\
&+ \frac{\not{\epsilon} (\not{p}' - \not{k} + m)(p' - k - z)_\alpha z_\delta \gamma^{\alpha\beta\delta} S_\Delta^{\beta\nu}(p' - k - z)}{(p' \cdot k)^2} \\
&\times (p' - k - z)_\mu z_\lambda \gamma^{\mu\nu\lambda} (\not{p}' - \not{k} + m) \not{q} \gamma_5 \Bigg\},
\end{aligned} \tag{B.19}$$

$$\begin{aligned}
\mathcal{M}_{3.6(b)} = &- \frac{e g_A h_A^2}{24 F_\pi^3 M_\Delta^2} \int \frac{\mathrm{d}^d z}{(2\pi)^d} \\
&\times \Bigg\{ \frac{\not{q} \gamma_5 (\not{p} + \not{k} + m)(p + k - z)_\alpha z_\delta \gamma^{\alpha\beta\delta} S_\Delta^{\beta\nu}(p + k - z)(p + k - z)_\mu \epsilon_\lambda \gamma^{\mu\nu\lambda}}{[z^2 - m_\pi^2] p \cdot k} \\
&+ \frac{(p' - k - z)_\alpha \epsilon_\delta \gamma^{\alpha\beta\delta} S_\Delta^{\beta\nu}(p' - k - z)(p' - k - z)_\mu z_\lambda \gamma^{\mu\nu\lambda} (\not{p}' - \not{k} + m) \not{q} \gamma_5}{[z^2 - m_\pi^2] p' \cdot k} \\
&- \frac{\not{q} \gamma_5 (\not{p} + \not{k} + m)(p - z)_\alpha \epsilon_\delta \gamma^{\alpha\beta\delta} S_\Delta^{\beta\nu}(p - z)(p - z)_\mu z_\lambda \gamma^{\mu\nu\lambda}}{[z^2 - m_\pi^2] p \cdot k} \\
&+ \frac{(p' - z)_\alpha z_\delta \gamma^{\alpha\beta\delta} S_\Delta^{\beta\nu}(p' - z)(p' - z)_\mu \epsilon_\lambda \gamma^{\mu\nu\lambda} (\not{p}' - \not{k} + m) \not{q} \gamma_5}{[z^2 - m_\pi^2] p' \cdot k} \Bigg\}.
\end{aligned} \tag{B.20}$$

The contribution of the diagrams corresponding to Fig. 3.6(c) vanishes after

dimensional regularization.

$$\mathcal{M}_{3.6(d)} = -\frac{eg_A h_A^2}{12F_\pi^3 M_\Delta^2}\int\frac{\mathrm{d}^d z}{(2\pi)^d}$$
$$\times\left\{\frac{(p+k)_\alpha q_\delta \gamma^{\alpha\beta\delta} S_\Delta^{\beta\nu}(p+k)(p+k)_\mu \epsilon_\lambda \gamma^{\mu\nu\lambda}(\not p - \not z + m)\not z\gamma_5}{[z^2-m_\pi^2][(p-z)^2-m^2]}\right.$$
$$\left.+\frac{\not z\gamma_5(\not p' - \not z + m)(p'-k)_\alpha \epsilon_\delta \gamma^{\alpha\beta\delta} S_\Delta^{\beta\nu}(p'-k)(p'-k)_\mu q_\lambda \gamma^{\mu\nu\lambda}}{[z^2-m_\pi^2][(p'-z)^2-m^2]}\right\}, \tag{B.21}$$

$$\mathcal{M}_{3.6(e)} = \frac{eg_A h_A^2}{12F_\pi^3 M_\Delta^2}\int\frac{\mathrm{d}^d z}{(2\pi)^d}$$
$$\times\left\{\epsilon\cdot z\not q\gamma_5(\not p + \not k + m)(p-z)_\alpha (z+k)_\delta \gamma^{\alpha\beta\delta}\right.$$
$$\times\frac{S_\Delta^{\beta\nu}(p-z)(p-z)_\mu z_\lambda \gamma^{\mu\nu\lambda}}{[z^2-m_\pi^2][(z+k)^2-m_\pi^2]p\cdot k}$$
$$-\epsilon\cdot z(p'-k-z)_\alpha (z+k)_\delta \gamma^{\alpha\beta\delta} S_\Delta^{\beta\nu}(p'-k-z)$$
$$\left.\times\frac{(p'-k-z)_\mu z_\lambda \gamma^{\mu\nu\lambda}(\not p' - \not k + m)\not q\gamma_5}{[z^2-m_\pi^2][(z+k)^2-m_\pi^2]p'\cdot k}\right\}, \tag{B.22}$$

$$\mathcal{M}_{3.6(f)} = \frac{eg_A h_A^2}{6F_\pi^3 M_\Delta^2}\int\frac{\mathrm{d}^d z}{(2\pi)^d}$$
$$\times\left\{\frac{\epsilon\cdot z(p+k)_\alpha q_\delta \gamma^{\alpha\beta\delta} S_\Delta^{\beta\nu}(p+k)(p+k)_\mu (z+k)_\lambda \gamma^{\mu\nu\lambda}(\not p - \not z + m)\not z\gamma_5}{[z^2-m_\pi^2][(z+k)^2-m_\pi^2][(p-z)^2-m^2]}\right.$$
$$+\frac{\epsilon\cdot z(\not z + \not k)\gamma_5(\not p' - \not k - \not z + m)(p'-k)_\alpha z_\delta \gamma^{\alpha\beta\delta}}{[z^2-m_\pi^2][(z+k)^2-m_\pi^2][(p'-k-z)^2-m^2]}$$
$$\left.\times S_\Delta^{\beta\nu}(p'-k)(p'-k)_\mu q_\lambda \gamma^{\mu\nu\lambda}\right\}, \tag{B.23}$$

$$\mathcal{M}_{3.6(g)} = -\frac{e g_A h_A^2}{12 F_\pi^3 M_\Delta^2} \int \frac{\mathrm{d}^d z}{(2\pi)^d}$$

$$\times \Bigg\{ \frac{(p+k)_\alpha q_\delta \gamma^{\alpha\beta\delta} S_\Delta^{\beta\nu}(p+k)(p+k)_\mu z_\lambda \gamma^{\mu\nu\lambda}(\not{p}+\not{k}-\not{z}+m)\not{\epsilon}(\not{p}-\not{z}+m)\not{z}\gamma_5}{[z^2-m_\pi^2][(p+k-z)^2-m^2][(p-z)^2-m^2]}$$

$$+ \frac{\not{z}\gamma_5(\not{p}'-\not{z}+m)\not{\epsilon}(\not{p}'-\not{k}-\not{z}+m)(p'-k)_\alpha z_\delta \gamma^{\alpha\beta\delta}}{[z^2-m_\pi^2][(p'-z)^2-m^2][(p'-k-z)^2-m^2]}$$

$$\times S_\Delta^{\beta\nu}(p'-k)(p'-k)_\mu q_\lambda \gamma^{\mu\nu\lambda} \Bigg\}, \tag{B.24}$$

$$\mathcal{M}_{3.6(h)} = -\frac{e g_A h_A^2}{24 F_\pi^3 M_\Delta^2} \int \frac{\mathrm{d}^d z}{(2\pi)^d}$$

$$\times \Bigg\{ \frac{(p'-z)_\alpha z_\delta \gamma^{\alpha\beta\delta}}{[z^2-m_\pi^2][(p+k-z)^2-m^2]p\cdot k}$$

$$\times S_\Delta^{\beta\nu}(p'-z)(p'-z)_\mu q_\lambda \gamma^{\mu\nu\lambda}(\not{p}+\not{k}-\not{z}+m)\not{z}\gamma_5(\not{p}+\not{k}+m)\not{\epsilon}$$

$$+ \frac{\not{z}\gamma_5(\not{p}'-\not{z}+m)(p+k-z)_\alpha q_\delta \gamma^{\alpha\beta\delta}}{[z^2-m_\pi^2][(p'-z)^2-m^2]p\cdot k}$$

$$\times S_\Delta^{\beta\nu}(p+k-z)(p+k-z)_\mu z_\lambda \gamma^{\mu\nu\lambda}(\not{p}+\not{k}+m)\not{\epsilon}$$

$$- \frac{\not{\epsilon}(\not{p}'-\not{k}+m)(p'-k-z)_\alpha z_\delta \gamma^{\alpha\beta\delta}}{[z^2-m_\pi^2][(p-z)^2-m^2]p'\cdot k}$$

$$\times S_\Delta^{\beta\nu}(p'-k-z)(p'-k-z)_\mu q_\lambda \gamma^{\mu\nu\lambda}(\not{p}-\not{z}+m)\not{z}\gamma_5$$

$$- \frac{\not{\epsilon}(\not{p}'-\not{k}+m)\not{z}\gamma_5(\not{p}'-\not{k}-\not{z}+m)(p-z)_\alpha q_\delta \gamma^{\alpha\beta\delta}}{[z^2-m_\pi^2][(p'-k-z)^2-m^2]p'\cdot k}$$

$$\times S_\Delta^{\beta\nu}(p-z)(p-z)_\mu z_\lambda \gamma^{\mu\nu\lambda} \Bigg\}, \tag{B.25}$$

$$\mathcal{M}_{3.6(i)} = \frac{e g_A h_A^2}{12 F_\pi^3 M_\Delta^2} \int \frac{\mathrm{d}^d z}{(2\pi)^d}$$
$$\times \left\{ \frac{(p'-z)_\alpha z_\delta \gamma^{\alpha\beta\delta} S_\Delta^{\beta\nu}(p'-z)(p'-z)_\mu q_\lambda \gamma^{\mu\nu\lambda}(\not{p}+\not{k}-\not{z}+m)\not{\epsilon}\gamma_5}{[z^2-m_\pi^2][(p+k-z)^2-m^2]} \right.$$
$$\left. + \frac{\not{\epsilon}\gamma_5(\not{p}'-\not{k}-\not{z}+m)(p-z)_\alpha q_\delta \gamma^{\alpha\beta\delta} S_\Delta^{\beta\nu}(p-z)(p-z)_\mu z_\lambda \gamma^{\mu\nu\lambda}}{[z^2-m_\pi^2][(p'-k-z)^2-m^2]} \right\}, \tag{B.26}$$

$$\mathcal{M}_{3.6(j)} = \frac{e g_A h_A^2}{12 F_\pi^3 M_\Delta^2} \int \frac{\mathrm{d}^d z}{(2\pi)^d}$$
$$\times \left\{ \frac{\not{z}\gamma_5(\not{p}'-\not{z}+m)(p+k-z)_\alpha q_\delta \gamma^{\alpha\beta\delta} S_\Delta^{\beta\nu}(p+k-z)(p+k-z)_\mu \epsilon_\lambda \gamma^{\mu\nu\lambda}}{[z^2-m_\pi^2][(p'-z)^2-m^2]} \right.$$
$$+ \frac{(p'-k-z)_\alpha \epsilon_\delta \gamma^{\alpha\beta\delta}}{[z^2-m_\pi^2][(p-z)^2-m^2]}$$
$$\left. \times S_\Delta^{\beta\nu}(p'-k-z)(p'-k-z)_\mu q_\lambda \gamma^{\mu\nu\lambda}(\not{p}-\not{z}+m)\not{z}\gamma_5 \right\}. \tag{B.27}$$

The diagrams of Fig. 3.6(k) do not contribute to the amplitude at the considered order, due to isospin cancellation.

$$\mathcal{M}_{3.6(l)} = -\frac{e g_A h_A^2}{6 F_\pi^3 M_\Delta^2} \int \frac{\mathrm{d}^d z}{(2\pi)^d}$$
$$\times \left\{ \frac{\epsilon \cdot z (p'-k-z)_\alpha (z+k)_\delta \gamma^{\alpha\beta\delta}}{[z^2-m_\pi^2][(z+k)^2-m_\pi^2][(p-z)^2-m^2]} \right.$$
$$\times S_\Delta^{\beta\nu}(p'-k-z)(p'-k-z)_\mu q_\lambda \gamma^{\mu\nu\lambda}(\not{p}-\not{z}+m)\not{z}\gamma_5$$
$$+ \frac{\epsilon \cdot z(\not{z}+\not{k})\gamma_5(\not{p}'-\not{k}-\not{z}+m)(p-z)_\alpha q_\delta \gamma^{\alpha\beta\delta}}{[z^2-m_\pi^2][(z+k)^2-m_\pi^2][(p'-k-z)^2-m^2]}$$
$$\left. \times S_\Delta^{\beta\nu}(p-z)(p-z)_\mu z_\lambda \gamma^{\mu\nu\lambda} \right\}, \tag{B.28}$$

$$\mathcal{M}_{3.6(m)} = -\frac{e g_A h_A^2}{12 F_\pi^3 M_\Delta^2} \int \frac{\mathrm{d}^d z}{(2\pi)^d}$$

$$\times \Bigg\{ \frac{(p'-z)_\alpha z_\delta \gamma^{\alpha\beta\delta}}{[z^2-m_\pi^2][(p+k-z)^2-m^2][(p-z)^2-m^2]}$$

$$\times S_\Delta^{\beta\nu}(p'-z)(p'-z)_\mu q_\lambda \gamma^{\mu\nu\lambda}(\not p + \not k - \not z + m)\not\epsilon(\not p - \not z + m)\not z\gamma_5$$

$$+ \frac{\not z\gamma_5(\not p' - \not z + m)\not\epsilon(\not p - \not k - \not z + m)(p-z)_\mu q_\lambda \gamma^{\mu\nu\lambda}}{[z^2-m_\pi^2][(p'-z)^2-m^2][(p'-k-z)^2-m^2]}$$

$$\times S_\Delta^{\beta\nu}(p-z)(p-z)_\alpha z_\delta \gamma^{\alpha\beta\delta} \Bigg\}. \tag{B.29}$$

B.2 Compton-scattering amplitudes

In the following, I use the definitions c_m, c_{bo} and c_{bi} for the charges of the meson and of the baryons outside and inside the loop, respectively. Furthermore, each channel has a particular isospin combination of the LECs D and F. Therefore I call the combination thereof c_{DF}. The values of this combination for the different channels are summarized in Tables B.1 and B.2. I denote the external baryon's mass as m_1, while that inside the loop has mass m. The amplitudes of the diagrams in Fig. 4.1 then read

$$\mathcal{M}_{4.1(a)} = \mathrm{i}\frac{e^2 c_m^2 c_{DF}^2}{4F_0^2} \int \frac{\mathrm{d}^d k}{(2\pi)^d} \frac{\not\epsilon^* \gamma_5(\not p + \not q - \not k + m)\not\epsilon\gamma_5}{[k^2-m_\pi^2][(p+q-k)^2-m^2]}, \tag{B.30}$$

$$\mathcal{M}_{4.1(b)} = -\mathrm{i}\frac{e^2 c_m c_{bo} c_{DF}^2}{8F_0^2 p\cdot q} \int \frac{\mathrm{d}^d k}{(2\pi)^d} \frac{\not\epsilon^* \gamma_5(\not p + \not q - \not k + m)\not k\gamma_5(\not p + \not q + m_1)\not\epsilon}{[k^2-m_\pi^2][(p+q-k)^2-m^2]}, \tag{B.31}$$

$$\mathcal{M}_{4.1(c)} = -\mathrm{i}\frac{e^2 c_m c_{bo} c_{DF}^2}{8F_0^2 p\cdot q} \int \frac{\mathrm{d}^d k}{(2\pi)^d} \frac{\not\epsilon^* (\not p + \not q + m_1)\not k\gamma_5(\not p + \not q - \not k + m)\not\epsilon\gamma_5}{[k^2-m_\pi^2][(p+q-k)^2-m^2]}. \tag{B.32}$$

The diagrams in Figs. 4.1(d) and 4.1(e) give no contribution to γ_0, as they have no depency on the photon energy ω.

$$\mathcal{M}_{4.1(f)} = \mathrm{i}\frac{e^2 c_{bo}^2 c_{DF}^2}{16F_0^2 (p\cdot q)^2} \int \frac{\mathrm{d}^d k}{(2\pi)^d} \frac{\not\epsilon^* (\not p + \not q + m_1)\not k\gamma_5(\not p + \not q - \not k + m)\not k\gamma_5(\not p + \not q + m_1)\not\epsilon}{[k^2-m_\pi^2][(p+q-k)^2-m^2]}, \tag{B.33}$$

	p	n	Σ^+	Σ^0
p	$D+F$	$\sqrt{2}(D+F)$	$\sqrt{2}(D-F)$	$D-F$
n	$\sqrt{2}(D+F)$	$-(D+F)$	0	$F-D$
Σ^+	$\sqrt{2}(D-F)$	0	$2F$	$-2F$
Σ^0	$D-F$	$F-D$	$-2F$	0
Σ^-	0	$\sqrt{2}(D-F)$	0	$2F$
Λ	$-\frac{D+3F}{\sqrt{3}}$	$-\frac{D+3F}{\sqrt{3}}$	$\frac{2D}{\sqrt{3}}$	$\frac{2D}{\sqrt{3}}$
Ξ^0	0	0	$\sqrt{2}(D+F)$	$-(D+F)$
Ξ^-	0	0	0	$D+F$

	Σ^-	Λ	Ξ^0	Ξ^-
p	0	$-\left(\frac{D+3F}{\sqrt{3}}\right)$	0	0
n	$\sqrt{2}(D-F)$	$-\left(\frac{D+3F}{\sqrt{3}}\right)$	0	0
Σ^+	0	$\frac{2D}{\sqrt{3}}$	$\sqrt{2}(D+F)$	0
Σ^0	$2F$	$\frac{2D}{\sqrt{3}}$	$-(D+F)$	$D+F$
Σ^-	$-2F$	$\frac{2D}{\sqrt{3}}$	0	$\sqrt{2}(D+F)$
Λ	$\frac{2D}{\sqrt{3}}$	0	$\frac{3F-D}{\sqrt{3}}$	$\frac{3F-D}{\sqrt{3}}$
Ξ^0	0	$\frac{3F-D}{\sqrt{3}}$	$F-D$	$\sqrt{2}(D-F)$
Ξ^-	$\sqrt{2}(D+F)$	$\frac{3F-D}{\sqrt{3}}$	$\sqrt{2}(D-F)$	$D-F$

Table B.1.: Values of the isospin constant c_{DF} for the different channels of the octet-baryon-to-octet-baryon transition via a pion or a kaon.

p	n	Σ^+	Σ^0	Σ^-	Λ	Ξ^0	Ξ^-
$\sqrt{3}F - \frac{D}{\sqrt{3}}$	$\sqrt{3}F - \frac{D}{\sqrt{3}}$	$\frac{2D}{\sqrt{3}}$	$\frac{2D}{\sqrt{3}}$	$\frac{2D}{\sqrt{3}}$	$-\frac{2D}{\sqrt{3}}$	$-\sqrt{3}F - \frac{D}{\sqrt{3}}$	$-\sqrt{3}F - \frac{D}{\sqrt{3}}$

Table B.2.: Values of the isospin constant c_{DF} for the coupling of an η meson to an octet baryon.

$$\mathcal{M}_{4.1(g)} = \mathrm{i}\frac{e^2 c_m c_{bo} c_{DF}^2}{4F_0^2 p\cdot q}\int \frac{\mathrm{d}^d k}{(2\pi)^d}\frac{k\cdot\epsilon^* \not{k}\gamma_5(\not{p}-\not{k}+m)(\not{k}+\not{q})\gamma_5(\not{p}+\not{q}+m_1)\not{\epsilon}}{[k^2-m_\pi^2][(k+q)^2-m_\pi^2][(p-k)^2-m^2]}, \tag{B.34}$$

$$\mathcal{M}_{4.1(h)} = \mathrm{i}\frac{e^2 c_m c_{bo} c_{DF}^2}{4F_0^2 p\cdot q}\int \frac{\mathrm{d}^d k}{(2\pi)^d}\frac{\not{\epsilon}^*(\not{p}+\not{q}+m_1)(\not{k}+\not{q})\gamma_5(\not{p}-\not{k}+m)\not{k}\gamma_5 k\cdot\epsilon}{[k^2-m_\pi^2][(k+q)^2-m_\pi^2][(p-k)^2-m^2]}, \tag{B.35}$$

$$\mathcal{M}_{4.1(i)} = -\,\mathrm{i}\frac{e^2 c_m^2 c_{DF}^2}{2F_0^2}\int \frac{\mathrm{d}^d k}{(2\pi)^d}\frac{k\cdot\epsilon^* \not{k}\gamma_5(\not{p}-\not{k}+m)\not{\epsilon}\gamma_5}{[k^2-m_\pi^2][(k+q)^2-m_\pi^2][(p-k)^2-m^2]}, \tag{B.36}$$

$$\mathcal{M}_{4.1(j)} = -\,\mathrm{i}\frac{e^2 c_m^2 c_{DF}^2}{2F_0^2}\int \frac{\mathrm{d}^d k}{(2\pi)^d}\frac{\not{\epsilon}^*\gamma_5(\not{p}-\not{k}+m)\not{k}\gamma_5 k\cdot\epsilon}{[k^2-m_\pi^2][(k+q)^2-m_\pi^2][(p-k)^2-m^2]}, \tag{B.37}$$

$$\mathcal{M}_{4.1(k)} = -\,\mathrm{i}\frac{e^2 c_m c_{bi} c_{DF}^2}{4F_0^2}\int \frac{\mathrm{d}^d k}{(2\pi)^d}\frac{\not{k}\gamma_5(\not{p}-\not{k}+m)\not{\epsilon}^*(\not{p}+\not{q}-\not{k}+m)\not{\epsilon}\gamma_5}{[k^2-m_\pi^2][(p+q-k)^2-m^2][(p-k)^2-m^2]}, \tag{B.38}$$

$$\mathcal{M}_{4.1(l)} = -\,\mathrm{i}\frac{e^2 c_m c_{bi} c_{DF}^2}{4F_0^2}\int \frac{\mathrm{d}^d k}{(2\pi)^d}\frac{\not{\epsilon}^*\gamma_5(\not{p}+\not{q}-\not{k}+m)\not{\epsilon}(\not{p}-\not{k}+m)\not{k}\gamma_5}{[k^2-m_\pi^2][(p+q-k)^2-m^2][(p-k)^2-m^2]}, \tag{B.39}$$

$$\mathcal{M}_{4.1(m)} = \mathrm{i}\frac{e^2 c_{bo} c_{bi} c_{DF}^2}{8F_0^2 p\cdot q}\int \frac{\mathrm{d}^d k}{(2\pi)^d}\frac{\not{k}\gamma_5(\not{p}-\not{k}+m)\not{\epsilon}^*(\not{p}+\not{q}-\not{k}+m)\not{k}\gamma_5(\not{p}+\not{q}+m_1)\not{\epsilon}}{[k^2-m_\pi^2][(p+q-k)^2-m^2][(p-k)^2-m^2]}, \tag{B.40}$$

$$\mathcal{M}_{4.1(n)} = \mathrm{i}\frac{e^2 c_{bo} c_{bi} c_{DF}^2}{8F_0^2 p\cdot q}\int \frac{\mathrm{d}^d k}{(2\pi)^d}\frac{\not\epsilon^*(\not p+\not q+m_1)\not k\gamma_5(\not p+\not q-\not k+m)\not\epsilon(\not p-\not k+m)\not k\gamma_5}{[k^2-m_\pi^2][(p+q-k)^2-m^2][(p-k)^2-m^2]}, \tag{B.41}$$

$$\mathcal{M}_{4.1(o)} = \mathrm{i}\frac{e^2 c_{bi}^2 c_{DF}^2}{4F_0^2}\int \frac{\mathrm{d}^d k}{(2\pi)^d}\frac{\not k\gamma_5(\not p-\not k+m)\not\epsilon^*}{[k^2-m_\pi^2][(p-k)^2-m^2]} \times \frac{(\not p+\not q-\not k+m)\not\epsilon(\not p-\not k+m)\not k\gamma_5}{[(p+q-k)^2-m^2][(p-k)^2-m^2]}, \tag{B.42}$$

$$\mathcal{M}_{4.1(p)} = -\,\mathrm{i}\frac{e^2 c_m c_{bi} c_{DF}^2}{2F_0^2}\int \frac{\mathrm{d}^d k}{(2\pi)^d}\frac{k\cdot\epsilon^*(\not k-\not q)\gamma_5}{[k^2-m_\pi^2][(k-q)^2-m_\pi^2]} \times \frac{(\not p+\not q-\not k+m)\not\epsilon(\not p-\not k+m)\not k\gamma_5}{[(p-k)^2-m^2][(p+q-k)^2-m^2]}. \tag{B.43}$$

For the diagrams of Fig. 4.2, I use the definition introduced in Eq. (2.41). Furthermore, apart from the masses m_1 and m and the constants c_m, c_{bo} and c_{bi} introduced before, I define Is_m and Is_p as the coupling constants of the vertices of the decuplet-to-octet baryon transition via a coupling to a meson or to a photon, respectively. Their values are summarized in Tables B.3 to B.5.

$$\mathcal{M}_{4.2(a)} = \frac{9e^2 g_M^2 \mathrm{Is}_p^2}{4m_1^2(m_1+M_\Delta)^2(m_1^2+2p\cdot q-M_\Delta)^2} \times (p_\mu+q_\mu)q_\alpha\epsilon^*_\beta\varepsilon^{\mu\nu\alpha\beta}S_\Delta^{\nu\nu'}(p+q)(p_{\mu'}+q_{\mu'})q_{\alpha'}\epsilon_{\beta'}\varepsilon^{\mu'\nu'\alpha'\beta'}, \tag{B.44}$$

$$\mathcal{M}_{4.2(b)} = -\,\mathrm{i}\frac{e^2 h_A^2 c_m^2 \mathrm{Is}_m^2}{4F_0^2 M_\Delta^2}\int \frac{\mathrm{d}^d k}{(2\pi)^d}\Bigg\{\gamma^{\mu\nu\lambda}\epsilon^*_\lambda(p+q-k)_\mu \times \frac{S_\Delta^{\nu\nu'}(p+q-k)}{k^2-m_\pi^2}\gamma^{\mu'\nu'\lambda'}\epsilon_{\lambda'}(p+q-k)_{\mu'}\Bigg\}, \tag{B.45}$$

$$\mathcal{M}_{4.2(c)} = -\,\mathrm{i}\frac{e^2 h_A^2 \mathrm{Is}_m^2 c_{bo}^2}{16F_0^2 M_\Delta^2 (p\cdot q)^2}\int \frac{\mathrm{d}^d k}{(2\pi)^d}\Bigg\{\not\epsilon^*(\not p+\not q)(p+q-k)_\mu k_\lambda\gamma^{\mu\nu\lambda} \times \frac{S_\Delta^{\nu\nu'}(p+q-k)}{k^2-m_\pi^2}(p+q-k)_{\mu'}k_{\lambda'}\gamma^{\mu'\nu'\lambda'}(\not p+\not q)\not\epsilon\Bigg\}, \tag{B.46}$$

	p	n	Σ^+	Σ^0	Σ^-	Λ	Ξ^0	Ξ^-
Δ^{++}	-1	0	1	0	0	0	0	0
Δ^+	$\sqrt{\frac{2}{3}}$	$-\frac{\sqrt{3}}{3}$	$\frac{\sqrt{3}}{3}$	$-\sqrt{\frac{2}{3}}$	0	0	0	0
Δ^0	$\frac{\sqrt{3}}{3}$	$\sqrt{\frac{2}{3}}$	0	$-\sqrt{\frac{2}{3}}$	$-\frac{\sqrt{3}}{3}$	0	0	0
Δ^-	0	1	0	0	-1	0	0	0
Σ^{*+}	$-\frac{\sqrt{3}}{3}$	0	$-\frac{\sqrt{6}}{6}$	$\frac{\sqrt{6}}{6}$	0	$\frac{\sqrt{2}}{2}$	$\frac{\sqrt{3}}{3}$	0
Σ^{*0}	$\frac{\sqrt{6}}{6}$	$-\frac{\sqrt{6}}{6}$	$-\frac{\sqrt{6}}{6}$	0	$\frac{\sqrt{6}}{6}$	$-\frac{\sqrt{2}}{2}$	$\frac{\sqrt{6}}{6}$	$-\frac{\sqrt{6}}{6}$
Σ^{*-}	0	$\frac{\sqrt{3}}{3}$	0	$\frac{\sqrt{6}}{6}$	$-\frac{\sqrt{6}}{6}$	$-\frac{\sqrt{2}}{2}$	0	$-\frac{\sqrt{3}}{3}$
Ξ^{*0}	0	0	$-\frac{\sqrt{3}}{3}$	$\frac{\sqrt{6}}{6}$	0	$\frac{\sqrt{2}}{2}$	$-\frac{\sqrt{6}}{6}$	$\frac{\sqrt{3}}{3}$
Ξ^{*-}	0	0	0	$\frac{\sqrt{6}}{6}$	$\frac{\sqrt{3}}{3}$	$-\frac{\sqrt{2}}{2}$	$-\frac{\sqrt{3}}{3}$	$-\frac{\sqrt{6}}{6}$
Ω^-	0	0	0	0	0	0	-1	1

Table B.3.: Values of the isospin constant Is_m for the different channels of the decuplet-to-octet baryon transition via a pion or a kaon.

Δ^{++}	Δ^+	Δ^0	Δ^-	Σ^{*+}	Σ^{*0}	Σ^{*-}	Ξ^{*0}	Ξ^{*-}	Ω
0	0	0	0	$-\frac{\sqrt{2}}{2}$	$\frac{\sqrt{2}}{2}$	$\frac{\sqrt{2}}{2}$	$-\frac{\sqrt{2}}{2}$	$\frac{\sqrt{2}}{2}$	0

Table B.4.: Values of the isospin constant Is_m for the decuplet-to-octet baryon transition via an η meson.

Δ^{++}	Δ^{+}	Δ^{0}	Δ^{-}	Σ^{*+}	$\Sigma^{*0}_{\to\Sigma^0}$	$\Sigma^{*0}_{\to\Lambda}$	Σ^{*-}	Ξ^{*0}	Ξ^{*-}	Ω
0	$\sqrt{\frac{2}{3}}$	$\sqrt{\frac{2}{3}}$	0	$-\sqrt{\frac{2}{3}}$	$\frac{\sqrt{6}}{6}$	$-\frac{\sqrt{2}}{2}$	0	$-\sqrt{\frac{2}{3}}$	0	0

Table B.5.: Values of the isospin constant Is_p for the decuplet-to-octet baryon electromagnetic transition. The Σ^{*0} can decay into either a Σ^0 or a Λ.

$$\mathcal{M}_{4.2(d)} = \mathrm{i}\frac{e^2 h_A^2 \mathrm{Is}_m^2 c_{bo} c_m}{8F_0^2 M_\Delta^2 p\cdot q}\int\frac{\mathrm{d}^d k}{(2\pi)^d}\Bigg\{\gamma^{\mu\nu\lambda}\epsilon^*_\lambda (p+q-k)_\mu$$

$$\times\frac{S_\Delta^{\nu\nu'}(p+q-k)}{k^2-m_\pi^2}(p+q-k)_{\mu'}k_{\lambda'}\gamma^{\mu'\nu'\lambda'}(\not{p}+\not{q})\not{\epsilon}\Bigg\}, \tag{B.47}$$

$$\mathcal{M}_{4.2(e)} = \mathrm{i}\frac{e^2 h_A^2 \mathrm{Is}_m^2 c_{bo} c_m}{8F_0^2 M_\Delta^2 p\cdot q}\int\frac{\mathrm{d}^d k}{(2\pi)^d}\Bigg\{\not{\epsilon}^*(\not{p}+\not{q})(p+q-k)_\mu k_\lambda\gamma^{\mu\nu\lambda}$$

$$\times\frac{S_\Delta^{\nu\nu'}(p+q-k)}{k^2-m_\pi^2}\gamma^{\mu'\nu'\lambda'}\epsilon_{\lambda'}(p+q-k)_{\mu'}\Bigg\}, \tag{B.48}$$

$$\mathcal{M}_{4.2(f)} = -\,\mathrm{i}\frac{e^2 h_A^2 \mathrm{Is}_m^2 c_m c_{bo}}{4F_0^2 M_\Delta^2 p\cdot q}\int\frac{\mathrm{d}^d k}{(2\pi)^d}\Bigg\{(p-k)_\mu k_\lambda\gamma^{\mu\nu\lambda}$$

$$\times\frac{k\cdot\epsilon^* S_\Delta^{\nu\nu'}(p-k)}{[k^2-m_\pi^2][(k+q)^2-m_\pi^2]}(p-k)_{\mu'}(k+q)_{\lambda'}\gamma^{\mu'\nu'\lambda'}(\not{p}+\not{q})\not{\epsilon}\Bigg\}, \tag{B.49}$$

$$\mathcal{M}_{4.2(g)} = -\,\mathrm{i}\frac{e^2 h_A^2 \mathrm{Is}_m^2 c_m c_{bo}}{4F_0^2 M_\Delta^2 p\cdot q}\int\frac{\mathrm{d}^d k}{(2\pi)^d}\Bigg\{\not{\epsilon}^*(\not{p}+\not{q})(p-k)_\mu(k+q)_\lambda\gamma^{\mu\nu\lambda}$$

$$\times\frac{k\cdot\epsilon S_\Delta^{\nu\nu'}(p-k)}{[k^2-m_\pi^2][(k+q)^2-m_\pi^2]}(p-k)_{\mu'}k_{\lambda'}\gamma^{\mu'\nu'\lambda'}\Bigg\}, \tag{B.50}$$

$$\mathcal{M}_{4.2(h)} = \mathrm{i}\frac{e^2 h_A^2 \mathrm{Is}_m^2 c_m^2}{2F_0^2 M_\Delta^2}\int\frac{\mathrm{d}^d k}{(2\pi)^d}\Bigg\{(p-k)_\mu k_\lambda\gamma^{\mu\nu\lambda}$$

$$\times \frac{k \cdot \epsilon^* S_\Delta^{\nu\nu'}(p-k)}{[k^2 - m_\pi^2][(k+q)^2 - m_\pi^2]} \gamma^{\mu'\nu'\lambda'} \epsilon_{\lambda'} (p-k)_{\mu'} \Bigg\}, \tag{B.51}$$

$$\mathcal{M}_{4.2(i)} = \mathrm{i} \frac{e^2 h_A^2 \mathrm{Is}_m^2 c_m^2}{2F_0^2 M_\Delta^2} \int \frac{\mathrm{d}^d k}{(2\pi)^d} \Bigg\{ \gamma^{\mu\nu\lambda} \epsilon_\lambda^* (p-k)_\mu$$

$$\times \frac{k \cdot \epsilon S_\Delta^{\nu\nu'}(p-k)}{[k^2 - m_\pi^2][(k+q)^2 - m_\pi^2]} (p-k)_{\mu'} k_{\lambda'} \gamma^{\mu'\nu'\lambda'} \Bigg\}. \tag{B.52}$$

As a test for the correctness of the calculations, I performed the substitutions

$$\omega \leftrightarrow -\omega \quad \text{and} \quad \epsilon^* \leftrightarrow \epsilon, \tag{B.53}$$

and verified that the amplitude of the crossed diagrams is reproduced. To obtain the final numerical results for the forward spin polarizability, the structure constants of the $\not{\epsilon}^* \not{\epsilon}$-terms are expanded up to the order ω^3 with the help of *Mathematica*. The coefficients of $\mathcal{O}(\omega^3)$ are then used to evaluate the integrals. It is interesting to note that in the work of Chapter 4 no diagram has to be renormalized, as at order $p^{7/2}$ no divergences or PCBT enter into the result of γ_0.

APPENDIX **C**

ALGEBRA FOR LOOP CALCULATIONS

In this thesis, I mainly use the Feynman parameterization to simplify the expressions in loop integrals. The idea is that denominators in the integral can be rewritten such that

$$\int \frac{\mathrm{d}^d k}{(2\pi)^d} \frac{1}{A_1 \dots A_n} = \int \frac{\mathrm{d}^d k}{(2\pi)^d} \int_0^1 \mathrm{d}f_1 \cdots \int_0^1 \mathrm{d}f_n \frac{\delta(1 - f_1 - \cdots - f_n)(n-1)!}{(A_1 f_1 + \cdots + A_n f_n)^n}$$

$$= \int \frac{\mathrm{d}^d k}{(2\pi)^d} \int_0^1 \mathrm{d}f_1 \cdots \int_0^{1-f_1\cdots-f_{n-1}} \mathrm{d}f_n \frac{\delta(1 - f_1 - \cdots - f_n)(n-1)!}{(A_1 f_1 + \cdots + A_n f_n)^n}, \tag{C.1}$$

where d is the dimension in Minkowski space, f_i are the Feynman parameters, and A_i are functions of k_μ and the momenta of the external particles. The last step is valid because of the δ-function. The first integration is then easily performed by just substituting one of the Feynman parameters — whichever most convenient — with the help of the δ-function, leading to an expression such as

$$\int \frac{\mathrm{d}^d k}{(2\pi)^d} \int_0^1 \mathrm{d}f_1 \cdots \int_0^{1-f_1\cdots-f_{n-2}} \mathrm{d}f_{n-1} \frac{(n-1)!}{[A_1 f_1 + \cdots + A_n(1 - f_1 - \cdots - f_{n-1})]^n}. \tag{C.2}$$

Next, one wishes to further reduce this expression, so that the integral takes the simple form

$$\int \frac{\mathrm{d}^d l}{(2\pi)^d} \frac{1}{(l^2 - \Delta)^n}, \tag{C.3}$$

which is then easily solved by the known dimensional regularization. This is done by completing the square in the denominator: the integration variable k_μ is shifted to l_μ such that the terms linear in k_μ vanish, leaving only a term proportional to l^2, and a number of terms independent of l_μ.

Once reduced to this type of expressions, dimensional regularization gives (refer to, e.g., Ref. [190]):

$$\int \frac{\mathrm{d}^d z}{(2\pi)^d} \frac{1}{(z^2-\Delta)^n} = \frac{(-1)^n \mathrm{i}}{(4\pi)^{d/2}} \frac{\Gamma\left(n-\frac{d}{2}\right)}{\Gamma(n)\Delta^{n-\frac{d}{2}}},$$

$$\int \frac{\mathrm{d}^d z}{(2\pi)^d} \frac{z^\mu z^\nu}{(z^2-\Delta)^n} = \frac{(-1)^{n-1} \mathrm{i}}{(4\pi)^{d/2}} \frac{\Gamma\left(n-\frac{d}{2}-1\right)}{\Gamma(n)\Delta^{n-\frac{d}{2}-1}} \frac{g^{\mu\nu}}{2},$$

$$\int \frac{\mathrm{d}^d z}{(2\pi)^d} \frac{z^\mu z^\nu z^\rho z^\sigma}{(z^2-\Delta)^n} = \frac{(-1)^n \mathrm{i}}{(4\pi)^{d/2}} \frac{\Gamma\left(n-\frac{d}{2}-2\right)}{\Gamma(n)\Delta^{n-\frac{d}{2}-2}} \frac{g^{\mu\nu}g^{\rho\sigma}+g^{\mu\rho}g^{\nu\sigma}+g^{\mu\sigma}g^{\nu\rho}}{4},$$

$$\int \frac{\mathrm{d}^d z}{(2\pi)^d} \frac{z^\mu z^\nu z^\rho z^\sigma z^\alpha z^\beta}{(z^2-\Delta)^n} = \frac{(-1)^{n-1} \mathrm{i}}{(4\pi)^{d/2}} \frac{\Gamma\left(n-\frac{d}{2}-3\right)}{\Gamma(n)\Delta^{n-\frac{d}{2}-3}} \times$$

$$\times \frac{1}{8}\Big[(g^{\mu\nu}g^{\rho\sigma}+g^{\mu\rho}g^{\nu\sigma}+g^{\mu\sigma}g^{\nu\rho})g^{\alpha\beta}+(g^{\beta\nu}g^{\rho\sigma}+g^{\beta\rho}g^{\nu\sigma}+g^{\beta\sigma}g^{\nu\rho})g^{\alpha\mu}$$

$$+(g^{\mu\beta}g^{\rho\sigma}+g^{\mu\rho}g^{\beta\sigma}+g^{\mu\sigma}g^{\beta\rho})g^{\alpha\nu}+(g^{\mu\nu}g^{\beta\sigma}+g^{\mu\beta}g^{\nu\sigma}+g^{\mu\sigma}g^{\nu\beta})g^{\alpha\rho}$$

$$+(g^{\mu\nu}g^{\rho\beta}+g^{\mu\rho}g^{\nu\beta}+g^{\mu\beta}g^{\nu\rho})g^{\alpha\sigma}\Big]. \tag{C.4}$$

To simplify the expressions that appear throughout this thesis, I use the definitions:

$$\lambda_0(\Delta) = \frac{\Gamma\left(-\frac{d}{2}\right)}{(4\pi)^{d/2}\Delta^{-\frac{d}{2}}} = \frac{\Delta^2}{32\pi^2}\left(\frac{2}{\epsilon} - \log\left(\frac{\Delta}{M_{\mathrm{Sc}}}\right) + \log(4\pi) - \gamma_E + \frac{3}{2} + \mathcal{O}(\epsilon)\right),$$

$$\lambda_1(\Delta) = \frac{\Gamma\left(1-\frac{d}{2}\right)}{(4\pi)^{d/2}\Delta^{1-\frac{d}{2}}} = -\frac{\Delta}{16\pi^2}\left(\frac{2}{\epsilon} - \log\left(\frac{\Delta}{M_{\mathrm{Sc}}}\right) + \log(4\pi) - \gamma_E + 1 + \mathcal{O}(\epsilon)\right),$$

$$\lambda_2(\Delta) = \frac{\Gamma\left(2-\frac{d}{2}\right)}{(4\pi)^{d/2}\Delta^{2-\frac{d}{2}}} = \frac{1}{16\pi^2}\left(\frac{2}{\epsilon} - \log\left(\frac{\Delta}{M_{\mathrm{Sc}}}\right) + \log(4\pi) - \gamma_E + \mathcal{O}(\epsilon)\right),$$

$$\lambda_3(\Delta) = \frac{\Gamma\left(3-\frac{d}{2}\right)}{(4\pi)^{d/2}\Delta^{3-\frac{d}{2}}} = \frac{1}{16\pi^2\Delta},$$

$$\lambda_4(\Delta) = \frac{\Gamma\left(4-\frac{d}{2}\right)}{(4\pi)^{d/2}\Delta^{4-\frac{d}{2}}} = \frac{1}{16\pi^2\Delta^2}, \tag{C.5}$$

where $\epsilon = 4 - d$ and M_{Sc} is the scale parameter, which in this work is set to the light-baryon mass. Furthermore, $\gamma_E = -\Gamma'(1)$ is the Euler-Mascheroni constant. I use two different minimal subtraction (MS) schemes, where terms proportional to

$$\frac{2}{\epsilon} + \log(4\pi) - \gamma_E + 1 \tag{C.6}$$

are subtracted in the case of the $\widetilde{\mathrm{MS}}$ prescription (Chapter 3), and for the case of $\overline{\mathrm{MS}}$ (Chapters 5 and 6) terms proportional to

$$\frac{2}{\epsilon} + \log(4\pi) - \gamma_E. \tag{C.7}$$

As mentioned before, in Chapter 4 no renormalization is needed for the extraction of the polarizability γ_0.

Special care has to be taken for amplitude terms which are proportional to the dimension $d = 4 - \epsilon$, which arise, e.g., from expressions as $g^{\mu\nu}\gamma_\mu\gamma_\nu = d$. The ϵ piece of these expressions cancels the divergence hidden in $\frac{2}{\epsilon}$, therefore leading to the appearance of additional finite terms which are not absorbed into the renormalization. Were one to set $d = 4$ from the very beginning, they would have erroneously disappeared.

Another thing that needs to be considered is the arisal of PCBT when computing loops that include internal baryon lines. A diagram of nominal order D might after integration contain terms of order $n < D$. These terms spoil the convergence of the chiral series, and therefore must be identified and renormalized. This is done in the EOMS scheme where, together with the divergences, these analytical expressions are also absorbed into the LECs of the lower-order Lagrangians. The identification of these terms is best done by expanding the result as a series in small external momenta and masses, and then isolating the terms of order $n < D$. As rather large expressions have to be dealt with, we opted to use *Mathematica* to perform this expansion, as explained in Appendix D.

APPENDIX **D**

COMPUTATIONAL TOOLS

Here I give a brief overview over the algebraic and numerical computational tools I used throughout this thesis. Note that many of them can deal with the same kinds of problems, the main difference lying in the speed of computation. By using several packages in parallel, I could on the one hand combine their individual strengths, and also cross check many results.

D.1 FORM

This programme is a very powerful algebraic tool for the amplitude calculations [76, 77]. A good tutorial and manual are given in Refs. [191, 192].

While the tree diagrams and some loop diagrams are simple to calculate with pen and paper, there is an explosion of terms when moving to diagrams with more than two propagators, or with propagators of more complicated structure, as is the case of the RS type spin-3/2 baryons. Therefore the results become prone to small mistakes, and it is useful and necessary to confront them with those obtained by means of computational tools.

Before moving to numerics, one is interested in the analytical structure of the results. The programme FORM avoids any "blackbox" problems, as every single definition is given by the user: one defines which quantities are scalars, vectors, tensors (commutable or non-commutable), or indices. Furthermore, the programme does not a priori know which rules apply to each of them, but the user also defines the commutation rules for the γ^μ, γ_5 matrices by hand, and explicitly states for which vectors the Dirac equations apply, and how.

When writing the loop diagrams with the help of the Feynman parameters, see Appendix C, one performs a shift in the integration variable in order to simplify the loop denominator, and to enable solving it by means of a simple dimensional regularization. This of course leads to a shift in the numerator

as well, which one can also implement in FORM. Finally, after applying the Dirac equation where possible, and performing the substitution of the integration variable by the structures of the dimensional regularization, the amplitude appears in terms of the structures needed, e.g., form factors. These one can then easily write in a format readable by other programmes, such as *Mathematica* [193], to then do the explicit numerical calculation.

D.2 Mathematica

Mathematica [193] is very useful if one wants to test first results fast, and also to quickly change parameters to be plotted. It is very visual and its capabilities have become ever more expansive over the years. The numerical integration usually converges well, also due to the existence of different routine options, and it is ideal to test the results for single parameter points. Unfortunately, when one deals with many data points or when one wants to plot over a range of energies or angles, then the computation turns out to be rather slow and other numerical tools should be used. But in any case it is very useful for a base of comparison, and also to easily visualize and handle analytic expressions.

Furthermore, this programme has the subprogrammes FeynCalc [78, 79] and LoopTools [194] implemented and very well tested.

D.2.1 FeynCalc and LoopTools

With FeynCalc [78, 79], one can perform the analytical calculation and reduction of amplitudes (especially useful for loop diagrams), as also done by FORM. Naturally the difference is that it is a blackbox, and therefore sometimes troubleshooting is complicated. Instead of the Feynman parameters, FeynCalc relies on the Pasarino-Veltman reduction. This yields analytical results even where the Feynman parameterization only allows for numerical integrations.

One has to take special care when using FeynCalc on structures with RS propagators, because the OneLoop routine that works perfectly for spin-1/2 particles as of version 9.0 shows some problems in that sector. But many of these issues have been resolved by the somewhat newer routine TID, therefore now allowing to work even with these more complicated structures. Note that FeynCalc is much slower than FORM.

FeynCalc gives out Passarino-Veltman structures which then have to be evaluated with another tool. I use the Mathematica package LoopTools [194]. The user chooses the scale of the dimensional regularization and the preferred prescription for the MS renormalization: in this thesis they are the baryon mass and the $\overline{MS}$ or $\widetilde{MS}$ schemes, respectively. The tool then calculates the corresponding value obtained from the analytical expressions given as input.

D.2.2 Determining the PCBT

As explained in Appendix C, when calculating loop diagrams with internal baryon loops, power-counting breaking terms might arise and have to be renormalized. In order to compute the series around small parameters p_i, the simplest approach is to set them proportional to a small scale ν:

$$p_i = \alpha_i \, \nu. \tag{D.1}$$

Then, one can expand the result in a series around ν up to ν^{n-1}, where n is the nominal order of the diagram. These are the terms that break the power counting, and that therefore have to be renormalized. After subtracting them, i.e., absorbing them into a redefinition of the LECs, one can set the small parameteres back to their original form:

$$\alpha_i = \frac{p_i}{\nu}. \tag{D.2}$$

D.3 Numerics

Minuit [195] is a programme distributed by CERN that searches for minima (with different minimization-routine options) in a function. In this work, the functions I minimize are those giving the χ^2 value between data points and the theoretical functions to describe them. Usually the minimization is non-trivial, as it depends on multiple parameters which can easily have several local minima. For the numerical evaluation of the models I used fortran, C++ and Python.

LIST OF FIGURES

3.1 Total cross sections for the two channels of pion photoproduction off proton targets. Data from Refs. [59, 60]. 18

3.2 Generic representation of the pion photoproduction process. The incoming photon and proton momenta are given by k and p, while those of the outgoing neutral pion and proton are denoted by q and p', respectively. 21

3.3 Tree diagrams for the π^0 photoproduction off protons. The crossed terms are also included in the calculation. The black dots represent vertices of chiral order p^1 to p^3. Diagram b) starts at $\mathcal{O}(p^3)$. 24

3.4 Δ tree diagram for the π^0 photoproduction off protons. The crossed term is also included in the calculation. 25

3.5 Loop diagrams for the π^0 photoproduction off protons including only the nucleonic intermediate states. The crossed terms are also calculated. 25

3.6 Loop diagrams for the π^0 photoproduction off protons for the Δ intermediate states. The crossed terms are also calculated. . . 26

3.7 Diagrams contributing to the proton self-energy with nucleon (a) and Δ (b) loop contributions. 29

3.8 Convergence of the chiral models at different photon energies in the laboratory frame. In the left panel, I show my calculation for three models: including only nucleon tree-level diagrams (red squares), adding the nucleonic loop contributions (blue circles), and finally the full model with the $\Delta(1232)$ resonance (green triangles). In the right panel, I compare the full model of this thesis (green triangles) with the relativistic IR (open circles) and HBChPT (filled circles) models from Ref. [57]. 36
3.9 Differential cross section as a function of the pion angle at different energies. The solid line corresponds to the best-fit theoretical model at $\mathcal{O}(p^{7/2})$. The experimental points are from Refs. [55, 83]. 39
3.10 Photon asymmetry as a function of the pion angle at different energies. The solid line corresponds to the best-fit theoretical model at $\mathcal{O}(p^{7/2})$. The experimental points are from Refs. [55, 83]. 40
3.11 Photon asymmetry and differential cross section as a function of the pion angle at two different photon energies: close to the threshold and at above 200 MeV in the laboratory frame. The solid, dashed, dash-dotted and dotted lines correspond to the full model, the full model without the Δ, the full model without the nucleon contributions and the best nucleonic fit without the Δ, respectively. The experimental points are from Refs. [55, 83]. 41
3.12 Real part of s-wave and p-wave multipoles from Ref. [55] — see also Ref. [56] — vs. our full-model calculation, as a function of the photon energy. The error bars are only statistical errors. The gray band above the energy axis shows the systematic error of the data [55]. 42
3.13 Imaginary part of the multipole E_0^+ from Ref. [84] vs. our full-model calculation, as a function of the photon energy. The error bars are only statistical errors. The gray band above the energy axis shows the systematic error of the data. 43

4.1 Diagrams contributing to γ_0 with spin-1/2 intermediate states. The crossed diagrams are obtained by the substitutions $\omega \leftrightarrow -\omega$ and $\not{\epsilon} \leftrightarrow \not{\epsilon}^*$. All the vertices that appear are couplings of the lowest-order Lagrangians. 53
4.2 Diagrams contributing to γ_0 with spin-3/2 intermediate states. The crossed diagrams are obtained by the substitutions $\omega \leftrightarrow -\omega$ and $\not{\epsilon} \leftrightarrow \not{\epsilon}^*$. Except for the tree diagram, which has vertices of a second-order Lagrangian, all the vertices that appear are couplings of the lowest-order Lagrangians. 54

5.1 Loop diagrams contributing to the calculation of the electromagnetic form factors at $\mathcal{O}(p^3)$. 68

5.2 Proton $G_E(Q^2)$ data [161] (red points) compared with the theoretical models: descriptions linear in q^2, with r_E^p from the muonic hydrogen lamb shift (short black dashes) or from the electron-scattering data (long blue dashes), as well as additional q^4 contributions from chiral loops (red thin line) and from the combination of the chiral-loop and vector-meson contributions (broad black line). 82

5.3 Meson-loop contributions to the spectral function $\mathrm{Im}(F_1)$ for the nucleons. The left column is dedicated to the proton, while the neutron results are shown on the right side. The first two rows show the contributions of the octet and decuplet intermediate states, respectively. The blue band corresponds to the π-loop contributions, the green band to the K-loop contributions, and the red one shows their combination. The bands are obtained by varying the values of the constants used between the physical $SU(3)$ average and the chiral limit. The last row shows the combination (red) of octet (blue) and decuplet contributions (green). 83

5.4 Meson-loop contributions to the spectral function $\mathrm{Im}(F_2)$ for the nucleons. The explanation of the figures and colors is as in Fig. 5.3. 84

5.5 Meson-loop contributions to the spectral function $\mathrm{Im}(F_1)$ for all the octet members. The combination (red) of octet (blue) and decuplet (green) contributions is shown. The bands are obtained by varying the values of the constants used between the physical $SU(3)$ average and the chiral limit. 86

5.6 Meson-loop contributions to the spectral function $\mathrm{Im}(F_2)$ for all the octet members. The explanation is as in Fig. 5.5. 87

5.7 Spectral functions of the nucleons, with vector-meson contributions. The left column shows the proton and the neutron is on the right. The upper panels show $\mathrm{Im}(F_1)$ and the lower ones $\mathrm{Im}(F_2)$. The red band shows the total $SU(3)$ chiral-loop contributions, while the orange lines show the vector-meson contributions. 88

5.8 Charge densities ρ_1 for all the octet members as functions of the transverse distance b. The combination (red) of chiral-loop (blue) and vector-meson (green) contributions is shown. The bands are obtained by varying the values of the constants used between the physical $SU(3)$ average and the chiral limit, in combination with varying the cut of the upper limit in the dispersive integral. 90
5.9 Magnetic densities $\tilde{\rho}_2$ for all the octet members as functions of the transverse distance b. The explanation is as in Fig. 5.8. . . . 91

6.1 Loops that can contribute to the CP-violating coupling of $\eta^{(\prime)}$ to the nucleon. The single solid lines stand for nucleons, the double lines for the Δ, the dashes for pions and the dotted lines for the $\eta^{(\prime)}$. The black box at the $\eta^{(\prime)}\pi\pi$ vertex indicates the CP violation. 101
6.2 Considered loops that can contribute to the neutron EDM. The solid line represents the neutron, the dotted line the $\eta^{(\prime)}$, the dashed lines are vector-meson contributions and the wavy line corresponds to the photon. The black box stands for a CP-violating vertex. 107

LIST OF TABLES

3.1 LEC values for the $\mathcal{O}(p^3)$ calculation. The fixed value is in boldface. 33

3.2 LEC values in the different versions of the $\mathcal{O}(p^{7/2})$ model. Fixed values appear in boldface. Note that in the fit g_0 is constrained to values between 1.05 and 1.08. 35

4.1 Numerical values for the hadron masses and decay constants used in the γ_0 calculations. The values are given in units of MeV. The physical-choice values for $SU(2)$ were taken as in Ref. [119], whereas for the chiral limit and for $SU(3)$ I followed Ref. [19]. 55

4.2 Numerical values for the unitless LECs used in the γ_0 calculations. The physical-choice values for $SU(2)$ were taken as in Ref. [119] — notice the difference by a factor 2 in the definition of h_A —, whereas for the chiral limit and for $SU(3)$ Ref. [19] was followed. The value for the coupling g_M is calculated through Eq. (4.8). 56

4.3 Numerical values for γ_0 obtained in the $SU(2)$ sector in this and in other works, in units of 10^{-4} fm^4. The choice of the numerical values for the constants in the present work can be found in Tables 4.1 and 4.2. The error in the results when including the $\Delta(1232)$ resonance arises from the uncertainty in the value of the low-energy constant g_M. 57

4.4 Decomposition of the proton and neutron polarizability results, in units of 10^{-4} fm^4, into the contributions coming from the different sets of diagrams, when using the chiral limit for the masses and low-energy constants. The difference in results when using physical values or the chiral limit can be seen as a systematical uncertainty. 58

4.5 Numerical values for γ_0 obtained in the present calculations, in units of 10^{-4} fm^4 in the $SU(3)$ sector. The choice of the numerical values for the constants in the covariant case can be found in Tables 4.1 and 4.2, both for the chiral limit and for the physical-average case. As for the HBChPT limit, I cite the results in Ref. [121], which were later corrected in our work in Ref. [122]. The errors in the results with the decuplet arise from the uncertainty in the value of the low-energy constant g_M. . . . 59

5.1 Values of the isospin constant Is_{mm} for the coupling of two pions to an octet baryon. 69

5.2 Values of the isospin constant Is_{mm} for the coupling of two kaons to an octet baryon. 69

5.3 Masses of the vector mesons and their electromagnetic decay widths into e^+e^- pairs. 73

5.4 Numerical values for the nucleon $\frac{\mathrm{d}^2}{(\mathrm{d}q^2)^2}G_E(q^2)|_{q^2=0}$ in units of GeV^{-4}, in an $SU(2)$ framework. The contributions coming from the diagrams with nucleon intermediate states, Figs. 5.1(a), 5.1(b), 5.1(d), 5.1(e), 5.1(g) and 5.1(h), and those with spin-3/2 intermediate states, Figs. 5.1(c), 5.1(f), 5.1(i) and 5.1(j), are shown separately. Furthermore, the contributions of the vector mesons ω, ρ and ϕ are listed. The values are shown both when taking the chiral limit of masses and LECs, and when taking the physical-average values of $SU(2)$. 78

5.5 Numerical values for the octet-baryon $\frac{\mathrm{d}^2}{(\mathrm{d}q^2)^2}G_E|_{q^2=0}$ in units of GeV^{-4}, in an $SU(3)$ framework. The values are shown both when taking the chiral limit of masses and LECs, and when taking the physical-average values of $SU(3)$. The further explanations are as in Table 5.4. 80

6.1 Parameters for the Lagrangians that involve vector mesons. . . . 106

6.2 Contributions to the upper limit of the neutron EDM from the current experimental upper limits of the η and η' branching ratios into two pions. The units are e cm. 110

B.1 Values of the isospin constant c_{DF} for the different channels of the octet-baryon-to-octet-baryon transition via a pion or a kaon. 149
B.2 Values of the isospin constant c_{DF} for the coupling of an η meson to an octet baryon. 150
B.3 Values of the isospin constant Is_m for the different channels of the decuplet-to-octet baryon transition via a pion or a kaon. . . 152
B.4 Values of the isospin constant Is_m for the decuplet-to-octet baryon transition via an η meson. 152
B.5 Values of the isospin constant Is_p for the decuplet-to-octet baryon electromagnetic transition. The Σ^{*0} can decay into either a Σ^0 or a Λ. 153

GLOSSARY

BC Burkhardt–Cottingham 48

CGLM Chew–Goldberger–Low–Nambu 21, 23

ChPT Chiral Perturbation Theory 1–7, 13, 16, 19, 20, 24, 44, 45, 49, 51, 52, 58, 60, 61, 65–67, 76, 77, 93, 94, 100, 105, 113–117, 119, 122–131, 133, 134

CL confidence level 98

EDM electric dipole moment 4, 16, 63, 98, 99, 106, 108, 110, 111, 114, 117–119, 126, 127, 131–134, 168

EFT effective field theory 2, 3, 5, 16, 49, 94, 123, 126

EOMS Extended On Mass Shell 4, 13, 17, 19, 27, 29, 31, 32, 44, 69, 93, 102, 113, 117, 124–127, 131, 133, 140, 157

GDH Gerasimov–Drell–Hearn 48

GGT Gell-Mann, Goldberger and Thirring 48, 51

HBChPT heavy-baryon ChPT 3, 16, 17, 19, 35–37, 45, 49, 55–59, 104, 114, 115, 124, 128, 129, 133, 164, 168

IR infrared regularization 4, 36, 124, 133, 164

LEC low-energy constant 3, 4, 6, 8, 9, 11, 12, 17, 19, 20, 27, 29, 30, 32–35, 37, 38, 45, 49, 51, 52, 56, 61, 65, 67, 77–80, 93, 94, 113–116, 118, 123–125, 127–129, 132, 148, 157, 161, 167, 168

LET low-energy theorem 2, 16

MAMI Mainz Microtron 16, 24, 47, 48, 64, 114, 127

MS minimal subtraction 27, 157, 160

PCBT power-counting breaking terms 4, 20, 27, 49, 58, 69, 113, 124, 125, 127, 154, 157, 161

QCD quantum chromodynamics 1–3, 5, 6, 16, 48, 60, 61, 65, 97, 98, 113, 114, 119, 121–123, 127, 134

RCS real Compton scattering 52

RS Rarita–Schwinger 9, 13, 56, 69, 103, 143, 159, 160

SD spin-dependent 47–51, 75

SI spin-independent 47, 50, 54, 75

SM Standard Model 97, 98

SSE small-scale expansion 14, 51, 67, 93, 126

VCS virtual Compton scattering 48

WFR wave-function renormalization 20, 27, 28, 32–35

ACKNOWLEDGEMENTS

First of all, I want to thank my advisor Manuel Vicente Vacas for supporting me during these past three and a half years. Thank you for always applying the exact right amount of pressure and speed, for guiding me when I was stuck, and for sharing your motivation with me. I appreciate it a lot that understanding the physics background and being mathematically precise are always your first priority. And also that you treat your colleagues as your equals, both with regard to physics as well as during the many fun discussions during coffee breaks and meals. I am only happy to obtain a PhD if it does not imply the end of our work together.

This thesis lives from fruitful discussions and projects with collaborators, and therefore I would like to thank José Manuel Alarcón, Daniel Cabrera, César Fernández-Ramírez, Thomas Gutsche, Andrew Jackura, Tim Ledwig, Valery Lyubovitskij, Vincent Mathieu, Ulf Meißner, Viktor Mokeev, Jannes Nys, Alessandro Pilloni, Zhifeng Sun, Adam Szczepaniak, Christian Weiss, and Alexey Zhevlakov.

If there are still typos in this thesis, it is surely not because of the lack of extremely careful reading of some very enduring people. Thus I would like to doubly thank my parents: not only for the inevitable family bond, but also for being patient and helpful partners of physics discussions. Also, I am thankful to Johann Brehmer for the destructively constructive comments on my thesis, and for sharing my non-obsessive love for academia.

Thank you, Moritz, for supporting me in all situations of panic and exagerated happiness without faltering, for understanding the importance of moving away, and even surprising me with an engagement ring.

My stay in Valencia was made possible thanks to the Santiago Grisolía scholarship and the support from the Universidad de Valencia. And the reason why I never felt alone but extremely welcome in this city was that I shared this

phase of life with my friends and colleagues. For all the relaxingly active sleepless nights and sunny days, I thank Francesca Aceti, Miguel Albaladejos, Luis Alvarez Ruso, Melahat Bayar, Vinícius Debastiani, Jorgivan Dias, Pedro Fernández, Paola Ferrario, Javier Garzón, Félix González, José Guzmán, Carlos Hidalgo, Lucia Hosekova, Joel Jones, Marija Kekic, Matthew King, Andrew Laing, Roberto Lineros, Juan Nieves, Eulogio Oset, Eduardo Saúl, Marco Serusi, Toshitaka Uchino, Aaron Vincent, En Wang, and Chuwen Xiao.

Warm thanks to Helen Westwater for the many productive hours she welcomed me in her café, with revigorating juices and an always smiling face.

BIBLIOGRAPHY

[1] E. E. Jenkins and A. V. Manohar. Baryon chiral perturbation theory using a heavy fermion Lagrangian. *Phys. Lett.*, B255:558–562, 1991. doi: 10.1016/0370-2693(91)90266-S.

[2] B. Kubis, T. R. Hemmert, and Ulf-G. Meissner. Baryon form-factors. *Phys.Lett.*, B456:240–247, 1999.

[3] T. Becher and H. Leutwyler. Baryon chiral perturbation theory in manifestly Lorentz invariant form. *Eur. Phys. J.*, C9:643–671, 1999. doi: 10.1007/s100530050518.

[4] H. Leutwyler. Effective field theory of the pion nucleon interaction. *PiN Newslett.*, 15:1, 1999.

[5] P. J. Ellis and H.-B. Tang. Pion nucleon scattering in a new approach to chiral perturbation theory. *Phys.Rev.*, C57:3356–3375, 1998.

[6] J. Gegelia and G. Japaridze. Matching heavy particle approach to relativistic theory. *Phys. Rev.*, D60:114038, 1999. doi: 10.1103/PhysRevD.60.114038.

[7] T. Fuchs, J. Gegelia, G. Japaridze, and S. Scherer. Renormalization of relativistic baryon chiral perturbation theory and power counting. *Phys. Rev.*, D68:056005, 2003. doi: 10.1103/PhysRevD.68.056005.

[8] T. Fuchs, J. Gegelia, and S. Scherer. Electromagnetic form-factors of the nucleon in relativistic baryon chiral perturbation theory. *J. Phys.*, G30:1407–1426, 2004. doi: 10.1088/0954-3899/30/10/008.

[9] B. C. Lehnhart, J. Gegelia, and S. Scherer. Baryon masses and nucleon sigma terms in manifestly Lorentz-invariant baryon chiral perturbation theory. *J. Phys.*, G31:89–104, 2005. doi: 10.1088/0954-3899/31/2/002.

[10] M. R. Schindler, T. Fuchs, J. Gegelia, and S. Scherer. Axial, induced pseudoscalar, and pion-nucleon form-factors in manifestly Lorentz-invariant chiral perturbation theory. *Phys. Rev.*, C75:025202, 2007. doi: 10.1103/PhysRevC.75.025202.

[11] M. R. Schindler, D. Djukanovic, J. Gegelia, and S. Scherer. Chiral expansion of the nucleon mass to order(q**6). *Phys. Lett.*, B649:390–393, 2007. doi: 10.1016/j.physletb.2007.04.034.

[12] L. S. Geng, J. Martin Camalich, L. Alvarez-Ruso, and M. J. Vicente Vacas. Leading SU(3)-breaking corrections to the baryon magnetic moments in Chiral Perturbation Theory. *Phys. Rev. Lett.*, 101:222002, 2008. doi: 10.1103/PhysRevLett.101.222002.

[13] L. S. Geng, J. Martin Camalich, and M. J. Vicente Vacas. SU(3)-breaking corrections to the hyperon vector coupling f(1)(0) in covariant baryon chiral perturbation theory. *Phys. Rev.*, D79:094022, 2009. doi: 10.1103/PhysRevD.79.094022.

[14] J. Martin Camalich, L. S. Geng, and M. J. Vicente Vacas. The lowest-lying baryon masses in covariant SU(3)-flavor chiral perturbation theory. *Phys. Rev.*, D82:074504, 2010. doi: 10.1103/PhysRevD.82.074504.

[15] J. M. Alarcon, J. Martin Camalich, and J. A. Oller. The chiral representation of the πN scattering amplitude and the pion-nucleon sigma term. *Phys. Rev.*, D85:051503, 2012. doi: 10.1103/PhysRevD.85.051503.

[16] T. Ledwig, J. Martin Camalich, V. Pascalutsa, and M. Vanderhaeghen. The Nucleon and $\Delta(1232)$ form factors at low momentum-transfer and small pion masses. *Phys. Rev.*, D85:034013, 2012. doi: 10.1103/PhysRevD.85.034013.

[17] Y.-H. Chen, D.-L. Yao, and H. Q. Zheng. Analyses of pion-nucleon elastic scattering amplitudes up to $O(p^4)$ in extended-on-mass-shell subtraction scheme. *Phys. Rev.*, D87:054019, 2013. doi: 10.1103/PhysRevD.87.054019.

[18] L. Alvarez-Ruso, T. Ledwig, J. Martin Camalich, and M. J. Vicente Vacas. Nucleon mass and pion-nucleon sigma term from a chiral analysis of lattice QCD data. *Phys. Rev.*, D88(5):054507, 2013. doi: 10.1103/PhysRevD.88.054507.

[19] T. Ledwig, J. Martin Camalich, L. S. Geng, and M. J. Vicente Vacas. Octet-baryon axial-vector charges and SU(3)-breaking effects in the semileptonic hyperon decays. *Phys. Rev.*, D90(5):054502, 2014. doi: 10.1103/PhysRevD.90.054502.

[20] V. Lensky, J. M. Alarcon, and V. Pascalutsa. Moments of nucleon structure functions at next-to-leading order in baryon chiral perturbation theory. *Phys. Rev.*, C90(5): 055202, 2014. doi: 10.1103/PhysRevC.90.055202.

[21] S. Weinberg. Dynamical approach to current algebra. *Phys.Rev.Lett.*, 18:188–191, 1967.

[22] R. F. Dashen. Chiral SU(3) x SU(3) as a symmetry of the strong interactions. *Phys.Rev.*, 183:1245–1260, 1969.

[23] J. Gasser and H. Leutwyler. Chiral Perturbation Theory to One Loop. *Annals Phys.*, 158:142, 1984. doi: 10.1016/0003-4916(84)90242-2.

[24] J. Gasser and H. Leutwyler. Chiral Perturbation Theory: Expansions in the Mass of the Strange Quark. *Nucl. Phys.*, B250:465–516, 1985. doi: 10.1016/0550-3213(85) 90492-4.

[25] H. Georgi. Effective field theory. *Ann.Rev.Nucl.Part.Sci.*, 43:209–252, 1993.

[26] H. W. Griesshammer, J. A. McGovern, D.R. Phillips, and G. Feldman. Using effective field theory to analyse low-energy Compton scattering data from protons and light nuclei. *Prog.Part.Nucl.Phys.*, 67:841–897, 2012.

[27] V. Bernard, N. Kaiser, and Ulf-G. Meissner. Chiral dynamics in nucleons and nuclei. *Int. J. Mod. Phys.*, E4:193–346, 1995. doi: 10.1142/S0218301395000092.

[28] S. Scherer. Introduction to chiral perturbation theory. *Adv.Nucl.Phys.*, 27:277, 2003.

[29] V. Pascalutsa, M. Vanderhaeghen, and S.-N. Yang. Electromagnetic excitation of the Delta(1232)-resonance. *Phys. Rept.*, 437:125–232, 2007. doi: 10.1016/j.physrep.2006.09.006.

[30] S. Weinberg. Phenomenological Lagrangians. *Physica*, A96:327–340, 1979. doi: 10.1016/0378-4371(79)90223-1.

[31] H. Georgi. *Weak Interactions and Modern Particle Theory.* 1984.

[32] N. Fettes, Ulf-G. Meissner, M. Mojzis, and S. Steininger. The Chiral effective pion nucleon Lagrangian of order p**4. *Annals Phys.*, 283:273–302, 2000. doi: 10.1006/aphy.2000.6059. [Erratum: Annals Phys.288,249(2001)].

[33] V. Pascalutsa. Quantization of an interacting spin - 3 / 2 field and the Delta isobar. *Phys. Rev.*, D58:096002, 1998. doi: 10.1103/PhysRevD.58.096002.

[34] V. Pascalutsa and R. Timmermans. Field theory of nucleon to higher spin baryon transitions. *Phys. Rev.*, C60:042201, 1999. doi: 10.1103/PhysRevC.60.042201.

[35] V. Pascalutsa. Correspondence of consistent and inconsistent spin - 3/2 couplings via the equivalence theorem. *Phys. Lett.*, B503:85–90, 2001. doi: 10.1016/S0370-2693(01)00140-X.

[36] V. Pascalutsa and M. Vanderhaeghen. Magnetic moment of the Delta(1232)-resonance in chiral effective field theory. *Phys. Rev. Lett.*, 94:102003, 2005. doi: 10.1103/PhysRevLett.94.102003.

[37] V. Pascalutsa and M. Vanderhaeghen. Chiral effective-field theory in the Delta(1232) region: I. Pion electroproduction on the nucleon. *Phys. Rev.*, D73:034003, 2006. doi: 10.1103/PhysRevD.73.034003.

[38] L. S. Geng, J. Martin Camalich, and M. J. Vicente Vacas. Leading-order decuplet contributions to the baryon magnetic moments in Chiral Perturbation Theory. *Phys. Lett.*, B676:63–68, 2009. doi: 10.1016/j.physletb.2009.04.061.

[39] L. S. Geng, J. Martin Camalich, and M. J. Vicente Vacas. Electromagnetic structure of the lowest-lying decuplet resonances in covariant chiral perturbation theory. *Phys. Rev.*, D80:034027, 2009. doi: 10.1103/PhysRevD.80.034027.

[40] J. Gasser, M. E. Sainio, and A. Svarc. Nucleons with Chiral Loops. *Nucl. Phys.*, B307:779–853, 1988. doi: 10.1016/0550-3213(88)90108-3.

[41] V. Lensky and V. Pascalutsa. Predictive powers of chiral perturbation theory in Compton scattering off protons. *Eur. Phys. J.*, C65:195–209, 2010. doi: 10.1140/epjc/s10052-009-1183-z.

[42] T. R. Hemmert, B. R. Holstein, and J. Kambor. Systematic 1/M expansion for spin 3/2 particles in baryon chiral perturbation theory. *Phys. Lett.*, B395:89–95, 1997. doi: 10.1016/S0370-2693(97)00049-X.

[43] T. R. Hemmert, B. R. Holstein, and J. Kambor. Chiral Lagrangians and delta(1232) interactions: Formalism. *J. Phys.*, G24:1831–1859, 1998. doi: 10.1088/0954-3899/24/10/003.

[44] N. M. Kroll and M. A. Ruderman. A theorem on photomeson production near threshold and the suppression of pairs in pseudoscalar meson theory. *Phys. Rev.*, 93:233–238, Jan 1954. doi: 10.1103/PhysRev.93.233. URL `http://link.aps.org/doi/10.1103/PhysRev.93.233`.

[45] P. De Baenst. An improvement on the kroll-ruderman theorem. *Nucl. Phys.*, B24: 633–652, 1970. doi: 10.1016/0550-3213(70)90451-7.

[46] A. I. Vainshtein and V. I. Zakharov. Low-energy theorems for photoproduction and electropion production at threshold. *Nucl. Phys.*, B36:589–604, 1972. doi: 10.1016/0550-3213(72)90238-6.

[47] E. Mazzucato et al. A Precise Measurement of Neutral Pion Photoproduction on the Proton Near Threshold. *Phys. Rev. Lett.*, 57:3144, 1986. doi: 10.1103/PhysRevLett.57.3144.

[48] R. Beck, F. Kalleicher, B. Schoch, J. Vogt, G. Koch, H. Stroher, V. Metag, J. C. McGeorge, J. D. Kellie, and S. J. Hall. Measurement of the p (gamma, pi0) cross-section at threshold. *Phys. Rev. Lett.*, 65:1841–1844, 1990. doi: 10.1103/PhysRevLett.65.1841.

[49] D. Drechsel and L. Tiator. Threshold pion photoproduction on nucleons. *J. Phys.*, G18:449–497, 1992. doi: 10.1088/0954-3899/18/3/004.

[50] V. Bernard and Ulf-G. Meissner. Chiral perturbation theory. *Ann. Rev. Nucl. Part. Sci.*, 57:33–60, 2007. doi: 10.1146/annurev.nucl.56.080805.140449.

[51] V. Bernard, N. Kaiser, J. Gasser, and Ulf-G. Meissner. Neutral pion photoproduction at threshold. *Phys. Lett.*, B268:291–295, 1991. doi: 10.1016/0370-2693(91)90818-B.

[52] V. Bernard, N. Kaiser, and Ulf-G. Meissner. Threshold pion photoproduction in chiral perturbation theory. *Nucl. Phys.*, B383:442–496, 1992. doi: 10.1016/0550-3213(92)90085-P.

[53] E. E. Jenkins and A. V. Manohar. Chiral corrections to the baryon axial currents. *Phys. Lett.*, B259:353–358, 1991. doi: 10.1016/0370-2693(91)90840-M.

[54] V. Bernard, N. Kaiser, and Ulf-G. Meissner. Aspects of near threshold neutral pion photoproduction off protons. *Eur. Phys. J.*, A11:209–216, 2001. doi: 10.1007/s100500170085.

[55] D. Hornidge et al. Accurate Test of Chiral Dynamics in the $\vec{\gamma}p \to \pi^0 p$ Reaction. *Phys. Rev. Lett.*, 111(6):062004, 2013. doi: 10.1103/PhysRevLett.111.062004.

[56] C. Fernandez-Ramirez and A. M. Bernstein. Upper Energy Limit of Heavy Baryon Chiral Perturbation Theory in Neutral Pion Photoproduction. *Phys. Lett.*, B724: 253–258, 2013. doi: 10.1016/j.physletb.2013.06.020.

[57] M. Hilt, S. Scherer, and L. Tiator. Threshold π^0 photoproduction in relativistic chiral perturbation theory. *Phys. Rev.*, C87(4):045204, 2013. doi: 10.1103/PhysRevC.87.045204,10.1103/PhysRevC.87.045204.

[58] M. Hilt, B. C. Lehnhart, S. Scherer, and L. Tiator. Pion photo- and electroproduction in relativistic baryon chiral perturbation theory and the chiral MAID interface. *Phys. Rev.*, C88:055207, 2013. doi: 10.1103/PhysRevC.88.055207.

[59] T. Fujii, T. Kondo, F. Takasaki, S. Yamada, S. Homma, K. Huke, S. Kato, H. Okuno, I. Endo, and H. Fujii. Photoproduction of Charged pi Mesons from Hydrogen and Deuterium in the Energy Range Between 250-MeV and 790-MeV. *Nucl. Phys.*, B120: 395–422, 1977. doi: 10.1016/0550-3213(77)90084-0.

[60] D. Menze, W. Pfeil, and R. Wilcke. Compilation of Pion Photoproduction Data. *Karlsruhe Zaed - PHYSICS DATA*, 7-1:306, 1977.

[61] A. N. Hiller Blin, T. Gutsche, T. Ledwig, and V. E. Lyubovitskij. Hyperon forward spin polarizability γ_0 in baryon chiral perturbation theory. *Phys. Rev.*, D92(9):096004, 2015. doi: 10.1103/PhysRevD.92.096004.

[62] J. M. Alarcon, J. Martin Camalich, and J. A. Oller. Improved description of the πN-scattering phenomenology in covariant baryon chiral perturbation theory. *Annals Phys.*, 336:413–461, 2013. doi: 10.1016/j.aop.2013.06.001.

[63] V. Pascalutsa and J. A. Tjon. Pion photoproduction on nucleons in a covariant hadron-exchange model. *Phys. Rev.*, C70:035209, 2004. doi: 10.1103/PhysRevC.70.035209.

[64] C. Fernandez-Ramirez, E. Moya de Guerra, and J. M. Udias. Effective Lagrangian approach to pion photoproduction from the nucleon. *Annals Phys.*, 321:1408–1456, 2006. doi: 10.1016/j.aop.2006.02.009.

[65] A. N. Hiller Blin, T. Ledwig, and M. J. Vicente Vacas. Chiral dynamics in the $\vec{\gamma}p \to p\pi^0$ reaction. *Phys. Lett.*, B747:217–222, 2015. doi: 10.1016/j.physletb.2015.05.067.

[66] A. N. Hiller Blin, T. Ledwig, and M. J. Vicente Vacas. $\Delta(1232)$ resonance in the $\vec{\gamma}p \to p\pi^0$ reaction at threshold. *Phys. Rev.*, D93(9):094018, 2016. doi: 10.1103/PhysRevD.93.094018.

[67] L. W. Cawthorne and J. A. McGovern. Impact of the Delta (1232) resonance on neutral pion photoproduction in chiral perturbation theory. *PoS*, CD15:072, 2016.

[68] D. Drechsel, S. S. Kamalov, and L. Tiator. Unitary Isobar Model - MAID2007. *Eur. Phys. J.*, A34:69–97, 2007. doi: 10.1140/epja/i2007-10490-6.

[69] A. Gasparyan and M. F. M. Lutz. Photon- and pion-nucleon interactions in a unitary and causal effective field theory based on the chiral Lagrangian. *Nucl. Phys.*, A848: 126–182, 2010. doi: 10.1016/j.nuclphysa.2010.08.006.

[70] R. L. Workman, W. J. Briscoe, M. W. Paris, and I. I. Strakovsky. Updated SAID analysis of pion photoproduction data. *Phys. Rev.*, C85:025201, 2012. doi: 10.1103/PhysRevC.85.025201.

[71] A. V. Anisovich, R. Beck, E. Klempt, V. A. Nikonov, A. V. Sarantsev, and U. Thoma. Pion- and photo-induced transition amplitudes to ΛK, ΣK, and $N\eta$. *Eur. Phys. J.*, A48:88, 2012. doi: 10.1140/epja/i2012-12088-3.

[72] H. Kamano, S. X. Nakamura, T. S. H. Lee, and T. Sato. Nucleon resonances within a dynamical coupled-channels model of πN and γN reactions. *Phys. Rev.*, C88(3): 035209, 2013. doi: 10.1103/PhysRevC.88.035209.

[73] V. Mathieu, G. Fox, and A. P. Szczepaniak. Neutral Pion Photoproduction in a Regge Model. *Phys. Rev.*, D92(7):074013, 2015. doi: 10.1103/PhysRevD.92.074013.

[74] P. Dennery. Theory of the Electro- and Photoproduction of pi Mesons. *Phys. Rev.*, 124:2000–2010, 1961. doi: 10.1103/PhysRev.124.2000.

[75] G. F. Chew, M. L. Goldberger, F. E. Low, and Y. Nambu. Relativistic dispersion relation approach to photomeson production. *Phys. Rev.*, 106:1345–1355, 1957. doi: 10.1103/PhysRev.106.1345.

[76] J. A. M. Vermaseren. New features of FORM. 2000.

[77] J. Kuipers, T. Ueda, J. A. M. Vermaseren, and J. Vollinga. FORM version 4.0. *Comput. Phys. Commun.*, 184:1453–1467, 2013. doi: 10.1016/j.cpc.2012.12.028.

[78] R. Mertig, M. Bohm, and A. Denner. FEYN CALC: Computer algebraic calculation of Feynman amplitudes. *Comput. Phys. Commun.*, 64:345–359, 1991. doi: 10.1016/0010-4655(91)90130-D.

[79] V. Shtabovenko, R. Mertig, and F. Orellana. New Developments in FeynCalc 9.0. *Comput. Phys. Commun.*, 207:432–444, 2016.

[80] S. Scherer and M. R. Schindler. A Primer for Chiral Perturbation Theory. *Lect. Notes Phys.*, 830:pp.1–338, 2012. doi: 10.1007/978-3-642-19254-8.

[81] V. Pascalutsa and D. R. Phillips. Effective theory of the delta(1232) in Compton scattering off the nucleon. *Phys. Rev.*, C67:055202, 2003. doi: 10.1103/PhysRevC.67.055202.

[82] V. Pascalutsa and M. Vanderhaeghen. Electromagnetic nucleon-to-Delta transition in chiral effective-field theory. *Phys. Rev. Lett.*, 95:232001, 2005. doi: 10.1103/PhysRevLett.95.232001.

[83] D. Hornidge. private communication.

[84] S. Schumann et al. Threshold π^0 photoproduction on transverse polarised protons at MAMI. *Phys. Lett.*, B750:252–258, 2015. doi: 10.1016/j.physletb.2015.09.015.

[85] C. Fernandez-Ramirez, A. M. Bernstein, and T. W. Donnelly. Low-Energy D-Wave Effects in Neutral Pion Photoproduction. *Phys. Lett.*, B679:41–44, 2009. doi: 10.1016/j.physletb.2009.07.011.

[86] C. Fernandez-Ramirez, A. M. Bernstein, and T. W. Donnelly. The Unexpected impact of D waves in low-energy neutral pion photoproduction from the proton and the extraction of multipoles. *Phys. Rev.*, C80:065201, 2009. doi: 10.1103/PhysRevC.80.065201.

[87] V. Pascalutsa. Nucleon polarizabilities and Delta-resonance magnetic moment in chiral EFT. *AIP Conf. Proc.*, 1374:370–375, 2011. doi: 10.1063/1.3647162.

[88] M. Schumacher. Polarizability of the nucleon and Compton scattering. *Prog. Part. Nucl. Phys.*, 55:567–646, 2005. doi: 10.1016/j.ppnp.2005.01.033.

[89] S. Ragusa. Third order spin polarizabilities of the nucleon. *Phys. Rev.*, D47:3757–3767, 1993. doi: 10.1103/PhysRevD.47.3757.

[90] S. Ragusa. Third order spin polarizabilities of the nucleon. 2. *Phys. Rev.*, D49:3157–3159, 1994. doi: 10.1103/PhysRevD.49.3157.

[91] T. R. Hemmert. Nucleon Compton scattering in chiral effective field theories. In *Chiral dynamics: Theory and experiment. Proceedings, 3rd Workshop, Newport News, USA, July 17-22, 2000*, pages 214–223, 2000.

[92] B. Pasquini, D. Drechsel, and M. Vanderhaeghen. Nucleon Polarizabilities: Theory. *Eur. Phys. J. ST*, 198:269–285, 2011. doi: 10.1140/epjst/e2011-01494-y.

[93] R. P. Hildebrandt, H. W. Griesshammer, and T. R. Hemmert. Nucleon polarizabilities from deuteron Compton scattering within a Green's-function hybrid approach. *Eur. Phys. J.*, A46:111–137, 2010. doi: 10.1140/epja/i2010-11024-y.

[94] B. R. Holstein and A. M. Nathan. Dispersion relations and the nucleon polarizability. *Phys. Rev.*, D49:6101–6108, 1994. doi: 10.1103/PhysRevD.49.6101.

[95] H. W. Griesshammer and D. Shukla. Nucleon Spin-Polarisabilities from Polarisation Observables in Low-Energy Deuteron Compton Scattering. *Eur. Phys. J.*, A46:249–269, 2010. doi: 10.1140/epja/i2010-11037-6,10.1140/epja/i2012-12076-7. [Erratum: Eur. Phys. J.A48,76(2012)].

[96] A. M. Baldin. Polarizability of nucleons. *Nucl. Phys.*, 18:310–317, 1960.

[97] S. D. Drell and A. C. Hearn. Exact Sum Rule for Nucleon Magnetic Moments. *Phys. Rev. Lett.*, 16:908–911, 1966. doi: 10.1103/PhysRevLett.16.908.

[98] S. B. Gerasimov. A Sum rule for magnetic moments and the damping of the nucleon magnetic moment in nuclei. *Sov. J. Nucl. Phys.*, 2:430–433, 1966. [Yad. Fiz.2,598(1965)].

[99] M. Gell-Mann, M. L. Goldberger, and W. E. Thirring. Use of causality conditions in quantum theory. *Phys. Rev.*, 95:1612–1627, 1954. doi: 10.1103/PhysRev.95.1612.

[100] T. R. Hemmert, B. R. Holstein, J. Kambor, and G. Knochlein. Compton scattering and the spin structure of the nucleon at low-energies. *Phys. Rev.*, D57:5746–5754, 1998. doi: 10.1103/PhysRevD.57.5746.

[101] C. W. Kao, T. Spitzenberg, and M. Vanderhaeghen. Burkhardt-Cottingham sum rule and forward spin polarizabilities in heavy baryon chiral perturbation theory. *Phys. Rev.*, D67:016001, 2003. doi: 10.1103/PhysRevD.67.016001.

[102] J. D. Bjorken. Applications of the Chiral U(6) x (6) Algebra of Current Densities. *Phys. Rev.*, 148:1467–1478, 1966. doi: 10.1103/PhysRev.148.1467.

[103] J. D. Bjorken. Inelastic Scattering of Polarized Leptons from Polarized Nucleons. *Phys. Rev.*, D1:1376–1379, 1970. doi: 10.1103/PhysRevD.1.1376.

[104] H. Burkhardt and W. N. Cottingham. Sum rules for forward virtual Compton scattering. *Annals Phys.*, 56:453–463, 1970. doi: 10.1016/0003-4916(70)90025-4.

[105] B. W. Filippone and X.-D. Ji. The Spin structure of the nucleon. *Adv. Nucl. Phys.*, 26:1, 2001. doi: 10.1007/0-306-47915-X_1.

[106] P. L. Anthony et al. Precision measurement of the proton and deuteron spin structure functions g(2) and asymmetries A(2). *Phys. Lett.*, B553:18–24, 2003. doi: 10.1016/S0370-2693(02)03015-0.

[107] M. Cummings. A Measurement of g_2^p at Low Q^2. *Int. J. Mod. Phys. Conf. Ser.*, 40: 1660025, 2016. doi: 10.1142/S2010194516600259.

[108] H. Dutz et al. First measurement of the Gerasimov-Drell-Hearn sum rule for H-1 from 0.7-GeV to 1.8-GeV at ELSA. *Phys. Rev. Lett.*, 91:192001, 2003. doi: 10.1103/PhysRevLett.91.192001.

[109] J. Ahrens et al. First measurement of the Gerasimov-Drell-Hearn integral for Hydrogen from 200 to 800 MeV. *Phys. Rev. Lett.*, 87:022003, 2001. doi: 10.1103/PhysRevLett.87.022003.

[110] B. Pasquini, P. Pedroni, and D. Drechsel. Higher order forward spin polarizability. *Phys. Lett.*, B687:160–166, 2010. doi: 10.1016/j.physletb.2010.03.007.

[111] A. M. Sandorfi, M. Khandaker, and C. S. Whisnant. Incompatibility of multipole predictions for the nucleon spin polarizability and Drell-Hearn-Gerasimov sum rules. *Phys. Rev.*, D50:R6681–R6685, 1994. doi: 10.1103/PhysRevD.50.R6681.

[112] D. Drechsel, B. Pasquini, and M. Vanderhaeghen. Dispersion relations in real and virtual Compton scattering. *Phys. Rept.*, 378:99–205, 2003. doi: 10.1016/S0370-1573(02)00636-1.

[113] D. Babusci, G. Giordano, A. I. L'vov, G. Matone, and A. M. Nathan. Low-energy Compton scattering of polarized photons on polarized nucleons. *Phys. Rev.*, C58: 1013–1041, 1998. doi: 10.1103/PhysRevC.58.1013.

[114] B. R. Holstein, D. Drechsel, B. Pasquini, and M. Vanderhaeghen. Higher order polarizabilities of the proton. *Phys. Rev.*, C61:034316, 2000. doi: 10.1103/PhysRevC.61.034316.

[115] V. Lensky, J. A. McGovern, D. R. Phillips, and V. Pascalutsa. What different variants of chiral EFT predict for the proton Compton differential cross section - and why. *Phys. Rev.*, C86:048201, 2012. doi: 10.1103/PhysRevC.86.048201.

[116] V. Lensky and J. A. McGovern. Proton polarizabilities from Compton data using covariant chiral effective field theory. *Phys. Rev.*, C89(3):032202, 2014. doi: 10.1103/PhysRevC.89.032202.

[117] B. R. Holstein and S. Scherer. Hadron Polarizabilities. *Ann. Rev. Nucl. Part. Sci.*, 64:51–81, 2014. doi: 10.1146/annurev-nucl-102313-025555.

[118] V. Bernard, N. Kaiser, J. Kambor, and Ulf-G. Meissner. Chiral structure of the nucleon. *Nucl. Phys.*, B388:315–345, 1992. doi: 10.1016/0550-3213(92)90615-I.

[119] V. Bernard, E. Epelbaum, H. Krebs, and Ulf-G. Meissner. New insights into the spin structure of the nucleon. *Phys. Rev.*, D87(5):054032, 2013. doi: 10.1103/PhysRevD.87.054032.

[120] V. Lensky, J. McGovern, and V. Pascalutsa. Predictions of covariant chiral perturbation theory for nucleon polarisabilities and polarised Compton scattering. *Eur. Phys. J.*, C75(12):604, 2015. doi: 10.1140/epjc/s10052-015-3791-0.

[121] K. B. Vijaya Kumar, A. Faessler, T. Gutsche, B. R. Holstein, and V. E. Lyubovitskij. Hyperon forward spin polarizabilty gamma0. *Phys. Rev.*, D84:076007, 2011. doi: 10.1103/PhysRevD.84.076007.

[122] A. N. Hiller Blin. Forward Polarizability of Hyperons in Chiral Perturbation Theory. *Diploma Thesis in Eberhard-Karls Universität Tübingen*, 2013.

[123] R. P. Hildebrandt, H. W. Griesshammer, and T. R. Hemmert. Spin polarizabilities of the nucleon from polarized low-energy Compton scattering. *Eur. Phys. J.*, A20:329–344, 2004. doi: 10.1140/epja/i2003-10154-7.

[124] K. A. Olive et al. Review of Particle Physics. *Chin. Phys.*, C38:090001, 2014. doi: 10.1088/1674-1137/38/9/090001.

[125] M. Engelhardt. Exploration of the electric spin polarizability of the neutron in lattice QCD. *PoS*, LATTICE2011:153, 2011.

[126] W. Detmold, B. C. Tiburzi, and A. Walker-Loud. Electromagnetic and spin polarisabilities in lattice QCD. *Phys. Rev.*, D73:114505, 2006. doi: 10.1103/PhysRevD.73.114505.

[127] C. F. Perdrisat, V. Punjabi, and M. Vanderhaeghen. Nucleon Electromagnetic Form Factors. *Prog. Part. Nucl. Phys.*, 59:694–764, 2007. doi: 10.1016/j.ppnp.2007.05.001.

[128] V. Punjabi, C. F. Perdrisat, M. K. Jones, E. J. Brash, and C. E. Carlson. The Structure of the Nucleon: Elastic Electromagnetic Form Factors. *Eur. Phys. J.*, A51:79, 2015. doi: 10.1140/epja/i2015-15079-x.

[129] R. Hofstadter and R. W. McAllister. Electron Scattering From the Proton. *Phys. Rev.*, 98:217–218, 1955. doi: 10.1103/PhysRev.98.217.

[130] M. R. Yearian and R. Hofstadter. Magnetic Form Factor of the Neutron. *Phys. Rev.*, 110(2):552, 1958. doi: 10.1103/PhysRev.110.552.

[131] R. Hofstadter. Electron scattering and nuclear structure. *Rev. Mod. Phys.*, 28:214–254, 1956. doi: 10.1103/RevModPhys.28.214.

[132] R. Hofstadter. On nucleon structure. In *Proceedings, 9th International Conference on High Energy Physics, v.1-2 (ICHEP59): Kiev, USSR, Jul 15-25, 1959*, volume Vol.1, pages 355–377, 1960. URL `https://inspirehep.net/record/1280981/files/c59-07-15-p355.pdf`.

[133] J. C. Bernauer et al. High-precision determination of the electric and magnetic form factors of the proton. *Phys. Rev. Lett.*, 105:242001, 2010. doi: 10.1103/PhysRevLett.105.242001.

[134] R. Pohl et al. The size of the proton. *Nature*, 466:213–216, 2010. doi: 10.1038/nature09250.

[135] U. D. Jentschura. Lamb Shift in Muonic Hydrogen. II. Analysis of the Discrepancy of Theory and Experiment. *Annals Phys.*, 326:516–533, 2011. doi: 10.1016/j.aop.2010.11.011.

[136] M. O. Distler, J. C. Bernauer, and T. Walcher. The RMS Charge Radius of the Proton and Zemach Moments. *Phys. Lett.*, B696:343–347, 2011. doi: 10.1016/j.physletb.2010.12.067.

[137] C. E. Carlson and M. Vanderhaeghen. Higher order proton structure corrections to the Lamb shift in muonic hydrogen. *Phys. Rev.*, A84:020102, 2011. doi: 10.1103/PhysRevA.84.020102.

[138] G. A. Miller, A. W. Thomas, J. D. Carroll, and J. Rafelski. Natural Resolution of the Proton Size Puzzle. *Phys. Rev.*, A84:020101, 2011. doi: 10.1103/PhysRevA.84.020101.

[139] K. Griffioen, C. Carlson, and S. Maddox. Consistency of electron scattering data with a small proton radius. *Phys. Rev.*, C93(6):065207, 2016. doi: 10.1103/PhysRevC.93.065207.

[140] H. W. Hammer and Ulf-G. Meissner. Updated dispersion theoretical analysis of the nucleon electromagnetic form-factors. *Eur. Phys. J.*, A20(3):469–473, 2004. doi: 10.1140/epja/i2003-10223-y.

[141] M. A. Belushkin, H. W. Hammer, and Ulf-G. Meissner. Novel evaluation of the two-pion contribution to the nucleon isovector form-factors. *Phys. Lett.*, B633:507–511, 2006. doi: 10.1016/j.physletb.2005.12.053.

[142] T. Yamazaki, Y. Aoki, T. Blum, H.-W. Lin, S. Ohta, S. Sasaki, R. Tweedie, and J. Zanotti. Nucleon form factors with 2+1 flavor dynamical domain-wall fermions. *Phys. Rev.*, D79:114505, 2009. doi: 10.1103/PhysRevD.79.114505.

[143] S. N. Syritsyn et al. Nucleon Electromagnetic Form Factors from Lattice QCD using 2+1 Flavor Domain Wall Fermions on Fine Lattices and Chiral Perturbation Theory. *Phys. Rev.*, D81:034507, 2010. doi: 10.1103/PhysRevD.81.034507.

[144] C. Alexandrou, M. Brinet, J. Carbonell, M. Constantinou, P. A. Harraud, P. Guichon, K. Jansen, T. Korzec, and M. Papinutto. Nucleon electromagnetic form factors in twisted mass lattice QCD. *Phys. Rev.*, D83:094502, 2011. doi: 10.1103/PhysRevD.83.094502.

[145] S. Collins et al. Dirac and Pauli form factors from lattice QCD. *Phys. Rev.*, D84:074507, 2011. doi: 10.1103/PhysRevD.84.074507.

[146] J. D. Bratt et al. Nucleon structure from mixed action calculations using 2+1 flavors of asqtad sea and domain wall valence fermions. *Phys. Rev.*, D82:094502, 2010. doi: 10.1103/PhysRevD.82.094502.

[147] N. Kaiser. Spectral functions of isoscalar scalar and isovector electromagnetic form-factors of the nucleon at two loop order. *Phys. Rev.*, C68:025202, 2003. doi: 10.1103/PhysRevC.68.025202.

[148] V. Bernard, H. W. Fearing, T. R. Hemmert, and Ulf-G. Meissner. The form-factors of the nucleon at small momentum transfer. *Nucl. Phys.*, A635:121–145, 1998. doi: 10.1016/S0375-9474(98)00175-4,10.1016/S0375-9474(98)00566-1. [Erratum: Nucl. Phys.A642,563(1998)].

[149] F.-J. Jiang and B. C. Tiburzi. Hyperon Electromagnetic Properties in Two-Flavor Chiral Perturbation Theory. *Phys. Rev.*, D81:034017, 2010. doi: 10.1103/PhysRevD.81.034017.

[150] B. Kubis and Ulf-G. Meissner. Low-energy analysis of the nucleon electromagnetic form-factors. *Nucl. Phys.*, A679:698–734, 2001. doi: 10.1016/S0375-9474(00)00378-X.

[151] S. J. Brodsky, H.-C. Pauli, and S. S. Pinsky. Quantum chromodynamics and other field theories on the light cone. *Phys. Rept.*, 301:299–486, 1998. doi: 10.1016/S0370-1573(97)00089-6.

[152] P. A. M. Dirac. Forms of Relativistic Dynamics. *Rev. Mod. Phys.*, 21:392–399, 1949. doi: 10.1103/RevModPhys.21.392.

[153] H. Leutwyler and J. Stern. Relativistic Dynamics on a Null Plane. *Annals Phys.*, 112:94, 1978. doi: 10.1016/0003-4916(78)90082-9.

[154] G. Peter Lepage and S. J. Brodsky. Exclusive Processes in Perturbative Quantum Chromodynamics. *Phys. Rev.*, D22:2157, 1980. doi: 10.1103/PhysRevD.22.2157.

[155] G. Hohler, E. Pietarinen, I. Sabba Stefanescu, F. Borkowski, G. G. Simon, V. H. Walther, and R. D. Wendling. Analysis of Electromagnetic Nucleon Form-Factors. *Nucl. Phys.*, B114:505–534, 1976. doi: 10.1016/0550-3213(76)90449-1.

[156] M. A. Belushkin, H. W. Hammer, and Ulf-G. Meissner. Dispersion analysis of the nucleon form-factors including meson continua. *Phys. Rev.*, C75:035202, 2007. doi: 10.1103/PhysRevC.75.035202.

[157] G. A. Miller, M. Strikman, and C. Weiss. Realizing vector meson dominance with transverse charge densities. *Phys. Rev.*, C84:045205, 2011. doi: 10.1103/PhysRevC.84.045205.

[158] M. Strikman and C. Weiss. Quantifying the nucleon's pion cloud with transverse charge densities. *Phys. Rev.*, C82:042201, 2010. doi: 10.1103/PhysRevC.82.042201.

[159] C. Granados and C. Weiss. Chiral dynamics and peripheral transverse densities. *JHEP*, 01:092, 2014. doi: 10.1007/JHEP01(2014)092.

[160] D. W. Higinbotham, A. A. Kabir, V. Lin, D. Meekins, B. Norum, and B. Sawatzky. Proton radius from electron scattering data. *Phys. Rev.*, C93(5):055207, 2016. doi: 10.1103/PhysRevC.93.055207.

[161] J. C. Bernauer. *Measurement of the elastic electron-proton cross section and separation of the electric and magnetic form factor in the Q^2 range from 0.004 to 1 (GeV/c)^2*. PhD thesis, Mainz U., Inst. Kernphys., 2010. URL `http://wwwa1.kph.uni-mainz.de/A1/publications/doctor/bernauer.pdf`.

[162] D. Drechsel, O. Hanstein, S. S. Kamalov, and L. Tiator. A Unitary isobar model for pion photoproduction and electroproduction on the proton up to 1-GeV. *Nucl. Phys.*, A645:145–174, 1999. doi: 10.1016/S0375-9474(98)00572-7.

[163] R. Machleidt, K. Holinde, and C. Elster. The Bonn Meson Exchange Model for the Nucleon Nucleon Interaction. *Phys. Rept.*, 149:1–89, 1987. doi: 10.1016/S0370-1573(87)80002-9.

[164] R. Machleidt. The High precision, charge dependent Bonn nucleon-nucleon potential (CD-Bonn). *Phys. Rev.*, C63:024001, 2001. doi: 10.1103/PhysRevC.63.024001.

[165] C. B. Dover and A. Gal. HYPERON NUCLEUS POTENTIALS. *Prog. Part. Nucl. Phys.*, 12:171–239, 1985. doi: 10.1016/0146-6410(84)90004-8.

[166] D. E. Soper. The Parton Model and the Bethe-Salpeter Wave Function. *Phys. Rev.*, D15:1141, 1977. doi: 10.1103/PhysRevD.15.1141.

[167] M. Burkardt. Impact parameter dependent parton distributions and off forward parton distributions for zeta $\to$ 0. *Phys. Rev.*, D62:071503, 2000. doi: 10.1103/PhysRevD.62.071503,10.1103/PhysRevD.66.119903. [Erratum: Phys. Rev.D66,119903(2002)].

[168] G. A. Miller. Densities, Parton Distributions, and Measuring the Non-Spherical Shape of the Nucleon. *Phys. Rev.*, C76:065209, 2007. doi: 10.1103/PhysRevC.76.065209.

[169] A. D. Sakharov. Violation of CP Invariance, c Asymmetry, and Baryon Asymmetry of the Universe. *Pisma Zh. Eksp. Teor. Fiz.*, 5:32–35, 1967. doi: 10.1070/PU1991v034n05ABEH002497. [Usp. Fiz. Nauk161,61(1991)].

[170] M. B. Gavela, P. Hernandez, J. Orloff, and O. Pene. Standard model CP violation and baryon asymmetry. *Mod. Phys. Lett.*, A9:795–810, 1994. doi: 10.1142/S0217732394000629.

[171] M. B. Gavela, P. Hernandez, J. Orloff, O. Pene, and C. Quimbay. Standard model CP violation and baryon asymmetry. Part 2: Finite temperature. *Nucl. Phys.*, B430:382–426, 1994. doi: 10.1016/0550-3213(94)00410-2.

[172] R. D. Peccei and H. R. Quinn. Constraints Imposed by CP Conservation in the Presence of Instantons. *Phys. Rev.*, D16:1791–1797, 1977. doi: 10.1103/PhysRevD.16.1791.

[173] R. J. Crewther, P. Di Vecchia, G. Veneziano, and E. Witten. Chiral Estimate of the Electric Dipole Moment of the Neutron in Quantum Chromodynamics. *Phys. Lett.*, B88:123, 1979. doi: 10.1016/0370-2693(80)91025-4,10.1016/0370-2693(79)90128-X. [Erratum: Phys. Lett.B91,487(1980)].

[174] K. Kawarabayashi and N. Ohta. On the Partial Conservation of the U(1) Current. *Prog. Theor. Phys.*, 66:1789, 1981. doi: 10.1143/PTP.66.1789.

[175] S. Dar. The Neutron EDM in the SM: A Review. hep-ph/0008248, 2000.

[176] A. Pich and E. de Rafael. Strong CP violation in an effective chiral Lagrangian approach. *Nucl. Phys.*, B367:313–333, 1991. doi: 10.1016/0550-3213(91)90019-T.

[177] Mikhail Gorchtein. Nucleon EDM and rare decays of eta and eta-prime mesons. hep-ph/0803.2906, 2008.

[178] C. Jarlskog and E. Shabalin. How large are the rates of the CP violating eta, eta-prime → pi pi decays? *Phys. Rev.*, D52:248–253, 1995. doi: 10.1103/PhysRevD.52.248.

[179] R. Aaij et al. Search for the *CP*-violating strong decays $\eta \to \pi^+\pi^-$ and $\eta'(958) \to \pi^+\pi^-$. 2016.

[180] T. Feldmann, P. Kroll, and B. Stech. Mixing and decay constants of pseudoscalar mesons. *Phys. Rev.*, D58:114006, 1998. doi: 10.1103/PhysRevD.58.114006.

[181] J. L. Goity, A. M. Bernstein, and B. R. Holstein. The Decay pi0 → gamma gamma to next to leading order in chiral perturbation theory. *Phys. Rev.*, D66:076014, 2002. doi: 10.1103/PhysRevD.66.076014.

[182] B. Aubert et al. Measurement of the eta and eta-prime transition form-factors at q**2 = 112-GeV**2. *Phys. Rev.*, D74:012002, 2006. doi: 10.1103/PhysRevD.74.012002.

[183] F. Ambrosino et al. A Global fit to determine the pseudoscalar mixing angle and the gluonium content of the eta-prime meson. *JHEP*, 07:105, 2009. doi: 10.1088/1126-6708/2009/07/105.

[184] V. Mathieu and V. Vento. Pseudoscalar glueball and eta - eta-prime mixing. *Phys. Rev.*, D81:034004, 2010. doi: 10.1103/PhysRevD.81.034004.

[185] R. Escribano, P. Masjuan, and P. Sanchez-Puertas. The η transition form factor from space- and time-like experimental data. *Eur. Phys. J.*, C75(9):414, 2015. doi: 10.1140/epjc/s10052-015-3642-z.

[186] A. A. Osipov, B. Hiller, and A. H. Blin. The $\pi^0 - \eta - \eta'$ mixing in a generalized multiquark interaction scheme. *Phys. Rev.*, D93(11):116005, 2016. doi: 10.1103/PhysRevD.93.116005.

[187] L. Tiator, C. Bennhold, and S. S. Kamalov. The Eta N N coupling in eta photoproduction. *Nucl. Phys.*, A580:455–474, 1994. doi: 10.1016/0375-9474(94)90909-1.

[188] W.-T. Chiang, S.-N. Yang, L. Tiator, and D. Drechsel. An Isobar model for eta photoproduction and electroproduction on the nucleon. *Nucl. Phys.*, A700:429–453, 2002. doi: 10.1016/S0375-9474(01)01325-2.

[189] T. E. O. Ericson and W. Weise. *Pions and Nuclei*, volume 74 of *International Series of Monographs on Physics*. Clarendon Press, Oxford, UK, 1988. ISBN 0198520085.

[190] M. E. Peskin and D. V. Schroeder. *An Introduction to quantum field theory*. 1995. ISBN 9780201503975, 0201503972.

[191] A. Heck. FORM for Pedestrians. 2000. URL `https://www.nikhef.nl/~form/maindir/documentation/tutorial/online/online.html`.

[192] J. A. M. Vermaseren, J. Kuipers, M. Tentyukov, T. Ueda, and J. Vollinga. FORM version 4.1 Reference manual. 2013. URL `https://www.nikhef.nl/~form/maindir/documentation/reference/online/online.html`.

[193] Wolfram Research Inc. Mathematica, Version 11.0, Champaign, Illinois (2016).

[194] T. Hahn. Feynman Diagram Calculations with FeynArts, FormCalc, and LoopTools. *PoS*, ACAT2010:078, 2010.

[195] F. James. MINUIT Function Minimization and Error Analysis: Reference Manual Version 94.1. 1994.

[196] A. M. Stasto, K. J. Golec-Biernat, and J. Kwiecinski. Geometric scaling for the total gamma* p cross-section in the low x region. *Phys. Rev. Lett.*, 86:596–599, 2001. doi: 10.1103/PhysRevLett.86.596.

[197] L. N. Hand, D. G. Miller, and R. Wilson. Electric and Magnetic Formfactor of the Nucleon. *Rev. Mod. Phys.*, 35:335, 1963. doi: 10.1103/RevModPhys.35.335.

[198] G. G. Simon, C. Schmitt, F. Borkowski, and V. H. Walther. Absolute electron Proton Cross-Sections at Low Momentum Transfer Measured with a High Pressure Gas Target System. *Nucl. Phys.*, A333:381–391, 1980. doi: 10.1016/0375-9474(80)90104-9.

[199] F. Borkowski, P. Peuser, G. G. Simon, V. H. Walther, and R. D. Wendling. Electromagnetic Form-Factors of the Proton at Low Four-Momentum Transfer. *Nucl. Phys.*, B93:461–478, 1975. doi: 10.1016/0550-3213(75)90514-3.

[200] J. J. Murphy, Y. M. Shin, and D. M. Skopik. Proton form factor from 0.15 to 0.79 fm-2. *Phys. Rev.*, C9:2125–2129, 1974. doi: 10.1103/PhysRevC.9.2125,10.1103/PhysRevC.10.2111. [Erratum: Phys. Rev.C10,2111(1974)].

[201] R. P. Hildebrandt, H. W. Griesshammer, T. R. Hemmert, and B. Pasquini. Signatures of chiral dynamics in low-energy compton scattering off the nucleon. *Eur. Phys. J.*, A20:293–315, 2004. doi: 10.1140/epja/i2003-10144-9.

[202] S. Weinberg. Effective chiral Lagrangians for nucleon - pion interactions and nuclear forces. *Nucl. Phys.*, B363:3–18, 1991. doi: 10.1016/0550-3213(91)90231-L.

[203] P. A. M. Guichon, G. Q. Liu, and A. W. Thomas. Virtual Compton scattering and generalized polarizabilities of the proton. *Nucl. Phys.*, A591:606–638, 1995. doi: 10.1016/0375-9474(95)00217-O.

[204] V. Pascalutsa and M. Vanderhaeghen. The Nucleon and delta-resonance masses in relativistic chiral effective-field theory. *Phys. Lett.*, B636:31–39, 2006. doi: 10.1016/j.physletb.2006.03.023.

[205] C. Alexandrou, T. Korzec, G. Koutsou, C. Lorce, J. W. Negele, V. Pascalutsa, A. Tsapalis, and M. Vanderhaeghen. Quark transverse charge densities in the Delta(1232) from lattice QCD. *Nucl. Phys.*, A825:115–144, 2009. doi: 10.1016/j.nuclphysa.2009.04.005.

[206] J. M. Alarcon, V. Lensky, and V. Pascalutsa. Chiral perturbation theory of muonic hydrogen Lamb shift: polarizability contribution. *Eur. Phys. J.*, C74(4):2852, 2014. doi: 10.1140/epjc/s10052-014-2852-0.

[207] X.-L. Ren, L. S. Geng, and J. Meng. Scalar strangeness content of the nucleon and baryon sigma terms. *Phys. Rev.*, D91(5):051502, 2015. doi: 10.1103/PhysRevD.91.051502.

[208] S. Aoki et al. Review of lattice results concerning low-energy particle physics. *Eur. Phys. J.*, C74:2890, 2014. doi: 10.1140/epjc/s10052-014-2890-7.

[209] X.-L. Ren, L. S. Geng, J. Martin Camalich, J. Meng, and H. Toki. Octet baryon masses in next-to-next-to-next-to-leading order covariant baryon chiral perturbation theory. *JHEP*, 12:073, 2012. doi: 10.1007/JHEP12(2012)073.

[210] X.-L. Ren, L. S. Geng, J. Meng, and H. Toki. Virtual decuplet effects on octet baryon masses in covariant baryon chiral perturbation theory. *Phys. Rev.*, D87(7):074001, 2013. doi: 10.1103/PhysRevD.87.074001.

[211] J. M. Alarcon, J. Martin Camalich, J. A. Oller, and L. Alvarez-Ruso. πN scattering in relativistic baryon chiral perturbation theory revisited. *Phys. Rev.*, C83:055205, 2011. doi: 10.1103/PhysRevC.83.055205,10.1103/PhysRevC.87.059901. [Erratum: Phys. Rev.C87,no.5,059901(2013)].

[212] T. Becher and H. Leutwyler. Low energy analysis of pi N $\to$ pi N. *JHEP*, 06:017, 2001. doi: 10.1088/1126-6708/2001/06/017.

[213] J. M. Alarcon, L. S. Geng, J. Martin Camalich, and J. A. Oller. The strangeness content of the nucleon from effective field theory and phenomenology. *Phys. Lett.*, B730:342–346, 2014. doi: 10.1016/j.physletb.2014.01.065.

[214] G. Gabadadze and M. Shifman. QCD vacuum and axions: What's happening? *Int. J. Mod. Phys.*, A17:3689–3728, 2002. doi: 10.1142/S0217751X02011357.

[215] R. Golub and K. Lamoreaux. Neutron electric dipole moment, ultracold neutrons and polarized He-3. *Phys. Rept.*, 237:1–62, 1994. doi: 10.1016/0370-1573(94)90084-1.

[216] E. P. Shabalin. THE ELECTRIC DIPOLE MOMENT OF THE NEUTRON IN A GAUGE THEORY. *Sov. Phys. Usp.*, 26:297, 1983. doi: 10.1070/PU1983v026n04ABEH004331. [Usp. Fiz. Nauk139,561(1983)].

[217] B. C. Regan, E. D. Commins, C. J. Schmidt, and D. DeMille. New limit on the electron electric dipole moment. *Phys. Rev. Lett.*, 88:071805, 2002. doi: 10.1103/PhysRevLett.88.071805.

[218] J. J Hudson, B. E. Sauer, M. R. Tarbutt, and E. A. Hinds. Measurement of the electron electric dipole moment using YbF molecules. *Phys. Rev. Lett.*, 89:023003, 2002. doi: 10.1103/PhysRevLett.89.023003.

[219] D. DeMille, F. Bay, S. Bickman, D. Kawall, D. Krause, S. E. Maxwell, and L. R. Hunter. Investigation of PbO as a system for measuring the electric dipole moment of the electron. *Phys. Rev.*, A61:052507, 2000. doi: 10.1103/PhysRevA.61.052507.

[220] P. G. Harris et al. New experimental limit on the electric dipole moment of the neutron. *Phys. Rev. Lett.*, 82:904–907, 1999. doi: 10.1103/PhysRevLett.82.904.

[221] C. A. Baker et al. An Improved experimental limit on the electric dipole moment of the neutron. *Phys. Rev. Lett.*, 97:131801, 2006. doi: 10.1103/PhysRevLett.97.131801.

[222] M. M. Dalton et al. Electroproduction of Eta Mesons in the S(11)(1535) Resonance Region at High Momentum Transfer. *Phys. Rev.*, C80:015205, 2009. doi: 10.1103/PhysRevC.80.015205.

[223] V. N. Gribov. Space-time description of hadron interactions at high-energies. 1973.

[224] S. Weinberg. Dynamics at infinite momentum. *Phys. Rev.*, 150:1313–1318, 1966. doi: 10.1103/PhysRev.150.1313.

[225] J. B. Kogut and D. E. Soper. Quantum Electrodynamics in the Infinite Momentum Frame. *Phys. Rev.*, D1:2901–2913, 1970. doi: 10.1103/PhysRevD.1.2901.

[226] J. D. Bjorken, J. B. Kogut, and D. E. Soper. Quantum Electrodynamics at Infinite Momentum: Scattering from an External Field. *Phys. Rev.*, D3:1382, 1971. doi: 10.1103/PhysRevD.3.1382.

[227] P. G. Ratcliffe. SU(3) breaking in hyperon beta decays: A Prediction for $\Xi^0 \to \Sigma^+ e\bar{\nu}^*$. *Phys.Rev.*, D59:014038, 1999.

[228] B. Kubis and Ulf-G. Meissner. Baryon form-factors in chiral perturbation theory. *Eur.Phys.J.*, C18:747–756, 2001.

[229] J. Beringer et al. Review of Particle Physics (RPP). *Phys.Rev.*, D86:010001, 2012.